Functional Mussel-inspired Coatings with Applications in Wastewater Treatment

by

Wenshuai Yang

A thesis submitted in partial fulfillment of the requirements for the degree of

Doctor of Philosophy

in

Materials Engineering

Department of Chemical and Materials Engineering
University of Alberta

Abstract

In marine bio-systems, robust mussel adhesion is achieved by the formation of a "bio-glue" layer between byssal plaque and substrates. By mimicking this mussel adhesion strategy, many mussel-inspired coatings have been designed for various environmental applications due to their high surface affinity. Nevertheless, it still remains a challenge to integrate different functionalities into these developed mussel-inspired coatings to fulfill the specific requirements of different water treatment processes. Moreover, current understanding of the underlying molecular interaction mechanism in the mussel-inspired coating assembly process is limited. In this thesis, different functional mussel-inspired coatings for eliminating organic pollutants or separating oily contaminants from water are designed and the corresponding molecular interactions in the coating assembly process are also investigated.

Water contamination by organic pollutants poses a serious threat to human health. Most catalysts developed for organic pollutants removal generally suffer from low catalytic efficiency. Herein, in the first work, silver nanoparticles (Ag NPs) functionalized magnetic graphene oxide (MGO) was synthesized with the assistance of a tannic acid (TA)/Fe^{3+} coating. The as-prepared nano-catalyst showed excellent catalytic reduction performance towards different organic pollutants. Specifically, the catalytic rate constant for methylene blue (model dye) removal was up to 0.054 s^{-1}, which was about ten times faster than most reported catalysts. It was also found that the as-prepared nanocomposite showed outstanding removal efficiency of *Escherichia coli* (*E. coli*) and can be easily regenerated through magnetic separation, indicating its potential in various environmental applications.

Oily wastewater generated during the oil refining process is regarded as one of the most hazardous wastes, severely affecting the local water resources. The membrane materials designed for oil/water separation generally suffer from surface fouling issues due to the undesired deposition of oily contaminants on the membrane surface. Thus, in the second project, an antifouling cellulose nanocrystal (CNC) coating was designed by anchoring CNCs onto substrates using a mussel-inspired adhesive layer composed of tannic acid/polyethylenimine/vanadium (TA/PEI/V). The underlying nano-mechanics in the coating process were investigated by applying the atomic force microscope (AFM) colloidal probe technique. The super hydrophilic CNCs coating showed a water contact angle of ~8 ° and exhibited outstanding antifouling properties towards oil contamination, protein adsorption, and cell attachment. The CNCs coating also maintained its structural integrity and wettability after cyclic friction tests. Moreover, the CNCs-coated membrane showed high water permeation flux (~ 6000 L m^{-2} h^{-1} bar^{-1}) and remarkable self-cleaning properties in the oil-in-water (O/W) emulsion separation process, demonstrating its great potential in oily wastewater purification.

Polyethylene glycol (PEG) has been widely applied in the fabrication of antifouling membranes for O/W emulsion separation due to its strong surface hydration property. However, most reported PEG coatings were fabricated by anchoring the PEG polymer chains onto substrates via weak and unstable non-covalent bonds, resulting in PEG coatings that easily detached from substrates. Therefore, in the third project, a durable PEG coating was fabricated by covalently anchoring the poly(ethylene glycol) diglycidyl ether (PEGDE) polymer onto the levodopa/polyethyleneimine (LP)-coated substrate. The PEGDE/LP coating showed outstanding stability and maintained its wettability under harsh solution conditions (acid/alkaline/salt). Moreover, the PEGDE/LP coating showed superior antifouling properties towards different kinds

of proteins such as bovine serum albumin (BSA). The antifouling mechanism of PEGDE/LP coating was investigated by directly measuring the interaction forces between the PEGDE/LP coating and BSA using the surface forces apparatus (SFA). Moreover, the PEGDE/LP-coated membrane could remove more than 99% O/W emulsion with enhanced water flux, indicating the outstanding performance of PEGDE/LP coating for O/W emulsion separation.

In this thesis, three novel functional coatings are developed by integrating different functionalities into mussel-inspired coatings for wastewater treatment. Moreover, the molecular interaction mechanisms during the coating assembly process are investigated. This work not only expands the application of functional mussel-inspired coatings in wastewater treatment processes but also gives new insight into the precise designing of functional coatings with tunable properties for a broad range of engineering and environmental applications.

Preface

Chapter 3 of this thesis was published as Wenshuai Yang, Wenjihao Hu, Jiawen Zhang, Wenda Wang, Ruiqi Cai, Mingfei Pan, Charley Huang, Xingzhen Chen, Bin Yan, and Hongbo Zeng, "Tannic acid/Fe^{3+} functionalized magnetic graphene oxide nanocomposite with high loading of silver nanoparticles as an ultra-efficient catalyst and disinfectant for wastewater treatment," *Chemical Engineering Journal*, 2021, 405, 126629. I designed the research under the supervision of Dr. Hongbo Zeng. I was responsible for the materials design, synthesis, and characterization, catalytic reduction test, data analysis, and manuscript composition. Dr. Ruiqi Cai contributed to the antibacterial test. Dr. Bin Yan contributed to the material magnetic property test. Dr. Wenjihao Hu, Dr. Jiawen Zhang, Dr. Wenda Wang, Mingfei Pan, Charley Huang, and Dr. Xingzhen Chen contributed to the manuscript revision. Dr. Hongbo Zeng and Dr. Bin Yan were the corresponding authors who were involved in concept formation and manuscript composition.

Chapter 4 of this thesis was published as Wenshuai Yang, Mingfei Pan, Jiawen Zhang, Ling Zhang, Fengcai Lin, Xiong Liu, Charley Huang, Xingzhen Chen, Jianmei Wang, Bin Yan, Hongbo Zeng, "A Universal Strategy for Constructing Robust and Antifouling Cellulose Nanocrystal Coating," *Advanced Functional Materials*, 2022, 32, 8, 2109989. I and Mingfei Pan contributed equally to this work. I and Mingfei Pan conceived the research under the supervision of Dr. Hongbo Zeng. I was responsible for the materials design and synthesis, antifouling test, and membrane oil/water separation test, as well as data analysis and the manuscript composition. Mingfei Pan was responsible for the AFM experiment and data analysis. Dr. Xiong Liu contributed to the anti-cell attachment test. Dr. Jiawen Zhang, Dr. Ling Zhang, Dr. Fengcai Lin, Charley Huang, Dr. Xingzhen Chen, Dr. Jianmei Wang, and Dr. Bin Yan contributed to the manuscript revision.

Dr. Hongbo Zeng was the corresponding author who was involved in concept formation and manuscript composition.

Chapter 5 of this thesis will be submitted for publication as Wenshuai Yang, Ziqian Zhao, Mingfei Pan, Lu Gong, Feiyi Wu, Charley Huang, Jianmei Wang, Xiaogang Wang, Hongbo Zeng, "Mussel-Inspired Polyethylene Glycol Coating for Constructing Antifouling Membrane for Water Purification," were submitted to *Journal of Colloid and Interface Science.* I conceived the research under the supervision of Dr. Hongbo Zeng. I designed experiments and conducted the data analysis, as well as manuscript composition. Ziqian Zhao contributed to the SFA force measurement. Feiyi Wu contributed to the surface zeta potential analysis. Mingfei Pan, Dr. Lu Gong, Dr. Jianmei Wang, Dr. Xiaogang Wang, and Charley Huang contributed to the manuscript revision. Dr. Hongbo Zeng was the supervisor and was involved in concept formation and manuscript composition.

Chapter 1, Chapter 2, and Chapter 6 are written by Wenshuai Yang originally.

Acknowledgments

First and foremost, I would like to express my sincere respect and gratitude to my supervisor Prof. Hongbo Zeng, a scholarly and responsible supervisor, who gave me great opportunities to study at the University of Alberta and introduced me to the fantastic world of functional coating materials and intermolecular interactions and helped me develop the critical skills and technical writing skills. I also really appreciate the great academic atmosphere and research facilities provided by Prof. Hongbo Zeng, as well as his insightful guidance, continuous encouragement, and great suggestions throughout my whole Ph.D. career.

Secondly, I would like to thank all my group members for their kindly help in my Ph.D. career. I want to thank Dr. Jiawen Zhang and Dr. Li Xiang for their inspired advice. Many thanks to Mingfei Pan, and Dr. Lu gong for their constant support of my research. I also want to thank Dr. Bin Yan for his great suggestion and help in both my academic research and career planning.

Thirdly, I would like to give my sincere gratitude to the Natural Sciences and Engineering Research Council of Canada (NSERC), the Canada Foundation for Innovation (CFI), the Future Energy Systems under the Canada First Research Excellence Fund, and the lab support from the Canada Foundation for Innovation and the Canada Research Chairs Program.

Finally, I also wish to give thanks to my parents for their continuous support and encouragement in my Ph.D. career. Special thanks to my girlfriend, Shuyao Zhou, as her love and reliable backup always gives me tremendous power to keep moving forward.

Table of Contents

List of Tables

List of Figures

Abbreviations and Symbols

O/W	oil-in-water
NPs	noble metal nanoparticles
Ag	silver
V^{3+}	vanadium ions
Co^{2+}	cobalt ions
Fe^{3+}	ferric ions
Lyso	lysozyme
K-carr	k-carrageenan
FTIC-BSA	fluorescein-conjugated bovine serum albumin
BSA	bovine serum albumin
HA	humic acid
PDA	polydopamine
TA	tannic acid
PVDF	polyvinylidene fluoride
PEI	polyethyleneimine
CNC	cellulose nanocrystal
L-Dopa	levodopa
LP	levodopa/polyethyleneimine
PEG	polyethylene glycol
PEGDE	poly (ethylene glycol) diglycidyl ether
GO	graphene oxide

Tollens' reagent	$Ag(NH_3)_2OH$ solution
Fe_3O_4	iron oxide
4-NP	4-nitrophenol
MB	methylene blue
BB	basic blue
MO	methyl orange
CR	Congo red
E. coli	*Escherichia coli*
CFU	colony-forming units
$NaBH_4$	sodium borohydride
CHO	Chinese hamster ovary
SEM	scanning electron microscopy
EDX	energy dispersive X-ray spectroscopy
FESEM	field emission scanning electron microscope
UV-Vis	ultraviolet-visible
QCM-D	quartz crystal microbalance with dissipation monitoring
TEM	transmission electron microscopy
HAAD-STEM	high angle annular dark-field scanning TEM
XPS	X-ray photoelectron spectroscopy
XRD	X-ray diffraction
BET	Brunauer–Emmett–Teller
IPC-MS	inductively coupled plasma mass spectrometry
RMS	root-mean-square

FT-IR	Fourier transforms infrared spectroscopy
SFA	surface forces apparatus
MBI	multiple beam interferometry
FECO	fringes of equal chromatic order
WCA	water in air contact angle
OCA	oil in water contact angle
AFM	atomic force microscope
TOC	total organic carbon
Δm	mass of protein adsorbed onto the sensor
Δf	change of frequency
C_0, C_t	initial and final concentrations of organic pollutants
t	time
k	catalytic rate constant
VSM	vibrating-sample magnetometer

Chapter 1. Introduction

The freshwater resource is of fundamental importance to daily human life.[1, 2] However, according to the World Resource Institute (WRI), more than half of the world's population will face water-stressed conditions before 2040.[3-5] As shown in Figure 1.1, only limited amount of freshwater (~1%) can be directly accessible.[6] However, the limited freshwater resource also faces severe contamination issues caused by untreated sewage and industrial effluents.[7-9]

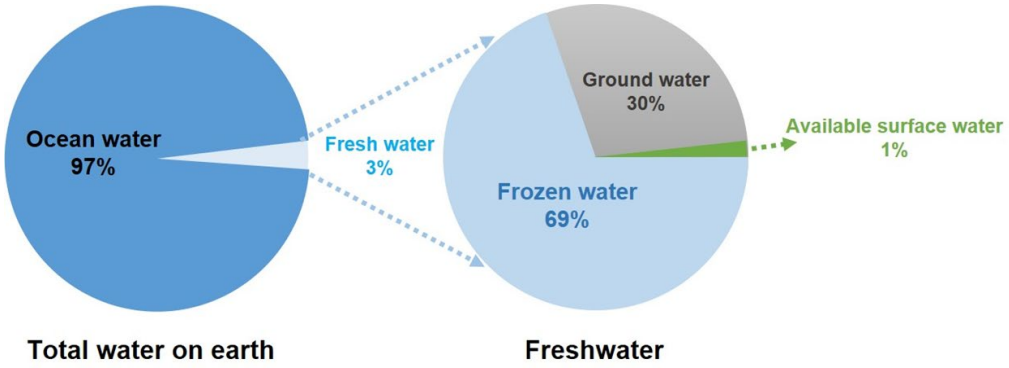

Figure 1.1 Water distribution on earth

Water contamination caused by organic pollutants, such as organic dyes or nitrophenols from textile or pesticide industries, has been one of the major concerns in recent years.[10, 11] For example, organic dyes are visible in water even with a concentration less than 1 ppm.[12] High concentration of organic dye in the water system will severely affect the photosynthesis of aquatic organisms.[13] Moreover, most organic pollutants, such as 4-nitrophenol, are highly poisonous and non-biodegradable, [14] which may pose a great threat to human health.[15-17] Thus, techniques that can effectively remove these organic pollutants from water systems are still highly desired.

Additionally, oil industries play an important role in the economy.[18] As more oil-related produces are explored, processed, and transported, the number of oil spill accidents also increases and has become another great environmental concern.[19-21] The leaked oil can cause severe

consequences to the living species in the water system,[22, 23] and may lead to a long-term impact on the sustainability of the aquatic ecosystem.[24, 25] Thus, developing effective methods to remove the oily contaminants from water is still in highly desired.

1.1 Removal of organic pollutants from water

1.1.1 Organic pollutants and their toxicity

Organic dyes are widely applied in the printing, textile, and paper industries. It is estimated that over 100,000 kinds of commercial organic dyes are produced every year with a total amount of over 1,000,000 tons,[26, 27] and more than 200 billion liters of colored effluents are produced annually.[14] As shown in Figure 1.2, the organic dyes generally have a π-conjugated system with one or more chromophore groups in their structure,[28] which can absorb visible light (400~700 nm). Thus, the dispersed dyes can reduce light penetration into water systems, leading to the death of aquatic plants by disrupting their photosynthesis.[29] Moreover, dye-polluted wastewater is highly toxic and may cause cancer or severe allergic reactions to humans.[30]

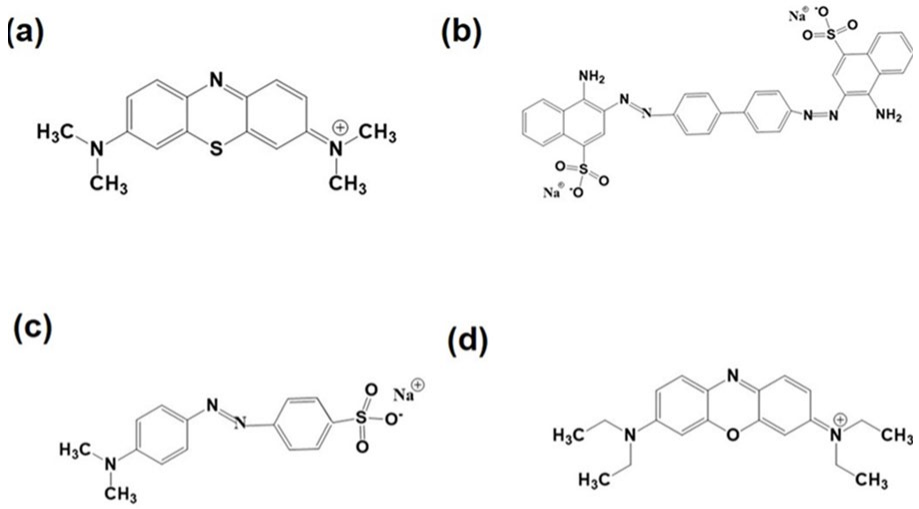

Figure 1.2 Chemical structure of (a) Methylene blue, (b) Congo red, (c) Methyl Orange, and (d) Basic blue.

Similar to organic dyes, nitrophenols produced in the pesticide production process are another category of organic pollutants.[31] Exposure to nitrophenols, such as 4-nitrophenol, may also lead to significant health risks, such as severe liver/kidney damage or skin irritation to humans.[32, 33] Thus, effective methods for the removal of organic pollutants are of great importance.

1.1.2 Methods for removal of organic pollutants

Numerous water treatment strategies have been developed and applied to remove the dispersed organic pollutants from the water. Existing methods can be divided into three categories, namely physical, biological, and chemical treatment methods.[34]

Physical methods, such as adsorption,[35] membrane filtration,[36] reverse osmosis,[37] coagulation and flocculation,[38] are straightforward approaches and widely applied in industries due to their ease of operation. However, these methods are generally costly and may require additional post-treatments. For example, adsorbents for dye removal suffer from severe fouling

issues in the practical application process. The small particles will continuously accumulate within the adsorbent, thus deteriorating its dye adsorption efficiency.[39]

Biological methods use living organisms,[40] such as bacteria [41] or fungi,[42] to degrade the organic pollutants. The utilization of microorganisms to remove dyes is popular due to its advantages of being environmentally friendly or having low cost. However, most biological methods need a long operation time and are only effective for certain types of dyes.[43] Moreover, time-consuming post-treatment processes may be required to prevent secondary pollution.

Chemical methods, such as oxidation,[44] irradiation,[45] Fenton reaction,[46], or catalytic reduction,[47] are commonly applied to degrade organic pollutants through designed chemical reaction processes. For example, in the Fenton reaction process, Fenton reagents are applied to generate a powerful oxidizing agent (•OH groups), which can effectively degrade the organic pollutants into non-toxic products.[48, 49] However, most chemical treatment methods require high amounts of energy and may generate toxic by-products in the reaction process, which limits their application in water treatment processes. Recently, catalytic reduction of organic pollutants by using noble metal nanoparticles (NPs), such as silver (Ag) NPs,[50] gold NPs,[51] or platinum NPs,[52] have been widely applied due to their ease of operation, high efficiency, and low energy consumption.

1.1.3 Catalytic reduction of organic pollutants

The catalytic reduction of organic pollutants is an electrochemical reaction process, which only happens on the surface of NPs.[53] The organic pollutants will first be adsorbed on the NPs before the catalytic reduction process begins. Then, the NPs serve as electron relays to transfer electrons from nucleophilic ions to the adsorbed organic pollutants, leading to the reduction of

organic pollutants into non-toxic produces.[54] The reduced products will automatically desorb from NPs surface and render new sites for the next catalytic reduction cycle. The catalytic rate constant can be expressed by the pseudo-first-order kinetic model: $\ln(C_t/C_0) = -kt$, where the C_0 and $C_t$were the initial and final concentrations of organic pollutants, t and k were time and catalytic rate constant, respectively.[55] The catalytic reduction rate constant can be affected by the solution conditions and size of NPs applied in the reaction process. Specifically, the smaller and non-aggregated NPs show higher catalytic performance due to their high surface-to-volume ratio.[56, 57] However, most reported NPs nano-catalysts are unstable in solution and will easily aggregate in aqueous environments, resulting in limited catalytic performance.

1.1.4 Mussel-inspired coating for catalyst immobilization

In order to prevent the aggregation of NPs in the catalytic reduction process, much effort has been devoted to immobilizing NPs onto various supporting materials with the assistance of an intermediate adhesive layer.[53, 58-60]

In the mussel adhesion process, mussel foot proteins (Mfps) play an important role to achieve robust mussel adhesion.[61, 62] By mimicking the solidification process of the Mfps, in 2007, *Messersmith et al.* fabricated a polydopamine (PDA) coating via oxidative polymerization of dopamine.[63] The formed PDA coating showed high surface affinity, which was able to adhere onto various surfaces via multiple interactions. Moreover, the functional groups on the PDA coating, such as amine, quinone, and catechol groups, showed strong reducing and metal ion chelating ability,[64-66] which can serve as an interlayer to reduce the metal ions into small NPs and tightly anchor these NPs onto supporting materials via coordination bonds.

However, the application of PDA coating in catalyst immobilization is limited due to its slow reaction rate, as it may take several hours to form the PDA coating on the substrate.[67] Recently, tannic acid (TA), a low-cost natural polyphenol with strong surface adhesion property,[68] has been shown to form a surface coating within minutes by co-deposition with metal ions.[69-71] For instance, in 2013, *Ejima et al.* reported a one-step coating by mixing TA and Fe^{3+} solutions under ambient conditions.[72] The uniform TA/Fe^{3+} coating was formed onto various substrates within one minute through coordination between TA and Fe^{3+} ions. The formed TA/Fe^{3+} coating showed similar reducing and metal ion chelating properties as PDA coating, which makes the TA/Fe^{3+} coating a promising candidate for immobilizing NPs onto substrates. For instance, *Li et al.* successfully immobilized Ag NPs (2~10 nm) onto TA/Fe^{3+} coated-nanospheres, which showed good stability for 4-nitrophenol reduction.[73] Even though much effort was devoted to fabricate NPs-based nano-catalysts, the catalytic rate constant of most reported catalysts are still low due to the limited NPs in the catalyst. Thus, fabrication of the NPs catalyst with outstanding catalytic performance towards various organic pollutants is still highly desired.

1.2 Removal of oily contaminants from water

With the rapid expansion of oil-related industries (such as mining, textile, or leather), plenty of the oily wastewater produced in our daily life is released into the water system. For instance, the 2010 Gulf of Mexico oil spill accidence caused 4.9 million barrels of crude oil to leak into the ocean and contaminated over 3200 km of seaside.[74, 75] Once these oily contaminants get into the water system, [76-78] three different oil-in-water(O/W) mixtures will be formed, including the free-floating oil (>150 μm), O/W mixtures (20–150 μm), and O/W emulsions (<20 μm).[79] The free-floating oil and O/W mixture will autonomously coalesce and separate from the water phase and can be easily removed from water phases.[80] However, the O/W emulsions are much more

stable in aqueous environments because of the adsorbed surfactants at the O/W interface.[81] Thus, separation of highly dispersed and stable O/W emulsion droplets (with a size smaller than 20 μm) from the aqueous phase is considered to be the most challenging task.

1.2.1 Methods of oily wastewater treatment

Various conventional techniques have been applied for the O/W emulsion separation. Chemical treatment methods, such as electrochemical method [82] or demulsification,[83] are energy-efficient methods for separating the O/W emulsion from water phases. However, these chemical treatment methods require high operation costs and may produce secondary pollution to the environment. The physical treatment methods, such as centrifugation,[84] flotation,[85] and adsorption,[86] provide a simple and low-cost way to remove free-floating oil from water phases. However, these conventional physical methods suffer from low efficiency in separating complex and highly dispersed O/W emulsions from the aqueous phase.

Membrane filtration is considered to be a promising way to effectively separate the dispersed O/W emulsion from water systems.[87] Compared to these conventional methods, pressure-driven membrane filtration, such as ultrafiltration and microfiltration, can continuously separate the dispersed O/W emulsion from water without adding any chemicals.[88] However, the commonly used membrane materials, such as polyvinylidene fluoride (PVDF) membrane, polyethersulfone (PES) membrane, and polytetrafluoroethylene (PTFE) membrane, are intrinsically hydrophobic.[89, 90] These hydrophobic membranes will be subjected to severe surface fouling by the undesired attachment of oily contaminants on the membrane surface in the O/W separation process, which may inevitably block the pores on the surface or inner structure of the membrane.[91, 92] The membrane fouling will lead to a sharp decline in water permeation flux, thus deteriorating the membrane separation efficiency in the O/W emulsion treatment process.

1.2.2 Application of antifouling membrane in O/W separation

In order to solve the membrane surface fouling issue in the O/W emulsion separation process, many efforts have been made to modify the surface wettability of the membrane to prevent the attachment of oily contaminants.[93, 94] Inspired by the antifouling property of fish scales, antifouling membranes have been developed by loading hydrophilic materials, such as inorganic particles,[95] polymeric materials,[96] zwitterionic polyelectrolytes,[97] onto membrane surfaces. These hydrophilic materials show high water affinity and can trap a layer of water molecules on their surfaces. The formed hydration layer on the membrane surface will serve as a physical barrier to prevent the attachment of oily contaminants onto the membrane during the O/W separation process.[98, 99] For instance, *Zhang et al.* engineered ultrathin silica (SiO_2) layer onto the membrane surface.[100] The super hydrophilic silicification layer endowed the membrane with outstanding antifouling properties towards a range of oily contaminates. The as-prepared membrane also achieved a high-water permeation flux in the O/W emulsion filtration test due to its low water transport resistance.

However, the challenge still remains, where most of the reported antifouling membranes were fabricated by directly depositing hydrophilic materials onto membrane surfaces through weak and non-covalent physical interactions.[101] Thus, the fabricated antifouling coatings were not stable in the O/W separation process. The hydrophilic coating would fall off from the membrane surface under small external environmental changes, which will decrease membrane antifouling performance. Moreover, the deposition of hydrophilic coatings onto inert substrates, such as the PTFE or PVDF membrane, is still challenging.

1.2.3 Application of mussel-inspired coating in antifouling membrane

By mimicking the mussel adhesion strategy, in which robust adhesion is achieved by the formation of a "bio-glue" layer between the mussel byssal and substrates,[102] the hydrophilic coatings can be also tightly anchored onto the membrane surface by constructing the "glue layer" between the hydrophilic coatings and substrates. In this strategy, the mussel-inspired coatings, such as PDA coatings,[103] will first be deposited onto the membrane surface to introduce abundant functional groups, such as catechol and quinone groups onto the membrane. These functional groups will serve as anchoring points to tightly link the hydrophilic layer onto the membrane via multiple covalent or non-covalent interactions. However, the conventional PDA coatings are not stable and prone to dissolve in the O/W separation process,[67] thus limiting its application as a stable "glue layer" for anchoring hydrophilic coatings.

To solve this issue, the phenol/amino co-deposition strategy is proposed to construct the robust "bio-glue" layer onto substrates.[104] In the phenol/amino co-deposition process, the amino groups will be covalently connected to the quinone groups via Schiff-base and Michael-addition reactions.[105] Compared to the PDA coatings, the phenol/amino coatings are more stable and show greater resistance to harsh solution conditions. Thus, the phenol/amino coatings, such as TA/ polyethyleneimine (PEI) [106] or PDA/PEI [107] coatings, are generally applied as a stable "glue layer" for anchoring the hydrophilic coating onto the membrane. For instance, *Yang et al.* fabricated an antifouling membrane by anchoring the hydrophilic silica layer onto the membrane with the assistance of PDA/PEI coating. The as-prepared membrane showed remarkable antifouling performance in the O/W emulsion separation process.[101]

However, in the phenol/amine coating process, large aggregates are generally formed on membrane surfaces due to the rapid and uncontrolled Schiff-base and Michael addition reaction in

the co-deposition processes.[108] The formed phenol/amine aggregates will block the porous structure of the membrane, thus decreasing the membrane O/W separation efficiency. Moreover, the aggregated phenol/amino coating is undesired for serving as a platform for anchoring the hydrophilic layer on the membrane due to its limited anchoring sites. Thus, in order to construct a robust and stable antifouling coating on the membrane, the non-aggregated and stable phenol/amino "glue layer" must be firstly fabricated by modulating the phenol/amine coating process.

1.3 Objectives

Despite many efforts have been made in developing different types of mussel-inspired coatings and exploring their potential applications in various fields, it remains a challenge to integrate target functionalities into mussel-inspired coatings to fulfill the specific requirements in water treatment processes, such as organic pollutant removal and O/W emulsion separation. Moreover, complete understanding of the molecular interaction mechanism in the assembly process of mussel-inspired coatings is not available. Revealing the underlying mechanism in the coating process will facilitate the fabrication of much more advanced mussel-inspired coatings with desirable structures.

The overall goal of this thesis is to develop functional mussel-inspired coatings and evaluate their performance in organic pollutants removal or O/W emulsion separation, as well as investigate the corresponding intermolecular mechanisms in the assembly process of mussel-inspired coatings.

The detailed objectives are listed as follows.

1. Develop a nano-catalyst with the assistance of mussel-inspired tannic acid (TA)/Fe^{3+} coating to remove organic pollutants from water, and investigate its catalytic performance towards various organic pollutants under different solution conditions and its corresponding catalytic reaction mechanism.

2. Develop an antifouling cellulose nanocrystals (CNCs) coating onto various substrates with the assistance of a mussel-inspired tannic acid/polyethylenimine/vanadium (TA/PEI/V) adhesive layer, and investigate the molecular interactions mechanism in the CNCs coating process as well as the separation performance and antifouling property of CNCs-coated membrane in the O/W separation process.

3. Develop a durable polyethylene glycol (PEG) antifouling coating with the assistance of mussel-inspired Levodopa/polyethyleneimine (LP) adhesive layer, and investigate its antifouling property towards different kinds of foulants and their corresponding antifouling mechanism; fabricate PEG-coated membrane and study its O/W emulsion separation performance and stability in harsh solution conditions.

1.4 Structure of the thesis

Chapter 1 introduces the wastewater-related challenges, followed by a brief review of wastewater treatment methods and the application of the mussel-inspired coating in these methods. The objectives of this work are presented.

Chapter 2 describes the major techniques used in this work.

Chapter 3 reports a high-efficient Ag NPs nanocomposite catalyst for organic pollutants removal. The nano-catalyst is prepared by loading Ag NPs onto magnetic graphene oxide (MGO) with the assistance of TA/Fe^{3+} coating. The catalytic reduction performance of as-prepared catalyst

towards different organic dyes and nitrophenols are studied. The effect of pH values and the reaction mechanism in the catalytic reduction process are discussed.

Chapter 4 introduces a universal and facile strategy to construct a robust and antifouling CNCs coating onto various substrates. The CNCs coating is composited of a TA/PEI/V intermediate adhesive layer and a self-assembled super-hydrophilic CNCs layer. The effect of V^{3+} ions in the coating process is investigated by using the atomic force microscope (AFM) colloidal probe technique. The as-prepared CNCs coating shows excellent antifouling and anti-abrasion properties. Moreover, this proposed CNCs coating strategy can be further applied in membrane surface functionalization, and the anti-oil fouling performance and O/W emulsion separation performance of as-prepared CNCs-coated membrane are studied.

Chapter 5 presents a durable PEG coating with antifouling property for O/W emulsion separation. The PEG coating is fabricated by covalently anchoring the hydrophilic poly (ethylene glycol) diglycidyl ether (PEGDE) layer onto Levodopa/polyethyleneimine (LP) adhesive layer via a ring-opening reaction. The stability of PEGDE/LP coating in harsh solution conditions is investigated. The antifouling property of as-prepared coating towards oily foulants and proteins is evaluated, and the antifouling mechanism is studied by using surface forces apparatus (SFA) force measurement. Moreover, the PEGDE-coated membrane is fabricated and the O/W emulsion separation performance and self-cleaning property of the as-prepared membrane are investigated.

Chapter 6 presents the conclusions and contributions of this work, and the perspectives of the future work are also provided.

Reference

(1) El Nemr, A.; Khaled, A.; Abdelwahab, O.; El-Sikaily, A. Treatment of wastewater containing toxic chromium using new activated carbon developed from date palm seed. *Journal of Hazardous Materials* **2008**, *152* (1), 263-275.

(2) Wacławek, S.; Lutze, H. V.; Grübel, K.; Padil, V. V.; Černík, M.; Dionysiou, D. D. Chemistry of persulfates in water and wastewater treatment: a review. *Chemical Engineering Journal* **2017**, *330*, 44-62.

(3) Biswas, A. K.; Tortajada, C. Water crisis and water wars: myths and realities. Taylor & Francis: **2019**; 35, 727-731.

(4) Simonovic, S. P. World water dynamics: global modeling of water resources. *Journal of Environmental Management* **2002**, *66* (3), 249-267.

(5) Santos, J. O.; Andrade, J. C. S.; Marinho, M. M. d. O.; Noyola, A.; Güereca, L. P. Greenhouse gas inventory of a state water and wastewater utility in Northeast Brazil. *Journal of Cleaner Production* **2015**, *104*, 168-176.

(6) Zhuang, S.; Qi, H.; Wang, X.; Li, X.; Liu, K.; Liu, J.; Zhang, H. Advances in Solar‐Driven Hygroscopic Water Harvesting. *Global Challenges* **2021**, *5* (1), 2000085.

(7) Song, Z.; Williams, C.; Edyvean, R. Sedimentation of tannery wastewater. *Water Research* **2000**, *34* (7), 2171-2176.

(8) Jury, W. A.; Vaux Jr, H. J. The emerging global water crisis: managing scarcity and conflict between water users. *Advances in agronomy* **2007**, *95*, 1-76.

(9) Qin, B.; Zhu, G.; Gao, G.; Zhang, Y.; Li, W.; Paerl, H. W.; Carmichael, W. W. A drinking water crisis in Lake Taihu, China: linkage to climatic variability and lake management. *Environmental management* **2010**, *45* (1), 105-112.

(10) Rashed, M. N. Adsorption technique for the removal of organic pollutants from water and wastewater. *Organic pollutants-monitoring, risk and treatment* **2013**, *7*, 167-194.

(11) Aleksić, M.; Kušić, H.; Koprivanac, N.; Leszczynska, D.; Božić, A. L. Heterogeneous Fenton type processes for the degradation of organic dye pollutant in water—The application of zeolite assisted AOPs. *Desalination* **2010**, *257* (1-3), 22-29.

(12) Mani, S.; Chowdhary, P.; Bharagava, R. N. Textile wastewater dyes: toxicity profile and treatment approaches. In *Emerging and eco-friendly approaches for waste management*, Springer, **2019**; 219-244.

(13) Saravanan, A.; Kumar, P. S.; Jeevanantham, S.; Karishma, S.; Tajsabreen, B.; Yaashikaa, P.; Reshma, B. Effective water/wastewater treatment methodologies for toxic pollutants removal: Processes and applications towards sustainable development. *Chemosphere* **2021**, *280*, 130595.

(14) Tkaczyk, A.; Mitrowska, K.; Posyniak, A. Synthetic organic dyes as contaminants of the aquatic environment and their implications for ecosystems: A review. *Science of the total environment* **2020**, *717*, 137222.

(15) Shafqat, M.; Khalid, A.; Mahmood, T.; Siddique, M. T.; Han, J. I.; Habteselassie, M. Y. Evaluation of bacteria isolated from textile wastewater and rhizosphere to simultaneously degrade azo dyes and promote plant growth. *Journal of Chemical Technology & Biotechnology* **2017**, *92* (10), 2760-2768.

(16) Islam, M. A.; Ali, I.; Karim, S. A.; Firoz, M. S. H.; Chowdhury, A.-N.; Morton, D. W.; Angove, M. J. Removal of dye from polluted water using novel nano manganese oxide-based materials. *Journal of Water Process Engineering* **2019**, *32*, 100911.

(17) Zhao, R.; Li, Y.; Sun, B.; Chao, S.; Li, X.; Wang, C.; Zhu, G. Highly flexible magnesium silicate nanofibrous membranes for effective removal of methylene blue from aqueous solution. *Chemical Engineering Journal* **2019**, *359*, 1603-1616.

(18) Dong, X.; Liu, H.; Chen, Z.; Wu, K.; Lu, N.; Zhang, Q. Enhanced oil recovery techniques for heavy oil and oilsands reservoirs after steam injection. *Applied energy* **2019**, *239*, 1190-1211.

(19) Wang, J.; He, J.; Ma, L.; Zhang, Y.; Zhao, Y.; Zhou, Y.; Li, K.; Qu, M. Buoyant and durable oil/water separation mesh for continuous and efficient collection of both oil slick and underwater oil leakage. *Separation and Purification Technology* **2019**, *229*, 115795.

(20) Chen, J.; Zhang, W.; Wan, Z.; Li, S.; Huang, T.; Fei, Y. Oil spills from global tankers: Status review and future governance. *Journal of cleaner production* **2019**, *227*, 20-32.

(21) Yong, J.; Huo, J.; Chen, F.; Yang, Q.; Hou, X. Oil/water separation based on natural materials with super-wettability: recent advances. *Physical Chemistry Chemical Physics* **2018**, *20* (39), 25140-25163.

(22) Liu, S.; Zhang, Q.; Fan, L.; Wang, R.; Yang, M.; Zhou, Y. 3D superhydrophobic sponge coated with magnesium hydroxide for effective oil/water mixture and emulsion separation. *Industrial & Engineering Chemistry Research* **2020**, *59* (25), 11713-11722.

(23) Wang, X.; Li, M.; Shen, Y.; Yang, Y.; Feng, H.; Li, J. Facile preparation of loess-coated membranes for multifunctional surfactant-stabilized oil-in-water emulsion separation. *Green Chemistry* **2019**, *21* (11), 3190-3199.

(24) Zhang, J.; Zeng, H. Intermolecular and Surface Interactions in Engineering Processes. *Engineering* **2021**, *7* (1), 63-83.

(25) Sutrisna, P. D.; Kurnia, K. A.; Siagian, U. W.; Ismadji, S.; Wenten, I. G. Membrane fouling and fouling mitigation in oil–water separation: A review. *Journal of Environmental Chemical Engineering* **2022**, 107532.

(26) Pang, Y. L.; Abdullah, A. Z. Current status of textile industry wastewater management and research progress in Malaysia: a review. *Clean–Soil, Air, Water* **2013**, *41* (8), 751-764.

(27) Dave, S. R.; Patel, T. L.; Tipre, D. R. Bacterial degradation of azo dye containing wastes. In *Microbial degradation of synthetic dyes in wastewaters*, Springer, **2015**; 57-83.

(28) Liu, Q. Pollution and Treatment of Dye Waste-Water. In *IOP Conference Series: Earth and Environmental Science*, **2020**; 514, 052001.

(29) Weldegebrieal, G. K. Synthesis method, antibacterial and photocatalytic activity of ZnO nanoparticles for azo dyes in wastewater treatment: A review. *Inorganic Chemistry Communications* **2020**, *120*, 108140.

(30) Khan, F. S. A.; Mubarak, N. M.; Tan, Y. H.; Khalid, M.; Karri, R. R.; Walvekar, R.; Abdullah, E. C.; Nizamuddin, S.; Mazari, S. A. A comprehensive review on magnetic carbon nanotubes and carbon nanotube-based buckypaper for removal of heavy metals and dyes. *Journal of Hazardous Materials* **2021**, *413*, 125375.

(31) Larous, S.; Meniai, A.-H. Elimination of organic pollutants from wastewater. Application to p-nitrophenol. *Desalination and Water Treatment* **2013**, *51* (25-27), 5014-5020.

(32) Deka, P.; Bhattacharjee, D.; Sarmah, P.; Deka, R. C.; Bharali, P. Catalytic reduction of water contaminant ‘4-nitrophenol’over manganese oxide supported Ni nanoparticles. *Trends in Asian water environmental science and technology* **2017**, 35-48.

(33) Bhatti, Z. I.; Toda, H.; Furukawa, K. p-Nitrophenol degradation by activated sludge attached on nonwovens. *Water Research* **2002**, *36* (5), 1135-1142.

(34) Katheresan, V.; Kansedo, J.; Lau, S. Y. Efficiency of various recent wastewater dye removal methods: A review. *Journal of environmental chemical engineering* **2018**, *6* (4), 4676-4697.

(35) Fan, J.; Shi, Z.; Lian, M.; Li, H.; Yin, J. Mechanically strong graphene oxide/sodium alginate/polyacrylamide nanocomposite hydrogel with improved dye adsorption capacity. *Journal of Materials Chemistry A* **2013**, *1* (25), 7433-7443.

(36) Liu, H.; Zhang, J.; Lu, M.; Liang, L.; Zhang, H.; Wei, J. Biosynthesis based membrane filtration coupled with iron nanoparticles reduction process in removal of dyes. *Chemical Engineering Journal* **2020**, *387*, 124202.

(37) Nataraj, S.; Hosamani, K.; Aminabhavi, T. Nanofiltration and reverse osmosis thin film composite membrane module for the removal of dye and salts from the simulated mixtures. *Desalination* **2009**, *249* (1), 12-17.

(38) Verma, A. K.; Dash, R. R.; Bhunia, P. A review on chemical coagulation/flocculation technologies for removal of colour from textile wastewaters. *Journal of environmental management* **2012**, *93* (1), 154-168.

(39) Guo, J.; Yang, Q.; Meng, Q.-W.; Lau, C. H.; Ge, Q. Membrane surface functionalization with imidazole derivatives to benefit dye removal and fouling resistance in forward osmosis. *ACS Applied Materials & Interfaces* **2021**, *13* (5), 6710-6719.

(40) Bhatia, D.; Sharma, N. R.; Singh, J.; Kanwar, R. S. Biological methods for textile dye removal from wastewater: A review. *Critical Reviews in Environmental Science and Technology* **2017**, *47* (19), 1836-1876.

(41) Jadhav, J.; Kalyani, D.; Telke, A.; Phugare, S.; Govindwar, S. Evaluation of the efficacy of a bacterial consortium for the removal of color, reduction of heavy metals, and toxicity from textile dye effluent. *Bioresource Technology* **2010**, *101* (1), 165-173.

(42) Couto, S. R. Dye removal by immobilised fungi. *Biotechnology advances* **2009**, *27* (3), 227-235.

(43) Kanagaraj, J.; Senthilvelan, T.; Panda, R. Degradation of azo dyes by laccase: biological method to reduce pollution load in dye wastewater. *Clean Technologies and Environmental Policy* **2015**, *17* (6), 1443-1456.

(44) Banerjee, P.; DasGupta, S.; De, S. Removal of dye from aqueous solution using a combination of advanced oxidation process and nanofiltration. *Journal of hazardous materials* **2007**, *140* (1-2), 95-103.

(45) Emami, Z.; Azizian, S. Preparation of activated carbon from date sphate using microwave irradiation and investigation of its capability for removal of dye pollutant from aqueous media. *Journal of Analytical and Applied Pyrolysis* **2014**, *108*, 176-184.

(46) García-Montaño, J.; Ruiz, N.; Munoz, I.; Domenech, X.; García-Hortal, J. A.; Torrades, F.; Peral, J. Environmental assessment of different photo-Fenton approaches for commercial reactive dye removal. *Journal of hazardous materials* **2006**, *138* (2), 218-225.

(47) Naseem, K.; Farooqi, Z. H.; Begum, R.; Irfan, A. Removal of Congo red dye from aqueous medium by its catalytic reduction using sodium borohydride in the presence of various inorganic nano-catalysts: a review. *Journal of cleaner production* **2018**, *187*, 296-307.

(48) Pinto, I. S.; Pacheco, P. H.; Coelho, J. V.; Lorençon, E.; Ardisson, J. D.; Fabris, J. D.; de Souza, P. P.; Krambrock, K. W.; Oliveira, L. C.; Pereira, M. C. Nanostructured δ-FeOOH: an efficient Fenton-like catalyst for the oxidation of organics in water. *Applied Catalysis B: Environmental* **2012**, *119*, 175-182.

(49) Zhang, C.; Yang, H.-C.; Wan, L.-S.; Liang, H.-Q.; Li, H.; Xu, Z.-K. Polydopamine-coated porous substrates as a platform for mineralized β-FeOOH nanorods with photocatalysis under sunlight. *ACS Applied Materials & Interfaces* **2015**, *7* (21), 11567-11574.

(50) Albukhari, S. M.; Ismail, M.; Akhtar, K.; Danish, E. Y. Catalytic reduction of nitrophenols and dyes using silver nanoparticles@ cellulose polymer paper for the resolution of waste water treatment challenges. *Colloids and Surfaces A: Physicochemical and Engineering Aspects* **2019**, *577*, 548-561.

(51) Azad, U. P.; Ganesan, V.; Pal, M. Catalytic reduction of organic dyes at gold nanoparticles impregnated silica materials: influence of functional groups and surfactants. *Journal of Nanoparticle Research* **2011**, *13* (9), 3951-3959.

(52) Dao, V.-D.; Tran, C. Q.; Ko, S.-H.; Choi, H.-S. Dry plasma reduction to synthesize supported platinum nanoparticles for flexible dye-sensitized solar cells. *Journal of Materials Chemistry A* **2013**, *1* (14), 4436-4443.

(53) Cui, K.; Yan, B.; Xie, Y.; Qian, H.; Wang, X.; Huang, Q.; He, Y.; Jin, S.; Zeng, H. Regenerable urchin-like Fe3O4@ PDA-Ag hollow microspheres as catalyst and adsorbent for enhanced removal of organic dyes. *Journal of hazardous materials* **2018**, *350*, 66-75.

(54) Xie, Y.; Yan, B.; Xu, H.; Chen, J.; Liu, Q.; Deng, Y.; Zeng, H. Highly regenerable mussel-inspired Fe3O4@ polydopamine-Ag core–shell microspheres as catalyst and adsorbent for methylene blue removal. *ACS applied materials & interfaces* **2014**, *6* (11), 8845-8852.

(55) Du, S.; Liao, Z.; Qin, Z.; Zuo, F.; Li, X. Polydopamine microparticles as redox mediators for catalytic reduction of methylene blue and rhodamine B. *Catalysis Communications* **2015**, *72*, 86-90.

(56) Ji, Z.; Shen, X.; Yue, X.; Zhou, H.; Yang, J.; Wang, Y.; Ma, L.; Chen, K. Facile synthesis of magnetically separable reduced graphene oxide/magnetite/silver nanocomposites with enhanced catalytic activity. *Journal of colloid and interface science* **2015**, *459*, 79-85.

(57) Mao, H.; Ji, C.; Liu, M.; Cao, Z.; Sun, D.; Xing, Z.; Chen, X.; Zhang, Y.; Song, X.-M. Enhanced catalytic activity of Ag nanoparticles supported on polyacrylamide/polypyrrole/graphene oxide nanosheets for the reduction of 4-nitrophenol. *Applied Surface Science* **2018**, *434*, 522-533.

(58) Yang, Y.; Ji, H.; Duan, H.; Fu, Y.; Xia, S.; Lü, C. Controllable synthesis of mussel-inspired catechol-formaldehyde resin microspheres and their silver-based nanohybrids for catalytic and antibacterial applications. *Polymer Chemistry* **2019**, *10* (33), 4537-4550.

(59) Islam, M. R.; Ferdous, M.; Sujan, M. I.; Mao, X.; Zeng, H.; Azam, M. S. Recyclable Ag-decorated highly carbonaceous magnetic nanocomposites for the removal of organic pollutants. *Journal of Colloid and Interface Science* **2020**, *562*, 52-62.

(60) Lu, J.; Fang, J.; Li, J.; Wang, C.; He, Z.; Zhu, L.-P.; Xu, Z.-K.; Zeng, H. Polydopamine Nanotubes Decorated with Ag Nanoparticles as Catalyst for the Reduction of Methylene Blue. *ACS Applied Nano Materials* **2019**.

(61) Lu, Q.; Danner, E.; Waite, J. H.; Israelachvili, J. N.; Zeng, H.; Hwang, D. S. Adhesion of mussel foot proteins to different substrate surfaces. *Journal of The Royal Society Interface* **2013**, *10* (79), 20120759.

(62) Zeng, H.; Hwang, D. S.; Israelachvili, J. N.; Waite, J. H. Strong reversible Fe3+-mediated bridging between dopa-containing protein films in water. *Proceedings of the National Academy of Sciences* **2010**, *107* (29), 12850-12853.

(63) Lee, H.; Dellatore, S. M.; Miller, W. M.; Messersmith, P. B. Mussel-inspired surface chemistry for multifunctional coatings. *science* **2007**, *318* (5849), 426-430.

(64) Wang, H.; Wang, Z.; Yue, R.; Gao, F.; Ren, R.; Wei, J.; Wang, X.; Kong, Z. Rapid preparation of adsorbent based on mussel inspired chemistry and simultaneous removal of heavy metal ions in water. *Chemical Engineering Journal* **2020**, *383*, 123107.

(65) Zhang, M.; Li, G.; Sun, X.; Jiang, Y.; Zhang, X. General promoting effect of polydopamine on supported noble metal catalysts. *Journal of Materials Chemistry A* **2017**, *5* (39), 20789-20796.

(66) Guo, L.; Liu, Q.; Li, G.; Shi, J.; Liu, J.; Wang, T.; Jiang, G. A mussel-inspired polydopamine coating as a versatile platform for the in situ synthesis of graphene-based nanocomposites. *Nanoscale* **2012**, *4* (19), 5864-5867.

(67) Zhang, C.; Ou, Y.; Lei, W. X.; Wan, L. S.; Ji, J.; Xu, Z. K. CuSO4/H2O2-induced rapid deposition of polydopamine coatings with high uniformity and enhanced stability. *Angewandte Chemie International Edition* **2016**, *55* (9), 3054-3057.

(68) Sileika, T. S.; Barrett, D. G.; Zhang, R.; Lau, K. H. A.; Messersmith, P. B. Colorless multifunctional coatings inspired by polyphenols found in tea, chocolate, and wine. *Angewandte Chemie* **2013**, *125* (41), 10966-10970.

(69) Rahim, M. A.; Björnmalm, M.; Suma, T.; Faria, M.; Ju, Y.; Kempe, K.; Müllner, M.; Ejima, H.; Stickland, A. D.; Caruso, F. Metal–phenolic supramolecular gelation. *Angewandte Chemie* **2016**, *128* (44), 14007-14011.

(70) Park, T.; Kim, W. I.; Kim, B. J.; Lee, H.; Choi, I. S.; Park, J. H.; Cho, W. K. Salt-induced, continuous deposition of supramolecular iron (III)–tannic acid complex. *Langmuir* **2018**, *34* (41), 12318-12323.

(71) Guo, Z.; Xie, W.; Lu, J.; Guo, X.; Xu, J.; Xu, W.; Chi, Y.; Takuya, N.; Wu, H.; Zhao, L. Tannic acid-based metal phenolic networks for bio-applications: a review. *Journal of Materials Chemistry B* **2021**, *9* (20), 4098-4110.

(72) Ejima, H.; Richardson, J. J.; Liang, K.; Best, J. P.; van Koeverden, M. P.; Such, G. K.; Cui, J.; Caruso, F. One-step assembly of coordination complexes for versatile film and particle engineering. *Science* **2013**, *341* (6142), 154-157.

(73) Li, D.; Xu, X.; Wang, X.; Li, R.; Cai, C.; Sun, T.; Zhao, Y.; Chen, L.; Xu, J.; Zhao, N. A General Surface Modification Method for Nanospheres via Tannic Acid-Fe Layer-by-Layer Deposition: Preparation of a Magnetic Nanocatalyst. *ACS Applied Nano Materials* **2019**.

(74) Zhang, J.; Liu, L.; Si, Y.; Yu, J.; Ding, B. Rational design of electrospun nanofibrous materials for oil/water emulsion separation. *Materials Chemistry Frontiers* **2021**, *5* (1), 97-128.

(75) Bozeman, B. The 2010 BP Gulf of Mexico oil spill: Implications for theory of organizational disaster. *Technology in Society* **2011**, *33* (3-4), 244-252.

(76) Kwon, G.; Post, E.; Tuteja, A. Membranes with selective wettability for the separation of oil–water mixtures. *MRS Communications* **2015**, *5* (3), 475-494.

(77) Lin, X.; Hong, J. Recent advances in robust superwettable membranes for oil–water separation. *Advanced Materials Interfaces* **2019**, *6* (12), 1900126.

(78) Yu, L.; Han, M.; He, F. A review of treating oily wastewater. *Arabian journal of chemistry* **2017**, *10*, S1913-S1922.

(79) Arumugham, T.; Kaleekkal, N. J.; Rana, D.; Doraiswamy, M. Separation of oil/water emulsions using nano MgO anchored hybrid ultrafiltration membranes for environmental abatement. *Journal of Applied Polymer Science* **2016**, *133* (1).

(80) Maggay, I. V.; Chang, Y.; Venault, A.; Dizon, G. V.; Wu, C.-J. Functionalized porous filtration media for gravity-driven filtration: Reviewing a new emerging approach for oil and water emulsions separation. *Separation and Purification Technology* **2021**, *259*, 117983.

(81) Pan, M.; Gong, L.; Xiang, L.; Yang, W.; Wang, W.; Zhang, L.; Hu, W.; Han, L.; Zeng, H. Modulating surface interactions for regenerable separation of oil-in-water emulsions. *Journal of Membrane Science* **2021**, 119140.

(82) Körbahti, B. K.; Artut, K. Electrochemical oil/water demulsification and purification of bilge water using Pt/Ir electrodes. *Desalination* **2010**, *258* (1-3), 219-228.

(83) Wang, R.; Feng, Y.; Xu, H.; Zou, Y.; Fan, L.; Zhang, R.; Zhou, Y. Effective demulsification for oil–water separation through metal–organic frameworks with an amphipathic micro-domain. *Materials Chemistry Frontiers* **2020**, *4* (10), 3086-3093.

(84) Liu, L.; Zhao, L.; Yang, X.; Wang, Y.; Xu, B.; Liang, B. Innovative design and study of an oil-water coupling separation magnetic hydrocyclone. *Separation and Purification Technology* **2019**, *213*, 389-400.

(85) Saththasivam, J.; Loganathan, K.; Sarp, S. An overview of oil–water separation using gas flotation systems. *Chemosphere* **2016**, *144*, 671-680.

(86) Jiang, J.; Zhang, Q.; Zhan, X.; Chen, F. A multifunctional gelatin-based aerogel with superior pollutants adsorption, oil/water separation and photocatalytic properties. *Chemical Engineering Journal* **2019**, *358*, 1539-1551.

(87) Chu, Z.; Feng, Y.; Seeger, S. Oil/water separation with selective superantiwetting/superwetting surface materials. *Angewandte Chemie International Edition* **2015**, *54* (8), 2328-2338.

(88) Al-Maas, M.; Hussain, A.; Matar, J. M.; Ponnamma, D.; Hassan, M. K.; Al-Maadeed, M. A. A.; Alamgir, K.; Adham, S. Validation and application of a membrane filtration evaluation protocol for oil-water separation. *Journal of Water Process Engineering* **2021**, *43*, 102185.

(89) Dmitrieva, E. S.; Anokhina, T. S.; Novitsky, E. G.; Volkov, V. V.; Borisov, I. L.; Volkov, A. V. Polymeric Membranes for Oil-Water Separation: A Review. *Polymers* **2022**, *14* (5), 980.

(90) Chen, W.; Su, Y.; Zheng, L.; Wang, L.; Jiang, Z. The improved oil/water separation performance of cellulose acetate-graft-polyacrylonitrile membranes. *Journal of Membrane Science* **2009**, *337* (1-2), 98-105.

(91) Qu, F.; Cao, A.; Yang, Y.; Mahmud, S.; Su, P.; Yang, J.; He, Z.; Lai, Q.; Zhu, L.; Tu, Z. Hierarchically superhydrophilic poly (vinylidene fluoride) membrane with self-cleaning fabricated by surface mineralization for stable separation of oily wastewater. *Journal of Membrane Science* **2021**, *640*, 119864.

(92) Zhu, X.; Tu, W.; Wee, K.-H.; Bai, R. Effective and low fouling oil/water separation by a novel hollow fiber membrane with both hydrophilic and oleophobic surface properties. *Journal of membrane science* **2014**, *466*, 36-44.

(93) Cai, Y.; Chen, D.; Li, N.; Xu, Q.; Li, H.; He, J.; Lu, J. A smart membrane with antifouling capability and switchable oil wettability for high-efficiency oil/water emulsions separation. *Journal of Membrane Science* **2018**, *555*, 69-77.

(94) Wang, Z.; Yang, J.; Song, S.; Guo, J.; Zheng, J.; Sherazi, T. A.; Li, S.; Zhang, S. Patterned, anti-fouling membrane with controllable wettability for ultrafast oil/water separation and liquid–liquid extraction. *Chemical Communications* **2020**, *56* (80), 12045-12048.

(95) Shen, X.; Xie, T.; Wang, J.; Liu, P.; Wang, F. An anti-fouling poly (vinylidene fluoride) hybrid membrane blended with functionalized ZrO 2 nanoparticles for efficient oil/water separation. *RSC advances* **2017**, *7* (9), 5262-5271.

(96) Zhao, Y.; Zhang, M.; Wang, Z. Underwater superoleophobic membrane with enhanced oil–water separation, antimicrobial, and antifouling activities. *Advanced Materials Interfaces* **2016**, *3* (13), 1500664.

(97) Zhu, Y.; Zhang, F.; Wang, D.; Pei, X. F.; Zhang, W.; Jin, J. A novel zwitterionic polyelectrolyte grafted PVDF membrane for thoroughly separating oil from water with ultrahigh efficiency. *Journal of Materials Chemistry A* **2013**, *1* (18), 5758-5765.

(98) Liu, Y.; Su, Y.; Cao, J.; Guan, J.; Zhang, R.; He, M.; Fan, L.; Zhang, Q.; Jiang, Z. Antifouling, high-flux oil/water separation carbon nanotube membranes by polymer-mediated surface charging and hydrophilization. *Journal of Membrane Science* **2017**, *542*, 254-263.

(99) Dong, D.; Zhu, Y.; Fang, W.; Ji, M.; Wang, A.; Gao, S.; Lin, H.; Huang, R.; Jin, J. Double-Defense Design of Super - Anti - Fouling Membranes for Oil/Water Emulsion Separation. *Advanced Functional Materials* **2022**, 2113247.

(100) Zhang, L.; Lin, Y.; Wu, H.; Cheng, L.; Sun, Y.; Yasui, T.; Yang, Z.; Wang, S.; Yoshioka, T.; Matsuyama, H. An ultrathin in situ silicification layer developed by an electrostatic attraction force strategy for ultrahigh-performance oil–water emulsion separation. *Journal of Materials Chemistry A* **2019**, *7* (42), 24569-24582.

(101) Yang, H.-C.; Pi, J.-K.; Liao, K.-J.; Huang, H.; Wu, Q.-Y.; Huang, X.-J.; Xu, Z.-K. Silica-decorated polypropylene microfiltration membranes with a mussel-inspired intermediate layer for oil-in-water emulsion separation. *ACS applied materials & interfaces* **2014**, *6* (15), 12566-12572.

(102) Zhang, C.; Xiang, L.; Zhang, J.; Gong, L.; Han, L.; Xu, Z.-K.; Zeng, H. Tough and alkaline-resistant mussel-inspired wet adhesion with surface salt displacement via polydopamine/amine synergy. *Langmuir* **2019**, *35* (15), 5257-5263.

(103) Xu, Z.; Li, L.; Liu, J.; Dai, C.; Sun, W.; Chen, J.; Zhu, Z.; Zhao, M.; Zeng, H. Mussel-inspired superhydrophilic membrane constructed on a hydrophilic polymer network for highly efficient oil/water separation. *Journal of Colloid and Interface Science* **2022**, *608*, 702-710.

(104) Qiu, W.-Z.; Wu, G.-P.; Xu, Z.-K. Robust coatings via catechol–amine codeposition: mechanism, kinetics, and application. *ACS applied materials & interfaces* **2018**, *10* (6), 5902-5908.

(105) Xiang, L.; Zhang, J.; Gong, L.; Han, L.; Zhang, C.; Yan, B.; Liu, J.; Zeng, H. Probing the interaction forces of phenol/amine deposition in wet adhesion: impact of phenol/amine mass ratio and surface properties. *Langmuir* **2019**, *35* (48), 15639-15650.

(106) Zhao, X.; Wang, R.; Lan, Y.; Wang, T.; Pan, J.; Liu, L. Engineering superwetting membranes through polyphenol-polycation-metal complexation for high-efficient oil/water separation: From polyphenol to tailored nanostructures. *Journal of Membrane Science* **2021**, *630*, 119310.

(107) Meng, L.; Lv, Y.; Deng, P.; Li, N.; Huang, M.; Mansouri, J.; Chen, V. Novel PVDF membrane with sandwich structure for enhanced membrane distillation. *Chemical Engineering Journal* **2021**, *415*, 128960.

(108) Zhang, Y.; Ma, J.; Shao, L. Ultra-thin trinity coating enabled by competitive reactions for unparalleled molecular separation. *Journal of Materials Chemistry A* **2020**, *8* (10), 5078-5085.

Chapter 2. Experimental techniques

2.1 Atomic force microscope (AFM)

Atomic force microscope (AFM) has been widely applied to characterize surface morphologies with sub-nanometer resolution and measure the interaction forces of two substrates at nanoscale.[1] The AFM mainly consists of a laser beam, cantilever, sharp probe tip, piezo transducer, and quadrant displacement sensor. In the AFM tapping mode, the AFM cantilever vibrates and drives the probe tip to oscillate at its resonance frequency near the sample surface, and the tip-sample interactions will cause changes in the amplitude of cantilever oscillation. To maintain the constant cantilever oscillation amplitude, feedback will be generated to adjust the position of the probe tip, which can be used to determine the sample topography.[2, 3] In this thesis, the surface morphologies of as-prepared mussel-inspired coatings were characterized by topographic imaging using atomic force microscope (AFM) with Bruker ICON AFM system (Bruker, Santa Barbara, CA) in tapping mode under ambient conditions.

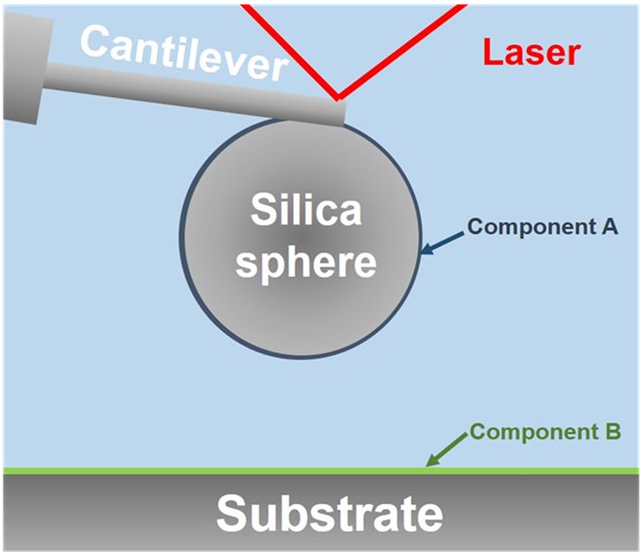

Figure 2.1 Schematic of the AFM colloidal probe technique.

As shown in Figure 2.1, The AFM colloidal probe technique has been applied to directly measure the interactions between the probe and different substrates at nanoscale. The silica probe is prepared by attaching a silica sphere (diameter ~5 μm) onto a tipless cantilever with two-component epoxy glue. The silica probe is then coated with component A through the dip-coating method.[4] The sensitivity of the piezo is calibrated by fitting the linear regime of the force curves measured between the silica probe and bare silica surface, and the spring constant of the silica probe is calibrated by the thermal tune method. In a typical force measurement procedure, the prepared silica probe is positioned over the surface (coated with component B) and then driven to approach and retract from the surface at a constant velocity (1 μm/s) until the maximum loading force is reached.[5] The deflection of the silica probe is detected by the laser beam detection system. The interaction forces are calculated by Hooke's law by using calibrated cantilever spring constant.[6]

In this thesis, the molecular interaction in the assembly process of mussel-inspired TA/PEI/V coating was investigated by using AFM colloidal probe technique. The as-prepared AFM silica probe and silicon wafer were treated using a UV Ozone cleaner, followed by immersion in PEI solutions (1 mg/mL^{-1}) for 2 hours, rinsing with DI water, and drying with pure nitrogen. In the force measurement experiments, both the PEI-coated silica probe and PEI-coated silicon wafer were placed in a fluid cell containing TA or TA/V^{3+} solutions. The corresponding force profiles between the silica probe and substrates are recorded by AFM software.

2.2 Surface forces apparatus (SFA)

The surface forces apparatus (SFA) was firstly designed by Tabor, Winterton, and Israelachvili in the late 1960s and early 1970s to measure the surface forces between two smooth

mica surfaces in vacuum and gas.[7, 8] SFA technique was then significantly upgraded by Israelachvili [9] by expanding the surface force measurements to a wide range of material systems under different liquid and vapor conditions.[10] The schematic diagram of SFA 2000 is shown in Figure 2.2.[11] The main components of SFA 2000 include the micrometers, the main chamber, the main stage with central simple-cantilever spring, and the lower disk holder and the upper disk holder. The separation distance between the lower and upper surfaces can be well controlled by four different controls for magnitudes from angstroms to millimeters with a resolution of 0.1 nm.

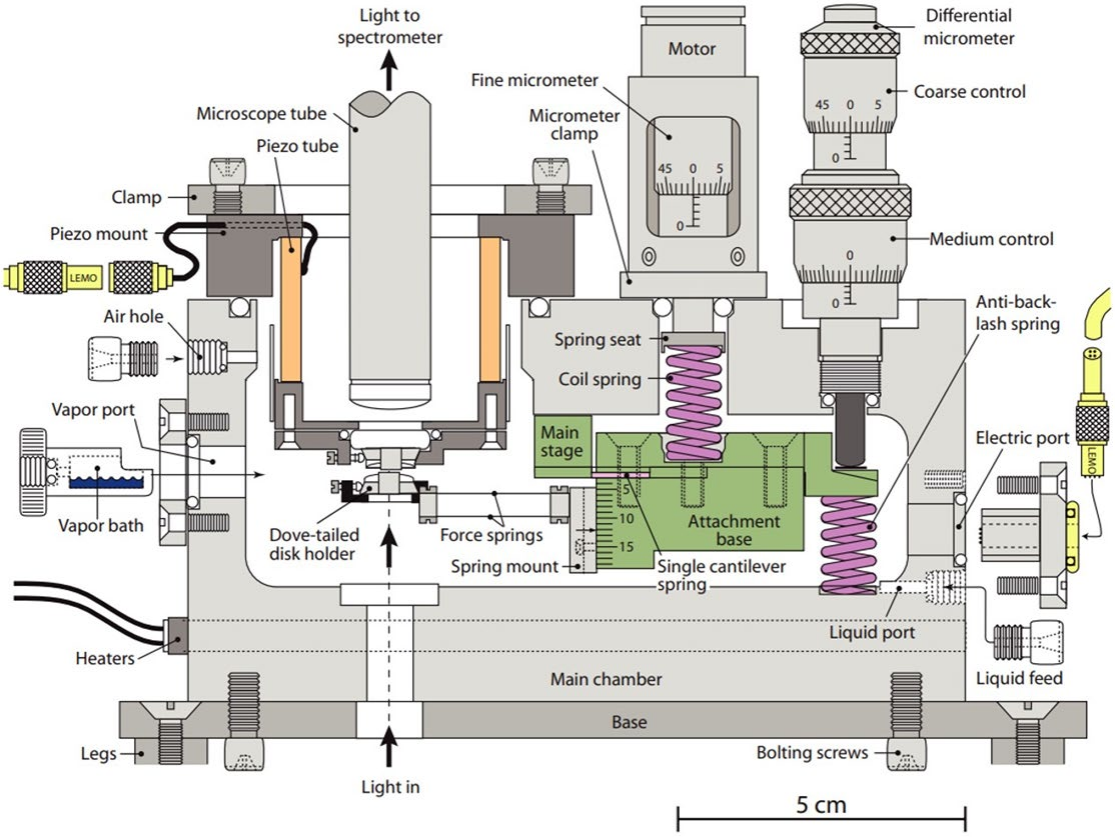

Figure 2.2 Schematic illustration of the SFA 2000.[11]

In a typical SFA experiment, two back-silvered thin mica sheets are glued onto two cylindrical silica disks (with the radius R=2cm). The two mica surfaces can be further modified by various surface coatings in a symmetric or asymmetric configuration. The two prepared mica

surfaces are mounted into the SFA chamber in a cross-cylinder configuration. The interaction between two mica surfaces is equivalent to a sphere (radius of R) approaching a flat surface when the separation distance D between two surfaces is much smaller than R. Light generated by a white light source is directed to pass through both mica surfaces, then the interference light is collected by a spectrometer and recorded using a camera.[8] In a typical normal force measurement process, the two mica surfaces are driven to approach and separate from each other, and the normal forces between two mica surfaces are obtained by using Hooke's law. The deformation of force spring can be calculated by measuring the difference between the moving distance of mica surface driven by motor and the actual separation distance between two micas surfaces as monitored by the multiple beam interferometry (MBI) by using the fringes of equal chromatic order (FECO).[12, 13] The force measured by using SFA can reach a resolution of ~10 nN and the accuracy of distance measurement is 0.1 nm.

In this thesis, the interaction between BSA and PEGDE/LP coating was measured by using SFA. Specifically, the PEGDE/LP coating and BSA coating were deposited on mica surfaces by immersing the mica sheets into the corresponding solutions for a certain time. Then, two as-prepared mica surfaces were mounted in the SFA chamber in a crossed-cylinder configuration with PBS buffer (0.13 M, pH 7.4) injected into the confined space between the two surfaces. The interaction forces between PEGDE/LP and BSA-coated mica surfaces in PBS buffer were measured as a function of the separation distance between two mica surfaces.

2.3 Other techniques

2.3.1 Scanning electron microscopy (SEM)

Scanning electron microscopy (SEM) is a powerful technique that can be applied to determine surface morphology.[14] In this project, the field emission scanning electron microscope (FESEM) (Zeiss) is applied to characterize synthesized material surface morphology. In a typical SEM scanning process, the electrons are generated from an electron gun, accelerated, and passed through a combination of lens to generate a focused electron beam. When the electron beam hits the sample surface, the secondary electrons, backscattered electrons, and characteristic X-rays will be generated. These signals will be collected by different detectors to form images that display material surface information.[15]

Moreover, the energy-dispersive X-ray spectroscopy (EDX) spectrum of FESEM is applied to determine the element distribution and concentration of materials.[16] The characterization X-ray generated from materials in the electron beam scanning process will be collected to quantitatively determine the element type and concentration.

In this thesis, the morphology and element distribution of membranes were characterized using SEM/EDX. Specifically, the membranes were cut into 1 cm * 1 cm pieces, followed by gold sputtering with the Denton Gold Sputter Unit to prevent charge buildup on the sample surface. The morphology and element mapping of the as-prepared membrane samples were characterized by FESEM with the acceleration voltage range from 10~20 kV.

2.3.2 Ultraviolet-visible (UV-Vis) spectroscopy

Ultraviolet-visible (UV-Vis) spectroscopy is used to determine the concentration of the organic molecules in the water phase by measuring the adsorption of lights in the ultraviolet and

visible light range.[17] The wavelength of the absorption peak is corresponding to the energy that needs to transfer the electron from the ground state to the excited state.[18] Moreover, the intensity of the characteristic peak is linear related to the organic molecular concentration in the solution.

In this thesis, the standard lines of different organic dyes, such as methylene blue (MB), Congo red (CR), methyl orange (MO), etc. were determined by linear fitting the intensities of characteristic peaks to the concentrations of dye solutions with known concentrations. Then, the concentration of organic dye in wastewater was determined by measuring the intensity of the corresponding characteristic peak by the UV-Vis analysis.

Reference

(1) Zeng, H. *Polymer adhesion, friction, and lubrication*; John Wiley & Sons, 2013.

(2) Magonov, S. N.; Reneker, D. H. Characterization of polymer surfaces with atomic force microscopy. *Annual Review of Materials Science* **1997**, *27* (1), 175-222.

(3) Eaton, P.; West, P. *Atomic force microscopy*; Oxford university press, **2010.**

(4) Zhang, C.; Gong, L.; Xiang, L.; Du, Y.; Hu, W.; Zeng, H.; Xu, Z.-K. Deposition and adhesion of polydopamine on the surfaces of varying wettability. *ACS applied materials & interfaces* **2017**, *9* (36), 30943-30950.

(5) Xie, L.; Cui, X.; Liu, J.; Lu, Q.; Huang, J.; Mao, X.; Yang, D.; Tan, J.; Zhang, H.; Zeng, H. Nanomechanical insights into versatile polydopamine wet adhesive interacting with liquid-infused and solid slippery surfaces. *ACS Applied Materials & Interfaces* **2021**, *13* (5), 6941-6950.

(6) Gong, L.; Wang, J.; Xiang, L.; Huang, J.; Fattahpour, V.; Roostaei, M.; Mamoudi, M.; Fermaniuk, B.; Luo, J.-L.; Zeng, H. Characterizing foulants on slotted liner and probing the surface interaction mechanisms in organic media with implication for an antifouling strategy in oil production. *Fuel* **2021**, *290*, 120008.

(7) Tabor, D.; Winterton, R. H. S. The direct measurement of normal and retarded van der Waals forces. *Proceedings of the Royal Society of London. A. Mathematical and Physical Sciences* **1969**, *312* (1511), 435-450.

(8) Zhang, J.; Zeng, H. Intermolecular and Surface Interactions in Engineering Processes. *Engineering* **2021**, *7* (1), 63-83.

(9) Israelachvili, J. N.; Adams, G. Direct measurement of long range forces between two mica surfaces in aqueous KNO3 solutions. *Nature* **1976**, *262* (5571), 774-776.

(10) Israelachvili, J. N.; McGuiggan, P. M. Adhesion and short-range forces between surfaces. Part I: New apparatus for surface force measurements. *Journal of Materials Research* **1990**, *5* (10), 2223-2231.

(11) Israelachvili, J.; Min, Y.; Akbulut, M.; Alig, A.; Carver, G.; Greene, W.; Kristiansen, K.; Meyer, E.; Pesika, N.; Rosenberg, K. Recent advances in the surface forces apparatus (SFA) technique. *Reports on Progress in Physics* **2010**, *73* (3), 036601.

(12) Israelachvili, J. Thin film studies using multiple-beam interferometry. *Journal of Colloid and Interface Science* **1973**, *44* (2), 259-272.

(13) Israelachvili, J. N. *Intermolecular and surface forces*; Academic press, 2011.

(14) Mohammed, A.; Abdullah, A. Scanning electron microscopy (SEM): A review. In *Proceedings of the 2018 International Conference on Hydraulics and Pneumatics—HERVEX, Băile Govora, Romania*, **2018**; 7-9.

(15) Zhou, W.; Apkarian, R.; Wang, Z. L.; Joy, D. Fundamentals of scanning electron microscopy (SEM). In *Scanning microscopy for nanotechnology*, Springer, **2006**; 1-40.

(16) Scimeca, M.; Bischetti, S.; Lamsira, H. K.; Bonfiglio, R.; Bonanno, E. Energy Dispersive X-ray (EDX) microanalysis: A powerful tool in biomedical research and diagnosis. *European journal of histochemistry: EJH* **2018**, *62* (1).

(17) Passos, M. L.; Saraiva, M. L. M. Detection in UV-visible spectrophotometry: Detectors, detection systems, and detection strategies. *Measurement* **2019**, *135*, 896-904.

(18) Guo, Y.; Liu, C.; Ye, R.; Duan, Q. Advances on water quality detection by UV-vis spectroscopy. *Applied Sciences* **2020**, *10* (19), 6874.

Chapter 3. Tannic acid/Fe^{3+} functionalized magnetic graphene oxide nanocomposite as an ultra-efficient catalyst for wastewater treatment

3.1 Introduction

Water contamination caused by discharged organic pollutants, such as dyes or nitrophenols, has become a severe environmental issue due to the freshwater scarcity problems.[1, 2] Organic pollutants containing aromatic structures are commonly stable in aqueous environments and pose a serious threat to human health and aquatic organisms.[3-6] A variety of strategies have been adopted for removing the organic pollutants, such as adsorption,[7, 8] filtration,[9] catalytic degradation,[10, 11] and catalytic reduction.[12] Comparatively, catalytic reduction of organic pollutants exhibits many advantages, including low-energy consumption, high-efficiency, and convenient operation.[13-16] Thus, various noble metal nanoparticles (NPs), such as gold,[17, 18] silver,[19] and platinum,[20] have been synthesized and applied in catalytic reduction processes, which have a large surface to volume ratios and display high catalytic activities towards the reduction of various organic pollutants.[21-24] Among these NPs, Ag NPs have been widely explored due to their comparative abundance and affordability, only about 1/50 of the cost of gold or platinum NPs.[25] Moreover, Ag NPs also exhibit a unique antimicrobial property, which could effectively eliminate microbial pathogens in wastewater.[26-28] However, the stability and catalytic performance of Ag NPs have been limited by the severe aggregation of Ag NPs in the aqueous media, which hinders their application as catalyst or disinfectant.

One commonly adopted strategy to improve the stability of Ag NPs is to immobilize them on supporting materials, such as metal oxide nanoparticles,[29, 30] functional polymers,[31] or carbon

materials.[14] Among these supporting materials, graphene oxide (GO), a two-dimensional (2D) structured carbon material, is considered to be promising for loading Ag NPs due to its ultra-high surface area (2630 m^2/g).[32-34] For instance, *Wang et al.* fabricated Ag NPs@GO nano-catalyst towards the catalytic reduction of 4-nitrophenol (4-NP) with a rate constant of 2.8×10^{-2} s^{-1} [14], which was superior to that of many reported Ag NP catalysts.[13, 26] Recently, magnetic graphene oxide (MGO) has been applied as supporting materials to load Ag NPs and the resulting magnetic nano-catalyst showed excellent recyclability through magnetic separation.[35, 36] Despite these advances, most reported Ag NP-based nano catalysts still require a high dosage to achieve the desirable catalytic performance to organic pollutants, typically with the catalyst concentrations between 0.5 mg/L and 5 mg/L,[37, 38] as the loading amount of Ag NPs on the reported catalysts is usually limited, *i.e.*, lower than 15 wt. %.[29, 35, 39] The main reason for this low loading of Ag NPs is that MGO nanosheets mainly possess rich oxygen-containing functional groups on the periphery but have limited ones on the basal plane. As for MGO, these functional groups are further occupied by Fe_3O_4 nanoparticles, which severely limits the deposition of the Ag NPs.[40] Generally, a higher loading of Ag NPs on the basal of MGO would result in severe Ag aggregation. To further explore and advance the application of the Ag NP based MGO nanocomposites as effective catalyst or disinfectant, the development of novel synthetic strategies to increase the loading of Ag NPs with smaller size on the basal surface is highly desirable.

Recently, tannic acid (TA)/Fe^{3+} complexation has emerged as a facile and versatile strategy to achieve multifunctional modification of various surfaces in biomedical and environmental applications.[41] The resulting uniform coatings possess abundant functional groups such as catechol and galloyl on the surfaces, which have strong coordination and reduction ability to Ag^+ ions. Therefore, we expect that adopting TA/Fe^{3+} complexation to modify MGO nanosheets might

provide a versatile platform for Ag NP immobilization on the whole surface of MGO. Herein, we present a new synthetic method to prepare Ag NPs@MGO nanocomposites with a much higher loading of Ag NPs via TA/Fe^{3+} complexation, as compared to previous studies. Notably, the loading of Ag NPs on the developed Ag@MGO-TA/Fe^{3+} nanocomposites can be as high as 30 wt.% without any obvious aggregation. This method endows the developed Ag@MGO-TA/Fe^{3+} nanocomposites with extraordinary catalytic reduction performance towards various organic pollutants, outstanding antimicrobial performance and recyclability. The catalytic rate constant of the as-prepared Ag@MGO-TA/Fe^{3+} nano-catalyst towards reduction of MB, a model organic dye, is about ten times higher than that of most NP-based catalysts reported previously. The Ag@MGO-TA/Fe^{3+} nanocomposite also exhibits a fast regeneration rate and high recyclability via magnetic separation. Meanwhile, the Ag@MGO-TA/Fe^{3+} nanocomposite can effectively inhibit the growth of *Escherichia coli* (*E. coli*), indicating its potential application as an effective disinfectant in wastewater treatment. On the basis of its facile preparation, outstanding catalytic and antimicrobial performance as well as its excellent recyclability, this work demonstrates the great potential of the Ag@MGO-TA/Fe^{3+} nanocomposite and also presents a promising strategy for rational design novel nanocomposite catalysts in wastewater purification and reclamation.

3.2 Experiment methods

3.2.1 Materials

Silver nitrate ($AgNO_3$), Iron (III) chloride hexahydrate ($FeCl_3 \cdot 6H_2O$), Iron (II) chloride tetrahydrate ($FeCl_2 \cdot 4H_2O$), sodium borohydride ($NaBH_4$), tannic acid (TA), methylene blue (MB), basic blue (BB), methyl orange (MO) and congo red (CR) were purchased from Sigma-Aldrich. Graphite flacks, 4-nitrophenol (4-NP) was purchased from Alfa Aesar. All chemicals in this study were used as received.

3.2.2 Preparation of MGO nanocomposite

GO was synthesized from graphite flakes using the modified Hummer's method [14]. The obtained GO nanosheets were further washed, centrifuged, dialyzed, and then dispersed in DI water to form a homogenous GO dispersion (1 mg/mL). Then, the MGO was prepared by a modified co-precipitation method [40]. Briefly, 50 mL GO dispersion (1mg/mL) was poured into a 100 ml three-necked flask and ultrasonicated before the next step. Then, $FeCl_3 \cdot 6\ H_2O$ (410 mg) and $FeCl_2 \cdot 4H_2O$ (145 mg) were dissolved in 20 ml DI water and added dropwise to the GO dispersion under stirring. After that, the above mixture was heated to 50 ℃ and the pH was adjusted to 10 by adding 30% ammonia solution, followed by increasing the temperature to 85 ℃ and maintained for 1 hour to finish the reaction. The obtained MGO nanocomposite was magnetically separated, filtered, washed by DI water and ethanol several times and dried for the next step.

3.2.3 Preparation of MGO-TA/Fe^{3+} nanocomposite

10 mg MGO was firstly dispersed in 20 mL DI water and ultrasonicated to form a homogenous dispersion. Then 0.2 mL $FeCl_3 \cdot 6\ H_2O$ (10 mg/mL) solution and 0.8 mL TA solution (10 mg/mL) were added into MGO dispersion, followed by adding Tris buffer (pH=8.5) solution to adjust the pH to 8. The above mixture was vigorously stirred for one minute to form TA/Fe^{3+} coating on MGO. Then, the TA/Fe^{3+} coated MGO was magnetically separated and washed by DI water to remove the excess TA, Fe^{3+} ions, and TA/Fe^{3+} aggregates in the product. The obtained black product was labeled as MGO-TA/Fe^{3+} nanocomposite.

3.2.4 Preparation of Ag@MGO-TA/Fe^{3+} nanocomposite

To immobilize Ag NPs on the surfaces of MGO-TA/Fe^{3+} nanocomposites, $Ag(NH_3)_2OH$ solution (Tollens' reagent) was firstly prepared by dropping 2 wt. % ammonia aqueous solution into 5 mg/mL $AgNO_3$ solution until brown precipitate dissolved. The pH value of the as-prepared MGO-TA/Fe^{3+} solution (1mg/mL) was adjusted to 8 by using Tris Buffer (pH=8.5) solution, then the freshly prepared $Ag(NH_3)_2OH$ solution (5 mg/mL) was slowly dropwise into 5 mL MGO-TA/Fe^{3+} solution (1 mg/mL) on shaker (200 rpm) at room temperature, the color of the mixture would turn from dark into dark brown, the mixture was keeping on shaking (200 rpm) for 8h to finish the reaction. Then, the obtained brown product was collected using an external magnet, washed, dried, and labeled as Ag-5@MGO-TA/Fe^{3+} nanocomposite. Moreover, the same procedure was applied to synthesize the Ag@MGO nanocomposite by using MGO instead of MGO-TA/Fe^{3+} nanocomposites. In addition, the same procedure was also used to prepared Ag-1@MGO-TA/Fe^{3+} and Ag-10@MGO-TA/Fe^{3+} nanocomposites by using 1mg/mL and 10 mg/mL $Ag(NH_3)_2OH$ solutions, respectively.

3.2.5 Characterization

The transmission electron microscopy (TEM), high resolution (HR)-TEM images, and scanning transmission electron microscope (STEM) - energy dispersive X - ray spectroscopy element (EDX) mapping results of the sample were taken by using a JEOL JEM-ARM200CF S/TEM with EDX operated at 200 kV condition. X-ray photoelectron spectroscopy (XPS) measurement was conducted on a Kratos Axis spectrometer using Al Kα radiation. The structure of the synthesized samples was characterized and confirmed by powder X-ray diffraction (XRD) patterns collected on a Bruker D8 X-ray diffractometer using Cu Kα radiation. The UV-Vis absorption spectra were obtained by using a Thermo Scientific Evolution 300 UV−Vis

spectrophotometer (Thermo Fisher Scientific). The Brunauer–Emmett–Teller (BET) surface areas of the samples were tested by the 7-point BET method by N_2 sorption (Autosorb-iQ-XR). Magnetic properties of the samples were characterized by applying the Quantum Design Physical Property Measurement System magnetometer with an applied field between −30000 Oe to 30000 Oe at room temperature. The inductively coupled plasma mass spectrometry (ICP-MS) was detected by using a Thermo Scientific ICAP-Q quadrupole.

3.2.6 Catalytic performance of Ag@MGO-TA/Fe^{3+} nanocomposites

The catalytic performance of Ag@MGO-TA/Fe^{3+} nanocomposites was investigated for the reduction of model organic pollutants: MB and 4-NP in the presence of $NaBH_4$. In a typical procedure of MB reduction, 100 μL of Ag-5@MGO-TA/Fe^{3+} solution (1 mg/mL) was added into 2 mL MB solution (40 ppm, 2 mL) in a quartz cuvette. Then 200 μL $NaBH_4$ (0.1 mol/L) was injected into the above solution to initiate the catalytic process, which was monitored by UV−Vis spectroscopy by monitoring the absorbance spectra of MB every fifteen seconds until the characteristic absorbance peak disappeared. In addition, methyl orange (MO), basic blue (BB), and congo red (CR) were used as other model dyes (40 ppm, 2 mL) to test the catalytic reduction performance of Ag-5@MGO-TA/Fe^{3+} catalyst (150 μL, 1 mg/mL) using the same procedure. To evaluate the catalytic reduction performance of Ag-5@MGO-TA/Fe^{3+} catalyst towards 4-NP, 1 mL $NaBH_4$ (0.2 mol/L) solution and 300 μL 1 mM 4-NP were added into 1.5 mL water, then 200 μL of Ag-5@MGO-TA/Fe^{3+} solution (1 mg/mL) was added into above solution under stirring. The catalytic reduction process was monitored by measuring in the change of the absorbance peak at 400 nm in the UV–vis spectroscopy. For the reusability test, the Ag-5@MGO-TA/Fe^{3+} catalyst in the reaction medium was separated and collected by applying an external magnetic field, followed by washing with water and ethanol before the next cycle.

3.2.7 Antimicrobial Assay

The spread plate method was used to evaluate the antimicrobial property of as-prepared Ag-5@MGO-TA/Fe^{3+} nanocomposite by employing *E. coli* as a model.[42] Ag-5@MGO-TA/Fe^{3+} nanocomposites were dispersed in *E. coli* suspensions (10^5 colony-forming units (CFU)/mL) with the concentration in each suspension ranging from 5 μg/mL to 25 μg/mL. The mixtures were transferred and evenly spread to each of the pre-warmed agar plates, followed by incubation at 37°C for 16 hours. The numbers of colonies on each agar plates after incubation were counted by visual inspection and compared with the number of colonies on the control plate (without Ag-5@MGO-TA/Fe^{3+}nanocomposite). In order to characterize the *E. coli* after treating with Ag-5@MGO-TA/Fe^{3+} nanocomposite, 5 mL of *E. coli* bacterial suspension treated and untreated with Ag-5@MGO-TA/Fe^{3+} nanocomposite was centrifuged at 4000 rpm for 10 min at 4 °C, washed twice with PBS buffer, followed by fixing with 2% glutaraldehyde solution for 24 h at 4 °C. The *E. coli* samples were dehydrated with sequential treatment of 50, 70, 80, 90, and 100% ethanol for 15 min, then the dehydrated *E. coli* was dried by using CO_2 critical point drying method. Finally, the dried samples were gold sputter-coated and imaged by applying FESEM.

3.3 Results and discussion

3.3.1 Synthesis and Characterizations of Materials

The procedure for preparing Ag@MGO-TA/Fe^{3+} nanocomposite is shown in Figure 3.1 Firstly, GO was synthesized from graphite flakes using the modified Hummer's method.[43] Then, MGO nanosheets were synthesized by depositing Fe_3O_4 nanoparticles on GO through the modified co-precipitation method.[40] The obtained MGO nanosheets were further modified with TA/Fe^{3+} coating by mixing $FeCl_3 \cdot 6H_2O$ solution into MGO solution containing TA. The hydrophilic groups of TA on MGO could help reduce the aggregation of MGO and enhance its stability and

dispersibility in aqueous solution. After the addition of the TA and Fe^{3+} solutions, the TA/Fe^{3+} film was formed on the MGO within one minute through the coordination between Fe^{3+} ions and the galloyl/catechol groups of TA.[41] Then taking the advantage of the reducing and coordination property of TA, abundant Ag^{+} ions from Tollens' reagent could be easily in-situ reduced into Ag NPs under the mild alkaline condition and anchored on the surface of MGO-TA/Fe^{3+} nanocomposites without any additional reductants.[42]

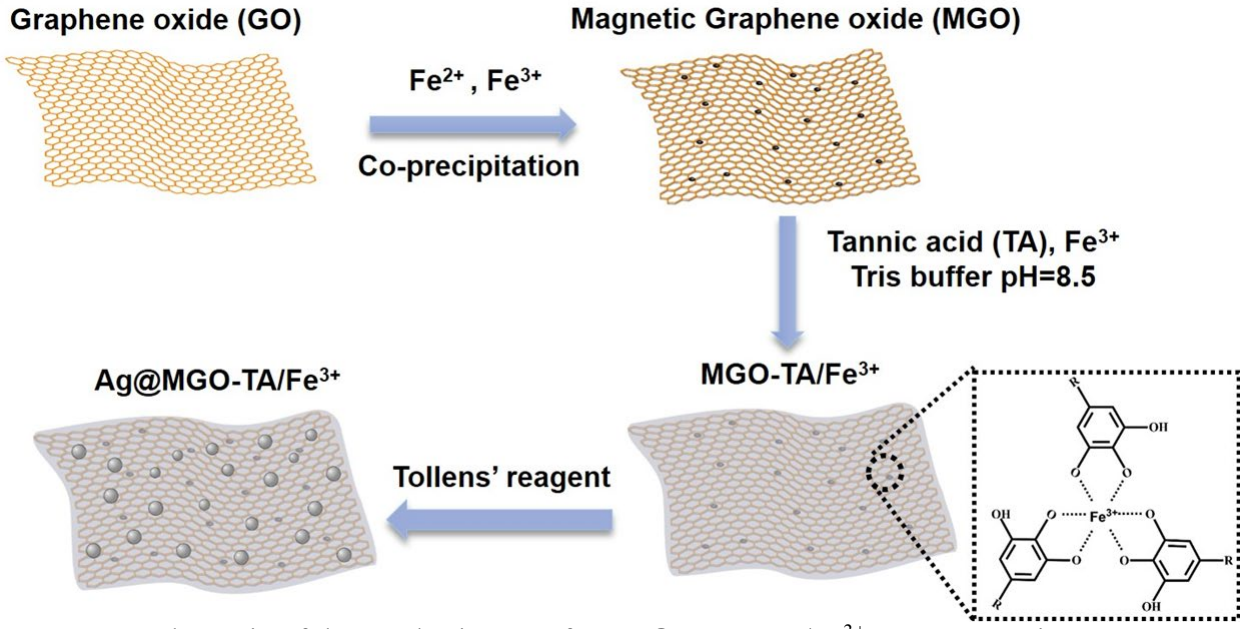

Figure 3.1 Schematic of the synthesis route for Ag@MGO-TA/Fe^{3+} nanocomposite.

The morphologies and crystal structures of the as-prepared MGO, MGO-TA/Fe^{3+}, and Ag@MGO-TA/Fe^{3+} nanocomposites were characterized by TEM. The TEM image of MGO in Figure 3.2(a) showed that the large amounts of Fe_3O_4 nanoparticles were uniformly anchored on the GO surface without aggregation. Compared to MGO, the morphology of MGO-TA/Fe^{3+} nanocomposites (Figure 3.2(b)) did not change obviously and the surface of MGO-TA/Fe^{3+} nanosheet became rougher after modification with TA/Fe^{3+} coating. The HRTEM image of MGO-TA/Fe^{3+} nanocomposite (Figure 3.2(c)) showed the presence of nanocrystals on its surface with

the d-spacing of 0.25 nm, corresponding to the (311) crystal plane of Fe_3O_4, demonstrating the successful deposition of Fe_3O_4 nanoparticles in the MGO-TA/Fe^{3+} nanocomposite. Furthermore, it was found that the zeta potentials of MGO nanosheets decreased from -17.6 mV to -43.7 mV after coated with TA/Fe^{3+} layer, which was caused by the existence of negatively charged catechol/galloyl groups of TA, confirming the formation of TA/Fe^{3+} coating on MGO (Figure S3.1).

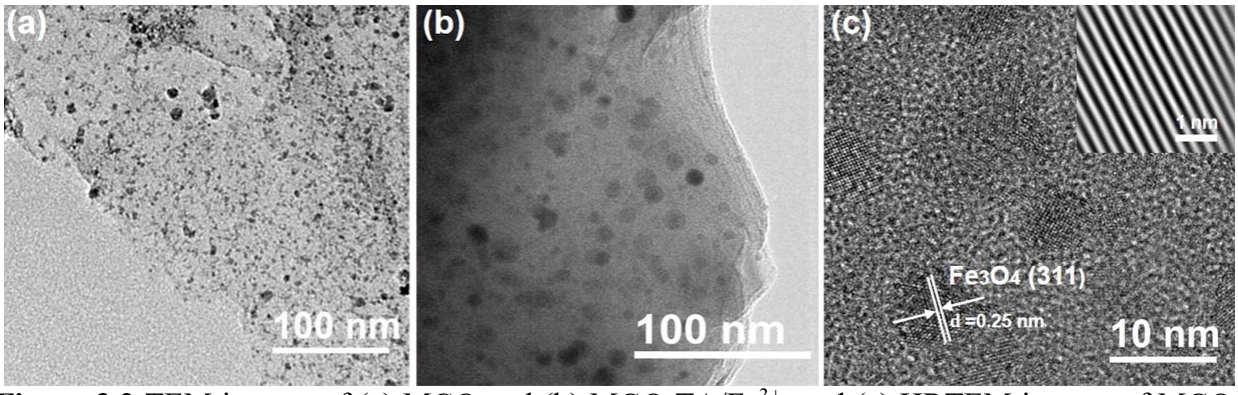

Figure 3.2 TEM images of (a) MGO and (b) MGO-TA/Fe^{3+}, and (c) HRTEM images of MGO-TA/Fe^{3+} nanocomposites.

The TEM images of Ag-5@MGO-TA/Fe^{3+} nanocomposite at different magnifications (Figure 3.3(a)~(b)) show that the sphere-like Ag NPs were successfully anchored on the MGO-TA/Fe^{3+} nanosheet. Moreover, the average size of Ag NPs was calculated as 16.4$\pm$4.1 nm from particle size distribution shown in Figure S3.2. The HRTEM image of Ag-5@MGO-TA/Fe^{3+} nanocomposite (Figure.3.3(c)) demonstrates that two kinds of sphere-like nanocrystals are present on the Ag-5@MGO-TA/Fe^{3+} surface. The d-spacing of these two kinds of crystalline regions were measured to be 0.23 nm and 0.25 nm from inversed Fast Fourier Transform (FFT) results (Figure 3.3(d)), respectively, corresponding to the (111) plain of face-centered cubic (fcc) Ag and the (311) crystal plane of Fe_3O_4, confirming the successful deposition of Ag and Fe_3O_4 nanoparticles on the Ag-5@MGO-TA/Fe^{3+} nanocomposite. Furthermore, high angle annular dark-field scanning TEM

(HAAD-STEM) image of the selected region (in the red frame) in Figure 3.3(b) and its corresponding STEM-energy dispersive X-ray spectroscopy (STEM-EDX) element mapping results were shown in Figure 3.3(e)~(h). The Ag signal (purple) presented in Figure 3.3(f) showed good agreement with the TEM results in Figure 3.3(b). The Fe (yellow) and O (blue) signals were detected all over the materials surface, indicating the formation of TA/Fe^{3+} layer on Ag-5**@**MGO-TA/Fe^{3+} nanocomposite. The yellow and blue spots found in Fe and O element mapping results also confirm the formation of Fe_3O_4 nanoparticles in the nanocomposite. In addition, the number density of Ag NPs on the Ag@MGO-TA/Fe^{3+} surface could be facilely turned by adjusting the concentration of $Ag(NH_3)_2OH$. As shown in Figure S3.3, the number density of Ag NPs on the nanocomposite surface increased with increasing the $Ag(NH_3)_2OH$ concentration from 1 mg/mL to 10 mg/mL. Moreover, the mass contents of Ag in Ag-1**@**MGO-TA/Fe^{3+}, Ag-5**@**MGO-TA/Fe^{3+}, and Ag-10**@**MGO-TA/Fe^{3+} were found to be 8.3 wt. %, 30.7 wt. %, and 44.8 wt. %, respectively, measured by inductively coupled plasma atomic emission spectrometry (ICP-MS).

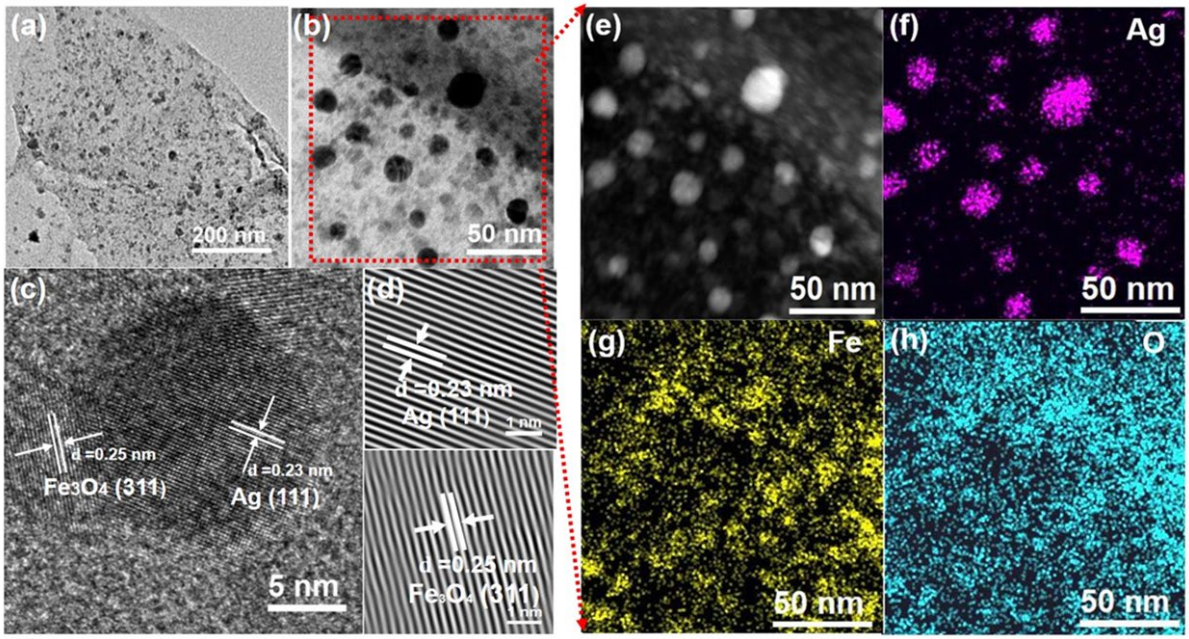

Figure 3.3 (a), (b)TEM images of Ag-5@MGO-TA/Fe^{3+} nanocomposite at different magnification; (c) HRTEM image and (d) FFT pattern of Ag-5@MGO-TA/Fe^{3+} nanocomposite; (e) HAADF-STEM image and (f)~(h) corresponding STEM-EDX mapping results (element Ag, Fe, and O) of Ag-5@MGO-TA/Fe^{3+} nanocomposite.

XPS measurements were conducted to further characterize the surface element composition and chemical bonding state of Ag-5@MGO-TA/Fe^{3+} nanocomposite. The survey spectrum shown in Figure 3.4(a) revealed that the presence of C, O, Fe and Ag in the Ag-5@MGO-TA/Fe^{3+} nanocomposite, which was consistent with the STEM-EDX mapping results. The high-resolution Fe 2p spectrum in Figure 3.4(b) can be deconvoluted into two peaks located at 711.2, and 725.3 eV, mainly attributed to the presence of Fe_3O_4 in the Ag-5@MGO-TA/Fe^{3+} nanocomposite. The high-resolution Ag 3d spectrum (Figure 3.4(c)) shows two peaks at 367.9 and 374.1 eV, which are typical binding energies of metallic state Ag. The C 1s spectrum in Figure 3.4(d) can be deconvoluted into three peaks at 284.5, 286.2, and 288.8 eV, which can be assigned to C=C, C-O, and C=O bonds in TA. These results are in accordance with the XRD spectra, as the

XRD pattern of Ag-5@MGO-TA/Fe^{3+} nanocomposite (Figure 3.4(e)) shows typical diffraction peaks at 2θ = 38.1 °, 44.3 °, 64.4 °, and 77.4 °, corresponding to (111), (200), (220), and (311) planes of the face-centered cubic (fcc) structure of Ag (PDF#98-000-0398) and the diffraction peaks at 2θ = 32.5 ° and 62.5 °corresponding to (311) and (440) crystal facets of Fe_3O_4. The chemical compositions of as-prepared MGO, MGO-TA/Fe^{3+}, and Ag-5@MGO-TA/Fe^{3+} nanocomposites were further investigated by FT-IR spectroscopy. As shown in Figure 3.4(f), after coating Fe_3O_4 nanoparticles on GO, the peaks from 1000 to 1300 cm^{-1} (the C–O–C vibration of epoxy groups), the peaks around 3400 cm^{-1} (the O–H vibration of hydroxyl groups) and the peak at 1627 cm^{-1} (the –C=O vibration of carboxylic groups) [44, 45] were weakened, which was caused by the reduction of the GO due to the high temperature in the co-precipitation process.[46] Moreover, the remaining oxygen-containing groups on GO would interact with the Fe ions to form iron oxide in the co-precipitation process, which leads to the further decrease of the intensity of the peaks of the oxygen-containing groups on MGO in FT-IR spectrum [40]. After coating the MGO with TA/Fe^{3+} layer, the new peaks at 1710, 1450, 1080 cm^{-1} corresponding to C=O, C-OH, and C-O-C stretching vibration can be observed due to the existence of TA in the nanocomposite. The characteristic peaks of TA have been highlighted in Figure 3.4(f) (in green square).[47] After immobilizing Ag NPs on the MGO-TA/Fe^{3+} nanocomposite, the stretching vibrations of C=O and C-OH groups decrease due to the coordination between the gallic/catechol groups of TA and the formed Ag NPs. In addition, given the fact that the surface area of catalyst plays a crucial role in their catalytic performance,[48] the BET surface areas of MGO and Ag-5@MGO-TA/Fe^{3+} nanocomposites were determined as 346.20 m^2/g and 126.37 m^2/g, respectively, by nitrogen adsorption measurements (Figure S3.4). Even though the surface area of MGO reduced after modification with TA/Fe^{3+} layer and Ag NPs, the BET surface area of Ag-5@MGO-TA/Fe^{3+} nanocomposite is still much

higher than that of most previously reported NPs catalysts, such as the urchin like Fe_3O_4@PDA-Ag NPs catalysts (48.04 m^2/g) or Ag@PDA nanotubes (43.90 m^2/g) nano-catalysts,[29, 48-50] which endows the Ag-5@MGO-TA/Fe^{3+} nanocomposite abundant active sites for organic pollutant molecular in the catalytic reduction reactions process.

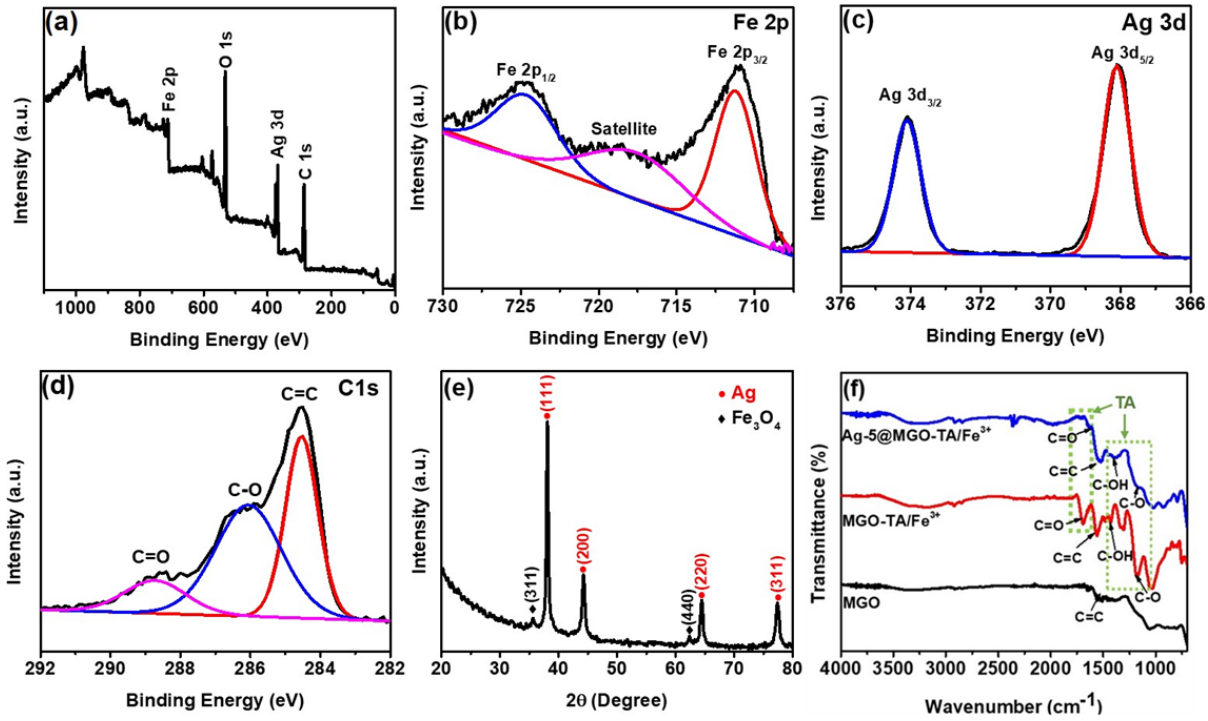

Figure 3.4 (a) Survey XPS spectrum and high-resolution XPS spectra of (b) Fe 2p, (c) Ag 3d, (d) C 1s of Ag-5@MGO-TA/Fe^{3+} nanocomposite; (e) XRD pattern of Ag-5@MGO-TA/Fe^{3+} nanocomposite; (f) FT-IR spectrums of MGO, MGO-TA/Fe^{3+}, and Ag-5@MGO-TA/Fe^{3+} nanocomposites.

The magnetic properties of as-prepared MGO, MGO-TA/Fe^{3+}, and Ag-5@MGO-TA/Fe^{3+} nanocomposites were characterized by Quantum Design PPMS magnetometer with an applied field between −30000 Oe to 30000 Oe at room temperature. As shown in Figure 3.5, almost no hysteresis loop was found in all spectra, indicating the superparamagnetic property of MGO and MGO-TA/Fe^{3+}, and Ag-5@MGO-TA/Fe^{3+} nanocomposites with the saturated magnetizations at

13.9 emu/g, 7.3 emu/g, and 4.8 emu/g, respectively. Compared to MGO, the slight reduction of the saturated magnetizations of Ag-5@MGO-TA/Fe^{3+} nanocomposite was caused by its reduced Fe_3O_4 content due to the functionalization of the TA/Fe^{3+} layer and Ag NPs.

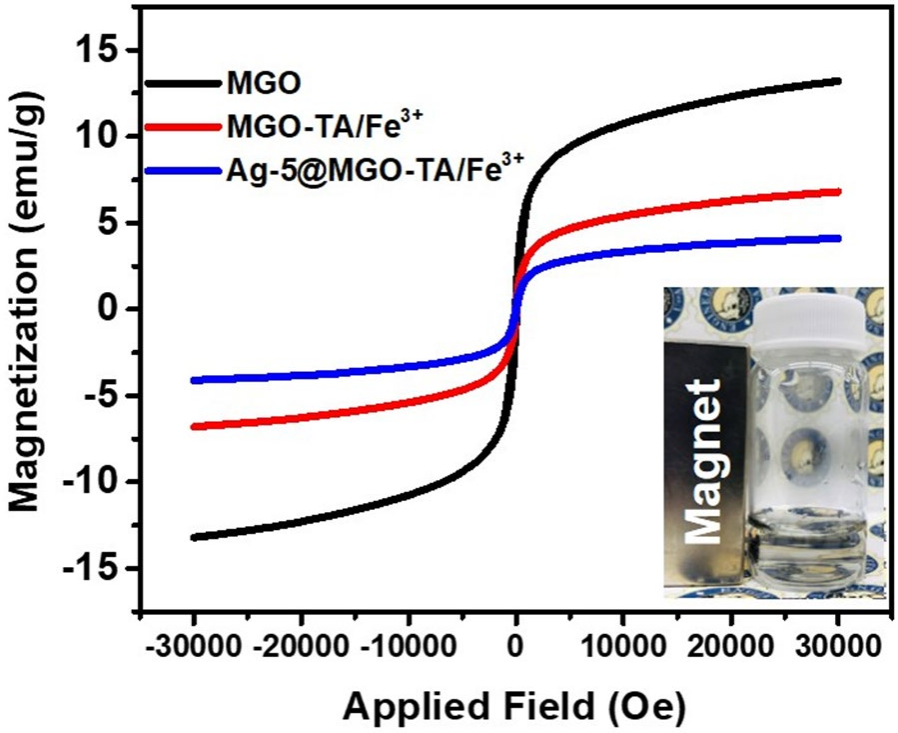

Figure 3.5 VSM curves of MGO, MGO-TA/Fe, and Ag-5@MGO-TA/Fe^{3+} nanocomposites. The insert photograph represents the separation of Ag-5@MGO-TA/Fe^{3+} nanocomposite from solution by applying a magnet bar.

3.3.2 Catalytic Performance of Ag@MGO-TA/Fe^{3+}nanocomposite

The catalytic reduction performance of as-prepared Ag@MGO-TA/Fe^{3+} nanocomposites was evaluated by catalyst reduction of MB in the presence of $NaBH_4$, which was monitored by UV-VIS spectroscopy. As shown in Figure 3.6(a)~(c), after adding Ag-1@MGO-TA/Fe^{3+}, Ag-5@MGO-TA/Fe^{3+}, and Ag-10@MGO-TA/Fe^{3+} catalysts in each of MB solution, the color of the MB solutions gradually disappeared within 120s, 75s, 90s, respectively, accompanied by the decreasing and disappearing of the characterize peak at 665 nm in each of the UV-Vis spectrum,

indicating the MB molecules were catalytic reduced by the catalyst. As the concentration of the $NaBH_4$ further excessed the concentration of MB in the reaction, the concentration of $NaBH_4$ could be considered as a constant. Thus, the reduction rates in this experiment were found to be well described by the pseudo-first-order kinetic model: $\ln(C_t/C_0) = -kt$, where the C_0 and C_t were the concentrations of MB at the initial stage and time t, respectively and the k here was the rate constant of the catalytic reaction.[39, 51] As shown in Figure 3.6(d), by linear fitting between $\ln(C_t/C_0)$ versus the time t, the rate constants of Ag-1@MGO-TA/Fe^{3+}, Ag-5@MGO-TA/Fe^{3+}, and Ag-10@MGO-TA/Fe^{3+}towards MB reduction were determined as 0.032 s^{-1}, 0.054 s^{-1}, 0.044 s^{-1}, respectively. The increased catalytic activity from Ag-1@MGO-TA/Fe^{3+} to Ag-5@MGO-TA/Fe^{3+} catalyst was attributed to the increased content of Ag NPs on the catalyst, which provided more active sites in the catalytic process. As for the Ag-10@MGO-TA/Fe^{3+} catalyst, the slightly reduced catalytic activity was caused by the slight decrease of active sites on the catalyst due to the aggregation of Ag NPs (Figure S3.3). Control experiments were also conducted by using Ag NPs or $NaBH_4$ as catalysts. As shown in Figure S3.5, no obvious change of MB concentration could be detected by only applying $NaBH_4$ in five minutes, indicating the important role of Ag NPs in the catalytic reduction process. Moreover, Ag NPs catalyst showed very limited MB catalytic rate compared to Ag-5@MGO-TA/Fe^{3+} catalyst due to the severe aggregation of Ag NPs. The Ag@MGO nanocomposite also showed limited catalytic performance and no obvious change of MB concentration could be detected by applying Ag@MGO without TA/Fe^{3+} coating within two minutes, which was due to the limited Ag content and the severe aggregation of Ag@MGO nanocomposite.

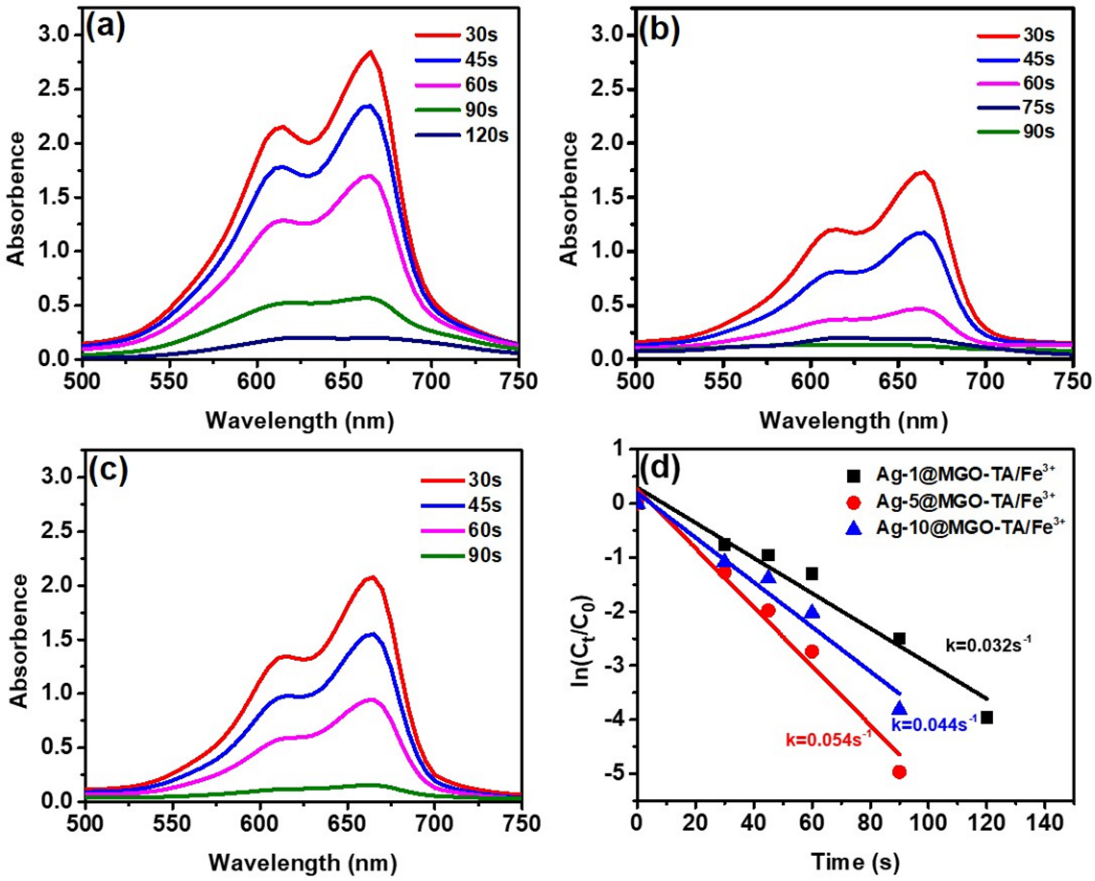

Figure 3.6 Successive UV−vis spectra for catalytic reduction of MB by applying (a) Ag-1@MGO-TA/Fe^{3+}, (b) Ag-5@MGO-TA/Fe^{3+}, and (c) Ag-10@MGO-TA/Fe^{3+} catalyst, (d) First-order kinetics plot of catalytic reduction of MB solution in the presence of Ag-1@MGO-TA/Fe^{3+}, Ag-5@MGO-TA/Fe^{3+}, and Ag-10@MGO-TA/Fe^{3+} catalysts.

The mechanism of catalytic reduction of MB by using the Ag@MGO-TA/Fe^{3+} catalyst in the presence of $NaBH_4$ could be explained by the electrochemical reaction, where Ag NPs facilitated the electrons transfer from BH_4^- to electrophilic MB on the surface of Ag NPs [29, 48, 51]. In the catalytic reduction process, the adsorption of MB on catalyst is the precondition of the following catalytic reduction process because the reduction of MB could only occur on the surface of Ag NPs [48, 52]. In this process, the adsorption of MB molecules on nano-catalyst would happen firstly through electrostatic interactions and π-π stacking interactions. In the following catalytic

reduction process, nucleophilic BH_4^- ions donated electrons to the Ag NPs on the nano-catalyst and then transferred to the electrophilic MB adsorbed on the Ag-5@MGO-TA/Fe^{3+} nano-catalyst, leading to the reduction of MB on the surfaces of Ag NPs on the nano-catalyst [51]. To further demonstrate this synergistic local enrichment mechanism, the MB adsorption test was carried out by applying Ag-5@MGO-TA/Fe^{3+} nanocomposites as adsorbent. As shown in Figure S3.6, the adsorption capacity of as-prepared Ag-5@MGO-TA/Fe^{3+} nanocomposites towards MB was determined as 345 mg/g under neutral pH condition (pH=7.4) of the nanocomposite suspension in water, which was attributed to the large surface area of Ag-5@MGO-TA/Fe^{3+} nanocomposites and the π-π stacking and electrostatic interaction between MB molecules and TA film on the nanocomposites [53]. The adsorption kinetic of Ag-5@MGO-TA/Fe^{3+} nanocomposites towards MB was also investigated. As shown in Figure S3.7, the adsorption of MB on Ag-5@MGO-TA/Fe^{3+} nanocomposites drastically increased at the first few minutes and then achieved equilibrium, indicating the active sites on nano-catalyst were rapidly occupied by MB molecules. Moreover, pseudo-first-order kinetic and pseudo-second-order kinetic model were used to describe the adsorption kinetic of Ag-5@MGO-TA/Fe^{3+} nanocomposites.

Pseudo-first-order kinetic model:

$$\log(q_e - q_t) = \log q_e - \frac{k_1 t}{2.303} \tag{3.1}$$

Pseudo-second-order kinetic model:

$$\frac{t}{q_t} = \frac{1}{q_e{}^2 k_2} + \frac{t}{q_e} \tag{3.2}$$

$q_e$and q_t (mg/g) are the amounts of MB adsorbed at equilibrium and at time t. the k_1 (/min) and k_2 (g/mg/min) are pseudo-first and pseudo-second order rate constants, respectively. All parameters were included in Table. S3.1, the pseudo-second-order model showed better coefficient

values (R^2) and the q_e calculated form pseudo-second-order model was closer to the experiment data, indicating a better fitting of data by applying pseudo-second-order model.

To further evaluate the catalytic performance of the Ag-5@MGO-TA/Fe^{3+} catalyst towards MB reduction, the MB reduction tests were conducted with different concentrations of Ag-5@MGO-TA/Fe^{3+} catalyst. As shown in Figure S3.8, the catalytic rate constants of MB reduction increased to 0.063 s^{-1} and 0.113 s^{-1} with the increasing concentration of Ag-5@MGO-TA/Fe^{3+} catalyst. As shown in Table 3.1, in order to compare the catalytic reduction performance of Ag-5@MGO-TA/Fe^{3+} catalyst with other reported catalysts for MB reduction, the rate constants of Ag-5@MGO-TA/Fe^{3+} catalyst were further normalized to the mass concentration of catalysts (M/V) used in reaction: $k' = k \cdot M^{-1} \cdot V$. The k' of Ag-5@MGO-TA/Fe^{3+} catalyst was calculated as 64.8 mL/(mg·min), which was about ten times faster than that of SMt@GO@Au NPs catalysts for MB reduction reported recently.[50] The exceptional catalytic reduction performance of Ag-5@MGO-TA/Fe^{3+} could be attributed to the synergistic adsorption of the MB molecules on the catalyst (345 mg/g) due to large surface area 126.37 m^2/g and the TA/Fe^{3+} film of Ag-5@MGO-TA/Fe^{3+} nanocomposite, leading to the local concentrated regime of MB around the Ag NPs, thus facilitating the electron transfer between the MB molecules and Ag NPs and enhancing the catalytic performance. Moreover, the abundant (30.7 wt.%) Ag NPs on the Ag-5@MGO-TA/Fe^{3+} nanocomposite also facilitated the catalytic process by providing large amounts of active sites with high catalytic activity to the reactants in the catalytic reduction reaction. The well-dispersed Ag NPs on the nano-catalyst has high catalytic activity owing to their large surface-to-volume ratio.

Table 3.1 Comparison of catalytic rate constants of different NPs-based catalysts towards MB reduction.

Pollutant	Catalysts	Rate constant *k* (/min)	Catalyst used(mg/mL)	*k'* (mL/(mg·min))	Ref
Methylene blue (MB)	Fe_3O_4@PDA-Ag	0.43	0.48	0.90	51
	Urchin Fe_3O_4@PDA-Ag	1.87	0.48	3.93	48
	Fe_3O_4@EDTA-Ag	1.83	0.60	3.05	29
	Ag/Fe_3O_4/C	0.34	1.10	0.31	54
	biochar/PDA/Ag	0.87	0.25	3.49	55
	SMt@GO@Au NPs	0.53	0.10	5.31	50
	Ag-5@MGO-TA/Fe^{3+}	3.24	0.05	64.80	This work

The influence of the initial pH on the catalytic reduction performance of the Ag-5@MGO-TA/Fe^{3+} catalyst has been evaluated by conducting MB catalytic reduction tests at different initiate pH conditions. As shown in Figure S3.9(a)~(d), the MB solutions with the initiate pH at 3, 5, 7, and 9 were all successfully reduced by Ag-5@MGO-TA/Fe^{3+} catalyst with the rate constants determined as 0.087 s^{-1}, 0.073 s^{-1}, 0.051 s^{-1}, and 0.037 s^{-1}, respectively, indicating the effectiveness of Ag-5@MGO-TA/Fe^{3+} catalyst at wide pH range. Moreover, it was found that the catalytic rate constants of Ag-5@MGO-TA/Fe^{3+} catalyst gradually increased with the decreasing initial pH value. Such results could be ascribed to the enhanced hydrolysis of $NaBH_4$ which provided much more BH_4^- groups to the Ag-5@MGO-TA/Fe^{3+} catalyst under the more acidic condition, thus accelerating the catalytic reaction process.[56]

Given that the Ag-5@MGO-TA/Fe^{3+} catalyst showed outstanding performance in MB reduction, we further evaluated the catalytic reduction performance of Ag-5@MGO-TA/Fe^{3+}

catalysts towards other organic pollutants including CR, BB, MO, and 4-NP. As shown in Figure 3.7(a)~(c), the UV-vis absorption peaks of CR, BB, and MO solutions disappeared within several minutes after adding the Ag-5@MGO-TA/Fe^{3+} catalyst, accompanied by fading of the dye solutions, demonstrating the universal catalytic capability of the as-prepared Ag-5@MGO-TA/Fe^{3+} on various organic dyes. Moreover, the catalytic rate constants of Ag-5@MGO-TA/Fe^{3+} catalyst towards different organic dyes were summarized in Figure 3.7(d). Additionally, 4-NP, a toxic organic pollutant discharged in the pesticide production process, was employed as another model pollutant to evaluate the catalytic reduction performance of the Ag-5@MGO-TA/Fe^{3+} catalyst. As shown in Figure 3.7(e), the characteristic UV-vis absorption peak of 4-NP at 400 nm gradually decreased after adding Ag-5@MGO-TA/Fe^{3+} catalyst and the new peak at 300 nm simultaneously appeared and increased, indicating the successful reduction of the 4-NP to 4-aminophenol (4-AP) with a rate constant determined as 0.052 s^{-1} (Figure 3.7(f)), which was superior to that of other previously reported NPs catalysts for 4-NP reduction under similar conditions (summarized in Table S3.2).

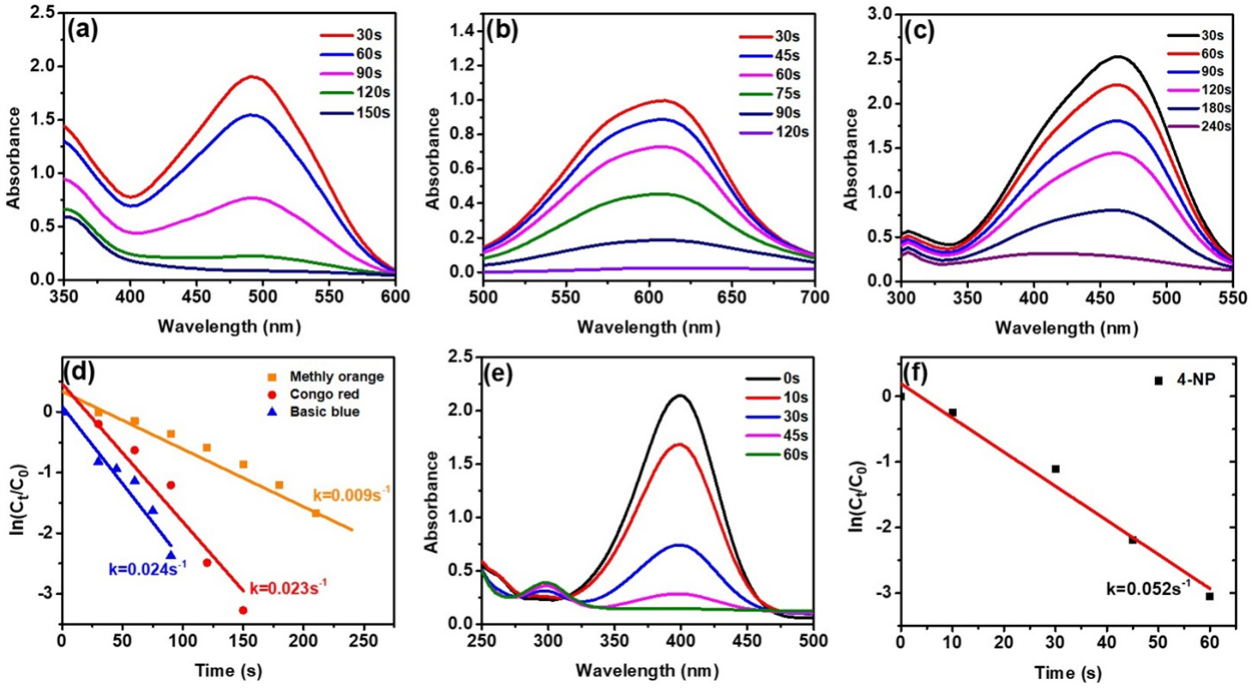

Figure 3.7 Successive UV−vis spectra for catalytic reduction of (a) CR, (b) BB, and (c) MO s by Ag-5@MGO-TA/Fe^{3+} catalyst. (d) First-order kinetics plots of catalytic reduction of CR, BB, and MO by Ag-5@MGO-TA/Fe^{3+} catalyst. (e) Successive UV−vis spectra for catalytic reduction of 4-NP by Ag-5@MGO-TA/Fe^{3+} catalyst and (f) First-order kinetics plots of catalytic reduction of 4-NP in the presence of Ag-5@MGO-TA/Fe^{3+} catalyst.

3.3.3 Recyclability of Ag-5@MGO-TA/Fe^{3+} catalyst

Owing to its magnetic property, After the catalytic reaction, the magnetic Ag-5@MGO-TA/Fe^{3+} catalyst could be facilely separated from the reaction medium by applying an external magnet bar, the magnetic separation process would last for about ten minutes to fully separate the Ag-5@MGO-TA/Fe^{3+} nanocomposite from the reaction medium. Figure 3.8 showed the recyclability of Ag-5@MGO-TA/Fe^{3+} catalyst towards the catalytic reduction of MB. The Ag-5@MGO-TA/Fe^{3+} catalyst was magnetically separated and washed with ethanol and deionized water for several times before being used in the next catalytic reduction cycle. It was found that the catalytic efficiency of Ag-5@MGO-TA/Fe^{3+} catalyst kept almost the same, with the removal

rate of MB still higher than 95% after five cycles, demonstrating the good stability of the Ag-5@MGO-TA/Fe^{3+} nanocomposite in the catalytic reaction.[57]

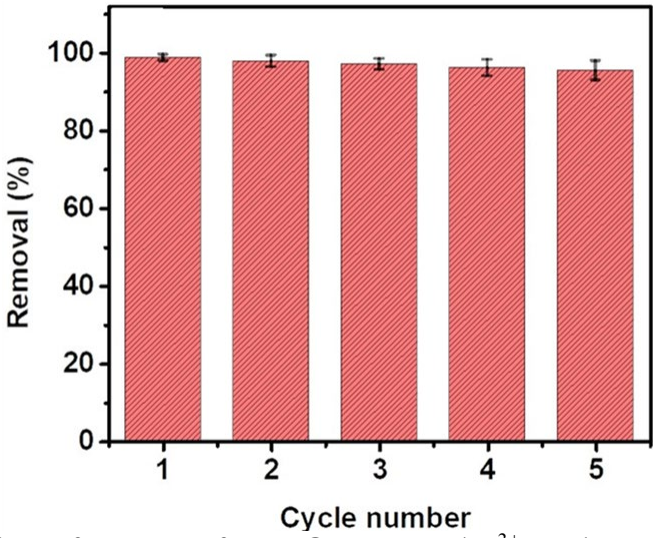

Figure 3.8 The catalytic performance of Ag-5@MGO-TA/Fe^{3+} catalyst towards the reduction of MB within five cycles.

3.3.4 Antimicrobial Property of Ag-5@MGO-TA/Fe^{3+} nanocomposite

Ag-5@MGO-TA/Fe^{3+} nanocomposite may also be applied as an effective antimicrobial agent to eliminate microbial pathogens in wastewater. *E. coli*, the most common bacterial species in water, was employed as a model bacterial species (10^5 CFU/mL) to evaluate the antimicrobial property of as-prepared Ag-5@MGO-TA/Fe^{3+} nanocomposite. As shown in Figure 3.9(a) ~(b), the presence of 5 μg/mL Ag-5@MGO-TA/Fe^{3+} nanocomposite effectively killed more than 50% *E. coli*. When increasing the concentration of Ag-5@MGO-TA/Fe^{3+} nanocomposite to 25 μg/mL, more than 99% *E. coli* was killed and no visible *E. coli* colonies were observed. The FESEM microscopy was applied to further analysis the surface morphology changes of the *E. coli* bacterial treated and untreated with Ag-5@MGO-TA/Fe^{3+} nanocomposite, as shown in Figure. 3.9(c), the untreated *E. coli* bacterial showed typically rod-like structure with the well–preserved cell wall. However, the cell wall of the *E. coli* was shrunk and broken after treating with Ag-5@MGO-

TA/Fe^{3+} nanocomposite (Figure 3.9(d)), demonstrating that the Ag NPs on the nanocomposite would induce severely damage to the cell wall *E. coli* bacterial.[26, 42]

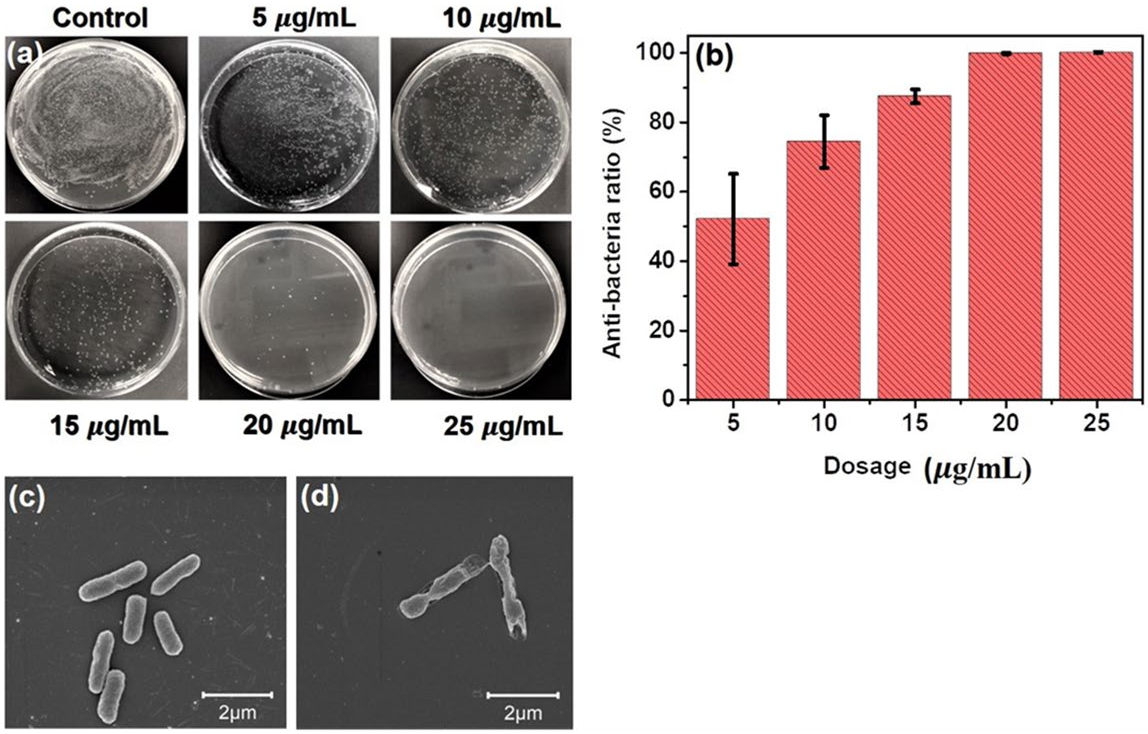

Figure 3.9 (a) Representative photographs of *E. coli* colonies after incubation with Ag-5@MGO-TA/Fe^{3+} nanocomposite. (b) Statistical data showing the percentage of *E. coli* killed by Ag-5@MGO-TA/Fe^{3+} nanocomposite at various concentrations. The SEM images of *E. coli* (c) untreated (d) treated with Ag-5@MGO-TA/Fe^{3+} nanocomposite.

3.4 Conclusions

In summary, Ag@MGO-TA/Fe^{3+} nanocomposites were successfully fabricated through a facile method by coupling the abundant Ag NPs with MGO-TA/Fe^{3+} nanocomposites by virtue of the strong coordination and reduction ability of TA. The Ag@MGO-TA/Fe^{3+} nanocomposites process an extraordinarily high loading of Ag NPs up to 30 wt. % without any obvious aggregation, which endows the as-prepared nanocomposite with excellent catalytic reduction performance towards a series of organic pollutants and outstanding disinfection control to bacteria. Specifically,

the catalytic rate constant of Ag-5@MGO-TA/Fe^{3+} catalyst towards the reduction of MB was 0.054 s^{-1} with an extremely low applying dosage of 0.05 mg/mL, which are substantially superior to that of NPs-based nano-catalysts reported previously. Such outstanding catalytic performance of the as-prepared Ag-5@MGO-TA/Fe^{3+} catalyst could be attributed to the abundant (~30.7 wt. %) Ag NPs, large surface area (126.37 m^2/g) of Ag-5@MGO-TA/Fe^{3+} catalyst, and the synergistic adsorption effect of the TA film, which enriches MB around the highly dispersed Ag NPs. Furthermore, the magnetic Ag-5@MGO-TA/Fe^{3+} nanocomposite could be facilely separated from the aqueous medium by applying an external magnetic field with the catalytic efficiency remained almost unchanged after five cycles. In addition, 20 μg/mL Ag-5@MGO-TA/Fe^{3+} nanocomposites exhibit disinfection action towards *E. coli* with ~100% killing efficacy. On the basis of its outstanding catalytic and antimicrobial performance as well as long life span of the as-prepared nanomaterial, Ag-5@MGO-TA/Fe^{3+} nanocomposites show great potential for various environmental applications with useful implications for designing advanced nanocomposite catalysts.

Supporting information

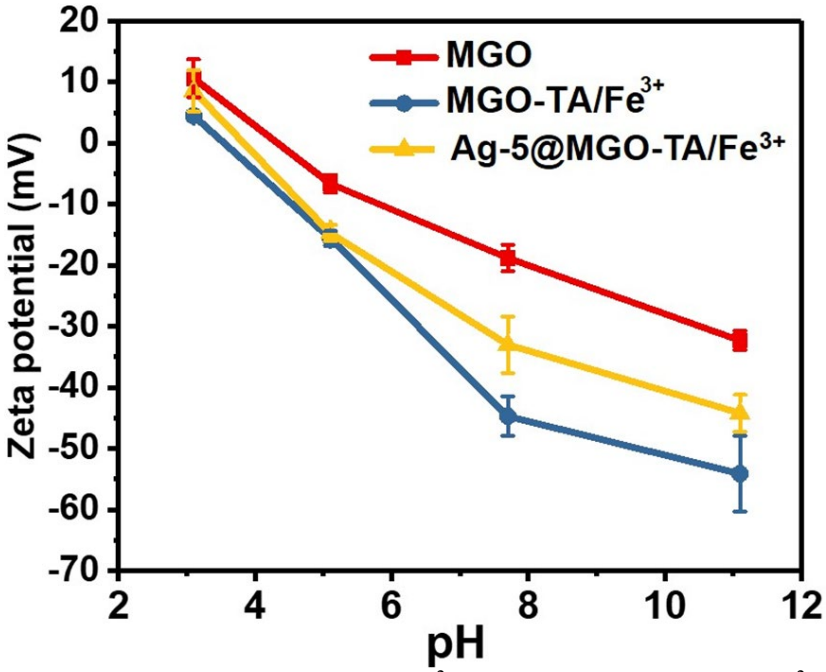

Figure S3.1 Zeta potential of MGO, MGO-TA/Fe^{3+}, and Ag-5@MGO-TA/Fe^{3+} nanocomposites under different pH conditions.

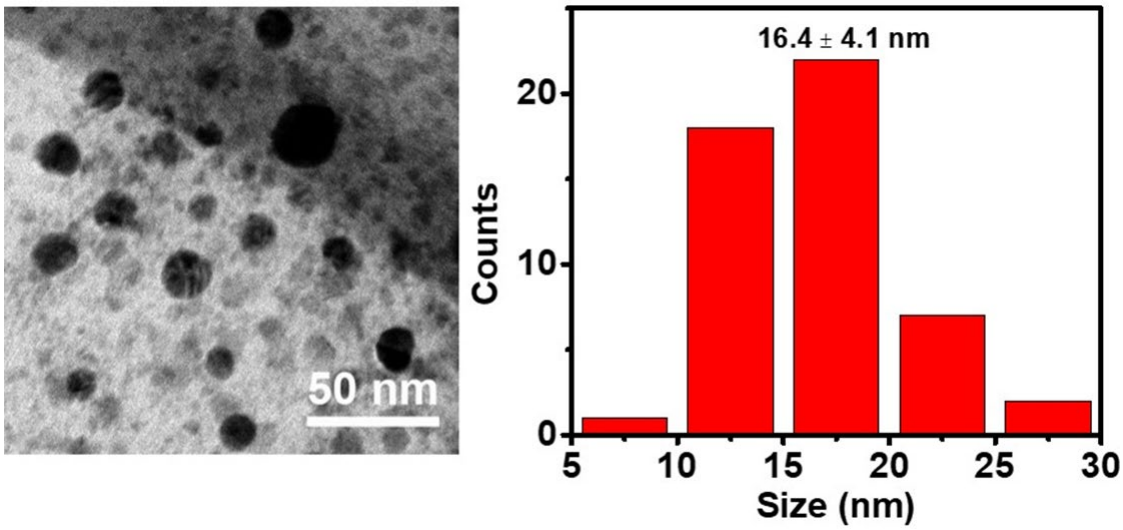

Figure S3.2 Size distribution of Ag NPs on the surface of Ag-5@MGO-TA/Fe^{3+} nanocomposites.

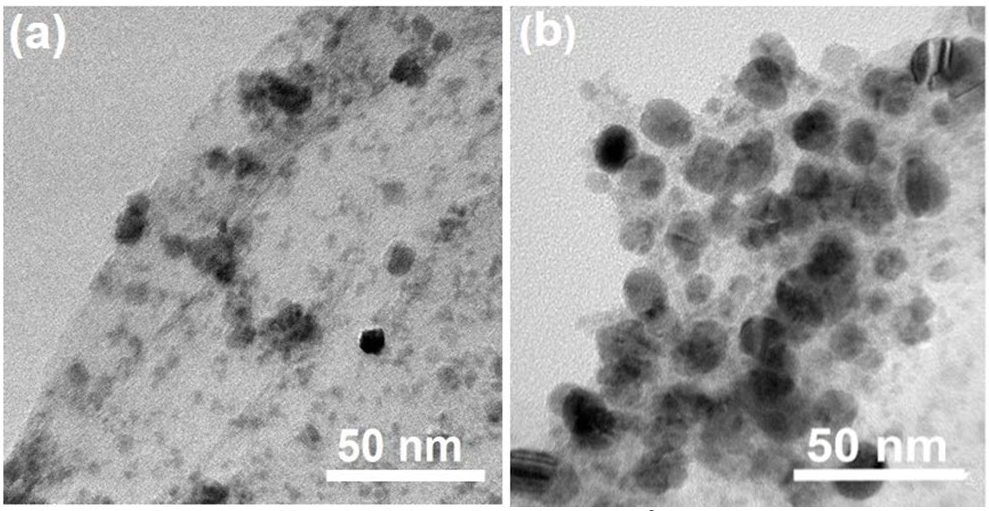

Figure S3.3. TEM images of (a) Ag-1@MGO-TA/Fe^{3+} and (b) Ag-10@MGO-TA/Fe^{3+} nanocomposite with different Ag contents.

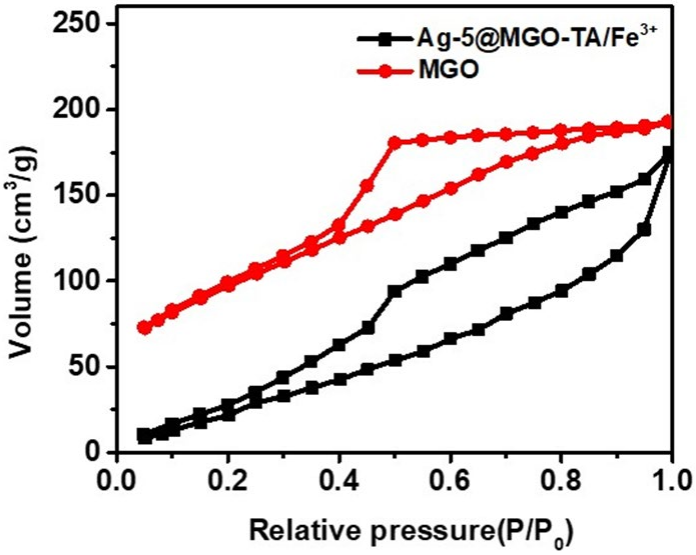

Figure S3.4 The N_2 adsorption/desorption isotherm curves of MGO and Ag-5@MGO-TA/Fe^{3+} nanocomposites.

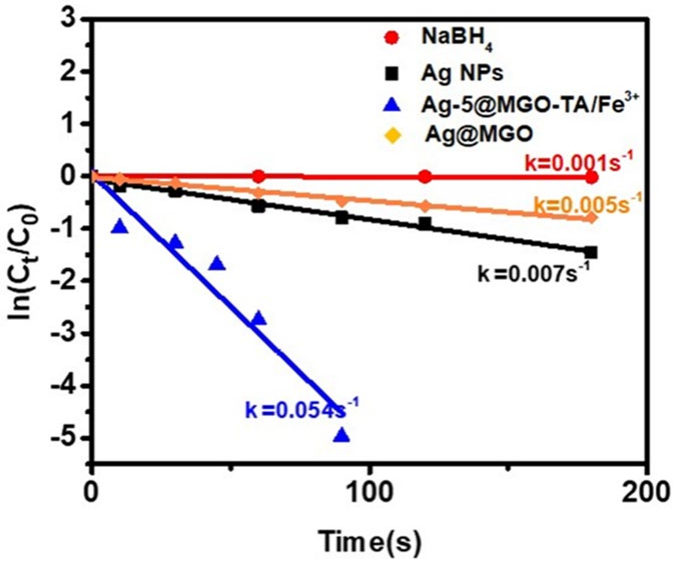

Figure S3.5 First-order kinetics plot of catalytic reduction of MB solution in the presence of (a)$NaBH_4$, (b) Ag NPs, (c)Ag-5@MGO-TA/Fe^{3+}, and (d) Ag@MGO nanocomposites with $NaBH_4$.

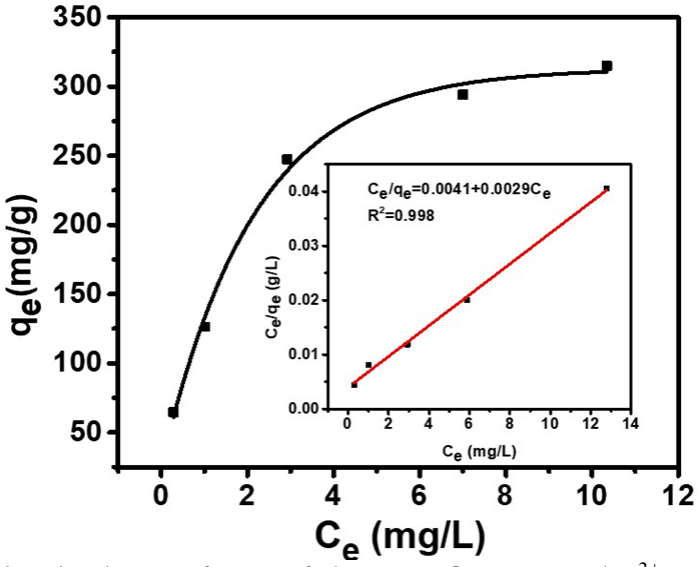

Figure S3.6 Adsorption isotherm of MB of the Ag-5@MGO-TA/Fe^{3+} nanocomposite and the linear regression by fitting the equilibrium adsorption data with Langmuir model (Inset). Adsorption condition: 1.5 mg adsorbent, 10 mL MB solution (10, 20, 40, 50 and 60 mg/L), room temperature, pH=7.4.

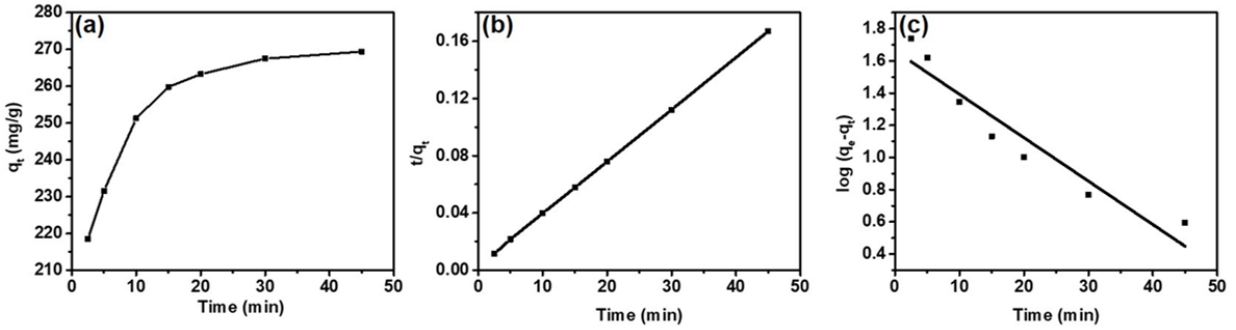

Figure S3.7 (a) Adsorption capacity q_t of MB on Ag-5@MGO-TA/Fe^{3+} nanocomposites as a function of adsorption time t. Fitting of the adsorption kinetics of MB on Ag-5@MGO-TA/Fe^{3+} nanocomposites using (b) the pseudo-second-order kinetic model and (c) pseudo-first-order kinetic model.

Table S3.1 Parameters for the fitting of the adsorption of MB on Ag-5@MGO-TA/Fe^{3+} nanocomposites using the pseudo-first-order and pseudo-second-order kinetic models.

Adsorbent		**Pseudo-first-order kinetics**			**Pseudo-second-order kinetics**		
Ag-5@MGO-TA/Fe^{3+}	**$q_{e,exp}$ (mg/g)**	**K_1 (/min)**	**$q_{e,cal}$ (mg/g)**	**R^2**	**K_2 (g/mg/min)**	**$q_{e,cal}$ (mg/g)**	**R^2**
	273.34	**0.062**	**46.015**	**0.912**	**$4.33x10^{-3}$**	**277.86**	**0.999**

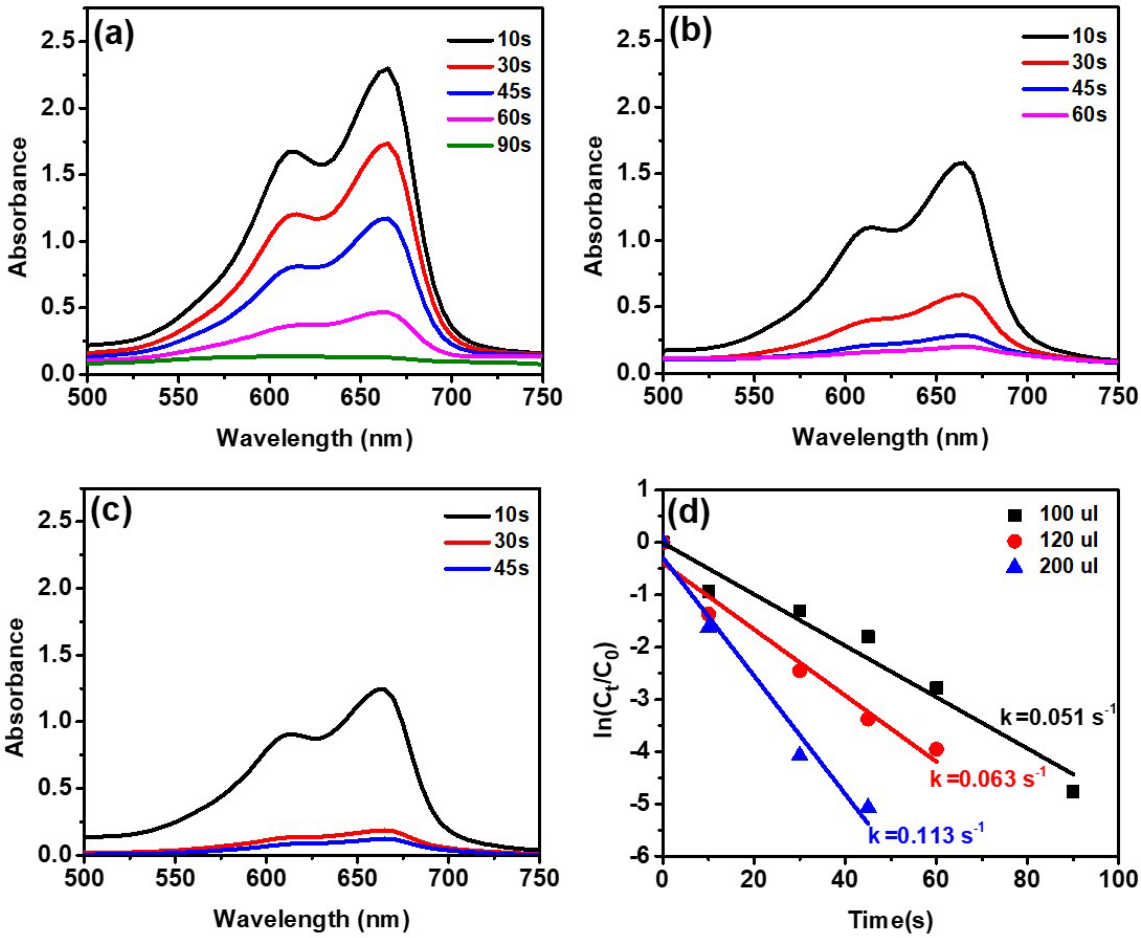

Figure S3.8 Successive UV−vis spectra for catalytic reduction of MB solution (40 ppm, 2mL) by adding (a) 100 μL, (b) 120 μL, and (c) 200 μL Ag-5@MGO-TA/Fe^{3+} catalyst (1 mg/mL) (d) First-order kinetics plot of catalytic reduction of MB solution in the presence of 100 μL, 120 μL, and 200 μL Ag-5@MGO-TA/Fe^{3+} nanocomposite (1 mg/mL).

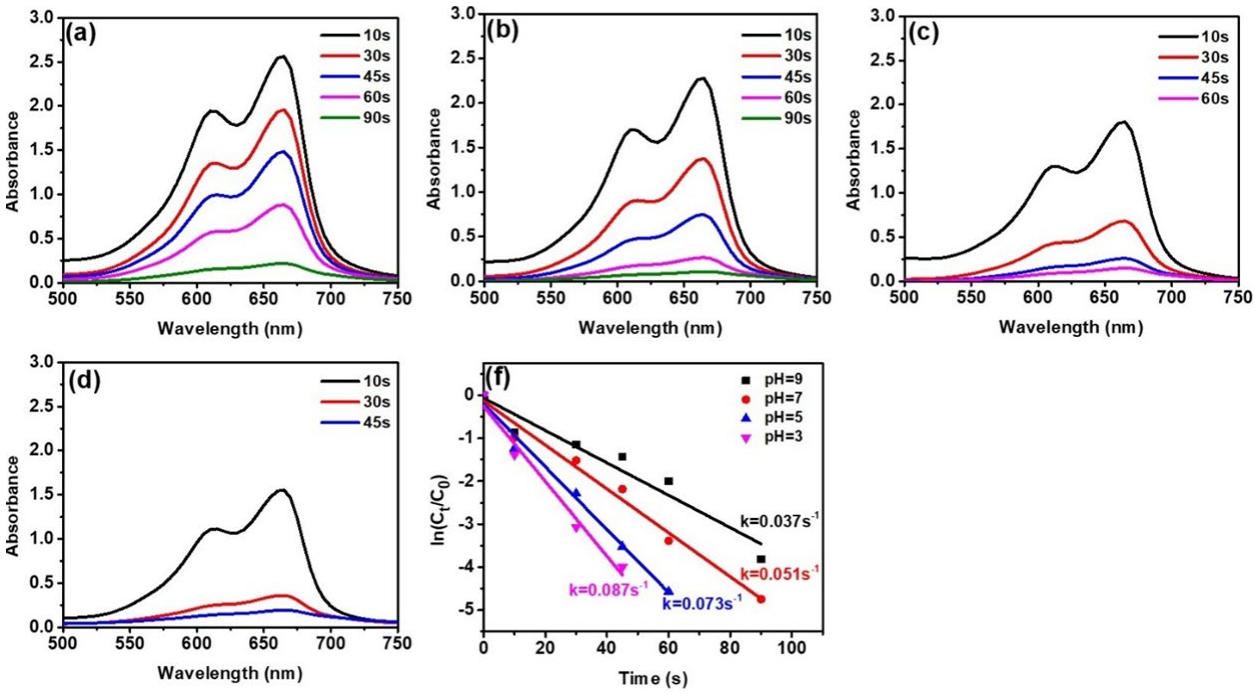

Figure S3.9 Successive UV−vis spectra for catalytic reduction of MB solution with initial pH value at (a) pH=9, (b) pH=7, (c) pH=5, and (d) pH=3 by applying Ag-5@MGO-TA/Fe^{3+} catalyst and (f) First-order kinetics plots of catalytic reduction of MB at different initiate pH conditions in the presence of Ag-5@MGO-TA/Fe^{3+} catalyst.

Table S3.2 Comparison of catalytic performance of NPs-based catalysts towards 4-NP reduction.

Pollutant	Catalysts	Rate constant *k* (/min)	Catalyst used(mg/mL)	*k*' (mL/(mg·min))	Ref
4-nitrophenol (4-NP)	Ag/PAM/PPy/GO	2.02	0.10	20.20	58
	Ag/TiO_2	1.17	0.75	1.56	59
	AgNPs@MWCNTs	0.47	0.33	1.42	60
	Ag@CNF	0.37	0.02	21.76	12
	Fe_3O_4/PDA@Ag	0.60	0.05	12.00	49
	Ag-5@MGO-TA/Fe	3.24	0.07	46.28	This work

Reference

(1) He, K.; Chen, G.; Zeng, G.; Chen, A.; Huang, Z.; Shi, J.; Huang, T.; Peng, M.; Hu, L. Three-dimensional graphene supported catalysts for organic dyes degradation. *Applied Catalysis B: Environmental* **2018**, *228*, 19-28.

(2) Ali, I. New generation adsorbents for water treatment. *Chemical reviews* **2012**, *112* (10), 5073-5091.

(3) Atarod, M.; Nasrollahzadeh, M.; Sajadi, S. M. Green synthesis of Pd/RGO/Fe3O4 nanocomposite using Withania coagulans leaf extract and its application as magnetically separable and reusable catalyst for the reduction of 4-nitrophenol. *Journal of colloid and interface science* **2016**, *465*, 249-258.

(4) Wacławek, S.; Lutze, H. V.; Grübel, K.; Padil, V. V.; Černík, M.; Dionysiou, D. D. Chemistry of persulfates in water and wastewater treatment: a review. *Chemical Engineering Journal* **2017**, *330*, 44-62.

(5) El Nemr, A.; Khaled, A.; Abdelwahab, O.; El-Sikaily, A. Treatment of wastewater containing toxic chromium using new activated carbon developed from date palm seed. *Journal of Hazardous Materials* **2008**, *152* (1), 263-275.

(6) Han, L.; Zhou, Y.; He, T.; Song, G.; Wu, F.; Jiang, F.; Hu, J. One-pot morphology-controlled synthesis of various shaped mesoporous silica nanoparticles. *Journal of materials science* **2013**, *48* (17), 5718-5726.

(7) Samadder, R.; Akter, N.; Roy, A. C.; Uddin, M. M.; Hossen, M. J.; Azam, M. S. Magnetic nanocomposite based on polyacrylic acid and carboxylated cellulose nanocrystal for the removal of cationic dye. *RSC Advances* **2020**, *10* (20), 11945-11956.

(8) Li, Y.; Du, Q.; Liu, T.; Peng, X.; Wang, J.; Sun, J.; Wang, Y.; Wu, S.; Wang, Z.; Xia, Y. Comparative study of methylene blue dye adsorption onto activated carbon, graphene oxide, and carbon nanotubes. *Chemical Engineering Research and Design* **2013**, *91* (2), 361-368.

(9) Zhang, P.; Gong, J.-L.; Zeng, G.-M.; Deng, C.-H.; Yang, H.-C.; Liu, H.-Y.; Huan, S.-Y. Cross-linking to prepare composite graphene oxide-framework membranes with high-flux for dyes and heavy metal ions removal. *Chemical Engineering Journal* **2017**, *322*, 657-666.

(10) Li, C.; Lou, Z.; Yang, Y.; Wang, Y.; Lu, Y.; Ye, Z.; Zhu, L. Hollowsphere nanoheterojunction of g-C3N4@ TiO2 with high visible light photocatalytic property. *Langmuir* **2019**, *35* (3), 779-786.

(11) Lei, J.; Liu, H.; Yin, D.; Zhou, L.; Liu, J. A.; Chen, Q.; Cui, X.; He, R.; Duan, T.; Zhu, W. Boosting the loading of metal single atoms via a bioconcentration strategy. *Small* **2020**, *16* (10), 1905920.

(12) Zhang, P.; Shao, C.; Zhang, Z.; Zhang, M.; Mu, J.; Guo, Z.; Liu, Y. In situ assembly of well-dispersed Ag nanoparticles (AgNPs) on electrospun carbon nanofibers (CNFs) for catalytic reduction of 4-nitrophenol. *Nanoscale* **2011**, *3* (8), 3357-3363.

(13) Xiao, W.; Zhang, Y.; Liu, B. Raspberrylike SiO2@ reduced graphene oxide@ AgNP composite microspheres with high aqueous dispersity and excellent catalytic activity. *ACS applied materials & interfaces* **2015**, *7* (11), 6041-6046.

(14) Wang, N.; Guan, B.; Zhao, Y.; Zou, Y.; Geng, G.; Chen, P.; Wang, F.; Liu, M. Sub‐10 nm Ag Nanoparticles/Graphene Oxide: Controllable Synthesis, Size‐Dependent and Extremely Ultrahigh Catalytic Activity. *Small* **2019**, *15* (23), 1901701.

(15) Jiao, T.; Zhao, H.; Zhou, J.; Zhang, Q.; Luo, X.; Hu, J.; Peng, Q.; Yan, X. Self-assembly reduced graphene oxide nanosheet hydrogel fabrication by anchorage of chitosan/silver and its

potential efficient application toward dye degradation for wastewater treatments. *ACS Sustainable Chemistry & Engineering* **2015**, *3* (12), 3130-3139.

(16) Zhu, X.-Y.; Lv, Z.-S.; Feng, J.-J.; Yuan, P.-X.; Zhang, L.; Chen, J.-R.; Wang, A.-J. Controlled fabrication of well-dispersed AgPd nanoclusters supported on reduced graphene oxide with highly enhanced catalytic properties towards 4-nitrophenol reduction. *Journal of colloid and interface science* **2018**, *516*, 355-363.

(17) Huang, J.; Yan, Y.; Xie, L.; Liu, H.; Huang, C.; Lu, Q.; Qiu, X.; Zeng, H. Probing the Self-Assembly and Nonlinear Friction Behavior of Confined Gold Nano-Particles. *Langmuir* **2019**, *35* (48), 15701-15709.

(18) Jin, L.; Liu, B.; Louis, M. E.; Li, G.; He, J. Highly Crystalline Mesoporous Titania Loaded with Monodispersed Gold Nanoparticles: Controllable Metal–Support Interaction in Porous Materials. *ACS Applied Materials & Interfaces* **2020**, *12* (8), 9617-9627.

(19) Cao, H.-L.; Liu, C.; Cai, F.-Y.; Qiao, X.-X.; Dichiara, A.; Tian, C.; Lü, J. In situ immobilization of ultra-fine Ag NPs onto magnetic Ag@ RF@ Fe3O4 core-satellite nanocomposites for the rapid catalytic reduction of nitrophenols. *Water Research* **2020**, 115882.

(20) Ye, W.; Yu, J.; Zhou, Y.; Gao, D.; Wang, D.; Wang, C.; Xue, D. Green synthesis of Pt–Au dendrimer-like nanoparticles supported on polydopamine-functionalized graphene and their high performance toward 4-nitrophenol reduction. *Applied Catalysis B: Environmental* **2016**, *181*, 371-378.

(21) Zhou, J.; Duan, B.; Fang, Z.; Song, J.; Wang, C.; Messersmith, P. B.; Duan, H. Interfacial assembly of mussel-inspired Au@ Ag@ polydopamine core–shell nanoparticles for recyclable nanocatalysts. *Advanced Materials* **2014**, *26* (5), 701-705.

(22) Yihan, S.; Mingming, L.; Guo, Z. Ag nanoparticles loading of polypyrrole-coated superwetting mesh for on-demand separation of oil-water mixtures and catalytic reduction of aromatic dyes. *Journal of colloid and interface science* **2018**, *527*, 187-194.

(23) Liu, B.; Kuo, C. H.; Chen, J.; Luo, Z.; Thanneeru, S.; Li, W.; Song, W.; Biswas, S.; Suib, S. L.; He, J. Ligand - Assisted Co - Assembly Approach toward Mesoporous Hybrid Catalysts of Transition - Metal Oxides and Noble Metals: Photochemical Water Splitting. *Angewandte Chemie International Edition* **2015**, *54* (31), 9061-9065.

(24) Xu, D.; Lv, H.; Liu, B. Encapsulation of metal nanoparticle catalysts within mesoporous zeolites and their enhanced catalytic performances: a review. *Frontiers in chemistry* **2018**, *6*, 550.

(25) Liao, G.; Fang, J.; Li, Q.; Li, S.; Xu, Z.; Fang, B. Ag-Based nanocomposites: synthesis and applications in catalysis. *Nanoscale* **2019**, *11* (15), 7062-7096.

(26) Song, Y.; Jiang, H.; Wang, B.; Kong, Y.; Chen, J. Silver-incorporated mussel-inspired polydopamine coatings on mesoporous silica as an efficient nanocatalyst and antimicrobial agent. *ACS applied materials & interfaces* **2018**, *10* (2), 1792-1801.

(27) Huang, J.; Huang, G.; An, C.; Xin, X.; Chen, X.; Zhao, Y.; Feng, R.; Xiong, W. Exploring the use of ceramic disk filter coated with Ag/ZnO nanocomposites as an innovative approach for removing Escherichia coli from household drinking water. *Chemosphere* **2020**, *245*, 125545.

(28) Islam, M. S.; Akter, N.; Rahman, M. M.; Shi, C.; Islam, M. T.; Zeng, H.; Azam, M. S. Mussel-inspired immobilization of silver nanoparticles toward antimicrobial cellulose paper. *ACS Sustainable Chemistry & Engineering* **2018**, *6* (7), 9178-9188.

(29) Sharif, H. M. A.; Mahmood, A.; Cheng, H.-Y.; Djellabi, R.; Ali, J.; Jiang, W.-L.; Wang, S.-S.; Haider, M. R.; Mahmood, N.; Wang, A.-J. Fe3O4 Nanoparticles Coated with EDTA and Ag

Nanoparticles for the Catalytic Reduction of Organic Dyes from Wastewater. *ACS Applied Nano Materials* **2019**, *2* (8), 5310-5319.

(30) Zhu, W.; Lei, J.; Li, Y.; Dai, L.; Chen, T.; Bai, X.; Wang, L.; Duan, T. Procedural growth of fungal hyphae/Fe3O4/graphene oxide as ordered-structure composites for water purification. *Chemical Engineering Journal* **2019**, *355*, 777-783.

(31) Tian, Q.; Yu, X.; Zhang, L.; Yu, D. Monodisperse raspberry-like multihollow polymer/Ag nanocomposite microspheres for rapid catalytic degradation of methylene blue. *Journal of colloid and interface science* **2017**, *491*, 294-304.

(32) Zhang, K.; Dwivedi, V.; Chi, C.; Wu, J. Graphene oxide/ferric hydroxide composites for efficient arsenate removal from drinking water. *Journal of hazardous materials* **2010**, *182* (1-3), 162-168.

(33) Li, B.; Cao, H.; Yin, G.; Lu, Y.; Yin, J. Cu 2 O@ reduced graphene oxide composite for removal of contaminants from water and supercapacitors. *Journal of Materials Chemistry* **2011**, *21* (29), 10645-10648.

(34) Bandara, N.; Esparza, Y.; Wu, J. Graphite oxide improves adhesion and water resistance of canola protein–graphite oxide hybrid adhesive. *Scientific reports* **2017**, *7* (1), 1-12.

(35) Ji, Z.; Shen, X.; Yue, X.; Zhou, H.; Yang, J.; Wang, Y.; Ma, L.; Chen, K. Facile synthesis of magnetically separable reduced graphene oxide/magnetite/silver nanocomposites with enhanced catalytic activity. *Journal of colloid and interface science* **2015**, *459*, 79-85.

(36) Cui, L.; Wang, Y.; Gao, L.; Hu, L.; Yan, L.; Wei, Q.; Du, B. EDTA functionalized magnetic graphene oxide for removal of Pb (II), Hg (II) and Cu (II) in water treatment: Adsorption mechanism and separation property. *Chemical engineering journal* **2015**, *281*, 1-10.

(37) Chi, Y.; Yuan, Q.; Li, Y.; Tu, J.; Zhao, L.; Li, N.; Li, X. Synthesis of Fe3O4@ SiO2–Ag magnetic nanocomposite based on small-sized and highly dispersed silver nanoparticles for catalytic reduction of 4-nitrophenol. *Journal of colloid and interface science* **2012**, *383* (1), 96-102.

(38) Das, R.; Sypu, V. S.; Paumo, H. K.; Bhaumik, M.; Maharaj, V.; Maity, A. Silver decorated magnetic nanocomposite (Fe3O4@ PPy-MAA/Ag) as highly active catalyst towards reduction of 4-nitrophenol and toxic organic dyes. *Applied Catalysis B: Environmental* **2019**, *244*, 546-558.

(39) Jeon, E. K.; Seo, E.; Lee, E.; Lee, W.; Um, M.-K.; Kim, B.-S. Mussel-inspired green synthesis of silver nanoparticles on graphene oxide nanosheets for enhanced catalytic applications. *Chemical Communications* **2013**, *49* (33), 3392-3394.

(40) Zhang, J.; Azam, M. S.; Shi, C.; Huang, J.; Yan, B.; Liu, Q.; Zeng, H. Poly (acrylic acid) functionalized magnetic graphene oxide nanocomposite for removal of methylene blue. *RSC Advances* **2015**, *5* (41), 32272-32282.

(41) Ejima, H.; Richardson, J. J.; Liang, K.; Best, J. P.; van Koeverden, M. P.; Such, G. K.; Cui, J.; Caruso, F. One-step assembly of coordination complexes for versatile film and particle engineering. *Science* **2013**, *341* (6142), 154-157.

(42) Xu, Z.; Wang, X.; Liu, X.; Cui, Z.; Yang, X.; Yeung, K. W. K.; Chung, J. C.; Chu, P. K.; Wu, S. Tannic acid/Fe3+/Ag nanofilm exhibiting superior photodynamic and physical antibacterial activity. *ACS applied materials & interfaces* **2017**, *9* (45), 39657-39671.

(43) Chen, J.; Yao, B.; Li, C.; Shi, G. An improved Hummers method for eco-friendly synthesis of graphene oxide. *Carbon* **2013**, *64*, 225-229.

(44) Lei, J.; Guo, Q.; Yin, D.; Cui, X.; He, R.; Duan, T.; Zhu, W. Bioconcentration and bioassembly of N/S co-doped carbon with excellent stability for supercapacitors. *Applied Surface Science* **2019**, *488*, 316-325.

(45) Yu, K.; Shao, P.; Meng, P.; Chen, T.; Lei, J.; Yu, X.; He, R.; Yang, F.; Zhu, W.; Duan, T. Superhydrophilic and highly elastic monolithic sponge for efficient solar-driven radioactive wastewater treatment under one sun. *Journal of Hazardous Materials* **2020**, *392*, 122350.

(46) Peng, G.; Zhang, M.; Deng, S.; Shan, D.; He, Q.; Yu, G. Adsorption and catalytic oxidation of pharmaceuticals by nitrogen-doped reduced graphene oxide/Fe3O4 nanocomposite. *Chemical Engineering Journal* **2018**, *341*, 361-370.

(47) Shen, H.; Duan, C.; Guo, J.; Zhao, N.; Xu, J. Facile in situ synthesis of silver nanoparticles on boron nitride nanosheets with enhanced catalytic performance. *Journal of Materials Chemistry A* **2015**, *3* (32), 16663-16669.

(48) Cui, K.; Yan, B.; Xie, Y.; Qian, H.; Wang, X.; Huang, Q.; He, Y.; Jin, S.; Zeng, H. Regenerable urchin-like Fe3O4@ PDA-Ag hollow microspheres as catalyst and adsorbent for enhanced removal of organic dyes. *Journal of hazardous materials* **2018**, *350*, 66-75.

(49) Mao, B.; An, Q.; Zhai, B.; Xiao, Z.; Zhai, S. Multifunctional hollow polydopamine-based composites (Fe 3 O 4/PDA@ Ag) for efficient degradation of organic dyes. *RSC Advances* **2016**, *6* (53), 47761-47770.

(50) Xiao, F.; Ren, H.; Zhou, H.; Wang, H.; Wang, N.; Pan, D. Porous Montmorillonite@ Graphene Oxide@ Au Nanoparticle Composite Microspheres for Organic Dye Degradation. *ACS Applied Nano Materials* **2019**, *2* (9), 5420-5429.

(51) Xie, Y.; Yan, B.; Xu, H.; Chen, J.; Liu, Q.; Deng, Y.; Zeng, H. Highly regenerable mussel-inspired Fe3O4@ polydopamine-Ag core–shell microspheres as catalyst and adsorbent for methylene blue removal. *ACS applied materials & interfaces* **2014**, *6* (11), 8845-8852.

(52) Ma, A.; Xie, Y.; Xu, J.; Zeng, H.; Xu, H. The significant impact of polydopamine on the catalytic performance of the carried Au nanoparticles. *Chemical Communications* **2015**, *51* (8), 1469-1471.

(53) Luo, J.; Lai, J.; Zhang, N.; Liu, Y.; Liu, R.; Liu, X. Tannic acid induced self-assembly of three-dimensional graphene with good adsorption and antibacterial properties. *ACS Sustainable Chemistry & Engineering* **2016**, *4* (3), 1404-1413.

(54) Zhu, M.; Wang, C.; Meng, D.; Diao, G. In situ synthesis of silver nanostructures on magnetic Fe 3 O 4@ C core–shell nanocomposites and their application in catalytic reduction reactions. *Journal of Materials Chemistry A* **2013**, *1* (6), 2118-2125.

(55) Li, H.; Jiang, D.; Huang, Z.; He, K.; Zeng, G.; Chen, A.; Yuan, L.; Peng, M.; Huang, T.; Chen, G. Preparation of silver-nanoparticle-loaded magnetic biochar/poly (dopamine) composite as catalyst for reduction of organic dyes. *Journal of colloid and interface science* **2019**, *555*, 460-469.

(56) Schlesinger, H.; Brown, H. C.; Finholt, A.; Gilbreath, J. R.; Hoekstra, H. R.; Hyde, E. K. Sodium borohydride, its hydrolysis and its use as a reducing agent and in the generation of hydrogen1. *Journal of the American Chemical Society* **1953**, *75* (1), 215-219.

(57) Zhu, M.; Diao, G. Magnetically recyclable Pd nanoparticles immobilized on magnetic Fe3O4@ C nanocomposites: preparation, characterization, and their catalytic activity toward Suzuki and Heck coupling reactions. *The Journal of Physical Chemistry C* **2011**, *115* (50), 24743-24749.

(58) Mao, H.; Ji, C.; Liu, M.; Cao, Z.; Sun, D.; Xing, Z.; Chen, X.; Zhang, Y.; Song, X.-M. Enhanced catalytic activity of Ag nanoparticles supported on polyacrylamide/polypyrrole/graphene oxide nanosheets for the reduction of 4-nitrophenol. *Applied Surface Science* **2018**, *434*, 522-533.

(59) Deshmukh, S.; Dhokale, R.; Yadav, H.; Achary, S.; Delekar, S. Titania–supported silver nanoparticles: An efficient and reusable catalyst for reduction of 4-nitrophenol. *Applied surface science* **2013**, *273*, 676-683.

(60) Alshehri, S. M.; Almuqati, T.; Almuqati, N.; Al-Farraj, E.; Alhokbany, N.; Ahamad, T. Chitosan based polymer matrix with silver nanoparticles decorated multiwalled carbon nanotubes for catalytic reduction of 4-nitrophenol. *Carbohydrate polymers* **2016**, *151*, 135-143.

Chapter 4. A Universal Strategy for Constructing Robust and Antifouling Cellulose Nanocrystal Coating for Oil-Water Separation

4.1 Introduction

Surface fouling caused by the undesired settlement of the foulants in wastewater like oil droplets, proteins, or microorganisms leads to serious problems in many industrial applications,[1, 2] especially in the application of membrane-based technologies.[3-8] The foulants accumulated on the membrane surface can severely deteriorate the membrane permeability, thus greatly decreasing the membrane effectiveness.[9-11] To solve this challenge, recently, inspired by the antifouling property of marine bio-system,[12] many innovative antifouling surfaces have been developed by incorporating hydrophilic materials such as polymers,[13-15] inorganic particles,[16-19] zwitterionic polyelectrolytes,[20] and metal oxides [21, 22] to trap water molecules in their micro-/nano-structures, serving as a physical barrier to inhibit oil adhesion,[23] protein adsorption,[20] or cell attachment[24] in their practical applications. However, most reported hydrophilic surfaces still lack a stable, adequate, and compact hydration layer, in particular for hydrophilic surfaces composed of soft and flexible polymer chains.[25-27] The water initially trapped in a soft structure can be easily excluded under abrasion or external pressure.[28] Therefore, nonflexible hydrophilic moieties with rigid structures have received much attention in constructing a robust and stable antifouling surface.

Cellulose nanocrystals (CNCs), a rigid nanomaterial (with Young's modulus in the range of 20~50 GPa) with abundant hydrophilic moieties on their surfaces, have been considered as a promising candidate for constructing robust and stable antifouling surfaces.[29-32] The superior hydrophilicity of CNCs can be well correlated with their molecular structure, in which hydroxyl and carboxyl groups are closely and densely, located on the surface of CNCs.[33, 34] These

hydrophilic groups on CNCs are orientationally confined, which will not be able to reorient when exposed to the air or even oil.[35] Taking the advantage of superior hydrophilicity and rigid structure of CNCs, a series of CNCs coatings have been developed. For instance, *Wu et al.* fabricated CNCs nano-paper and CNCs coated-mesh by vacuum filtration method, which showed outstanding antifouling performance in the oil/water separation process.[36] However, most reported CNCs-based coatings have weak adhesion ability to substrate surfaces, even small external environmental changes (e.g., abrasion, presence of acid/alkaline solution) can inevitably cause CNCs to fall off from the surfaces. The resulting fragile and sparse coating would inevitably be penetrated and contaminated by pollutants.[37-39] Thus, a universal coating method is needed to engineer robust and dense CNCs coating on diverse substrate surfaces, which still remains a challenge.

Many marine bio-systems, such as mussel or barnacle, show intriguing wet adhesion capability.[40-44] For example, the robust and durable mussel adhesion in complex seawater is attributed to the formation of byssal thread and interfacial bio-glue layer with substrates using the so-called mussel foot proteins (Mfps).[13, 45-47] The formed bio-glue layer shows high affinity to the substrates via multiple intermolecular interactions and serves as a highly adaptive intermediate adhesive layer for tightly linking the byssal threads to substrates via both covalent or non-covalent interactions.[1, 48-51] Inspired by this bio-glue effect in mussel adhesion, a phenol/amine coating with abundant catechol and amine groups, that can be deposited by mimicking the solidification process of Mfps, may be able to serve as a universal intermediate adhesive layer for tightly bonding dispersed CNCs as CNCs coating on various substrates.[47, 52-54] However, the challenge still remains, as most phenol/amine intermediate adhesive layers suffer from severe stability issues and may also result in large aggregates due to the rapid and uncontrolled Schiff-base/Michael addition reaction during deposition,[53, 55] which is undesired for serving as a platform for anchoring CNCs. To

address this challenge, recently, vanadium (V), a specie accumulated in mussels byssal threads, was proven capable to modulate the Mfps solidification process by forming complexes with catechol groups.[56, 57] It is proposed in this work that introducing V^{3+} ions in phenol/amine self-assembly may control the Schiff-base/Michael addition reaction by competing with the amine groups to interact with the catechol groups through coordination bonds, thus modulating the structure of formed phenol/amine coating. Such a modified phenol/amine coating has the potential to act as a promising intermediate adhesive layer for tightly anchoring CNCs as CNCs coating on the substrate.

Herein, we reported a universal and simple strategy to construct robust CNCs coating which includes an intermediate adhesive layer compositing of tannic acid (TA)/polyethylenimine (PEI)/V^{3+} ions and a self-assembled CNCs layer. The interaction forces involved in the self-assembly process were directly quantified by using the atomic force microscope (AFM) colloidal probe technique. The obtained CNCs coating featured a densely packed structure with outstandingly low root-mean-square (RMS) roughness of ~2 nm, exhibiting excellent antifouling properties to inhibit oil adhesion, protein (e.g., bovine serum albumin (BSA)) adsorption and cell (e.g., Chinese hamster ovary (CHO) cell) attachment onto surface, and maintaining its structural integrity and wettability after cyclic friction tests. More importantly, the developed CNCs coating strategy has been further applied in membrane modification for O/W emulsion treatment. The CNCs coated-PVDF membrane shows ultra-high water flux (6200 L m^{-2} h^{-1} bar^{-1}) in the separation of toluene-in-water emulsion, outstanding durability under harsh environment, and achieves nearly 100% permeating flux recovery ratio in separation of toluene-in-water emulsion containing various foulants.

4.2 Experimental methods

4.2.1 Materials

Cellulose nanocrystal solution (6 wt.% solution in water) was purchased from Cellulose lab, Canada. Tris(hydroxymethyl)aminomethane, tannic acid (TA), polyethylenimine (PEI) (Mn~800 Da), vanadium (III) chloride (VCl_3), iron chloride hexahydrate ($FeCl_3 \cdot 6H_2O$), and cobalt chloride ($CoCl_2$) were purchased from Sigma-Aldrich and used as received. The solvents including toluene, chloroform, hexane, and soybean oil were purchased from Sigma-Aldrich without purification. Bovine serum albumin (BSA), fluorescein-conjugated bovine serum albumin (FITC-BSA), 4′6-Diamidine-2′-phenylindole (DAPI), and sodium dodecyl sulfate (SDS) were purchased from Alfa Aesar. Durapore® PVDF membranes (diameter ~ 47mm, pore seize ~ 0.22 um) were purchased from Millipore Co. Ltd.

4.2.2 Preparation of TA/PEI/V and CNCs coatings

The TA/PEI/V and CNCs coating were deposited on various substrates (such as silicon wafer, gold, mica, glass, and PVDF membrane) via a self-assembly method. Specifically, the substrates were thoroughly washed with water/ethanol mixture and then placed in an ultraviolet (UV)/Ozone cleaner for 15 min. Then VCl_3 (2, 5, 10 mg mL^{-1}), PEI (1 mg mL^{-1}), and TA (2 mg mL^{-1}) were all dissolved in Tris buffer (10 mmol, pH=8) solution to prepare the casting solution. The substrates were immersed in the casting solution for 8 h to complete the co-deposition process and denoted as TA/PEI/V-coated substrates. For the comparison, the same procedure was also applied to prepared TA/PEI/Fe and TA/PEI/Co coated-substrates by using $FeCl_3$ and $CoCl_2$ solutions instead of VCl_3 solution. For the following CNCs coating process, the CNC casting solution (0.05 mg mL^{-1}) was first sonicated for 30 minutes to form a homogenous solution. The TA/PEI/V coated-substrates were then immersed into the CNCs solution on the shaker for 4, 6,

and 10 h, respectively, and denoted as CNCs-coated substrates. Finally, the as-prepared CNCs-coated substrates were thoroughly washed with ethanol/water and dried with nitrogen.

4.2.3 Surface Characterization

The chemical structures of as-prepared coatings were analyzed by X-ray photoelectron spectroscopy (XPS) Kratos Axis spectrometer using Al Kα radiation, Fourier transforms infrared spectroscopy (FTIR) (Thermo Scientific Nicolet, iS50 FT-IR), and UV-Vis spectroscopy (Thermo Scientific Evolution 300). The morphologies of the fabricated coatings were characterized by AFM imaging (Bruker ICON AFM, Santa Barbara, CA) operated in a tapping mode under ambient conditions in air. A contact angle goniometer (Ramé-Hart instrument, NJ) was applied to evaluate the water contact angle of as-prepared coatings. The surface charge property of the coating materials was characterized using an Electrokinetic Analyzer (Anton Paar Surpass). The surface morphology and elements distribution of TA/PEI/V and CNCs-coated membranes were characterized by a field-emission scanning electron microscope (FESEM) (Zeiss Sigma 300 VP-FESEM, Germany) with energy-dispersive X-ray spectroscopy (EDX).

4.2.4 Force measurements using AFM colloidal probe technique

The AFM force measurements were conducted by using an MFP-3D AFM instrument (Asylum Research, Santa Barbara, USA). The silica probe was prepared by attaching a silica microsphere (diameter ~5 μm) onto a tipless AFM cantilever (Bruker, Santa Barbara, USA) using two-component epoxy glue. The as-prepared AFM silica probe and silicon wafer were treated using a UV Ozone cleaner, followed by immersion in PEI solutions (1 mg mL^{-1}), rinsing with DI water, and drying with pure nitrogen. In the force measurement experiments, both the PEI-coated silica probe and PEI-coated silicon wafer were placed in a fluid cell containing TA (10 mmol) or TA/V^{3+} ions (10 mmol/10 mmol) solutions. The spring constant of the AFM colloidal probe was

calibrated using the Hutter and Bechhoefer method.[58] For each force measurement, the PEI-coated silica probe was driven to approach and retract from the opposing substrate at a fixed velocity of 1 μm/s. The interaction forces were determined using Hooke's law by monitoring the cantilever deflection.[59]

4.2.5 Evaluation of the Antifouling Properties of CNCs coating

Laser scan confocal microscopy (Zeiss LSM 710) was applied to qualitatively determine the adsorption behaviors of fluorescein-conjugated bovine serum albumin (FITC−BSA) on the bare and CNCs-coated substrate. Specifically, the bare and CNCs-coated substrates were immersed into the FITC-BSA (0.1 mg mL^{-1}) in PBS solution (0.13 M, pH=7.4) for 2 h, followed by rinsing with PBS buffer to remove the loosely bound proteins before conducting the confocal fluorescence microscopy imaging.

The quartz crystal microbalance (QCM) (Q-Sense, Sweden) was then employed to quantify the adsorption amount of a model protein (BSA) on the bare or CNCs-coated silica sensors (QSX-303, Biolin Scientific, Gothenburg, Sweden). The BSA adsorbed on a sensor surface will lead to the change of the sensor's resonance frequency (Δf), which can be related to the adsorbed mass of BSA (Δm) on the silica sensor by the Sauerbrey equation:[60]

$$\Delta m = \frac{C\Delta f}{n} \tag{4.1}$$

Where the Δf is the change of frequency in Hz, C is a constant as 17.7 ng $Hz^{-1}cm^{-2}$, and n is the overtone number.

4.2.6 Cell attachment test

The Chinese hamster ovary (CHO) cells were used as the model cells to evaluate the anti-cell attachment property of as-prepared CNCs coating. The CHO cells were firstly cultured in Dulbecco's Modified Eagle Medium/Nutrient Mixture F-12 (DMEM/F-12) supplemented with L-glutamine, 10% fetal bovine serum (FBS), and penicillin-streptomycin. The bare and CNCs-coated silicon wafers were placed in a 24-well cell culture plate and sterilized by exposure to the UV lights for 1 h. Then the CHO cells were seeded on the surface of bare and CNCs-coated substrates at the density of 1×10^5 cells and incubated for 24 h at 37 ℃. After incubation, the bare and CNCs-coated substrates were washed with PBS buffer to remove nonadherent cells, and stained by DAPI before conducting a laser scanning confocal fluorescent microscope imaging. The CHO cell coverage ratios on the substrates were quantified by Image J software.

4.2.7 Friction test

The stability and durability of the as-prepared CNCs coating were investigated using an Anton Paar Nano Tribometer (NTR^3) with the ball-on-disk configuration under reciprocating motions.[61-63] In a typical friction test, A bearing titanium ball with a diameter of 2 mm was used as the counter-facing ball. The frequency and the sliding amplitude were set at 0.1 Hz and 2 mm, respectively, with applied normal load ranging from 1 mN to 35 mN.

4.2.8 Membrane separation experiment

The separation performance of CNCs-coated PVDF membrane was evaluated by using surfactant-stabilized 1 wt.% toluene, hexane, chloroform, or soybean oil-in-water emulsion and 20 ppm SDS surfactant were obtained by applying homogenizer (IKA T-18 Ultra Turrax, Germany) at 12,000 rpm for 15 min as the model emulsion solutions for oil/water separation experiment. The size distribution of prepared emulsion was characterized by dynamic laser scattering measurement

using a Zetasizer Nano ZSP system (Malvern Panalytical, United Kingdom). For a typical test, the membrane was placed in a dead-end filtration setup and pre-wetted by DI water. The separation test was initiated by flowing the emulsions through the membrane. The permeating flux of membranes could be calculated by using the following equation:

$$J = \frac{\Delta V}{S \cdot \Delta t \cdot \Delta P} \tag{4.2}$$

Where ΔV is the volume of filtrate permeated through the membrane in a certain period Δt during the test, S is the effective membrane surface area, and ΔP is the pressure difference between ambient and evacuation pressure.

The filtrate was collected and total organic carbon (TOC) analysis was then conducted to calculate the oil separation efficiency (η) based on the initial (C_i) and final (C_f) oil content according to the following equation:

$$\eta(\%) = \left(1 - \frac{C_f}{C_i}\right) \times 100\% \tag{4.3}$$

To evaluate the antifouling property of the membranes, the variation of water flux of the membranes with the filtration time was monitored during each toluene-in-water emulsion separation cycle. After each filtration cycle, the membrane was thoroughly washed by DI water before the next cycle.

4.3 Results and discussion

4.3.1 TA/PEI/V coating and CNCs coating fabrication and characterization

The CNCs coating was fabricated by a facile self-assembly method as schematically shown in Figure 4.1(a)~(c). The TA/PEI/V intermediate adhesive layer was firstly deposited on substrate through Schiff-base/Michael addition reaction between TA/PEI [64] and coordination reaction

between TA/V^{3+} ions [65] under mild alkaline conditions (pH ~ 8). The formed TA/PEI/V intermediate adhesive layer introduced abundant functional groups including amino groups and catechol groups on substrate as anchoring points for CNCs. By immersing the as-prepared TA/PEI/V-coated substrate in the CNC solution, the highly dispersed CNCs were employed as building units and assembled as CNCs coating on the formed TA/PEI/V intermediate adhesive layer. The morphologies of as-prepared TA/PEI/V and CNCs coatings were characterized by AFM topographic imaging: As shown in Figure 4.1(d), the formed TA/PEI/V coating showed a root-mean-square (RMS) roughness of ~2.0 nm with closely packed TA/PEI/V aggregates on the surface. After the CNCs assembly, as shown in Figure 4.1(e), the rod-like CNCs were densely packed on the TA/PEI/V intermediate adhesive layer with the RMS roughness of ~2.1 nm, indicating the CNCs layer was successfully deposited on the substrate.

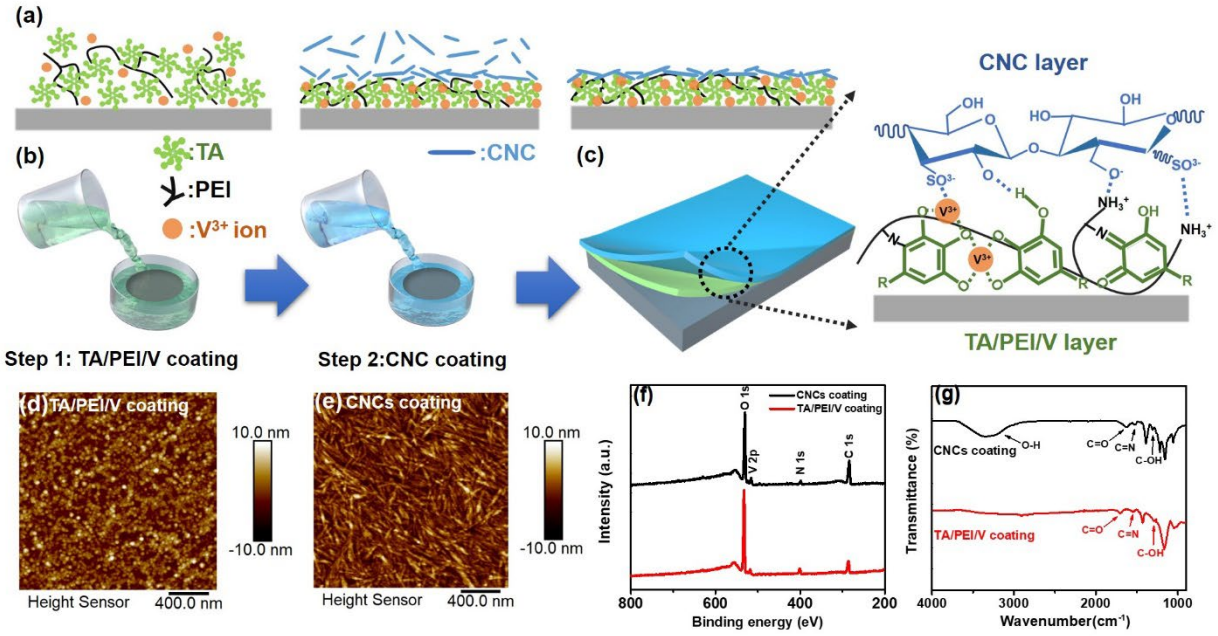

Figure 4.1 (a), (b) Schematic diagram of the assembly process for preparing the TA/PEI/V and CNCs coatings; (c) Structure of the CNCs coating; AFM images of as-prepared (d) TA/PEI/V and (e) CNCs coatings; (f) XPS survey scan and (g) FT-IR results of TA/PEI/V and CNCs coating.

The chemical components of as-prepared TA/PEI/V and CNCs coatings were characterized by X-ray photoelectron spectroscopy (XPS). As shown in Figure 4.1(f), the peaks of N 1s, V 2p, O 1s, and C 1s were found in both XPS spectra of TA/PEI/V and CNCs coatings, which were in agreement with the coating compositions as designed. The high-resolution spectra of N 1s of TA/PEI/V coating shown in Figure S4.1 also indicated the formation of C−N and C=N bonds between TA and PEI.[47] Moreover, the C/O ratio increased from 0.62 for TA/PEI/V coating to 0.87 for the CNCs coating, which was attributed to the incorporation of the carbon-rich CNCs layer. The Fourier transform infrared (FT-IR) spectra of TA/PEI/V and CNCs coatings were shown in Figure 4.1(g), the vibration peak at 1625 cm^{-1} in both spectra of TA/PEI/V and CNCs coatings were attributed to the C=N bond stretching.[66] Moreover, compared with the FT-IR spectra of TA/PEI/V coating, the new wide peak at 3340 cm^{-1} in the FT-IR spectra of CNCs coating was corresponding to the O-H vibration, which can be attributed to the existence of hydroxyl groups of CNCs. Additionally, this CNCs coating strategy can be further applied to modify different types of substrates, including silicon wafer, mica, glass, and gold surfaces (Figure S4.2), demonstrating the excellent universality of the CNCs coating strategy. Moreover, the morphologies of TA/PEI/V intermediate adhesive layers and the corresponding CNCs coatings can be modulated by changing the V^{3+} concentration from 2 mg mL^{-1} to 10 mg mL^{-1}: As shown in Figure 4.2(a), the low V^{3+} ions content (2 mg mL^{-1}) caused the aggregated TA/PEI/V coating with the RMS roughness of ~2.3 nm, thus leading to the formation of rough CNCs coating with low CNCs number density on the substrate; By increasing the V^{3+} ions content to 5 mg mL^{-1}, the smooth TA/PEI/V coating was obtained with the RMS roughness decreasing from ~2.3 nm to ~2.0 nm (Figure 4.2(b)), resulting in the formation of densely packed CNCs coating on the substrate; However, as shown in Figure 4.2(c), continuously increasing V^{3+} ions content to 10 mg mL^{-1} would lead to sparse TA/PEI/V

coating with the RMS roughness further decreasing to ~1.8 nm, and the resulting CNCs coating showed a less compact structure due to the limited anchoring sites on the substrate.

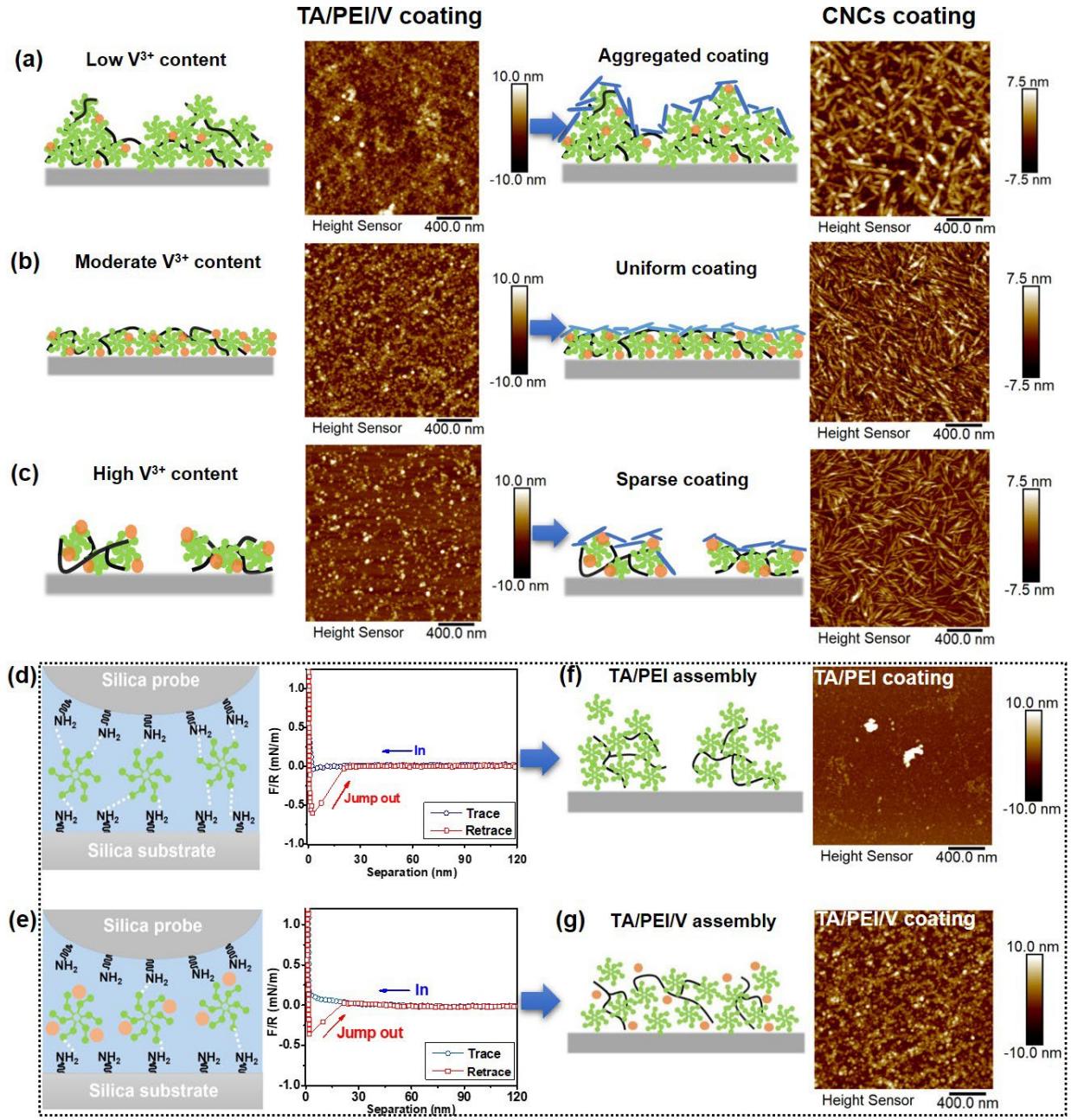

Figure 4.2 Illustrations and topographic AFM images of TA/PEI/V intermediate adhesive layer and corresponding CNCs coatings prepared with (a) 2 mg mL^{-1}, (b) 5 mg mL^{-1}, and (c) 10 mg mL^{-1} V^{3+} ions; Force–distance profiles relative to the interaction between PEI-coated silica probe and

PEI-coated silica substrate in the presence of (d) 10 mmol TA; (e) 10 mmol TA and 10 mmol V^{3+} ions; The AFM images of (f) TA/PEI coating and (g) TA/PEI/V coating.

To elucidate the effect of V^{3+} ions on the TA/PEI/V self-assembly process, the atomic force microscope (AFM) colloid probe technique was employed to directly measure the correlated surface interactions in the TA/PEI/V self-assembly process. The method for preparation of the silica probe in AFM force measurement was reported previously,[67] and the schematics of AFM colloidal probe force measurement setup and the SEM image of a typical silica probe were shown in Figure S4.3. Figure 4.2(d)~(e) showed the measured force profiles between the PEI-coated silica probe and PEI supported on a silica substrate in the 10 mmol TA and 10 mmol/10mmol TA/V^{3+} ions solutions at pH 6.4, respectively. As shown in Figure 4.2(d), in the presence of 10 mmol TA, a significant adhesion (F/R~0.65 mN m^{-1}) was measured between two PEI-coated surfaces during the retraction process, which was possibly originated from the Schiff-base/Michael addition reaction between TA and PEI.[47] Notably, as shown in Figure 4.2(e), in the presence of 10 mmol/10mmol TA/V^{3+} ions solution, the measured adhesion during the retraction process decreased from ~0.65 mN m^{-1} to ~0.35 mN m^{-1}, which was probably attributed to the V^{3+} ions occupying the catechol groups of TA via coordination reaction, thus suppressing the Schiff-base/Michael addition reaction between the TA and PEI. To further illustrate this V^{3+} ions modulated TA/PEI assembly process, the morphologies of TA/PEI and TA/PEI/V coatings were characterized by AFM topographic imaging. As shown in Figure 4.2(f), without V^{3+} ions, only a few large aggregates were formed via Schiff-base/Michael addition between TA/PEI, which was confirmed by the appearance of the peak at ~325 nm in the UV-vis spectra (Figure S4.4);[68] However, in the presence of V^{3+} ions, small TA/PEI/V aggregates were formed and closely packed on the substrate (Figure 4.2(g)). Moreover, in the TA/PEI/V assembly process, the new peaks at

~475 nm corresponding to the TA/V^{3+} coordination also appeared in the UV-vis spectrum (Figure S4.4),[56, 69] demonstrating the V^{3+} ions controlled the TA/PEI assembly process through forming TA/V^{3+} complex, thereby modulating the structure of the TA/PEI/V coating. To extend this TA/PEI/V coating strategy, different transition metal ions (Fe^{3+} and Co^{2+} ions) were used to replace V^{3+} ions in the self-assembly process. As shown in Figure S4.5, compared to the TA/PEI/V coating, both TA/PEI/Fe and TA/PEI/Co coatings showed a aggregated structure, which can be attributed to the relatively weak coordination capacity of Fe^{3+} and Co^{2+} compared to V^{3+} ions (with coordination capacity order of $V^{3+} > Fe^{3+} > Co^{2+}$).[70-72]

To investigate the effect of TA/PEI/V intermediate adhesive layer on the following CNCs assembly process, the morphologies of CNCs coatings with/without TA/PEI/V intermediate adhesive layer were further characterized by the AFM topographic imaging and shown in Figure S4.6. Without the TA/PEI/V intermediate adhesive layer, a severely aggregated CNCs coating with the RMS roughness of ~3.3 nm was formed, which was attributed to the inhomogeneous stacking of CNCs on the surface; In contrast, in the presence of TA/PEI/V intermediate adhesive layer, the compact CNCs coating was formed with the RMS roughness decreasing from ~3.3 nm to ~2.1 nm, indicating the existence of strong adhesion between CNC and TA/PEI/V intermediate adhesive layer. To unravel this adhesion mechanism in the CNCs assembly process, the AFM colloidal probe technique was employed to directly measure the interaction forces between TA/PEI/V-coated silica probe and CNCs-coated substrate in the saline solution of 1 mmol NaCl at pH 6.4 in Figure S4.7. The strong adhesion (F/R~0.62 mN m^{-1}) was measured between TA/PEI/V and CNCs coatings in the retraction process, which was probably contributed from the synergistic effect of various interactions including electrostatic interaction, hydrogen bonding, coordination reaction, and so on.[35] Moreover, the morphologies of CNCs coating could be further

regulated by adjusting the CNCs assembly time ranging from 4 h to 10 h. As shown in Figure S4.8, by extending the CNCs assembly process from 4 h to 6 h and 10 h, the RMS roughness of resulting CNCs coating gradually increasing from ~2.1 nm to ~2.4 nm, which was due to the stacking of excess CNCs with extended CNCs assembly time.

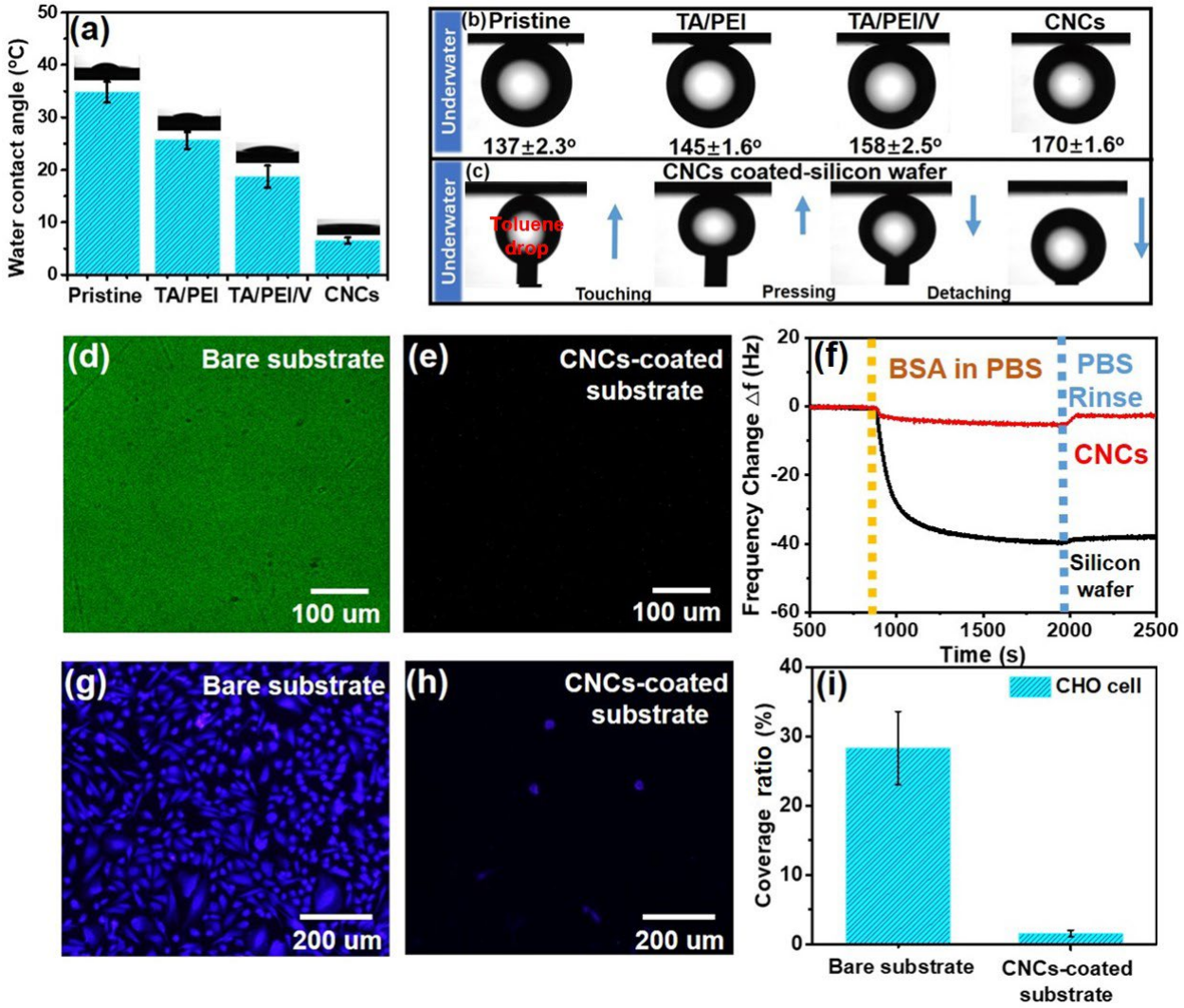

Figure 4.3 (a) Water contact angle in air and (b) Toluene drop contact angle in water of pristine, TA/PEI, TA/PEI/V, CNCs-coated silicon wafers; (c) Toluene drop attaching and detaching experiment on CNCs-coated silicon wafer; Confocal fluorescence microscopy imaging of FTIC-BSA adsorption on the (d) bare silicon wafer and (e) CNCs-coated silicon wafer; (f) Changes in

the frequency associated with the adsorption of the BSA on the bare and CNCs-coated silicon sensors; Representative fluorescence microscopy images CHO cells attached to the bare silicon wafer (g) and CNCs-coated silicon wafer (h); (i) Effect of CNCs coating on the attachment of CHO cells to silicon wafer. Shown were averaged from three independent experiments ($p<0.001$).

4.3.2 Antifouling property of CNCs coating

The surface wettability of as-prepared coatings was firstly evaluated by measuring their water contact angle in air (WCA) oil contact angle (OCA) in water: As shown in Figure 4.3(a), the WCA of TA/PEI and TA/PEI/V coating were ~25 ^{o} and ~20^{o}, respectively; Notably, the WCA of CNCs coating was further decreasing to ~8^{o}, indicating much-enhanced surface hydrophilicity due to the incorporation of super-hydrophilic CNCs layer on the substrate.[36] Moreover, OCA of CNCs coating in water was also measured: The toluene drop was strongly repelled by the CNCs-coated surface, exhibiting a very large OCA of ~170° (Figure 4.3(b)), even when the toluene drop was strongly compressed towards the CNCs coating (Figure 4.3(c)), the toluene drop deformed significantly but the contact angle remained almost unchanged during the compression process. Moreover, no toluene drop residue was detected after retracting the toluene drop from the CNCs coating, further demonstrating the excellent anti-oil adhesion property of CNCs coating.

The antifouling property of as-prepared CNCs coating was firstly evaluated by conducting the bovine serum albumin (BSA) adsorption test. The bare and CNCs-coated silicon wafers were exposed to the FITC-BSA in PBS buffer for 2 h before the confocal fluorescence microscopy imaging. As shown in Figure 4.3(d), the uniform and intense fluorescence signal was detected on the bare silicon wafer, indicating the significant adsorption of BSA on the surface; In contrast, no obvious fluorescence signal was detected on the CNCs-coated silicon wafer (Figure 4.3(e)), demonstrating the excellent protein-repellent performances of as-prepared CNCs coating.

Moreover, the quantitative BSA adsorption test was conducted by quartz crystal microbalance (QCM) to quantify the adsorption amount of BSA on the bare and CNCs-coated silica sensor. As shown in Figure 4.3(f), obvious adsorption of the BSA happened on the bare silica sensor, evidenced by the significant decrease of the frequency after exposing the bare silica sensor to BSA solution. Moreover, the adsorbed BSA on the bare silica sensor was persistent and could not be washed off by rinsing with PBS buffer. In contrast, only a neglectable amount of BSA was adsorbed on the CNCs-coated silica sensor and can be readily washed off by rinsing with PBS buffer, indicating the outstanding protein-repellent property of CNCs coating, which was attributed to the presence of closely packed hydrophilic CNCs on the substrate, acting as a strong physical barrier to prevent the diffusion and penetration of BSA on the substrate.[39] In addition to the surface fouling caused by the protein adsorption, the surface biofouling caused by cell adhesion is another concern for the practical applications of antifouling materials.[24, 73] Thus, the anti-cell attachment property of as-prepared CNCs coating was evaluated by directly seeding the Chinese hamster ovary (CHO) cells onto the bare and CNCs-coated silicon wafers, with the attachment monitored using fluorescence imaging: While a large number of CHO cells (purple spots) were attached to the bare silicon wafer, with ~28% of the surface covered by CHO cells (Figure 4.3(g)~(i)), only a low population of CHO cells were attached to the CNCs-coated silicon wafer, with ~1% of the surface covered by CHO cells (Figure 4.3(h)~(i)), demonstrating an excellent anti-cell attachment property of the CNCs coating, which presumably is attributed to the presence of a compact hydration layer in the CNCs coating.

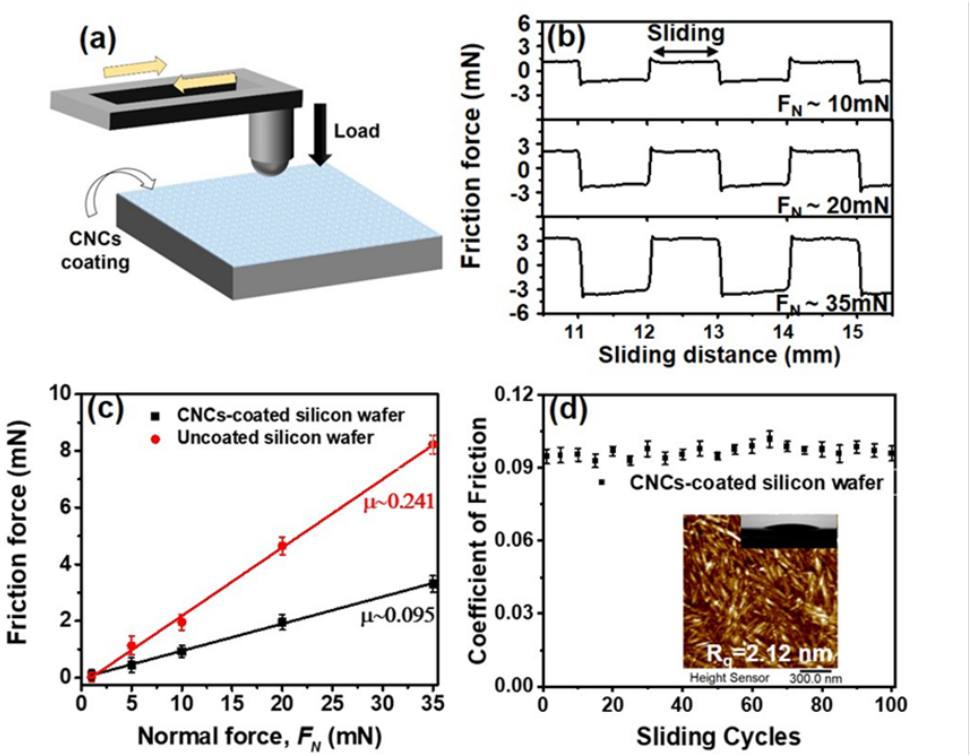

Figure 4.4 (a) The setup of NTR^3 nano tribometer for conducting reciprocating ball-on-disk friction test; (b) Typical shear forces versus sliding distance traces with the load increasing from 10 to 35 mN on CNCs-coated silicon wafer; (c) The friction coefficient of bare silicon wafer and CNCs-coated silicon wafer; (d) The change of friction coefficient of CNCs-coated silicon wafer within 100 friction cycles and the AFM images and WCA of the CNCs-coated silicon wafer after friction test.

4.3.3 Mechanical property of CNCs coating

The stability of as-prepared CNCs coating was evaluated by conducting the reciprocating ball-on-disk friction test by NTR^3 nano tribometer (Figure 4.4(a)). Figure 4.4(b) showed the typical shear force versus sliding distance traces of CNCs coating with the normal load increasing from 10 mN to 35 mN. The dynamic sliding with a small static friction force was observed with the normal load at 10 mN, and no significant increase of friction was found with the normal load increasing to 35 mN, indicating the CNCs coating remained its structural integrity in the friction

test.[74, 75] Moreover, as shown in Figure 4.4(c), the measured friction coefficients of bare silicon wafer and CNCs-coated silicon wafer were determined to be ~0.24 and ~0.09, respectively. The decreased friction coefficient of CNCs coating could be attributed to the formation of the confined hydration layer by the water molecules trapped in rigid CNCs coating,[76-78] which was difficult to be excluded by external pressure and served as a remarkable lubricate in the friction test.[60] To further evaluate the wear-resistance property of CNCs coating, the changing of the friction coefficient of CNCs coating was monitored in 100 reciprocating friction cycles with the normal load at 10 mN. As shown in Figure 4.4(d), the friction coefficient of fabricated CNCs coating was almost unchanged after 100 reciprocating friction cycles. Moreover, the morphology and WCA of CNCs coating after friction test were shown in the insert photo in Figure 4.4(d), it is found that the CNCs were still densely packed on the surface with the WCA remaining almost unchanged, demonstrating the outstanding anti-wear property of as-prepared CNCs coating.

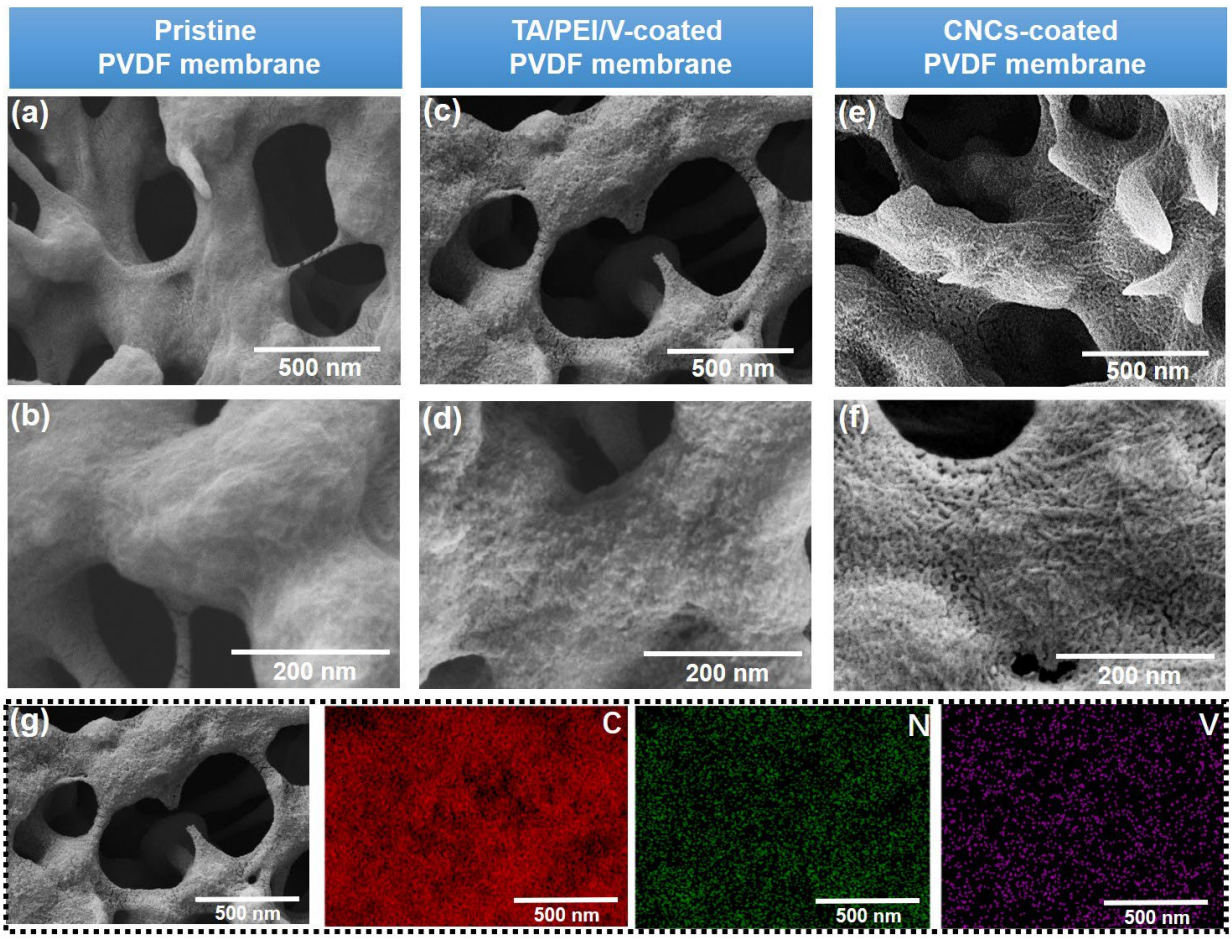

Figure 4.5 SEM images of the top view of (a), (b) Pristine PVDF membrane; (c),(d) TA/PEI/V-coated PVDF membrane; (e).(f) CNCs-coated PVDF membrane; (g) EDX element mappings of TA/PEI/V-coated PVDF membrane.

4.3.4 CNCs-coated membrane fabrication and characterization

To expand the application of the developed CNCs coating strategy, CNCs coating was further deposited on the polyvinylidene fluoride (PVDF) membranes to evaluate its potential application in oil/water separation. In the CNCs coating process, the TA/PEI/V intermediate adhesive layer was firstly deposited on the PVDF membrane surface before assembling CNCs layer. Compared to the morphology of the pristine PVDF membrane shown in Figure 4.5(a)~(b), the TA/PEI/V-coated membrane showed a layer of densely packed nano-aggregates on the surface

(Figure 4.5(c)~(d)), indicating the successful formation of TA/PEI/V intermediate adhesive layer on the membrane. Moreover, the corresponding EDX mapping results of the top surface (Figure 4.5(g)) and cross-section (Figure S4.9) of TA/PEI/V-coated membrane showed a uniform distribution of C, N, V elements on the membrane, indicating the homogeneous structure of the deposited TA/PEI/V intermediate adhesive layer on membrane.

The CNCs-coated membrane was fabricated by assembling CNCs on the as-prepared TA/PEI/V-coated membrane. The morphology of the resulting CNCs-coated membrane was also characterized by SEM. As shown in Figure 4.5(e), a compact and homogeneous CNCs layer was observed on the membrane surface, and the enlarged SEM image of the CNCs-coated membrane in Figure 4.5(f) also demonstrated that the CNCs were densely packed on the membrane surface without sacrificing the intrinsically porous structure of the membrane. The highly dense structure of CNCs coating deposited on membrane was similar to the structure of CNCs-coated silicon wafer characterized by the topographic AFM imaging. Moreover, the element distributions of CNCs coated-membrane were characterized by SEM/EDX, the C and O mass contents of CNCs coating were determined as 58.7 wt.% and 3.9 wt.%, respectively, exceeding that of TA/PEI/V-coated membrane (52.6 wt.% and 2.6 wt.%, respectively), which was due to the deposition of the CNCs layer on the membrane surface.

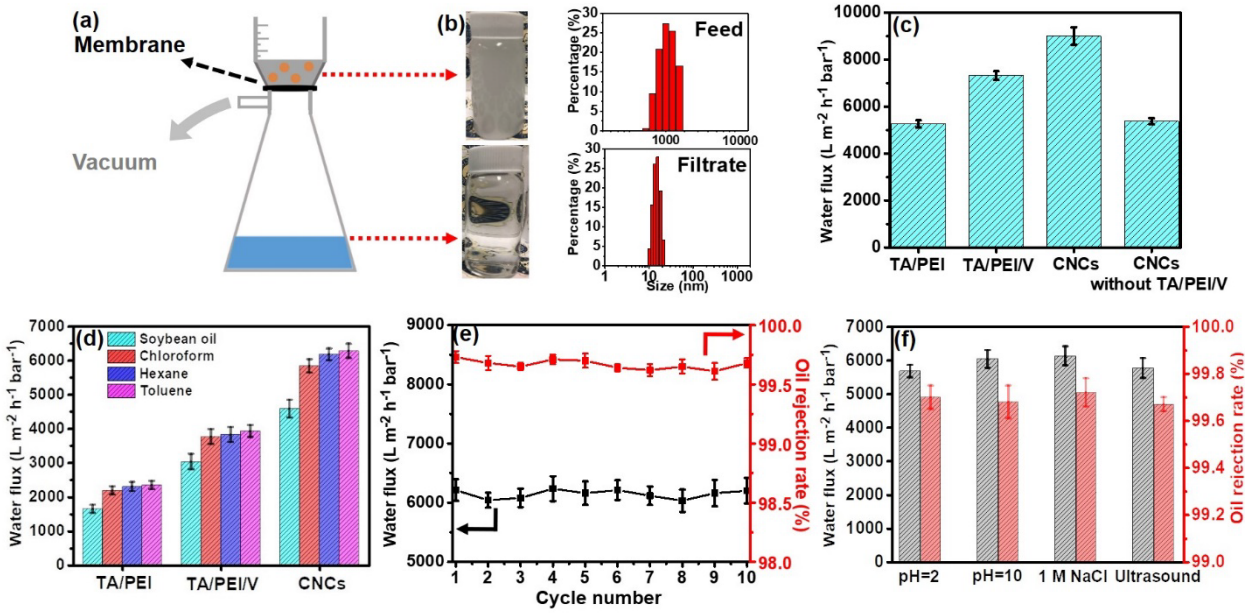

Figure 4.6 (a) Schematic of the dead-end vacuum filtration device; (b) Photographs and size distribution of the toluene-in-water emulsion before and after filtration; (c) Pure water flux of as-prepared membranes; (d) Water permeation flux of as-prepared membrane for separating toluene-in-water, hexane-in-water, chloroform-in-water, and soybean-in-water emulsions; (e) Cyclic toluene-in-water emulsion separation performance of CNCs-coated PVDF membrane; (f) The toluene-in-water emulsion separation performance of CNCs-coated PVDF membrane under different harsh conditions.

4.3.5 Oil/water emulsion separation by CNCs-coated membrane

Figure 4.6(a) showed the schematic of the dead-end vacuum filtration setup for evaluating the pure water flux and oil-in-water (O/W) emulsion separation performance of as-prepared membranes: As shown in Figure 4.6(c), the pure water fluxes of the TA/PEI and TA/PEI/V-coated membranes were determined as ~4500 L m^{-2} h^{-1} bar^{-1} and ~7000 L m^{-2} h^{-1} bar^{-1}. Notably, the pure water flux of the CNCs-coated membrane was over 9000 L m^{-2} h^{-1} bar^{-1}, the increased water flux of the CNCs-coated membrane was attributed to the existence of super-hydrophilic CNCs layer on

the membrane surface.[79] However, if the CNCs were directly deposited on the membrane without the TA/PEI/V intermediate adhesive layer, the pure water flux of the resulting CNCs-coated membrane was only about ~4500 L m^{-2} h^{-1} bar^{-1}, probably caused by the severe membrane pore blocking by the large CNCs aggregates on membrane surface. In the toluene-in-water emulsion separation process, the as-prepared toluene-in-water emulsion was milky and stable, with an average toluene droplet size of 1000 nm (Figure 4.6(b)). After filtration, the collected filtrate became transparent and clean with the toluene droplet size decreasing to 10 nm, which was possibly attributed to the existence of the small number of surfactant micelles or dissolved microdroplets, indicating the successful toluene-in-water emulsion separation by using as-prepared membranes.[80, 81] Moreover, Figure 4.6(d) showed the water permeation flux of as-prepared membranes in separation of different types of emulsions including toluene-in-water, chloroform-in-water, hexane-in-water, and soybean oil-in-water emulsions: The CNCs-coated membrane showed the permeation flux of over 6000 L m^{-2} h^{-1} bar^{-1} for the separation of toluene-in-water, chloroform-in-water, hexane-in-water emulsions. The outstanding separation performance of CNCs-coated membrane can be attributed to the ultra-low water transport resistance of densely packed super-hydrophilic CNCs layer on membrane.[17] Additionally, the relatively lower permeation flux of CNCs-coated membrane for separation soybean oil-in-water emulsion (~4500 L m^{-2} h^{-1} bar^{-1}) was due to the high viscosity of soybean oil, leading to the increased intrinsic resistance in the separation process.[82]. For the cyclic filtration test, the rejection rate (~99.6%) and permeation flux (~6000 L m^{-2} h^{-1} bar^{-1}) of CNCs-coated membrane remained unchanged within ten toluene-in-water emulsion filtration cycles (Figure 4.6(e)), and the SEM imaging and EDX results (Figure S4.10) of the CNCs-coated membrane after cyclic filtration test also indicated its morphology and element composition were almost unchanged, indicating the

excellent recyclability and stability of fabricated CNCs-coated membrane. To further investigate the durability of the CNCs-coated membrane in the harsh environment, the CNCs-coated membrane was treated with acid/alkali/saline solutions or ultrasound before conducting the toluene-in-water emulsion separation test. As shown in Figure 4.6(f), no obvious change of the toluene-in-water emulsion separation performance of CNCs-coated membrane was found, indicating the great stability of CNCs-coated membrane even under harsh conditions.

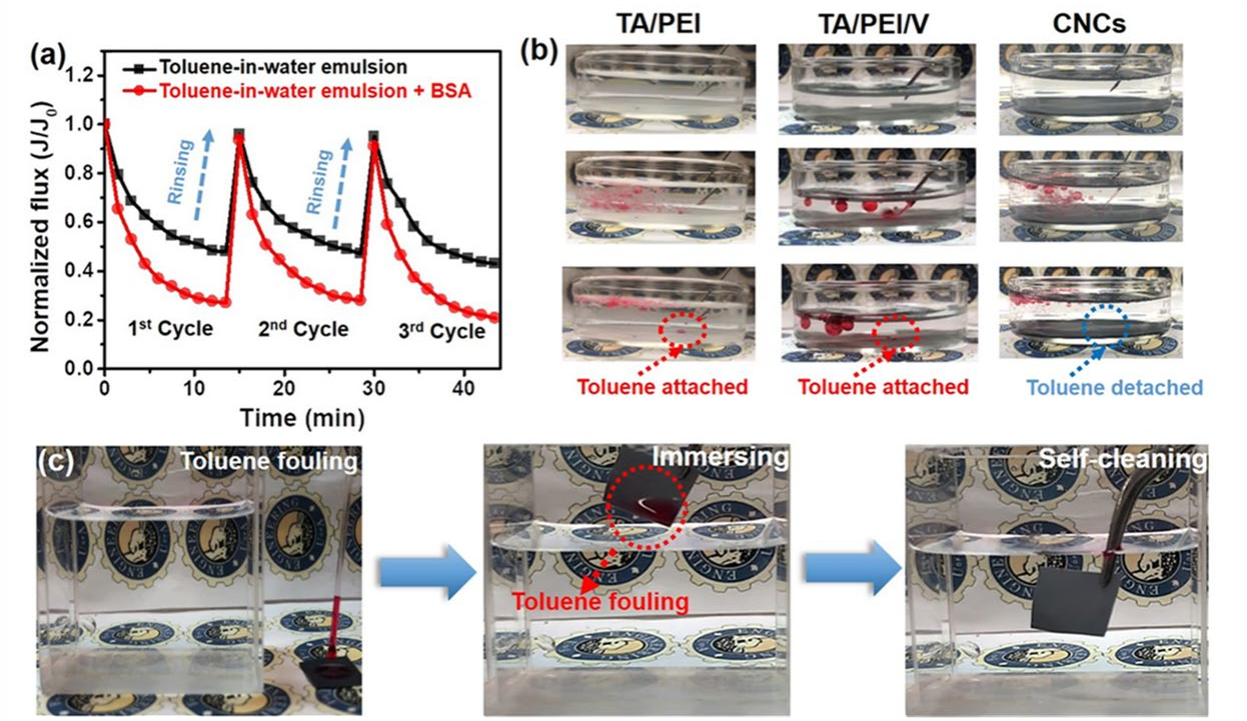

Figure 4.7 (a) Time-dependent permeability of CNCs-coated PVDF membrane in the separation of toluene-in-water emulsion and toluene-in-water emulsion with BSA; (b) Photographs of anti-oil (toluene) adhesion performance for as-prepared membranes; (c) Self-cleaning process of CNCs coated-PVDF membrane after toluene fouling.

The antifouling property of the CNCs-coated membrane was determined by monitoring the variation of water permeating flux during the toluene-in-water emulsion separation process. As shown in Figure 4.7(a): The rapid decline of normalized permeation flux happened in the initial

stage of the toluene-in-water emulsion separation process, which was due to the formation of filtration cake on the membrane;[20] Then, the decline of the normalized permeating flux became slower until reaching ~48% of the initial permeation flux; After the simple hydraulic washing, the decreased normalized permeation flux of CNCs-coated membrane could be recovered with recovery efficiency higher than 98% after three toluene-in-water emulsion separation cycles. Moreover, for the toluene-in-water emulsion containing other foulants such as BSA, the permeation flux of CNCs-coated membrane further declined to ~25% of the initial permeation flux in the first filtration cycle, which was due to the more severe pore blocking caused by BSA fouling.[83] Notably, the permeation flux of CNCs-coated membrane can be also recovered after hydraulic washing, with the recovery ratio higher than 95% after 3 cycles. These results indicated that the CNCs-coated membrane exhibited excellent antifouling performance to both toluene-in-water emulsion and other foulants such as BSA, which was attributed to the closely packed CNCs coating that captured a compact hydration layer on the membrane surface, thus the filtration cake could easily be washed away from the membrane surface.[1, 84] Moreover, the self-cleaning property of CNCs coated-membrane was verified by the toluene droplet (dyed by Oil red O) jetting test shown in Figure 4.7(b), the high-speed toluene drops were bounced back from the surface of CNCs-coated membrane, while the toluene drop residues were attached on the surfaces of TA/PEI and TA/PEI/V-coated membranes. Additionally, Figure 4.7(c) showed the self-cleaning process of CNCs-coated membrane towards oil contamination: The membrane was firstly contaminated by several toluene droplets (dyed by Oil red O) and then immersed in water. The attached toluene droplets would spontaneously detach from the membrane and move to the air/water interface, which demonstrated the ultra-low oil (toluene) adhesion property of the fabricated CNCs-coated membrane.

4.4 Conclusions

In this study, the simple and universal coating strategy has been proposed for constructing robust CNCs coating compositing of a TA/PEI/V intermediate adhesive layer and a self-assembled CNCs layer. Introducing V^{3+} ions in the assembly process significantly reduced the roughness of resulting TA/PEI/V coating via coordination chemistry, thus achieving the highly dense CNCs coating with the outstandingly low RMS roughness (~2 nm). The as-prepared CNCs coating could effectively prevent the oil adhesion, protein adsorption, and cell attachment on the surface, and maintain its structural integrity and wettability (with the WCA~8°) even after 100 friction cycles. Moreover, the CNCs coating can be further deposited on the membrane surface without sacrificing the porous structure of membrane, endowing the membrane with superior high permeation flux (over 6000 L m^{-2} h^{-1} bar^{-1}) and nearly 100% flux recovery ratio for separation of toluene-in-water emulsion containing various foulants. Overall, this work provides a unique strategy to realize the densely packing of rigid materials as a robust coating onto any surfaces, giving new insight into the precise designing of robust coating with tunable properties for a broad range of engineering and environmental applications.

Supporting information

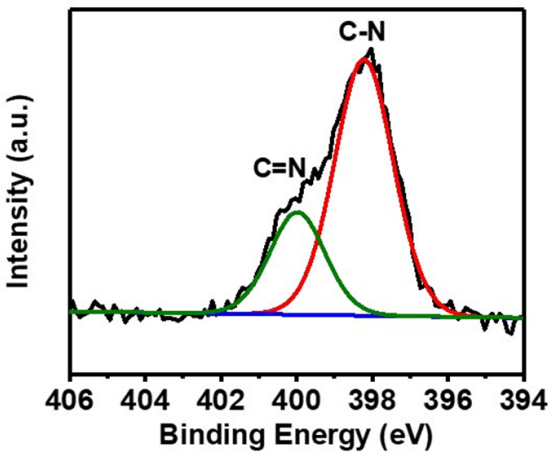

Figure S4.1 High-resolution spectra of N 1s of TA/PEI/V coating.

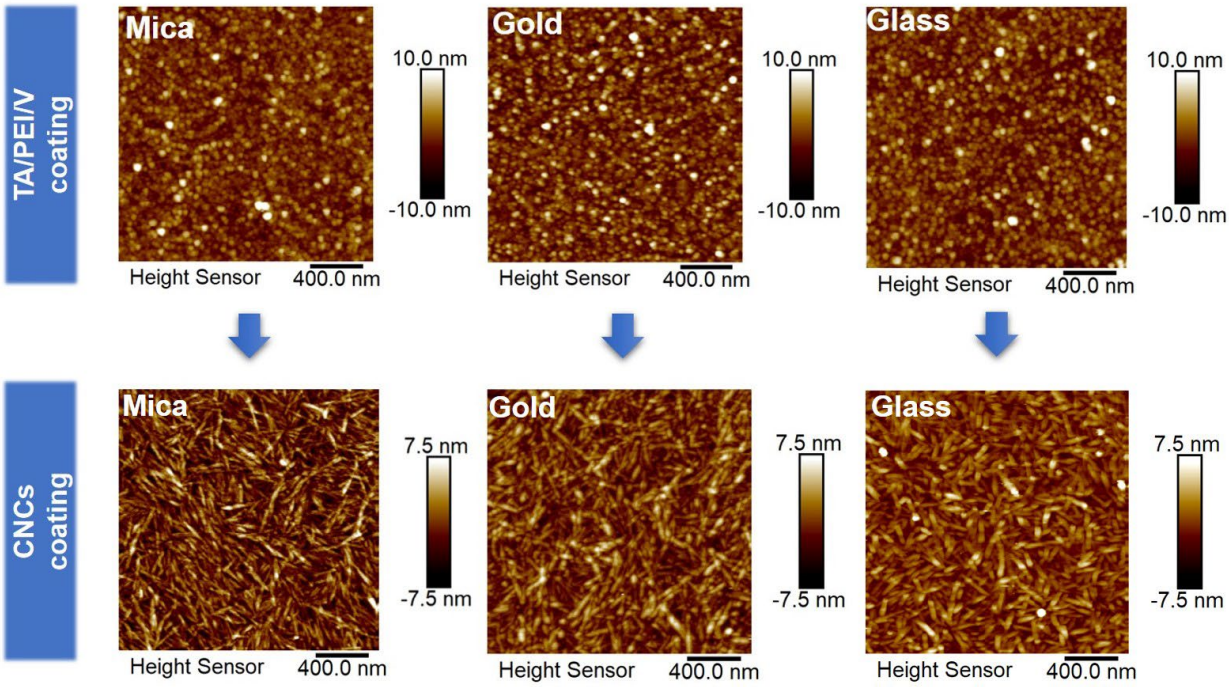

Figure S4.2. AFM images of TA/PEI/V intermediate adhesive layer and resulting CNCs coatings on mica, gold, and glass surfaces.

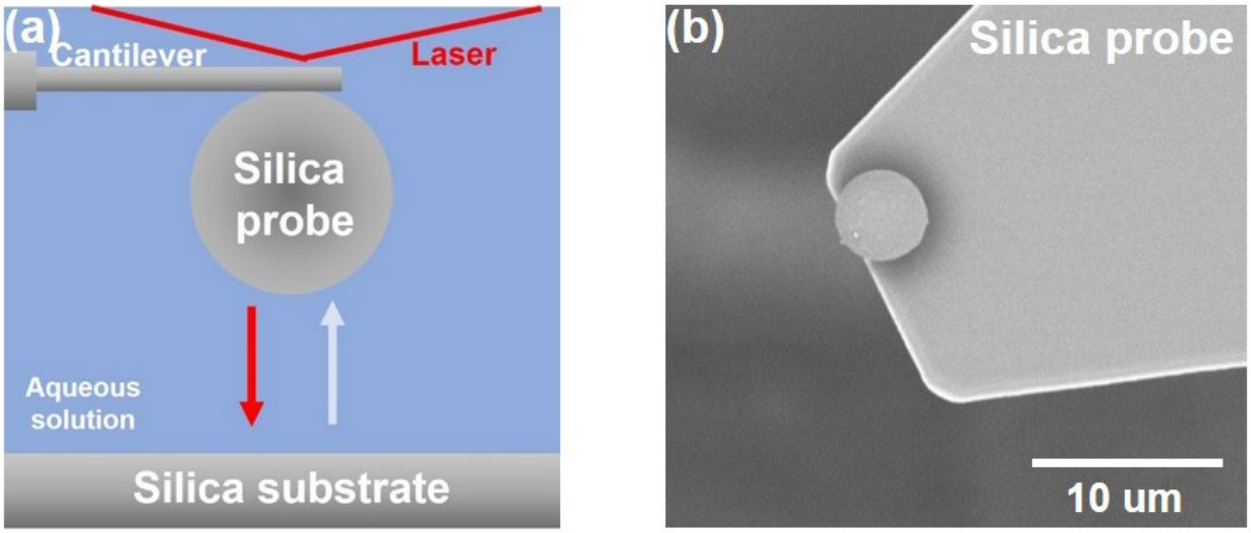

Figure S4.3 (a) Schematics of AFM colloidal probe force measurement setup and (b) the SEM image of a typical silica probe.

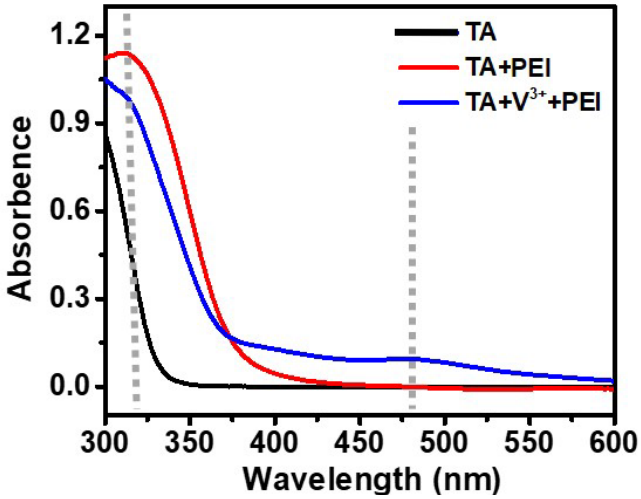

Figure S4.4 UV-vis spectra of TA, TA/PEI, TA/PEI/V solutions.

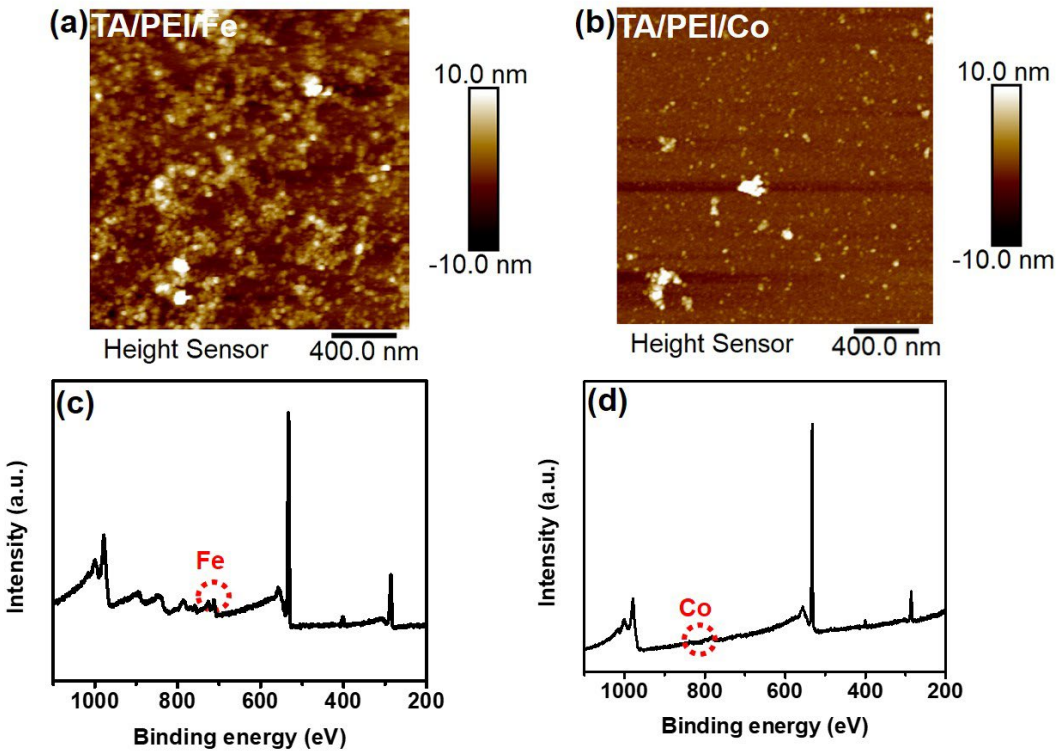

Figure S4.5 The AFM images of (a) TA/PEI/Fe and (b) TA/PEI/Co coating and XPS results of (c) TA/PEI/Fe and (d) TA/PEI/Co coating.

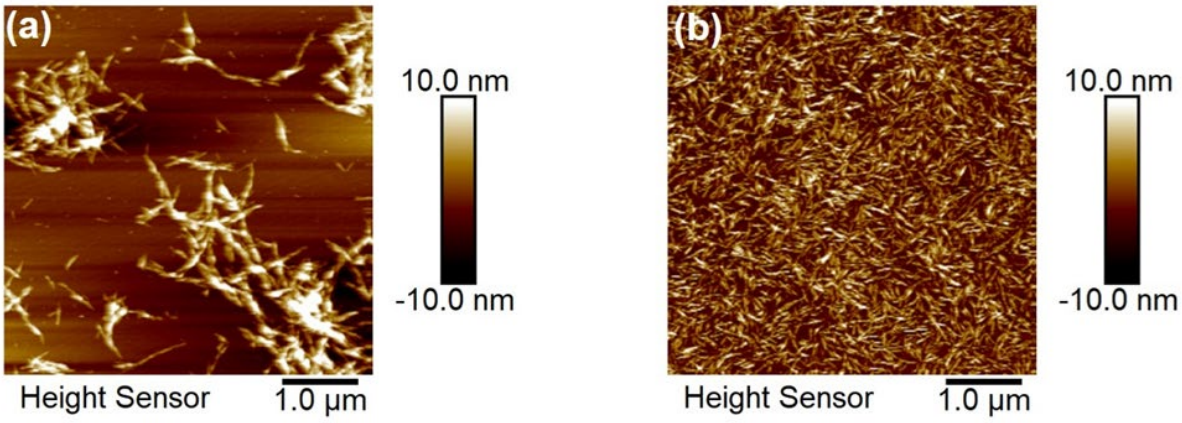

Figure S4.6 AFM images of CNCs-coated surfaces (a) without and (b) with TA/PEI/V intermediate adhesive layer.

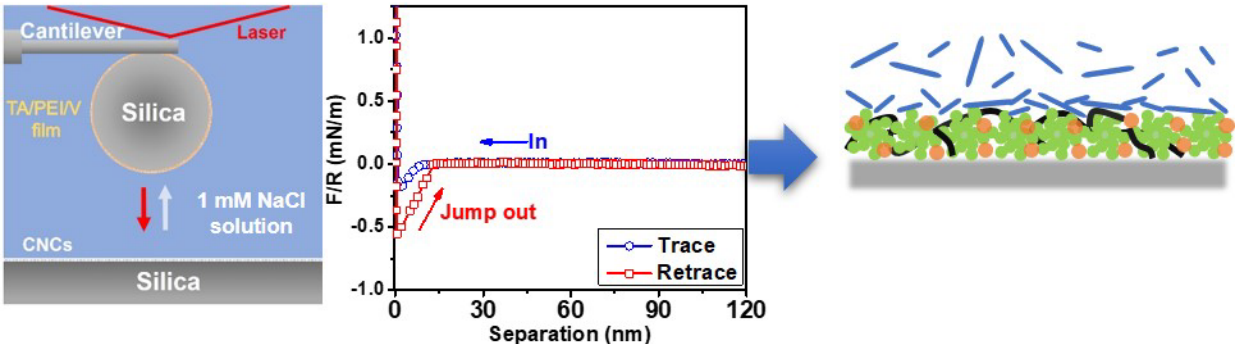

Figure S4.7 Force–distance profiles relative to TA/PEI/V-coated silica probe and CNCs-coated silica substrate at 1 mM NaCl, pH 6.4.

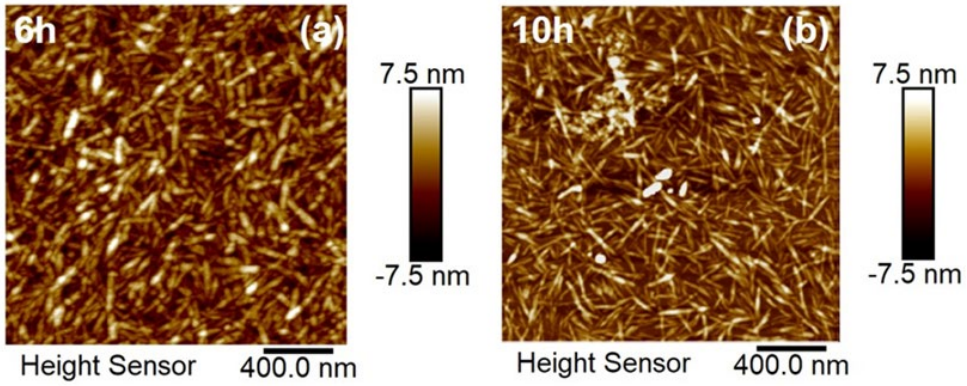

Figure S4.8 AFM images of CNCs coating with the CNCs assembly time of (a) 6h and (b) 10h.

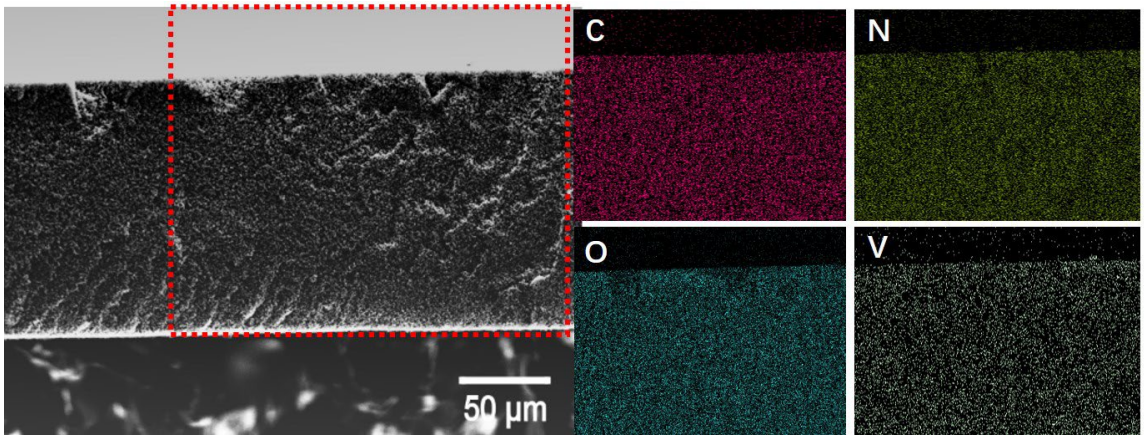

Figure S4.9 EDX mapping results of cross-section of TA/PEI/V-coated PVDF membrane.

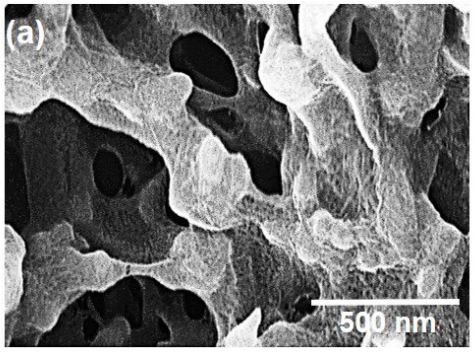

(b)

CNCs-coated membrane before test		CNCs-coated membrane after test	
C	58.7	C	59.8
N	1.5	N	1.2
F	35.1	F	33.3
O	3.9	O	4.7
V	0.8	V	1.0

Figure S4.10 The (a) SEM image and (b) EDX results of CNCs-coated PVDF membrane after cyclic test.

Reference

(1) Gao, S.; Zhu, Y.; Wang, J.; Zhang, F.; Li, J.; Jin, J. Layer - by - Layer Construction of Cu2+/Alginate Multilayer Modified Ultrafiltration Membrane with Bioinspired Superwetting Property for High - Efficient Crude - Oil - in - Water Emulsion Separation. *Advanced Functional Materials* **2018**, *28* (49), 1801944.

(2) Miao, D.; Huang, Z.; Wang, X.; Yu, J.; Ding, B. Continuous, spontaneous, and directional water transport in the trilayered fibrous membranes for functional moisture wicking textiles. *Small* **2018**, *14* (32), 1801527.

(3) Khatib, Z.; Faucher, M.; Sellman, E. Field Evaluation of Disc-Stack Centrifuges for Separating Oil/Water Emulsions on Offshore Platforms. In *SPE Annual Technical Conference and Exhibition*, **1995**

; Society of Petroleum Engineers.

(4) Yu, L.; Han, M.; He, F. A review of treating oily wastewater. *Arabian journal of chemistry* **2017**, *10*, S1913-S1922.

(5) Tanudjaja, H. J.; Hejase, C. A.; Tarabara, V. V.; Fane, A. G.; Chew, J. W. Membrane-based separation for oily wastewater: A practical perspective. *Water research* **2019**, *156*, 347-365.

(6) Chen, R.; Zhang, Y.; Xie, Q.; Chen, Z.; Ma, C.; Zhang, G. Transparent Polymer - Ceramic Hybrid Antifouling Coating with Superior Mechanical Properties. *Advanced Functional Materials* **2021**, *31* (19), 2011145.

(7) Fan, J. B.; Song, Y.; Wang, S.; Meng, J.; Yang, G.; Guo, X.; Feng, L.; Jiang, L. Directly coating hydrogel on filter paper for effective oil–water separation in highly acidic, alkaline, and salty environment. *Advanced Functional Materials* **2015**, *25* (33), 5368-5375.

(8) Chen, X.; Huang, G.; An, C.; Feng, R.; Wu, Y.; Huang, C. Plasma-induced PAA-ZnO coated PVDF membrane for oily wastewater treatment: Preparation, optimization, and characterization through Taguchi OA design and synchrotron-based X-ray analysis. *Journal of Membrane Science* **2019**, *582*, 70-82.

(9) Tummons, E.; Han, Q.; Tanudjaja, H. J.; Hejase, C. A.; Chew, J. W.; Tarabara, V. V. Membrane fouling by emulsified oil: A review. *Separation and Purification Technology* **2020**, *248*, 116919.

(10) Ge, J.; Zong, D.; Jin, Q.; Yu, J.; Ding, B. Biomimetic and superwettable nanofibrous skins for highly efficient separation of oil‐in‐water emulsions. *Advanced Functional Materials* **2018**, *28* (10), 1705051.

(11) Maan, A. M.; Hofman, A. H.; de Vos, W. M.; Kamperman, M. Recent developments and practical feasibility of polymer‐based antifouling coatings. *Advanced functional materials* **2020**, *30* (32), 2000936.

(12) Wang, Z.; Yang, H.-C.; He, F.; Peng, S.; Li, Y.; Shao, L.; Darling, S. B. Mussel-inspired surface engineering for water-remediation materials. *Matter* **2019**, *1* (1), 115-155.

(13) Zhang, C.; Ma, M.-Q.; Chen, T.-T.; Zhang, H.; Hu, D.-F.; Wu, B.-H.; Ji, J.; Xu, Z.-K. Dopamine-triggered one-step polymerization and codeposition of acrylate monomers for functional coatings. *ACS applied materials & interfaces* **2017**, *9* (39), 34356-34366.

(14) Zhou, X.; Wang, L.; Wei, Z.; Weng, G.; He, J. An Adaptable Tough Elastomer with Moisture‐Triggered Switchable Mechanical and Fluorescent Properties. *Advanced Functional Materials* **2019**, *29* (34), 1903543.

(15) Yu, Q.; You, X.; Wu, H.; Su, Y.; Zhang, R.; Liu, Y.; Yang, C.; Shen, J.; Yuan, J.; Jiang, Z. Ultrathin fluorinated self-cleaning membranes via coordination-driven metal-bridging assembly for water purification. *Journal of Materials Chemistry A* **2020**, *8* (8), 4505-4514.

(16) Wu, J.; Ding, Y.; Wang, J.; Li, T.; Lin, H.; Wang, J.; Liu, F. Facile fabrication of nanofiber- and micro/nanosphere-coordinated PVDF membrane with ultrahigh permeability of viscous water-in-oil emulsions. *Journal of Materials Chemistry A* **2018**, *6* (16), 7014-7020.

(17) Zhang, L.; Lin, Y.; Wu, H.; Cheng, L.; Sun, Y.; Yasui, T.; Yang, Z.; Wang, S.; Yoshioka, T.; Matsuyama, H. An ultrathin in situ silicification layer developed by an electrostatic attraction force strategy for ultrahigh-performance oil–water emulsion separation. *Journal of Materials Chemistry A* **2019**, *7* (42), 24569-24582.

(18) Jin, L.; Su, X.; Shi, J.; Shih, K. C.; Cintron, D.; Cai, T.; Nieh, M. P.; Chen, O.; Suib, S. L.; Jain, M. Crystalline Mesoporous Complex Oxides: Porosity - Controlled Electromagnetic Response. *Advanced Functional Materials* **2020**, *30* (15), 1909491.

(19) Azam, M. S.; Cai, C.; Gibbs, J. M.; Tyrode, E.; Hore, D. K. Silica surface charge enhancement at elevated temperatures revealed by interfacial water signals. *Journal of the American Chemical Society* **2020**, *142* (2), 669-673.

(20) Zhu, Y.; Wang, J.; Zhang, F.; Gao, S.; Wang, A.; Fang, W.; Jin, J. Zwitterionic nanohydrogel grafted PVDF membranes with comprehensive antifouling property and superior cycle stability for oil - in - water emulsion separation. *Advanced Functional Materials* **2018**, *28* (40), 1804121.

(21) Yang, H.-C.; Xie, Y.; Chan, H.; Narayanan, B.; Chen, L.; Waldman, R. Z.; Sankaranarayanan, S. K.; Elam, J. W.; Darling, S. B. Crude-oil-repellent membranes by atomic layer deposition: oxide interface engineering. *ACS nano* **2018**, *12* (8), 8678-8685.

(22) Yang, X.; Sun, P.; Zhang, H.; Xia, Z.; Waldman, R. Z.; Mane, A. U.; Elam, J. W.; Shao, L.; Darling, S. B. Polyphenol - sensitized atomic layer deposition for membrane interface hydrophilization. *Advanced Functional Materials* **2020**, *30* (15), 1910062.

(23) Zhang, C.; Wu, B.-H.; Ma, M.-Q.; Wang, Z.; Xu, Z.-K. Ultrathin metal/covalent–organic framework membranes towards ultimate separation. *Chemical Society Reviews* **2019**, *48* (14), 3811-3841.

(24) Li, L.; Yan, B.; Yang, J.; Chen, L.; Zeng, H. Novel mussel - inspired injectable self - healing hydrogel with anti - biofouling property. *Advanced Materials* **2015**, *27* (7), 1294-1299.

(25) Kang, T.; Oh, D. X.; Heo, J.; Lee, H.-K.; Choy, S.; Hawker, C. J.; Hwang, D. S. Formation, removal, and reformation of surface coatings on various metal oxide surfaces inspired by mussel adhesives. *ACS Applied Materials & Interfaces* **2015**, *7* (44), 24656-24662.

(26) Zhang, F.; Ren, D.; Huang, L.; Zhang, Y.; Sun, Y.; Liu, D.; Zhang, Q.; Feng, W.; Zheng, Q. 3D Interconnected Conductive Graphite Nanoplatelet Welded Carbon Nanotube Networks for Stretchable Conductors. *Advanced Functional Materials* **2021**, 2107082.

(27) Qin, M.; Xu, Y.; Cao, R.; Feng, W.; Chen, L. Efficiently controlling the 3D thermal conductivity of a polymer nanocomposite via a hyperelastic double - continuous network of graphene and sponge. *Advanced Functional Materials* **2018**, *28* (45), 1805053.

(28) Yu, Y.; Yuk, H.; Parada, G. A.; Wu, Y.; Liu, X.; Nabzdyk, C. S.; Youcef - Toumi, K.; Zang, J.; Zhao, X. Multifunctional "hydrogel skins" on diverse polymers with arbitrary shapes. *Advanced Materials* **2019**, *31* (7), 1807101.

(29) Usov, I.; Nyström, G.; Adamcik, J.; Handschin, S.; Schütz, C.; Fall, A.; Bergström, L.; Mezzenga, R. Understanding nanocellulose chirality and structure–properties relationship at the single fibril level. *Nature communications* **2015**, *6* (1), 1-11.

(30) Li, F.; Biagioni, P.; Bollani, M.; Maccagnan, A.; Piergiovanni, L. Multi-functional coating of cellulose nanocrystals for flexible packaging applications. *Cellulose* **2013**, *20* (5), 2491-2504.

(31) Yao, K.; Meng, Q.; Bulone, V.; Zhou, Q. Flexible and responsive chiral nematic cellulose nanocrystal/poly (ethylene glycol) composite films with uniform and tunable structural color. *Advanced Materials* **2017**, *29* (28), 1701323.

(32) Bethke, K.; Palantöken, S.; Andrei, V.; Roß, M.; Raghuwanshi, V. S.; Kettemann, F.; Greis, K.; Ingber, T. T.; Stückrath, J. B.; Valiyaveettil, S. Functionalized cellulose for water purification, antimicrobial applications, and sensors. *Advanced Functional Materials* **2018**, *28* (23), 1800409.

(33) Thomas, B.; Raj, M. C.; Joy, J.; Moores, A.; Drisko, G. L.; Sanchez, C. m. Nanocellulose, a versatile green platform: from biosources to materials and their applications. *Chemical Reviews* **2018**, *118* (24), 11575-11625.

(34) Samadder, R.; Akter, N.; Roy, A. C.; Uddin, M. M.; Hossen, M. J.; Azam, M. S. Magnetic nanocomposite based on polyacrylic acid and carboxylated cellulose nanocrystal for the removal of cationic dye. *RSC Advances* **2020**, *10* (20), 11945-11956.

(35) Huang, S.; Wang, D. A Simple Nanocellulose Coating for Self-Cleaning upon Water Action: Molecular Design of Stable Surface Hydrophilicity. *Angewandte Chemie* **2017**, *129* (31), 9181-9185.

(36) Wu, M.-B.; Zhang, C.; Pi, J.-K.; Liu, C.; Yang, J.; Xu, Z.-K. Cellulose nanocrystals as anti-oil nanomaterials for separating crude oil from aqueous emulsions and mixtures. *Journal of Materials Chemistry A* **2019**, *7* (12), 7033-7041.

(37) Park, C. H.; Jeon, S.; Park, S.-H.; Shin, M. G.; Park, M. S.; Lee, S.-Y.; Lee, J.-H. Cellulose nanocrystal-assembled reverse osmosis membranes with high rejection performance and excellent antifouling. *Journal of Materials Chemistry A* **2019**, *7* (8), 3992-4001.

(38) Hou, Y.; Guan, Q.-F.; Xia, J.; Ling, Z.-C.; He, Z.; Han, Z.-M.; Yang, H.-B.; Gu, P.; Zhu, Y.; Yu, S.-H. Strengthening and Toughening Hierarchical Nanocellulose via Humidity-Mediated Interface. *ACS nano* **2020**, *15*(1), 1310–1320.

(39) Li, L.; Yan, B.; Zhang, L.; Tian, Y.; Zeng, H. Mussel-inspired antifouling coatings bearing polymer loops. *Chemical Communications* **2015**, *51* (87), 15780-15783.

(40) Lu, Q.; Danner, E.; Waite, J. H.; Israelachvili, J. N.; Zeng, H.; Hwang, D. S. Adhesion of mussel foot proteins to different substrate surfaces. *Journal of The Royal Society Interface* **2013**, *10* (79), 20120759.

(41) Zeng, Y.; Du, X.; Hou, W.; Liu, X.; Zhu, C.; Gao, B.; Sun, L.; Li, Q.; Liao, J.; Levkin, P. A. UV-Triggered Polydopamine Secondary Modification: Fast Deposition and Removal of Metal Nanoparticles. *Advanced Functional Materials* **2019**, *29* (34), 1901875.

(42) Xie, C.; Wang, X.; He, H.; Ding, Y.; Lu, X. Mussel-inspired hydrogels for self-adhesive bioelectronics. *Advanced Functional Materials* **2020**, *30* (25), 1909954.

(43) Xiang, L.; Lin, J.; Yang, Q.; Lin, S.; Chen, S.; Yan, B. Facile preparation of hierarchical porous polydopamine microspheres for rapid removal of chromate from the wastewater. *Journal of Leather Science and Engineering* **2020**, *2* (1), 1-10.

(44) Wang, G.; Xiang, J.; Lin, J.; Xiang, L.; Chen, S.; Yan, B.; Fan, H.; Zhang, S.; Shi, X. Sustainable Advanced Fenton-like Catalysts Based on Mussel-Inspired Magnetic Cellulose Nanocomposites to Effectively Remove Organic Dyes and Antibiotics. *ACS Applied Materials & Interfaces* **2020**, *12* (46), 51952-51959.

(45) Zeng, H.; Hwang, D. S.; Israelachvili, J. N.; Waite, J. H. Strong reversible Fe3+-mediated bridging between dopa-containing protein films in water. *Proceedings of the National Academy of Sciences* **2010**, *107* (29), 12850-12853.

(46) Zhang, C.; Gong, L.; Xiang, L.; Du, Y.; Hu, W.; Zeng, H.; Xu, Z.-K. Deposition and adhesion of polydopamine on the surfaces of varying wettability. *ACS applied materials & interfaces* **2017**, *9* (36), 30943-30950.

(47) Xiang, L.; Zhang, J.; Gong, L.; Han, L.; Zhang, C.; Yan, B.; Liu, J.; Zeng, H. Probing the interaction forces of phenol/amine deposition in wet adhesion: impact of phenol/amine mass ratio and surface properties. *Langmuir* **2019**, *35* (48), 15639-15650.

(48) Zhang, C.; Xiang, L.; Zhang, J.; Gong, L.; Han, L.; Xu, Z.-K.; Zeng, H. Tough and alkaline-resistant mussel-inspired wet adhesion with surface salt displacement via polydopamine/amine synergy. *Langmuir* **2019**, *35* (15), 5257-5263.

(49) Lee, B. P.; Messersmith, P. B.; Israelachvili, J. N.; Waite, J. H. Mussel-inspired adhesives and coatings. *Annual review of materials research* **2011**, *41*, 99-132.

(50) Lin, Q.; Gourdon, D.; Sun, C.; Holten-Andersen, N.; Anderson, T. H.; Waite, J. H.; Israelachvili, J. N. Adhesion mechanisms of the mussel foot proteins mfp-1 and mfp-3. *Proceedings of the National Academy of Sciences* **2007**, *104* (10), 3782-3786.

(51) Zhong, Q. Z.; Richardson, J. J.; He, A.; Zheng, T.; Lafleur, R. P.; Li, J.; Qiu, W. Z.; Furtado, D.; Pan, S.; Xu, Z. K. Engineered Coatings via the Assembly of Amino - Quinone Networks. *Angewandte Chemie International Edition* **2021**, *60* (5), 2346-2354.

(52) Lv, Y.; Yang, S.-J.; Du, Y.; Yang, H.-C.; Xu, Z.-K. Co-deposition kinetics of polydopamine/polyethyleneimine coatings: effects of solution composition and substrate surface. *Langmuir* **2018**, *34* (44), 13123-13131.

(53) Yang, S.-J.; Zou, L.-Y.; Liu, C.; Zhong, Q.; Ma, Z.-Y.; Yang, J.; Ji, J.; Müller-Buschbaum, P.; Xu, Z.-K. Codeposition of Levodopa and Polyethyleneimine: Reaction Mechanism and Coating Construction. *ACS Applied Materials & Interfaces* **2020**, *12* (48), 54094-54103.

(54) Podsiadlo, P.; Liu, Z.; Paterson, D.; Messersmith, P. B.; Kotov, N. A. Fusion of seashell nacre and marine bioadhesive analogs: high-strength nanocomposite by layer-by-layer assembly of clay and L-3, 4-dihydroxyphenylalanine polymer. *Advanced Materials* **2007**, *19* (7), 949-955.

(55) Zhang, Y.; Ma, J.; Shao, L. Ultra-thin trinity coating enabled by competitive reactions for unparalleled molecular separation. *Journal of Materials Chemistry A* **2020**, *8* (10), 5078-5085.

(56) Holten-Andersen, N.; Jaishankar, A.; Harrington, M. J.; Fullenkamp, D. E.; DiMarco, G.; He, L.; McKinley, G. H.; Messersmith, P. B.; Lee, K. Y. C. Metal-coordination: using one of nature's tricks to control soft material mechanics. *Journal of Materials Chemistry B* **2014**, *2* (17), 2467-2472.

(57) Park, J. P.; Song, I. T.; Lee, J.; Ryu, J. H.; Lee, Y.; Lee, H. Vanadyl–catecholamine hydrogels inspired by ascidians and mussels. *Chemistry of Materials* **2015**, *27* (1), 105-111.

(58) Hutter, J. L.; Bechhoefer, J. Calibration of atomic-force microscope tips. *Review of Scientific Instruments* **1993**, *64* (7), 1868-1873.

(59) Butt, H.-J.; Cappella, B.; Kappl, M. Force measurements with the atomic force microscope: Technique, interpretation and applications. *Surface science reports* **2005**, *59* (1-6), 1-152.

(60) Han, L.; Xiang, L.; Zhang, J.; Chen, J.; Liu, J.; Yan, B.; Zeng, H. Biomimetic lubrication and surface interactions of dopamine-assisted zwitterionic polyelectrolyte coatings. *Langmuir* **2018**, *34* (38), 11593-11601.

(61) Yi, J.; Nguyen, K.-C. T.; Wang, W.; Yang, W.; Pan, M.; Lou, E.; Major, P. W.; Le, L. H.; Zeng, H. Polyacrylamide/Alginate double-network tough hydrogels for intraoral ultrasound imaging. *Journal of Colloid and Interface Science* **2020**.

(62) Wei, Q.; Liu, X.; Yue, Q.; Ma, S.; Zhou, F. Mussel-Inspired One-Step Fabrication of Ultralow-Friction Coatings on Diverse Biomaterial Surfaces. *Langmuir* **2019**, *35* (24), 8068-8075.

(63) Li, M.; Li, Y.; Xue, F.; Jing, X. A robust and versatile superhydrophobic coating: Wear-resistance study upon sandpaper abrasion. *Applied Surface Science* **2019**, *480*, 738-748.

(64) Wang, W.; Xiang, L.; Gong, L.; Hu, W.; Huang, W.; Chen, Y.; Asha, A. B.; Srinivas, S.; Chen, L.; Narain, R. Injectable, self-healing hydrogel with tunable optical, mechanical, and antimicrobial properties. *Chemistry of Materials* **2019**, *31* (7), 2366-2376.

(65) Prajatelistia, E.; Ju, S. W.; Sanandiya, N. D.; Jun, S. H.; Ahn, J. S.; Hwang, D. S. Tunicate-Inspired Gallic Acid/Metal Ion Complex for Instant and Efficient Treatment of Dentin Hypersensitivity. *Advanced healthcare materials* **2016**, *5* (8), 919-927.

(66) Yang, H.-C.; Liao, K.-J.; Huang, H.; Wu, Q.-Y.; Wan, L.-S.; Xu, Z.-K. Mussel-inspired modification of a polymer membrane for ultra-high water permeability and oil-in-water emulsion separation. *Journal of Materials Chemistry A* **2014**, *2* (26), 10225-10230.

(67) Gong, L.; Wang, J.; Xiang, L.; Huang, J.; Fattahpour, V.; Roostaei, M.; Mamoudi, M.; Fermaniuk, B.; Luo, J.-L.; Zeng, H. Characterizing foulants on slotted liner and probing the surface interaction mechanisms in organic media with implication for an antifouling strategy in oil production. *Fuel* **2021**, *290*, 120008.

(68) He, M.; Sun, H.; Sun, H.; Yang, X.; Li, P.; Niu, Q. J. Non-organic solvent prepared nanofiltration composite membrane from natural product tannic acid (TA) and cyclohexane-1, 4-diamine (CHD). *Separation and Purification Technology* **2019**, *223*, 250-259.

(69) Sever, M. J.; Wilker, J. J. Absorption spectroscopy and binding constants for first-row transition metal complexes of a DOPA-containing peptide. *Dalton Transactions* **2006**, (6), 813-822.

(70) Johnson, D. A.; Nelson, P. G. Factors determining the ligand field stabilization energies of the hexaaqua 2+ complexes of the first transition series and the Irving-Williams order. *Inorganic Chemistry* **1995**, *34* (22), 5666-5671.

(71) Guo, J.; Ping, Y.; Ejima, H.; Alt, K.; Meissner, M.; Richardson, J. J.; Yan, Y.; Peter, K.; Von Elverfeldt, D.; Hagemeyer, C. E. Engineering multifunctional capsules through the assembly of metal–phenolic networks. *Angewandte Chemie International Edition* **2014**, *53* (22), 5546-5551.

(72) Mesko, M.; Xiang, L.; Bohle, S.; Hwang, D. S.; Zeng, H.; Harrington, M. J. Catechol-Vanadium Binding Enhances Cross-Linking and Mechanics of a Mussel Byssus Coating Protein. *Chemistry of Materials* **2021**, *33*(16), 6530–6540

(73) Wang, C.; Wang, T.; Hu, P.; Shen, T.; Xu, J.; Ding, C.; Fu, J. Dual-functional anti-biofouling coatings with intrinsic self-healing ability. *Chemical Engineering Journal* **2020**, *389*, 123469.

(74) Huang, J.; Qiu, X.; Xie, L.; Jay, G. D.; Schmidt, T. A.; Zeng, H. Probing the molecular interactions and lubrication mechanisms of purified full-length recombinant human proteoglycan 4 (rhPRG4) and hyaluronic acid (HA). *Biomacromolecules* **2019**, *20* (2), 1056-1067.

(75) Huang, J.; Yan, Y.; Xie, L.; Liu, H.; Huang, C.; Lu, Q.; Qiu, X.; Zeng, H. Probing the Self-Assembly and Nonlinear Friction Behavior of Confined Gold Nano-Particles. *Langmuir* **2019**, *35* (48), 15701-15709.

(76) Raviv, U.; Laurat, P.; Klein, J. Fluidity of water confined to subnanometre films. *Nature* **2001**, *413* (6851), 51-54.

(77) Chen, M.; Briscoe, W. H.; Armes, S. P.; Klein, J. Lubrication at physiological pressures by polyzwitterionic brushes. *science* **2009**, *323* (5922), 1698-1701.

(78) Jahn, S.; Klein, J. Hydration lubrication: the macromolecular domain. *Macromolecules* **2015**, *48* (15), 5059-5075.

(79) Pan, M.; Gong, L.; Xiang, L.; Yang, W.; Wang, W.; Zhang, L.; Hu, W.; Han, L.; Zeng, H. Modulating surface interactions for regenerable separation of oil-in-water emulsions. *Journal of Membrane Science* **2021**, 119140.

(80) Yang, X.; Yan, L.; Ma, J.; Bai, Y.; Shao, L. Bioadhesion-inspired surface engineering constructing robust, hydrophilic membranes for highly-efficient wastewater remediation. *Journal of Membrane Science* **2019**, *591*, 117353.

(81) Cheng, X.; Sun, Z.; Yang, X.; Li, Z.; Zhang, Y.; Wang, P.; Liang, H.; Ma, J.; Shao, L. Construction of superhydrophilic hierarchical polyacrylonitrile nanofiber membranes by in situ asymmetry engineering for unprecedently ultrafast oil–water emulsion separation. *Journal of Materials Chemistry A* **2020**, *8* (33), 16933-16942.

(82) He, Z.; Miller, D. J.; Kasemset, S.; Wang, L.; Paul, D. R.; Freeman, B. D. Fouling propensity of a poly (vinylidene fluoride) microfiltration membrane to several model oil/water emulsions. *Journal of Membrane Science* **2016**, *514*, 659-670.

(83) Cheng, X.; Liang, H.; Ding, A.; Qu, F.; Shao, S.; Liu, B.; Wang, H.; Wu, D.; Li, G. Effects of pre-ozonation on the ultrafiltration of different natural organic matter (NOM) fractions: membrane fouling mitigation, prediction and mechanism. *Journal of membrane science* **2016**, *505*, 15-25.

(84) Zhang, J.; Zhang, L.; Cui, X.; Gong, L.; Xiang, L.; Shi, C.; Hu, W.; Zeng, H. Scalable polyzwitterion–polydopamine coating for regenerable oil/water separation and underwater self-

cleaning of stubborn heavy oil fouling without pre-hydration. *Chemical Communications* **2018**, *54* (70), 9734-9737.

Chapter 5. Mussel-Inspired Polyethylene Glycol Coating for Constructing Antifouling Membrane for Oil-Water Separation

5.1 Introduction

Surface fouling caused by the undesired deposition of oily contamination and biomolecules has been a serious issue in many industrial applications such as maritime operations[1-4], medicine[5-7], food industries[8, 9], and water treatment process[10-16]. Especially for the membrane materials applied in the oil/water separation process[17-19]. In this process, the membrane surface fouling initiated by the non-specific adsorption of a large number of proteins or oily contaminants would block the inner pores of the membrane[20]. The severe pore-blocking may increase the water transfer resistance and inevitably lead to the dramatic decrease of membrane water permeation flux, thus greatly deteriorating the oil/water separation performance of the membrane[21-24]. Therefore, the design of an antifouling membrane that can effectively reduce the deposition of biomolecules and oily contamination onto its surface is critical to the applications of membrane materials in the water treatment processes.

Surface hydration plays a pivotal role in the fabrication of antifouling surfaces by weakening the non-specific attraction between the foulants and the surfaces[25-28]. Thus, many hydrophilic polymers, such as polyethylene glycol (PEG)[29-31] or polyacrylamide (PAM)[32], have been applied to fabricate antifouling coatings. Among these antifouling coatings, PEG coating, formed by anchoring PEG polymer onto target surfaces, has been considered as an effective antifouling coating strategy to prevent protein adsorption and oily contaminants because of its strong hydration and steric hindrance[33-35]. Despite the much progress achieved, However, some challenging issues still remain. Most reported PEG coatings were fabricated by directly anchoring the PEG polymer

on substrates via weak and unstable non-covalent bonds (e.g., hydrogen bond or metal coordination)[36], which was unable to functionalize many inert surfaces, such as polyvinylidene fluoride (PVDF) membrane. Thus, the resulting PEG coating was generally unstable under harsh environments and may fall off the substrate surfaces, leading to the deterioration of its antifouling performance[37]. Therefore, a durable PEG coating with excellent antifouling properties is still highly desired.

In the marine bio-systems, robust mussel adhesion is achieved by the formation of a "bio-glue" layer composed of mussel foot adhesive proteins (Mfps) to toughly adhere to various substrates [38-44]. Inspired by this bio-glue effect, the PEG coating can be firmly anchored on the substrates with the assistance of a bio-glue layer on the substrate. Recently, L-3,4-dihydroxy-l-phenylalanine (L-Dopa), a main component in Mfps, was found to be able to self-assemble as a poly(L-Dopa) layer and deposit on various substrates via both physical and chemical interactions[45, 46]. Thus, the poly(L-Dopa) coating may serve as a bio-glue layer and provide abundant functional groups for anchoring PEG coating on the substrate. However, the challenge still remains, most reported poly(L-Dopa)-based coatings were soluble and prone to dissolve in alkaline solution, which limits its application as a stable platform for anchoring PEG polymer as a stable coating. To solve this issue, a robust surface coating strategy was proposed via the L-Dopa/polyethyleneimine (PEI) co-deposition method[47]. Compared with the poly(L-Dopa) coatings, the L-Dopa/PEI coating formed by Michael-addition and Schiff-base reactions between amines and phenol groups showed great resistance to the varying solution chemistry with the desired long-term stability[48, 49]. Moreover, the abundant amino groups on the L-Dopa/PEI coating can serve as anchoring points to covalently link the epoxy-modified functional polymers onto substrates via "one-step" ring-opening reaction[50, 51], providing the possibility to covalently link a PEG coating onto various substrates.

Herein, inspired by the mussel adhesion strategy, we have proposed a facile strategy to fabricate durable and antifouling PEG coating onto various substrates. In this strategy, the L-Dopa/PEI bio-glue layer is firstly co-deposited on the substrates, providing abundant amino groups as the anchoring points for PEG polymer. Then, the poly(ethylene glycol) diglycidyl ether (PEGDE), a hydrophilic PEG polymer chain with epoxy groups on both chain ends, was covalently anchored as PEG coating on the L-Dopa/PEI coated-substrate via the ring-opening reaction. The formed PEGDE/LP coating features a highly dense structure with super hydrophilic nature (with a WCA~ 15°), endowing the substrates with excellent antifouling ability to prevent the adsorption of various proteins (such as bovine serum albumin (BSA)) onto substrates, which is also characterized by molecular force measurements between PEGDE/LP coating and BSA using a surface forces apparatus (SFA). Moreover, the as-prepared PEGDE/LP coating shows great stability and maintains its structure and wettability after acid/alkane/salt solution treatment. To further expand the application of the as-proposed PEGDE/LP coating strategy, the PEGDE/LP coating was used to functionalize a PVDF membrane. The as-prepared PEGDE/LP-coated PVDF membrane exhibited a high-water permeation flux (~3000 L m^{-2} h^{-1} bar^{-1}) for separation of oil-in-water (O/W) emulsion, and also showed over 90% water flux recovery ratio in separation O/W emulsions containing other foulants such as the BSA or humic acid (HA), further demonstrating the outstanding antifouling property of PEG coating in the membrane separation process.

5.2 Experimental methods

5.2.1 Materials

L-3,4-dihydroxy-l-phenylalanine (L-Dopa, ⩾98%), polyethyleneimine (PEI, Mn: 600, ⩾98%), poly(ethylene glycol) diglycidyl ether (PEGDGE, Mn: 500, ⩾99%), toluene (⩾99%), heptane (⩾98%), pentane (⩾99%), chloroform (⩾99%,), hexane (⩾95%), and sodium dodecyl sulfate (SDS, ⩾99%), humic acid (HA, ⩾99%), bovine serum albumin (BSA, ⩾98%), L-lysine (⩾ 98%), k-carrageenan (K-carr), pepsin (Pep, ⩾99%), lysozyme (Lyso, from hen egg white,⩾99%) and phosphate-buffered saline (PBS) (tablet) was purchased from Sigma-Aldrich (Canada). Bovine serum albumin fluorescein conjugate (FITC-BSA) was purchased from Fisher Scientific (Canada). Durapore® PVDF membrane (pore size 0.22 ~ um diameter ~ 47mm,) was purchased from Millipore Co. Ltd. Water used in this paper was generated from Barnstead Smart2Pure pro water purification system (Thermo Scientific). All the chemicals were used as received in this study.

5.2.2 Preparation of PEGDE/LP coating

The PEGDE/LP-coated surfaces were fabricated through a step-by-step dip-coating method. Specifically, the substrates (silicon wafer or PVDF membrane) were thoroughly washed in water/ethanol mixture and then cleaned by ultraviolet (UV)/Ozone surface cleaner for 15 min. Then, the LP bio-glue layer was firstly fabricated via L-Dopa and PEI co-deposition, in this process, the L-Dopa solution (2 mg/mL) and PEI solution (5, 10, 15 mg/mL) were well-dissolved in 10 mM Tris buffer as the LP casting solution. The cleaned substrates were prewetted by Tris buffer and then immersed in the LP casting solution for 4 h to finish the co-deposition process and labeled as LP coating. In the next step, the PEGDE was anchored onto the formed LP layer through the ring-opening reaction as a PEG coating. Specifically, the PEGDE was firstly dissolved in (deionized water) DI water and ultrasound for 10 minutes to get a homogenous solution (10 mg/mL), and the

as-prepared LP-coated substrates were immersed into the PEGDE solution for 8 hours at 60℃ to finish the reaction. The obtained substrates were washed with ethanol/water three times, dried with nitrogen, and labeled as PEGDE/LP-coated substrates.

5.2.3 Surface Characterization

The surface chemical structures of the as-prepared LP coating and PEGDE/LP coating were analyzed by Fourier transform infrared spectroscopy (FTIR) and X-ray photoelectron spectroscopy (XPS) with Kratos Axis spectrometer at Al Kα radiation. The LP co-deposition process was monitored by applying Thermo Scientific Evolution 300 UV-Vis spectrophotometer (Thermo Fisher Scientific). The morphologies of as-prepared LP and PEGDE/LP-coated silicon wafers were characterized by the by topographic imaging using atomic force microscope (AFM) with Bruker ICON AFM system (Bruker, Santa Barbara, CA) in tapping mode. The morphologies and element distributions of LP and PEGDE/LP-coated PVDF membranes were characterized by the field-emission scanning electron microscope (FESEM) (Zeiss Sigma 300 VP-FESEM, Germany) with energy-dispersive X-ray spectroscopy (EDX), respectively. The static water contact angles of as-prepared coatings were measured by using a contact angle goniometer (Ramé-Hart instrument, NJ). The surface zeta-potentials of as-prepared LP and PEGDE/LP-coated silicon wafers were characterized by Anton Paar SurPASS. The underwater oil adhesion test was conducted by using integrated thin film drainage apparatus (ITFDA).

5.2.4 Evaluation of the Antifouling Properties of PEGDE/LP coating

The adsorbed mass of protein (bovine serum albumin (BSA)) of the as-prepared PEGDE/LP coating was monitored by quartz crystal microbalance (QCM) in real-time. The amounts of BSA adsorbed on silica sensors with or without PEGDE/LP coating were determined based on the frequency change (Δf) of the QCM sensor by the following Sauerbrey equation[52]:

$$\Delta m = \frac{C\Delta f}{n} \quad (5\text{-}1)$$

Where the Δf is corresponding to the change of frequency (Hz) in the QCM test, the C is a constant for 17.7 ng $Hz^{-1}cm^{-2}$, and the n is the overtone number.

Moreover, the interaction between BSA and as-prepared PEGDE/LP coating was measured by using Surface Forces Apparatus (SFA)[28, 53]. For a typical normal force test, two back-silvered mica with the same thickness (1~5 μm) were first glued onto two cylindrical silica disks (radius R = 2 cm). The PEGDE/LP coating and BSA coating were deposited on mica surfaces by immersing the mica sheets into the corresponding solutions for a certain time. Then, two desired surfaces were mounted in the SFA chamber in a crossed-cylinder configuration with PBS buffer (0.13 M, pH 7.4) injected into the confined space between the two surfaces. The interaction forces between PEGDE/LP and BSA-coated mica surfaces in PBS buffer were measured as a function of the separation distance between two mica surfaces, which was monitored by the multiple beam interferometry by using the optical interference fringes of equal chromatic order (FECO). The surface forces were determined based on Hooke's law. The surface forces were calculated based on Hooke's law, and the reference distance (D = 0) was set as the adhesive contact of two bare mica surfaces in the air[54].

5.2.5 Membrane oil/water separation experiment

The separation performance of the PEGDE/LP-coated PVDF membrane was evaluated by using a dead-end filtration device. The oil-in-water (O/W) emulsions with 1 wt.% oil (toluene, hexane, chloroform, soybean oil) and 20 ppm SDS surfactant were prepared by using a homogenizer (IKA T-18 Ultra Turrax, Germany) at 12, 000 rpm for 10 min. The oil droplet size distribution of the O/W emulsions before and after conducting the membrane filtration process

was characterized by dynamic laser scattering measurement using a Zetasizer Nano ZSP system (Malvern Panalytical, NANO, United Kingdom). In the O/W emulsion separation process, the membrane was pre-wetted by DI water and fixed in the dead-end filtration device, followed by flowing the O/W emulsions through the membrane. The water permeating flux of membranes could be calculated by using the following equation[48, 55]:

$$J = \frac{\Delta V}{S \cdot \Delta t \cdot \Delta P} \tag{5-2}$$

Where the ΔV is the volume of filtrate collected in a certain period Δt, S is the effective membrane surface area, and ΔP is the applied pressure difference between ambient and evacuation pressure.

To calculate the separation efficiency, the total organic carbon (TOC) analysis was applied to calculate the oil content in the collected filtrate. The membrane separation efficiency was calculated by the following equation:

$$\eta(\%) = \left(1 - \frac{C_f}{C_i}\right) \times 100\% \tag{5-3}$$

Where the η is the membrane separation efficiency, and the C_i and C_f were corresponding to the oil content in the O/W emulsion before and after filtration, respectively.

Moreover, the anti-biofouling property of as-prepared membranes in the O/W separation process was evaluated by measuring the variation of water flux of the membranes in the separation of different kinds of emulsion such as O/W emulsion, O/W emulsion+ BSA (1 g/L), and O/W emulsion+ HA (0.2 g/L). The filtration time during each separation cycle was recorded in real-time. After each filtration cycle, the membrane was thoroughly washed with DI water for 5 minutes before conducting the next cycle of the filtration cycle.

5.3 Results and discussion

5.3.1 PEGDE/LP coating fabrication and characterization

Figure. 5.1(a) shows the illustration of the surface coating strategy for anchoring a layer of PEG coating on various substrates. Briefly, the L-Dopa/PEI (LP) was firstly assembled on the substrates through the co-deposition process. The LP co-deposition process was monitored by the UV-Vis spectrum shown in Figure S5.1: the new characteristic peak at 350 nm was attributed to the Schiff base reaction between amines and phenol groups of L-Dopa and PEI[17, 56], leading to the formation of small LP nano-aggregates, being driven to the substrates and growing as LP coating. In the following PEGDE assembly process, the epoxy groups at both chain ends of PEGDE would interact with the amino groups on the formed LP bio-glue layer via a ring-opening reaction[57, 58], leading to the formation of PEGDE coating onto the substrate. Moreover, the topography AFM imaging method was applied to characterize the morphology of as-prepared coatings, as shown in Figure 5.1(b), the LP coating showed a uniform and highly dense structure with a low surface roughness (Rq~1.2 nm), After the PEGDE assembly process, the resulting PEGDE/LP coating was still uniform with the root-mean-square roughness (Rq) increasing to ~1.7 nm due to the formation of PEGDE layer. Moreover, the surface hydrophilicity was monitored in the step-by-step coating process, as shown in Figure 5.1(c). Compared to the LP coating, the formed PEGDE/LP coating showed enhanced surface hydrophilicity with the water contact angle (WCA) reducing from ~25° to ~15°, which was attributed to the introduction of a super hydrophilic PEGDE layer[59]. Additionally, the change of the surface zeta potential in the coating process was further characterized under neutral conditions (pH=7.4). As shown in Figure 5.1(d), the surface zeta potential of the bare silicon wafer was about ~ -60 mV, and the surface zeta potential LP coated substrate was increased to ~ +10 mV, which was due to the incorporation of positively charged

PEI onto substrate. Compared with LP-coated substrate, the zeta potential of PEGDE/LP-coated substrate was decreased to ~ -25 mV, as attributed to the modification of the PEGDE layer onto surface.

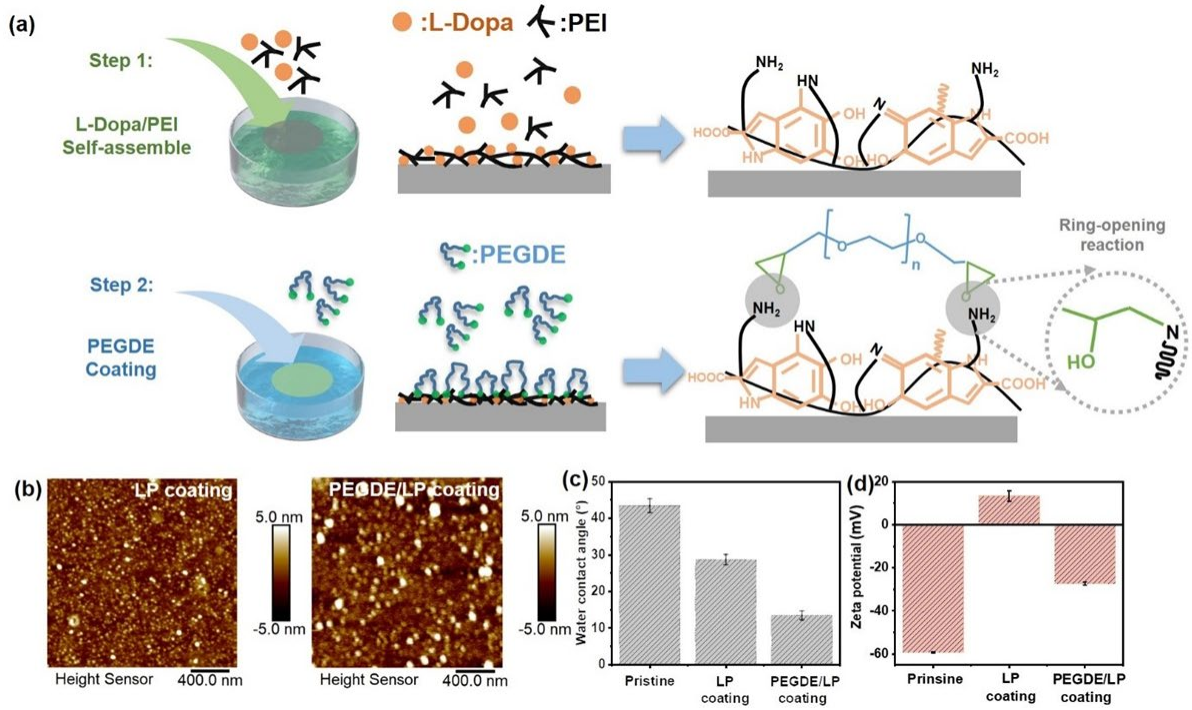

Figure 5.1 (a) Schematic of the synthesis route of PEGDE/LP coating; (b) AFM images of LP coating and PEGDE/LP coating of resulting PEGDE/LP coating; (c) The water contact angles and (d) zeta potentials of bare silicon wafer, LP-coated silicon wafer, and PEGDE/LP-coated silicon wafer (Data was reported as means ± standard deviation (SD) for n = 3 independent experiments).

Since the structure of PEGDE/LP coating was governed by the bridging effect of amnio groups on LP bio-glue layer towards the epoxy groups of PEGDE polymer through ring-opening reaction. Thus, the influence of the density of the amnio groups in the LP bio-glue layer on the structure of the resulting PEGDE/LP coating was further investigated by changing the PEI concentration in the self-assembly process. Without PEI, almost no coating was formed in the deposition process (Figure S5.2), which was due to the slow oxidative polymerization rate and the

electrostatic repulsion of carboxyl groups of L-Dopa[47]; As shown in Figure S5.3, at low PEI content (5 mg/mL), the PEI was in short supply to crosslink with L-Dopa, leading to the sparse LP layer and thus the defective PEGDE/LP coating; By increasing the PEI content to 10 mg/mL, the L-DOPA was well covalently crosslinked with adequate PEI to form a uniform LP layer with highly dense amnio groups, thus resulting in the PEGDE/LP coating with highly dense structure. However, when further increasing the PEI content to 15 mg/mL, the formed LP coating became sparse and aggregated, which was due to LP co-deposition process being suppressed by the high concentration of PEI [38, 49]. Conclusively, suitable PEI content in the co-deposition process would not only provide sufficient amino groups for anchoring the PEGDE polymer chain but also avoid aggregation of the formed PEGDE coating.

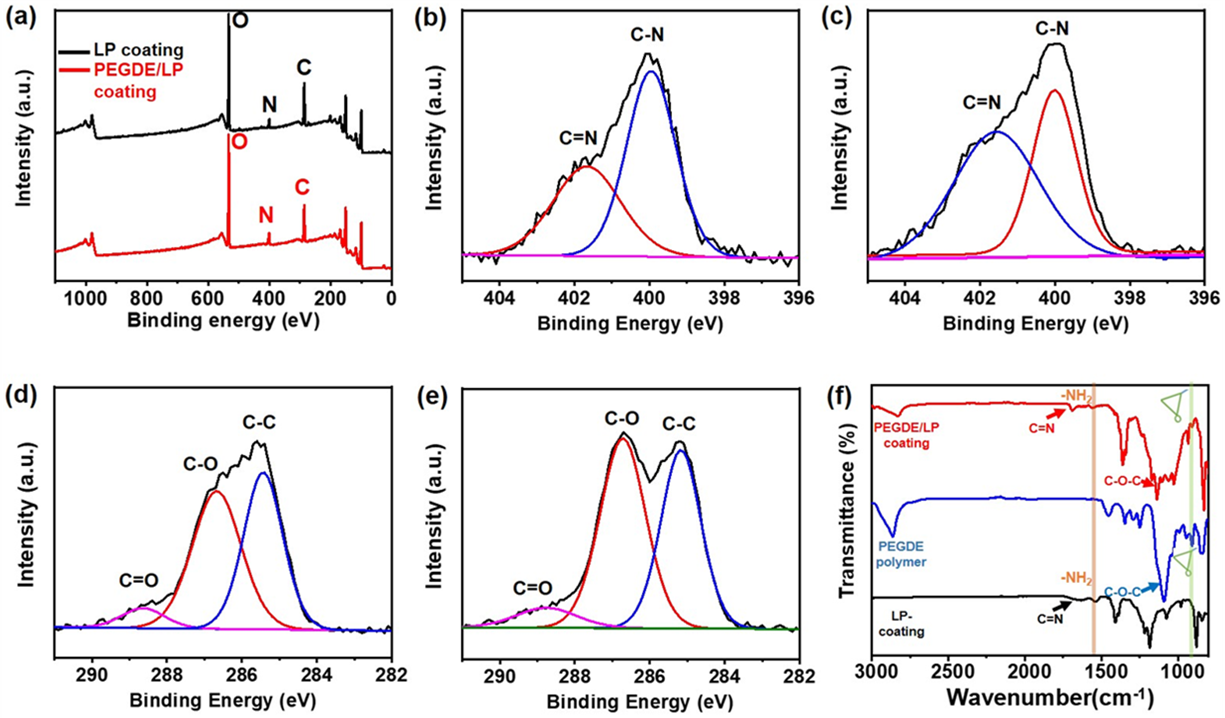

Figure 5.2 (a) XPS survey scan of LP and LP/PEGDE coating; High-resolution N1s spectrum of (b) LP coating and (c) LP/PEGDE coating; High-resolution C1s spectrum of (d) LP coating and (e) LP/PEGDE coating; (f) FTIR spectrum of PEGDE polymer, LP coating, and PEGDE/LP coating.

The surface element composition and chemical bonding states of as-prepared coatings were further characterized by the X-ray photoelectron spectrometer (XPS). As shown in Figure 5.2(a), the survey scan spectrum revealed the presence of C, O, and N elements in both LP coating and PEGDE/LP coating. As shown in Figure 5.2(b)~(c), the C-N and C=N bonds observed in the high-resolution N1s spectrum of both LP coating and PEGDE/LP coating suggested the formation of Schiff bases/Michael addition reaction in the L-Dopa/PEI co-deposition process. Moreover, the C 1s spectrum of LP coating and PEGDE/LP coating in Figure 5.2(d)~(e) can be deconvoluted into three peaks at 284.7, 286.8, and 288.5 eV, which can be assigned to C=C, C-O, and C=O bonds.[60, 61] Compared to the C 1s spectrum of LP-coating, the C-O ratio in the C1s high-resolution spectrum of PEGDE/LP coating was much higher than LP coating, which may be attributed to the incorporation of abundant C-O groups of PEGDE polymer chains. The chemical bonding states of LP coating and PEGDE/LP coating were further characterized by FT-IR spectroscopy. As shown in Figure 5.2(f), the peaks observed around 1690 cm^{-1} and 1600 cm^{-1} in both FT-IR spectrums of LP coating and PEGDE/LP coating were attributed to the stretching vibration of C=N bond by Schiff bases reaction, and the stretching peak of $–NH_2$ group of PEI, respectively.[47, 62] For the FT-IR spectrum of PEGDE polymer, the peak around 1060 cm^{-1} observed was attributed to the stretching vibration peak of C-O-C groups in the PEGDE polymer chain. The ring-opening reaction between PEGDE polymer and LP coating can be demonstrated by detecting the change of stretching vibration of the epoxy groups and $-NH_2$ groups from the FTIR spectra. As shown in Figure 5.2(f), the stretching vibration at around 1600 cm^{-1} was attributed to the $-NH_2$ groups of PEI in the LP coating. Moreover, for the PEGDE polymer, the stretching vibration at around 920 cm^{-1} was attributed to the epoxy groups. After the PEGDE coating process, the stretching vibrations of epoxy groups and $-NH_2$ groups on the FTIR spectra of PEGDE/LP coating were

weakened, indicating that the successful crosslinking between epoxy groups and -NH_2 groups through ring-opening reaction,[50] Moreover, the surface zeta potentials decreased from ~ +10 mV to ~ -25 mV after the PEGDE coating process, indicating that the positively charged -NH_2 groups on the LP coating were consumed by reacting with the epoxy groups of PEGDE polymer.

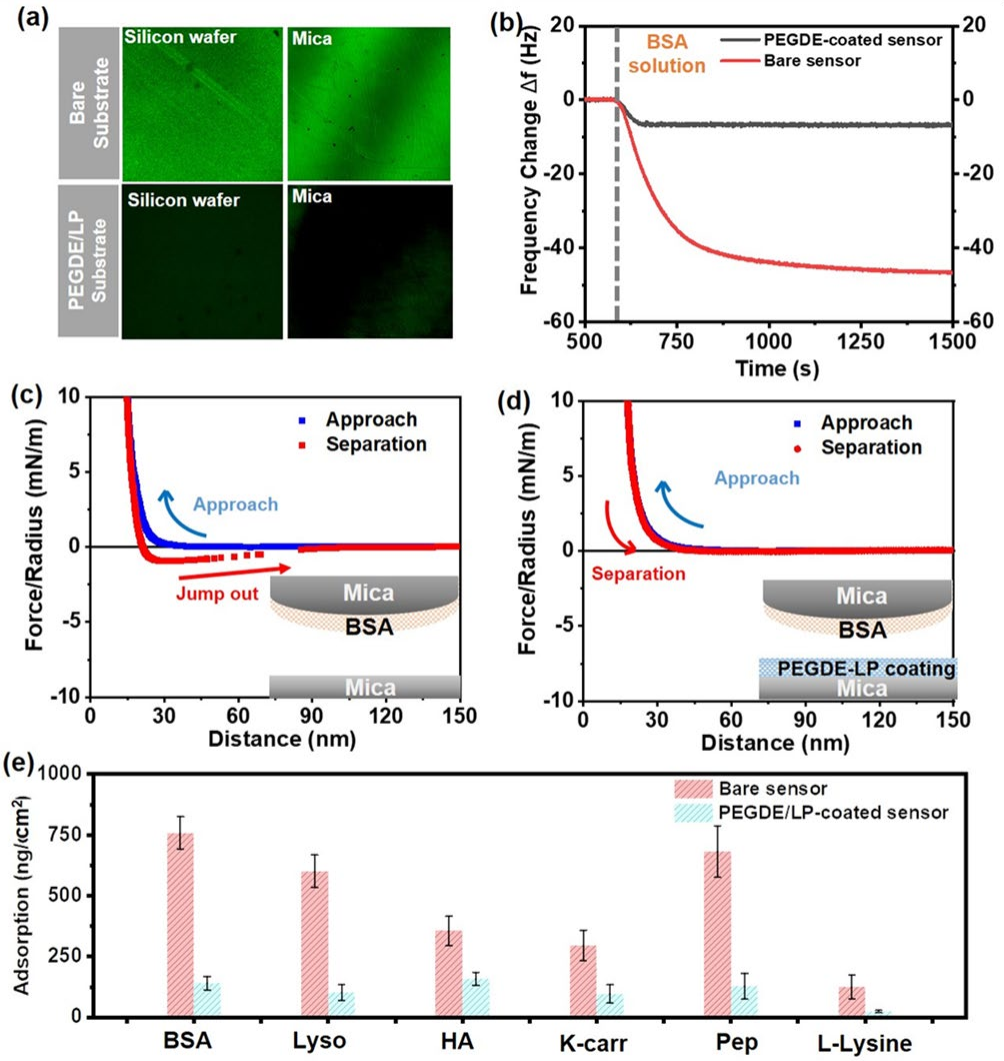

Figure 5.3 (a) The fluorescence microscope image of bare and PEGDE/LP coated-silicon wafer/mica after exposing FTIC-BSA for 2 h; (b) Changes of the frequency associated with the adsorption of the BSA on the bare and PEGDE/LP-coated silicon sensors in the QCM test; Force−distance profiles measured between the BSA layer and (c) bare or (d) PEGDE/LP-coated

mica surfaces in PBS buffer (The experimental configuration of SFA setup was shown in the insert picture). (e) The anti-protein adsorption performance of and PEGDE/LP coated-silicon wafer towards different kinds of proteins. (Data was reported as means ± SD for n = 3 independent experiments).

5.3.2 Antifouling property and mechanism of PEGDE/LP coating

The protein-repellent property of PEGDE/LP coating was evaluated by using FTIC-BSA as the model foulant with confocal fluorescence microscopy imaging method. As shown in Figure 5.3(a), the bare silicon wafer and mica surfaces showed uniform and intense fluorescence signals after exposure to the FITC-BSA solution for 2 h, which was caused by the significant BSA adsorption on the silicon surface. Notably, no obvious fluorescence signals were observed on the PEGDE/LP-coated silicon wafer and mica surfaces under the same conditions, indicating that the PEGDE/LP coating effectively prevents the adsorption of BSA. To further investigate the antifouling property of PEGDE/LP coating towards BSA adsorption, the quantitively BSA adsorption on the silicon sensors with/without PEGDE/LP coating was conducted was by using a QCM. As for the bare silicon sensor, contact with BSA solution would lead to an obvious increase of frequency in the QCM spectrum, indicating the significant BSA adsorption on the surface (Figure 5.3(b)). In contrast, for the PEGDE/LP-coated silicon sensor, only a small amount of BSA fouling was adsorbed on the PEGDE/LP-coated silicon sensor, demonstrating the excellent antifouling property of PEGDE/LP coating. Additionally, different kinds of foulants such as K-carr, Lyso, Pep, L-lysine, and HA were further applied to evaluate the antifouling property of as-prepared PEGDE/LP coating. As shown in Figure 5.3(e), foulant solutions will all lead to obvious adsorption onto the bare silicon sensor; In contrast, only a neglectable amount of different foulants

were adsorbed on the PEGDE/LP-coated silicon sensor, indicating the outstanding and universal antifouling property of as-prepared PEGDE/LP coating.

For a better understanding of the excellent antifouling property of as-prepared coating, the normal force interactions between the PEGDE/LP coating and BSA coating (Figure S5.4) were directly measured by using SFA with the experiment setup shown in the insert schematics of Figure 5.3(c). As shown in Figure 5.3(c), obvious adhesion (~ 1 mN/m) was observed when bare mica surface and the BSA-coated surface were brought into contact and separated, indicating the BSA showed high affinity to deposition on the mica surface. On the contract, as shown in Figure 5.3(d), the measured force-distance profiles showed a pure repulsion between PEGDE/LP coating and BSA coating during the surface approach and separation process, indicating that there was no adhesion hysteresis. Such pure repulsion was mainly attributed to the strong hydration and steric repulsion of the high-anchoring density of PEGDE polymer on the substrate, serving as a physical barrier to prevent direct contact between BSA and substrate,[59, 63] which was consistent with the above QCM and fluorescence images results. Thus, both QCM and SFA results indicated the significant role of PEGDE/LP coating in the antifouling process.

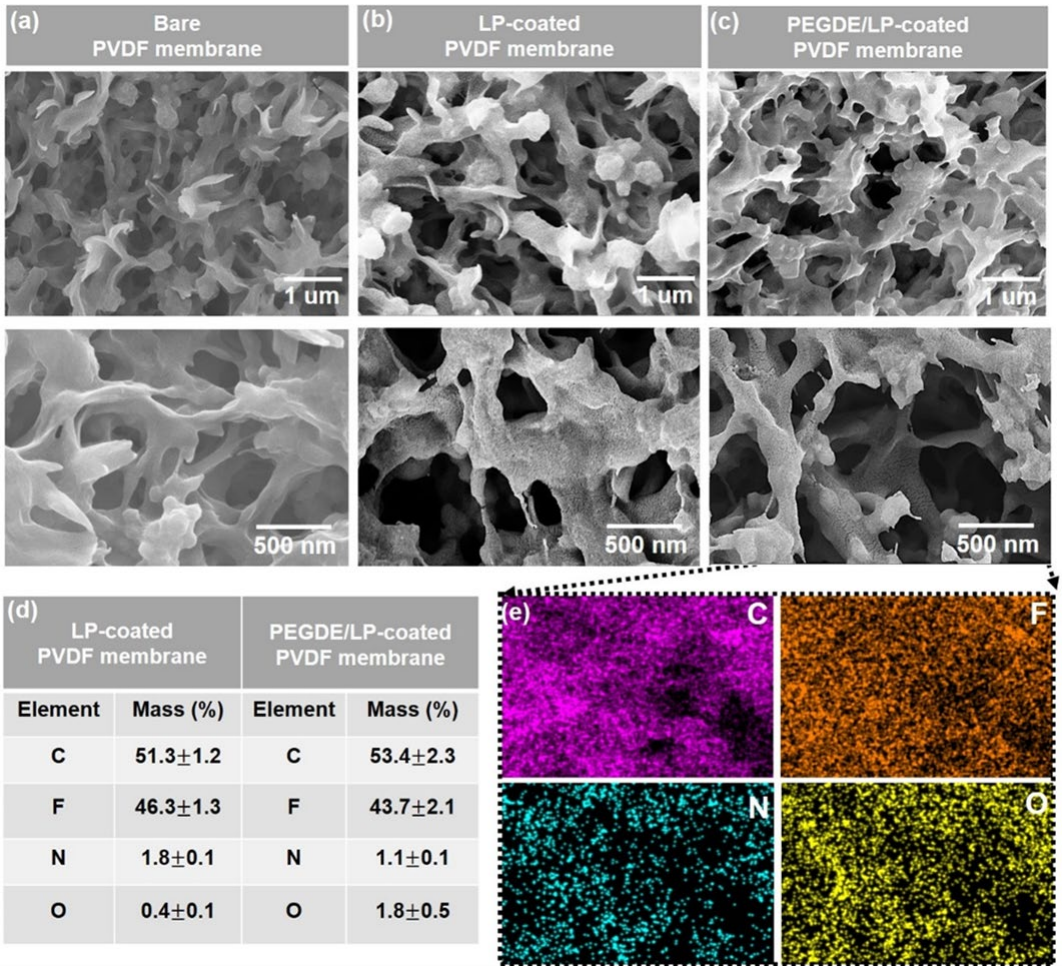

LP-coated PVDF membrane		PEGDE/LP-coated PVDF membrane	
Element	Mass (%)	Element	Mass (%)
C	51.3±1.2	C	53.4±2.3
F	46.3±1.3	F	43.7±2.1
N	1.8±0.1	N	1.1±0.1
O	0.4±0.1	O	1.8±0.5

Figure 5.4 SEM images of (a) bare PVDF membrane, (b) LP-coated PVDF membrane, (c) PEGDE/LP-coated PVDF membrane; (d) Summary of EDX results of LP and PEGDE/LP-coated membrane (Data was reported as means ± SD for n = 3 for the scanning tests per sample); (e) EDX mapping results of PEGDE/LP-coated membrane.

5.3.3 PEGDE/LP-coated membrane fabrication

The as-proposed PEGDE coating strategy can be further used to fabricate an antifouling membrane applied in the oil/water (O/W) emulsion separation process. The morphologies of as-prepared membranes were characterized by scanning electron microscope (SEM) and shown in Figure 5.4. The SEM images of the pristine PVDF membrane in Figure 5.4(a) showed a highly porous structure with a smooth surface. Moreover, the LP-coated membrane showed a relatively

rough structure with the layer of nano-aggregates uniformly coating on the surface, indicating the successful deposition of the LP layer on the membrane (Figure 5.4(b)). Compared to the LP-coated PVDF membrane, the PEGDE/LP-coated membrane surface showed an increased surface roughness (Figure 5.4(c)), which can be attributed to the assembly of the PEGDE layer on the LP-coated membrane. Meanwhile, the mass contents of the C and O increased from ~51.3 wt.% and ~0.4 wt.% of LP-coated membrane to ~53.4 wt.% and ~1.8 wt.% of PEGDE/LP-coated membrane (Figure 5.4(d)), which can be attributed to the incorporation of the PEGDE layer on the membrane surface. Moreover, the corresponding EDX element mapping results of the PEGDE/LP-coated membrane showed a uniform distribution of C, N, and O elements on the membrane surface (Figure 5.4(e)), demonstrating the homogeneous structure of the as-prepared PEGDE/LP-coated membrane.

5.3.4 Wettability of PEGDE/LP-coated membrane

The wettability of as-prepared membranes was further characterized by measuring their water contact angle (WCA). As shown in Figure 5.5(a), the PVDF membrane without modification exhibited a hydrophobic nature with the WCA~90°, For the LP-coated membrane, the corresponding WCA slight declined to ~40° due to the attachment of a small number of hydrophilic moieties onto membrane surface; After depositing the hydrophilic PEGDE layer onto the membrane, the PEGDE/LP-coated membrane showed a significantly declined WCA with the water droplets instantaneously spreading on membrane within several seconds. Moreover, the comprehensive underwater oil contact angles (OCA) of the PEGDE/LP-coated membrane towards different oils including toluene, pentane, and heptane were further investigated (Figure S5.5). It could be observed that the PEGDE/LP-coated membrane showed high OCAs (~160°) for all

different kinds of oil droplets, demonstrating the underwater superoleophobicity of as-prepared PEGDE/LP-coated membrane.

The stability of as-prepared membrane was systematically evaluated by monitoring the wettability of the PEGDE/LP-coated membrane under acid/alkaline/salt solution conditions. As shown in Figure 5.5(b) and Figure S5.6, the underwater OCA of PEGDE/LP-coated membrane remained almost unchanged under a wide pH range (2~10) and different kinds of salt conditions (1M salt solutions), demonstrating the great stability of PEGDE/LP-coated membrane under acid/alkaline/salt solution conditions, which can be attributed to the formation of covalent bonds between PEGDE polymers and the underlying LP-coated substrates.

Additionally, the dynamic oil adhesion test with an "approach–compress–detach" process was conducted by using integrated thin-film drainage apparatus (ITFDA) to evaluate the anti-oil adhesion property of as-prepared membranes. The setup of ITFDA was shown in Figure 5.5(c). In a typical dynamic oil adhesion test process, a toluene droplet (~ 2 mm) was held at the end of capillary tube, pressed onto the membrane surfaces, and then retracted from the membrane surface driven by a diaphragm of high-frequency speaker. The "approach–compress–detach" process was recorded using a camera.[64]. As shown in Figure 5.5(d), the oil droplet would spontaneously spread onto the pristine PVDF membrane after coming into contact with the membrane surface due to the hydrophobic nature of the PVDF membrane. On the contract, the oil droplets can be easily lifted after contacting with PEGDE/LP-coated membrane, and almost no shape deformation of the oil droplet was observed in the detach process, indicating the outstanding oil-repellent properties of the as-prepared PEGDE/LP-coated membrane.

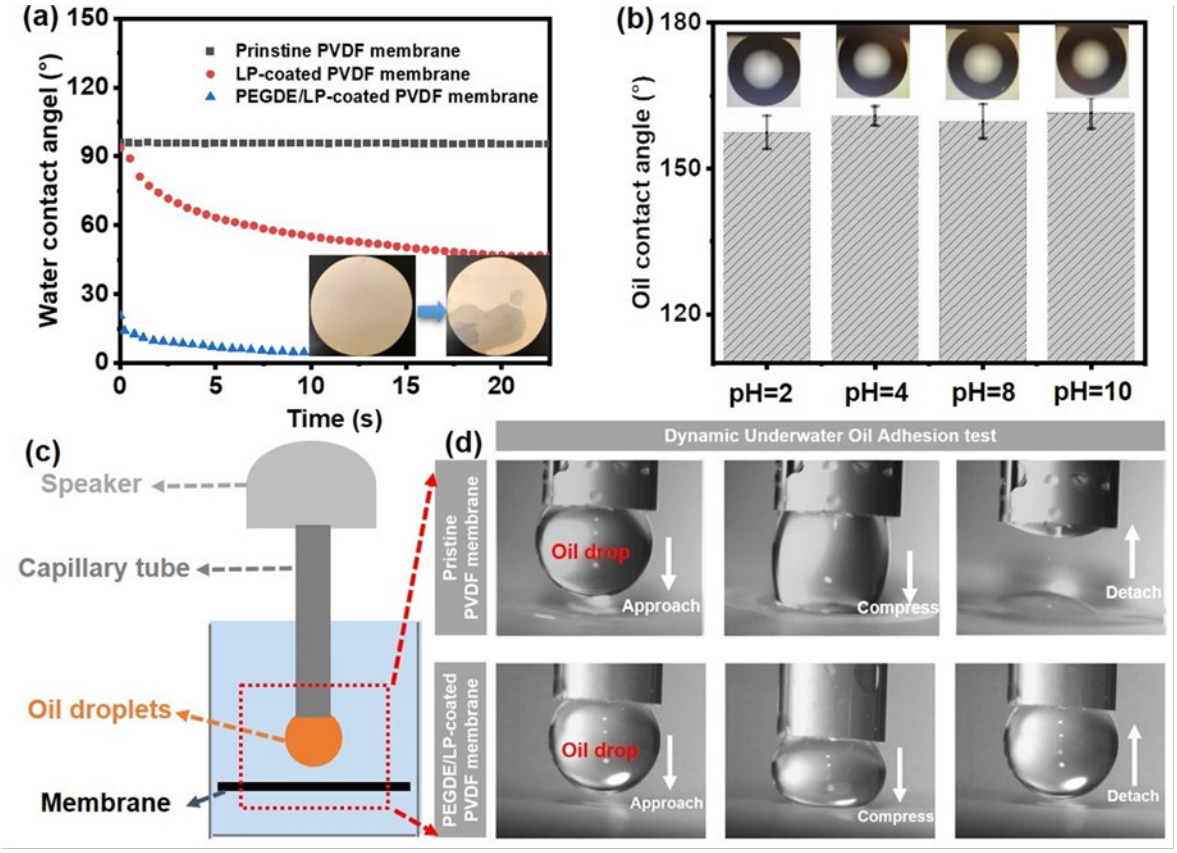

Figure 5.5 (a) The change of WCA versus time profile of bare PVDF membrane, LP-coated PVDF membrane, and PEGDE/LP-coated PVDF membrane; (b) Underwater oil contact angle of PEGDE/LP-coated PVDF membrane at different pH conditions (Data was reported as means ± SD for n = 3 independent experiments); (c) Schematic diagram of ITFDA setup; (d) Underwater oil adhesion test of bare PVDF membrane and PEGDE/LP-coated PVDF membrane.

5.3.5 Oil/water emulsion separation performance of PEGDE/LP-coated membrane

The filtration performances of as-prepared membranes were evaluated by using the vacuum filtration device (Figure 5.6(a)). As shown in Figure 5.6(b), the pure water flux of the pristine PVDF membrane was limited due to its hydrophobic nature. Notably, the pure water fluxes of PEGDE/LP-coated membrane were significantly increased to ~8000 L m^{-2} h^{-1} bar^{-1}. This enhanced water flux can be attributed to the existence of hydrophilic PEGDE/LP coating on the

membrane surface, which can effectively reduce the water permeation resistance in the filtration process[55, 65]. Moreover, the pure water flux of the PEGDE/LP-coated membrane remained almost unchanged under different solution conditions (Figure 5.6(c)), indicating the good stability of PEGDE/LP coating under harsh conditions. For the oil-in-water (O/W) emulsion separation process, the obtained O/W emulsion was milky and stable, and the size distribution of the oil droplets in the emulsion was ~ 1000 nm (Figure 5.6(a)). After the filtration process, the milky-like O/W emulsion turned to be clean and transparent, and the size distribution of the oil droplets after filtration decreased from ~1000 nm to ~10 nm, demonstrating the successful O/W separation by using the as-prepared membranes. It should be noted that the peak at ~10 nm was attributed to the SDS micelle rather than oil droplets[18]. Moreover, Figure 5.6(d) showed the water permeation flux of the LP-coated membrane and PEGDE/LP-coated membrane for the separation of different kinds of O/W emulsions. The LP-coated membrane showed a water permeation flux ~1000 L m^{-2} h^{-1} bar^{-1} for separation of the chloroform-in-water emulsion, hexane-in-water emulsion, and toluene-in-water emulsion. Notably, the water permeation flux of PEGDE/LP-coated membrane increased from ~1000 L m^{-2} h^{-1} bar^{-1} to ~3000 L m^{-2} h^{-1} bar^{-1} for separation of chloroform-in-water emulsion, hexane-in-water emulsion, and toluene-in-water emulsion, which can be attributed to the enhanced surface hydrophilicity of membrane by incorporation of the hydrophilic PEGDE layer on the membrane, resulting in low mass transfer resistance of membrane for water permeation [11, 66]. The separation performance of the as-prepared membrane was summarized and compared with other state-of-art anti-oil materials in Table. S5.1. To further characterize the stability of PEGDE/LP-coated membrane in the O/W separation process, the cyclic O/W separation test was also conducted, as shown in Figure 5.6(e), the water permeation flux and oil rejection rate of as-prepared PEGDE/LP-coated membrane almost remained unchanged within

five O/W separation cycles, indicating the outstanding stability of the as-prepared membrane in the O/W separation process. Moreover, in order to demonstrate the stability of PEGDE/LP coated membrane in the oil-in-salty water emulsion separation process. The O/W emulsion separation test was conducted under saline water conditions. As shown in Figure S5.7, the PEGDE/LP coated membrane showed a water permeation flux ~3000 L m^{-2} h^{-1} bar^{-1} for the separation of hexane-in-water emulsion and toluene-in-water emulsion with 1M NaCl, which was similar to the water permeation flux of PEGDE/LP coated membrane for the separation of O/W emulsion without salt, indicating the outstanding stability of PEGDE/LP coated membrane under saline water environment.

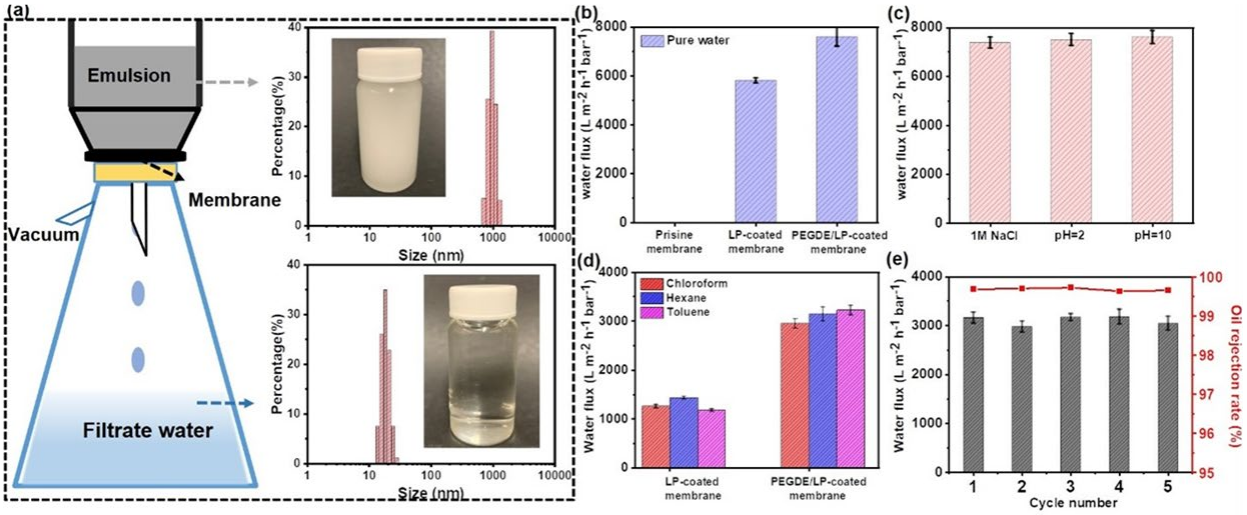

Figure 5.6 (a) The diagram of dead-end filtration device and the size distribution of emulsion before and after filtration; (b) Pure water flux of bare PVDF membrane, LP-coated PVDF membrane, and PEGDE/LP-coated PVDF membrane; (c) Water flux of PEGDE/LP-coated PVDF membrane under different solution conditions; (d) Oil-in-water (O/W) emulsion separation performance of PEGDE/LP-coated PVDF membrane; (e) Cyclic O/W emulsion separation test of PEGDE/LP-coated PVDF membrane. (Data was reported as means ± SD for n = 3 independent experiments in (b) to (e)).

To evaluate the antifouling performance of as-prepared membrane in the oil/water separation process, the filtration-cleaning cyclic test of as-prepared PEGDE/LP-coated membrane was conducted to monitor the real-time variation of water permeation flux in the separation of O/W emulsions containing model foulants such as BSA and HA. As shown in Figure 5.7(a), for the real-time separation of SDS stabilized O/W emulsion by the PEGDE/LP-coated membrane: In the first stage, a rapid decline in initial water permeation flux is observed, which can be attributed to the possible formation of a filtration cake on the membrane surface.[20, 67] In the second stage, the decline rate of the water permeation flux was slower until to a nearly constant rate (~20% of the initiate water permeation flux). In the third stage, the water permeation flux of PEGDE/LP-coated membrane can be easily restored after simply hydraulic washing. The recovery rate of the PEGDE/LP-coated membrane was over 90% of the initial water permeation flux after two cycles, indicating its outstanding antifouling properties for separation of the oily emulsion, it can be attributed to the hydrophilic PEGDE layer that captured a dense hydration layer on the membrane surface, showing ultralow adhesion to the emulsion droplets, thus the formed filtration cake on the membrane surface can easily be removed by simply hydraulic wash.[68] To further investigate the antifouling performance of as-prepared PEGDE/LP-coated membrane, two more different O/W emulsions containing BSA and HA were applied to conduct the real-time separation test.[11, 69] Notably, it was worth noting that the PEGDE/LP-coated membrane can still restore ~90% of the water permeation flux after two cycles by rinsing with DI water, further indicating that the great recyclability and reusability of the PEGDE/LP-coated membrane, and the outstanding antifouling properties of PEGDE/LP-coated membrane towards oily contamination and other troublesome foulants including surfactants or proteins that may cause membrane fouling.

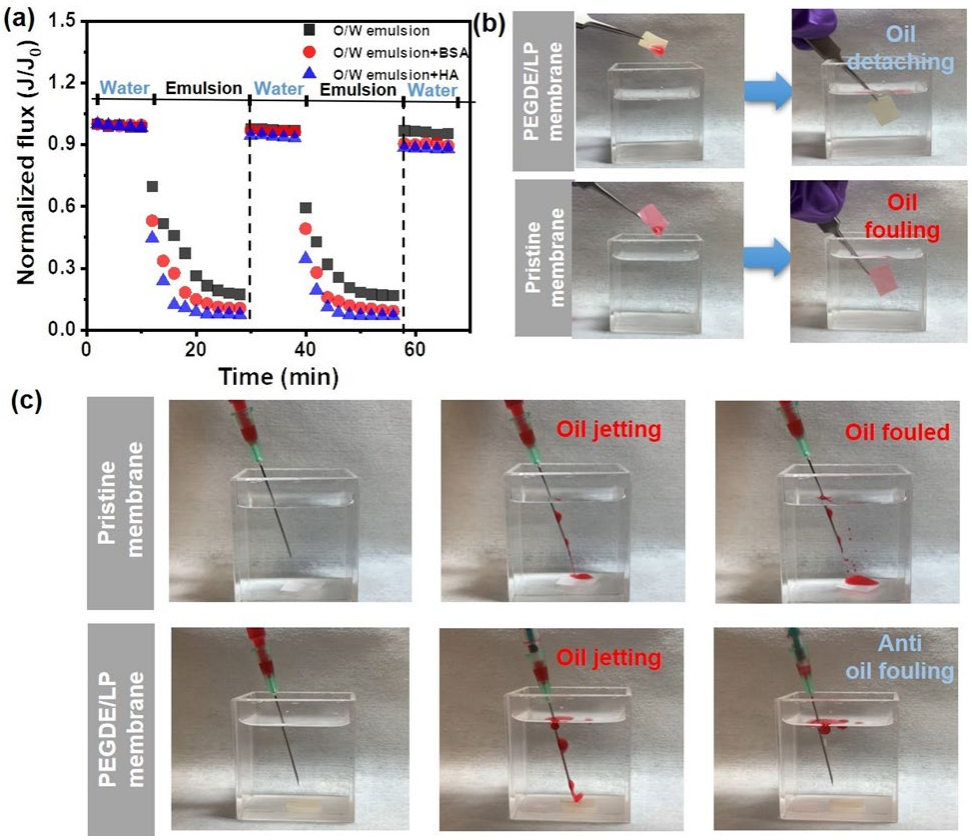

Figure 5.7 (a) The real-time O/W emulsion, O/W emulsion+BSA, and O/W emulsion+HA separation test by using PEGDE/LP-coated membrane; (b) The oil fouling and self-cleaning test of bare PVDF membrane and PEGDE/LP-coated membrane; (c) The underwater oil jetting experiment of bare PVDF membrane and PEGDE/LP-coated membrane.

To further investigate the antifouling property of the as-prepared membrane, as shown in Figure 5.7(b), the membranes were firstly fouled by toluene droplets and then immersed in water, the oil droplets were attached to the bare PVDF membrane even after immersing in water. Notably, the oil droplets onto PEGDE/LP-coated membrane were easily detached from the membrane under underwater conditions, which was attributed to the super-hydrophilic nature of PEGDE/LP coating on the membrane surface. Moreover, the anti-oil fouling property of the PEGDE/LP coated membrane was verified by the underwater oil jetting test shown in Figure 5.7(c): The toluene drops were bounced back from the surface of the PEGDE/LP-coated membrane, while the oil drop

residues were easily attached on the surfaces of bare PVDF membrane, further demonstrating the anti-oil adhesion property of as-prepared membrane.

5.4 Conclusions

This work reports a novel strategy to construct a durable antifouling coating by integrating a bio-inspired bio-glue layer and a covalently anchored hydrophilic PEG layer. The developed PEGDE/LP coating featured a densely packed structure with super-hydrophilic nature (with a WCA~15°) and endowing the PEGDE/LP-coated substrates with superior antifouling properties to resist oily contamination and adhesion of various proteins, such as BSA or HA. Moreover, the as-prepared PEGDE/LP-coated PVDF membrane exhibited outstanding stability and maintained its wettability under acid/alkane/salt treatment due to the covalently crosslinked structure of PEGDE/LP coating. The PEGDE/LP-coated PVDF membrane also showed enhanced water flux (over 3000 L m^{-2} h^{-1} bar^{-1}) and achieved ~ 90% water flux recovery ratio for separation of different kinds of O/W emulsions.

Compared to previously reported membranes for O/W emulsion separation [74-76], the PEGDE/LP-coated membrane developed in this work shows improved antifouling property, enhanced stability in harsh conditions, and outstanding O/W emulsion separation performance. Such a combination of these desirable features into the developed antifouling membrane makes it a promising candidate for the practical O/W emulsion separation.

For the further study, colloidal probe atomic force microscope techniques will be applied to investigated the assembling mechanisms in the PEG coating process and to help develop advance antifouling coatings for various water treatment processes.

Supporting information

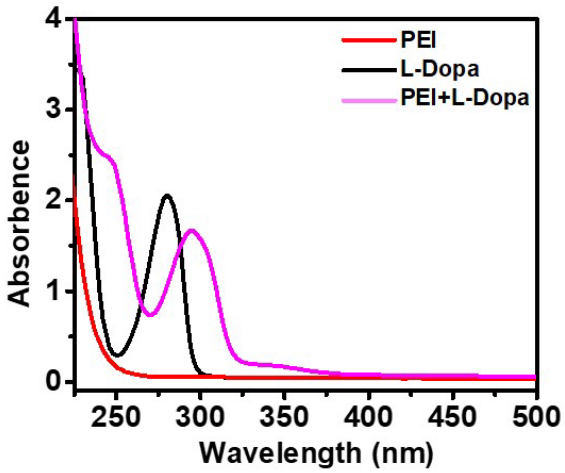

Figure S5.1 The UV-Vis spectrum of PEI, L-Dopa, PEI/L-Dopa solutions

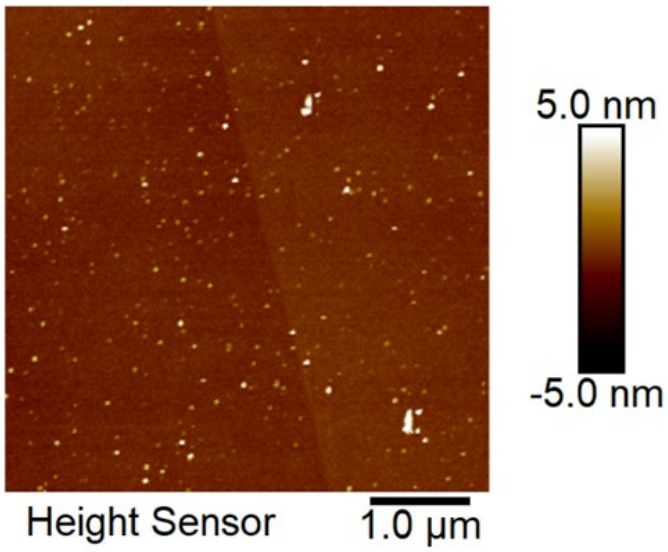

Figure S5.2 The AFM images of L-dopa coating.

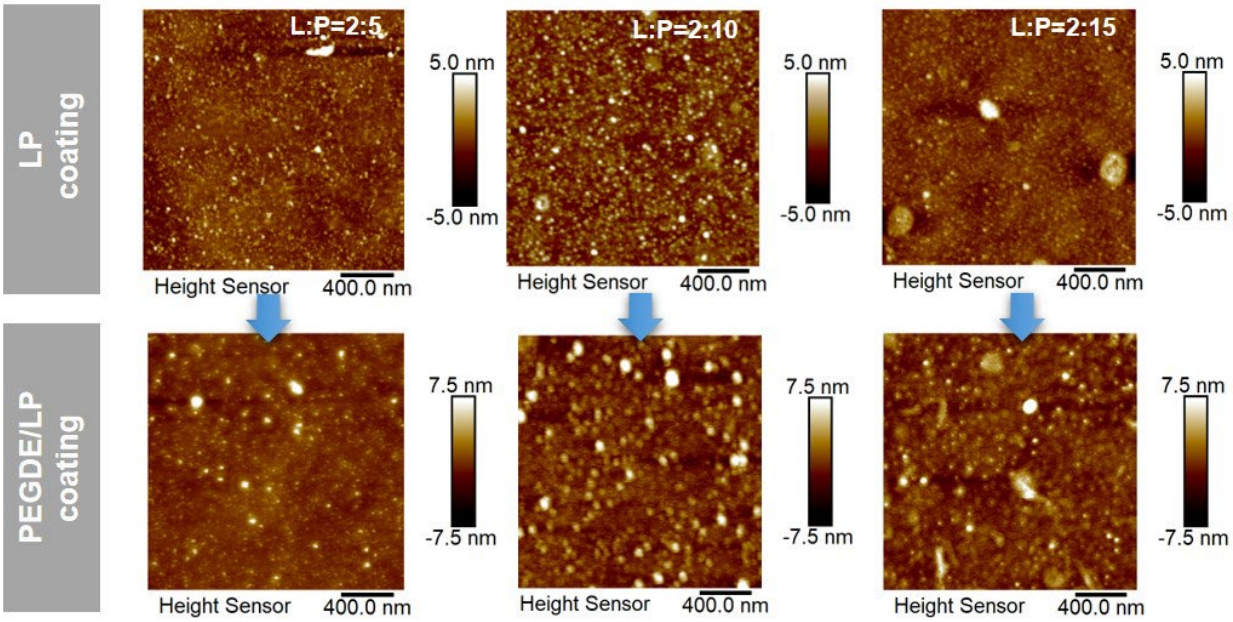

Figure S5.3 The AFM images of LP coating and corresponding PEGDE/LP coating with PEI concentration ranging from 5 mg/mL to 15 mg/mL.

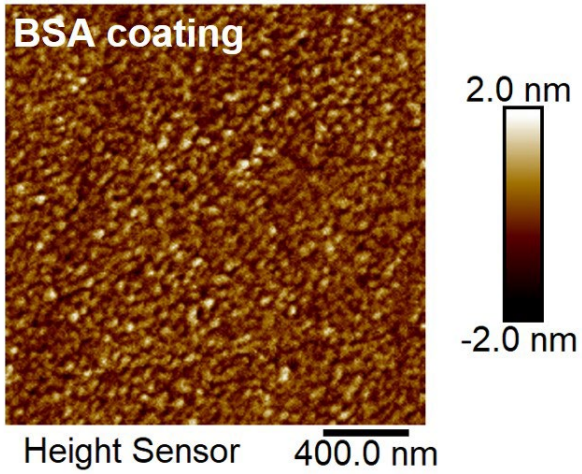

Figure S5.4 The AFM images of BSA coating.

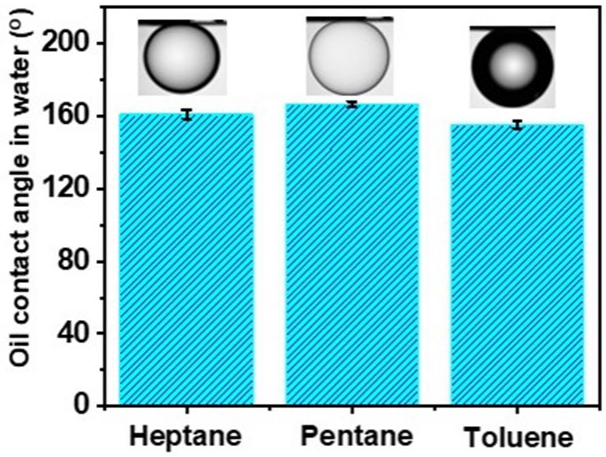

Figure S5.5 The OCA of PEGDE/LP-coated membrane towards different kinds of oil. (Data was reported as means ± SD for n = 3 independent experiments).

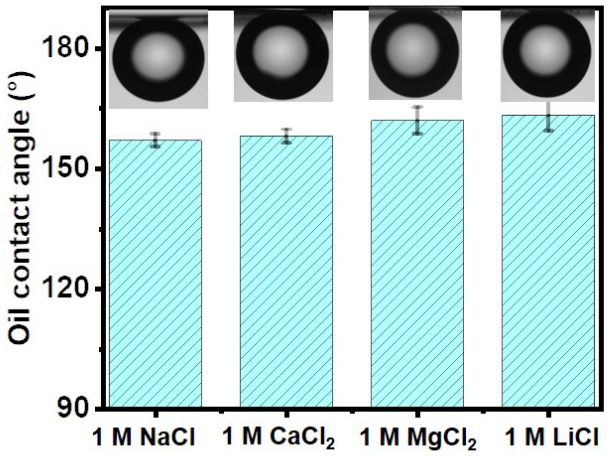

Figure S5.6 The OCA of PEGDE/LP-coated membrane under different salt conditions. (Data was reported as means ± SD for n = 3 independent experiments).

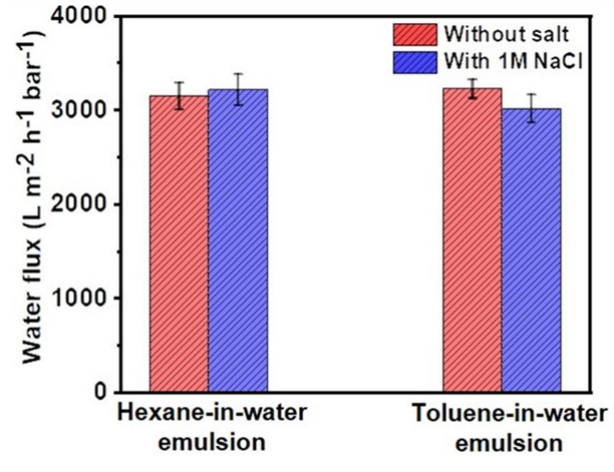

Figure S5.7 Separation performance of PEGDE/LP coated membrane for the O/W emulsions with/without salt (Data was reported as means ± SD for n = 3 independent experiments).

Table S5.1 The summary of O/W separation performance of different anti-oil materials.

Anti-oil material	Substrate	Method	Type of oil	Water flux ($L/m^2/h/bar$)	Ref
SnO_2 coating	PVDF membrane (0.22 um)	Atomic layer deposition	O/W emulsion	~800	70
Cu^{2+}/alginate coating	PAA-g-PVDF (0.065 um)	Layer-by-layer assembly	O/W emulsion	~1300	18
Zwitterionic nanohydrogel	PVDF membrane (0.22 um)	Chemical grafting	O/W emulsion	~1200	11
TA/APTES	PVDF membrane (0.22 um)	Self-assembly	O/W emulsion	~2000	48
TiO_2/PVDF	PVDF membrane (0.22 um)	Co-deposition	O/W emulsion	~700	71
TA/cysteamine coating	PVDF membrane (0.22 um)	Co-deposition	O/W emulsion	~2000	72
PEGDE/LP coating	PVDF membrane (0.22 um)	Layer-by-layer assembly	O/W emulsion	~3000	This work

Reference

(1) Maan, A. M.; Hofman, A. H.; de Vos, W. M.; Kamperman, M. Recent developments and practical feasibility of polymer-based antifouling coatings. *Advanced functional materials* **2020**, *30* (32), 2000936.

(2) Ren, J.; Han, P.; Wei, H.; Jia, L. Fouling-resistant behavior of silver nanoparticle-modified surfaces against the bioadhesion of microalgae. *ACS applied materials & interfaces* **2014**, *6* (6), 3829-3838.

(3) Guo, H.; Liu, X.; Zhao, W.; Xie, C.; Zhu, Y.; Wen, C.; Li, Q.; Sui, X.; Yang, J.; Zhang, L. A polyvinylpyrrolidone-based surface-active copolymer for an effective marine antifouling coating. *Progress in Organic Coatings* **2021**, *150*, 105975.

(4) Mandal, S.; Song, G.; Ackerman, M.; Paskaluk, S.; Gholamreza, F. Characterization of textile fabrics under various thermal exposures. *Textile research journal* **2013**, *83* (10), 1005-1019.

(5) Winkeljann, B.; Bauer, M. G.; Marczynski, M.; Rauh, T.; Sieber, S. A.; Lieleg, O. Covalent Mucin Coatings Form Stable Anti-Biofouling Layers on a Broad Range of Medical Polymer Materials. *Advanced Materials Interfaces* **2020**, *7* (4), 1902069.

(6) Zander, Z. K.; Becker, M. L. Antimicrobial and antifouling strategies for polymeric medical devices. *ACS Macro Lett.* **2018**, *7*(1), 16–25.

(7) Liu, Q.; Singha, P.; Handa, H.; Locklin, J. Covalent grafting of antifouling phosphorylcholine-based copolymers with antimicrobial nitric oxide releasing polymers to enhance infection-resistant properties of medical device coatings. *Langmuir* **2017**, *33* (45), 13105-13113.

(8) Selim, M. S.; El-Safty, S. A.; Shenashen, M. A.; Higazy, S. A.; Elmarakbi, A. Progress in biomimetic leverages for marine antifouling using nanocomposite coatings. *Journal of Materials Chemistry B* **2020**, *8* (17), 3701-3732.

(9) Wang, F.; Zhang, H.; Yu, B.; Wang, S.; Shen, Y.; Cong, H. Review of the research on anti-protein fouling coatings materials. *Progress in Organic Coatings* **2020**, *147*, 105860.

(10) Rana, D.; Matsuura, T. Surface modifications for antifouling membranes. *Chemical reviews* **2010**, *110* (4), 2448-2471.

(11) Zhu, Y.; Wang, J.; Zhang, F.; Gao, S.; Wang, A.; Fang, W.; Jin, J. Zwitterionic nanohydrogel grafted PVDF membranes with comprehensive antifouling property and superior cycle stability for oil-in-water emulsion separation. *Advanced Functional Materials* **2018**, *28* (40), 1804121.

(12) Park, C. H.; Jeon, S.; Park, S.-H.; Shin, M. G.; Park, M. S.; Lee, S.-Y.; Lee, J.-H. Cellulose nanocrystal-assembled reverse osmosis membranes with high rejection performance and excellent antifouling. *Journal of Materials Chemistry A* **2019**, *7* (8), 3992-4001.

(13) Sun, X.; Zeng, H.; Tang, T. Effect of non-ionic surfactants on the adsorption of polycyclic aromatic compounds at water/oil interface: A molecular simulation study. *Journal of Colloid and Interface Science* **2021**, *586*, 766-777.

(14) Li, L.; Guo, Q.; Lv, B.; Zheng, M.; Zhan, W.; Liu, Y.; Xu, W.; Wang, R.; Zeng, H.; Mao, B. Surface modified silver/magnetite nanocomposite activating hydrogen peroxide for efficient degradation of chlorophenols. *Journal of Colloid and Interface Science* **2022**, *617*, 246-256.

(15) Hu, W.; Xie, L.; Zeng, H. Novel sodium alginate-assisted MXene nanosheets for ultrahigh rejection of multiple cations and dyes. *Journal of Colloid and Interface Science* **2020**, *568*, 36-45.

(16) Parashkooh, H. I.; Jian, C. Data Mining Guided Molecular Investigations on the Coalescence of Water-in-Oil Droplets. *Energy & Fuels* **2022**, *36* (4), 1811-1824.

(17) Yang, H.-C.; Liao, K.-J.; Huang, H.; Wu, Q.-Y.; Wan, L.-S.; Xu, Z.-K. Mussel-inspired modification of a polymer membrane for ultra-high water permeability and oil-in-water emulsion separation. *Journal of Materials Chemistry A* **2014**, *2* (26), 10225-10230.

(18) Gao, S.; Zhu, Y.; Wang, J.; Zhang, F.; Li, J.; Jin, J. Layer - by - Layer Construction of Cu2+/Alginate Multilayer Modified Ultrafiltration Membrane with Bioinspired Superwetting Property for High - Efficient Crude - Oil - in - Water Emulsion Separation. *Advanced Functional Materials* **2018**, *28* (49), 1801944.

(19) Zou, D.; Chen, X.; Drioli, E.; Ke, X.; Qiu, M.; Fan, Y. Facile co-sintering process to fabricate sustainable antifouling silver nanoparticles (AgNPs)-enhanced tight ceramic ultrafiltration membranes for protein separation. *Journal of Membrane Science* **2020**, *593*, 117402.

(20) Yang, X.; Sun, H.; Pal, A.; Bai, Y.; Shao, L. Biomimetic silicification on membrane surface for highly efficient treatments of both oil-in-water emulsion and protein wastewater. *ACS applied materials & interfaces* **2018**, *10* (35), 29982-29991.

(21) He, Z.; Miller, D. J.; Kasemset, S.; Wang, L.; Paul, D. R.; Freeman, B. D. Fouling propensity of a poly (vinylidene fluoride) microfiltration membrane to several model oil/water emulsions. *Journal of Membrane Science* **2016**, *514*, 659-670.

(22) Zhao, X.; Zhang, R.; Liu, Y.; He, M.; Su, Y.; Gao, C.; Jiang, Z. Antifouling membrane surface construction: Chemistry plays a critical role. *Journal of Membrane Science* **2018**, *551*, 145-171.

(23) Mauter, M. S.; Wang, Y.; Okemgbo, K. C.; Osuji, C. O.; Giannelis, E. P.; Elimelech, M. Antifouling ultrafiltration membranes via post-fabrication grafting of biocidal nanomaterials. *ACS applied materials & interfaces* **2011**, *3* (8), 2861-2868.

(24) Jian, C.; Liu, Q.; Zeng, H.; Tang, T. A molecular dynamics study of the effect of asphaltenes on toluene/water interfacial tension: surfactant or solute? *Energy & fuels* **2018**, *32* (3), 3225-3231.

(25) Goetz, L. A.; Jalvo, B.; Rosal, R.; Mathew, A. P. Superhydrophilic anti-fouling electrospun cellulose acetate membranes coated with chitin nanocrystals for water filtration. *Journal of Membrane Science* **2016**, *510*, 238-248.

(26) Damodaran, V. B.; Murthy, N. S. Bio-inspired strategies for designing antifouling biomaterials. *Biomaterials research* **2016**, *20* (1), 1-11.

(27) Pan, M.; Gong, L.; Xiang, L.; Yang, W.; Wang, W.; Zhang, L.; Hu, W.; Han, L.; Zeng, H. Modulating surface interactions for regenerable separation of oil-in-water emulsions. *Journal of Membrane Science* **2021**, 119140.

(28) Han, L.; Xiang, L.; Zhang, J.; Chen, J.; Liu, J.; Yan, B.; Zeng, H. Biomimetic lubrication and surface interactions of dopamine-assisted zwitterionic polyelectrolyte coatings. *Langmuir* **2018**, *34* (38), 11593-11601.

(29) Kim, S.; Gim, T.; Jeong, Y.; Ryu, J. H.; Kang, S. M. Facile construction of robust multilayered PEG films on polydopamine-coated solid substrates for marine antifouling applications. *ACS applied materials & interfaces* **2017**, *10* (9), 7626-7631.

(30) Xing, C.-M.; Meng, F.-N.; Quan, M.; Ding, K.; Dang, Y.; Gong, Y.-K. Quantitative fabrication, performance optimization and comparison of PEG and zwitterionic polymer antifouling coatings. *Acta biomaterialia* **2017**, *59*, 129-138.

(31) Xu, Z.; Li, L.; Liu, J.; Dai, C.; Sun, W.; Chen, J.; Zhu, Z.; Zhao, M.; Zeng, H. Mussel-inspired superhydrophilic membrane constructed on a hydrophilic polymer network for highly efficient oil/water separation. *Journal of Colloid and Interface Science* **2022**, *608*, 702-710.

(32) Zhao, M.; Yang, Y.; Yu, H.; Zhang, X.; Tian, X.; Fu, S.; Zhang, H. Improving the biofouling resistance of polyamide thin-film composite membrane via grafting polyacrylamide brush on the surface by in-situ atomic transfer radical polymerization. *Journal of Membrane Science* **2021**, *629*, 119283.

(33) Shin, E.; Lim, C.; Kang, U. J.; Kim, M.; Park, J.; Kim, D.; Choi, W.; Hong, J.; Baig, C.; Lee, D. W. Mussel-inspired copolyether loop with superior antifouling behavior. *Macromolecules* **2020**, *53* (9), 3551-3562.

(34) Zhai, Y.; Chen, X.; Yuan, Z.; Han, X.; Liu, H. A mussel-inspired catecholic ABA triblock copolymer exhibits better antifouling properties compared to a diblock copolymer. *Polymer Chemistry* **2020**, *11* (28), 4622-4629.

(35) Shui, T.; Pan, M.; Lu, Y.; Zhang, J.; Liu, Q.; Nikrityuk, P. A.; Tang, T.; Liu, Q.; Zeng, H. High-efficiency and durable removal of water-in-heavy oil emulsions enabled by delignified and carboxylated basswood with zwitterionic nanohydrogel coatings. *Journal of Colloid and Interface Science* **2022**, *612*, 445-458.

(36) Kang, T.; Banquy, X.; Heo, J.; Lim, C.; Lynd, N. A.; Lundberg, P.; Oh, D. X.; Lee, H.-K.; Hong, Y.-K.; Hwang, D. S. Mussel-inspired anchoring of polymer loops that provide superior surface lubrication and antifouling properties. *Acs Nano* **2016**, *10* (1), 930-937.

(37) Tian, S.; Jiang, D.; Pu, J.; Sun, X.; Li, Z.; Wu, B.; Zheng, W.; Liu, W.; Liu, Z. A new hybrid silicone-based antifouling coating with nanocomposite hydrogel for durable antifouling properties. *Chemical Engineering Journal* **2019**, *370*, 1-9.

(38) Zhang, C.; Xiang, L.; Zhang, J.; Gong, L.; Han, L.; Xu, Z.-K.; Zeng, H. Tough and alkaline-resistant mussel-inspired wet adhesion with surface salt displacement via polydopamine/amine synergy. *Langmuir* **2019**, *35* (15), 5257-5263.

(39) Zeng, H.; Hwang, D. S.; Israelachvili, J. N.; Waite, J. H. Strong reversible Fe3+-mediated bridging between dopa-containing protein films in water. *Proceedings of the National Academy of Sciences* **2010**, *107* (29), 12850-12853.

(40) Lu, Q.; Danner, E.; Waite, J. H.; Israelachvili, J. N.; Zeng, H.; Hwang, D. S. Adhesion of mussel foot proteins to different substrate surfaces. *Journal of The Royal Society Interface* **2013**, *10* (79), 20120759.

(41) Zhang, X.; Chen, J.; He, J.; Bai, Y.; Zeng, H. Mussel-inspired adhesive and conductive hydrogel with tunable mechanical properties for wearable strain sensors. *Journal of Colloid and Interface Science* **2021**, *585*, 420-432.

(42) Li, L.; Yan, B.; Yang, J.; Chen, L.; Zeng, H. Novel mussel-inspired injectable self-healing hydrogel with anti-biofouling property. *Advanced Materials* **2015**, *27* (7), 1294-1299.

(43) Yang, B.; Ayyadurai, N.; Yun, H.; Choi, Y. S.; Hwang, B. H.; Huang, J.; Lu, Q.; Zeng, H.; Cha, H. J. In vivo residue-specific dopa-incorporated engineered mussel bioglue with enhanced adhesion and water resistance. *Angewandte Chemie* **2014**, *126* (49), 13578-13582.

(44) Islam, M. S.; Akter, N.; Rahman, M. M.; Shi, C.; Islam, M. T.; Zeng, H.; Azam, M. S. Mussel-inspired immobilization of silver nanoparticles toward antimicrobial cellulose paper. *ACS Sustainable Chemistry & Engineering* **2018**, *6* (7), 9178-9188.

(45) Zhang, H.; Yu, L.; Ma, X.; Peng, Y.; Hu, J.; Ruan, S. Self-cleaning poly (L-dopa)-based coatings with exceptional underwater oil repellency for crude oil/water separation. *Applied Surface Science* **2020**, *510*, 145402.

(46) Huang, Q.; Liu, M.; Guo, R.; Mao, L.; Wan, Q.; Zeng, G.; Huang, H.; Deng, F.; Zhang, X.; Wei, Y. Facile synthesis and characterization of poly (levodopa)-modified silica nanocomposites via self-polymerization of levodopa and their adsorption behavior toward Cu 2+. *Journal of Materials Science* **2016**, *51* (21), 9625-9637.

(47) Yang, S.-J.; Zou, L.-Y.; Liu, C.; Zhong, Q.; Ma, Z.-Y.; Yang, J.; Ji, J.; Müller-Buschbaum, P.; Xu, Z.-K. Codeposition of Levodopa and Polyethyleneimine: Reaction Mechanism and Coating Construction. *ACS Applied Materials & Interfaces* **2020**, *12* (48), 54094-54103.

(48) Wang, Z.; Han, M.; Zhang, J.; He, F.; Peng, S.; Li, Y. Investigating and significantly improving the stability of tannic acid (TA)-aminopropyltriethoxysilane (APTES) coating for enhanced oil-water separation. *Journal of Membrane Science* **2020**, *593*, 117383.

(49) Xiang, L.; Zhang, J.; Gong, L.; Han, L.; Zhang, C.; Yan, B.; Liu, J.; Zeng, H. Probing the interaction forces of phenol/amine deposition in wet adhesion: impact of phenol/amine mass ratio and surface properties. *Langmuir* **2019**, *35* (48), 15639-15650.

(50) Sun, Z. K.; Zhou, Y.; Jiao, Y.; Cheng, X. Q.; Zhang, Y.; Wang, P.; Liang, H.; Yang, X.; Drioli, E.; Figoli, A. Multi-hydrophilic functional network enables porous membranes excellent anti-fouling performance for highly efficient water remediation. *Journal of Membrane Science* **2020**, *608*, 118191.

(51) Tong, W.; Zhang, Y.; Zhang, Q.; Luan, X.; Duan, Y.; Pan, S.; Lv, F.; An, Q. Achieving significantly enhanced dielectric performance of reduced graphene oxide/polymer composite by covalent modification of graphene oxide surface. *Carbon* **2015**, *94*, 590-598.

(52) Liu, J.; Cui, X.; Huang, J.; Xie, L.; Tan, X.; Liu, Q.; Zeng, H. Understanding the stabilization mechanism of bitumen-coated fine solids in organic media from non-aqueous extraction of oil sands. *Fuel* **2019**, *242*, 255-264.

(53) Lim, C.; Huang, J.; Kim, S.; Lee, H.; Zeng, H.; Hwang, D. S. Nanomechanics of poly (catecholamine) coatings in aqueous solutions. *Angewandte Chemie International Edition* **2016**, *55* (10), 3342-3346.

(54) Israelachvili, J.; Min, Y.; Akbulut, M.; Alig, A.; Carver, G.; Greene, W.; Kristiansen, K.; Meyer, E.; Pesika, N.; Rosenberg, K. Recent advances in the surface forces apparatus (SFA) technique. *Reports on Progress in Physics* **2010**, *73* (3), 036601.

(55) Zhang, L.; Lin, Y.; Wu, H.; Cheng, L.; Sun, Y.; Yasui, T.; Yang, Z.; Wang, S.; Yoshioka, T.; Matsuyama, H. An ultrathin in situ silicification layer developed by an electrostatic attraction force strategy for ultrahigh-performance oil–water emulsion separation. *Journal of Materials Chemistry A* **2019**, *7* (42), 24569-24582.

(56) Lv, Y.; Yang, S.-J.; Du, Y.; Yang, H.-C.; Xu, Z.-K. Co-deposition kinetics of polydopamine/polyethyleneimine coatings: effects of solution composition and substrate surface. *Langmuir* **2018**, *34* (44), 13123-13131.

(57) Tang, C.; Brodie, P.; Li, Y.; Grishkewich, N. J.; Brunsting, M.; Tam, K. C. Shape recoverable and mechanically robust cellulose aerogel beads for efficient removal of copper ions. *Chemical Engineering Journal* **2020**, *392*, 124821.

(58) Lau, S. K.; Yong, W. F. Recent Progress of Zwitterionic Materials as Antifouling Membranes for Ultrafiltration, Nanofiltration, and Reverse Osmosis. *ACS Applied Polymer Materials* **2021**, *3* (9), 4390-4412.

(59) Li, L.; Yan, B.; Zhang, L.; Tian, Y.; Zeng, H. Mussel-inspired antifouling coatings bearing polymer loops. *Chemical Communications* **2015**, *51* (87), 15780-15783.

(60) Wang, Z.; Han, M.; Zhang, J.; He, F.; Xu, Z.; Ji, S.; Peng, S.; Li, Y. Designing preferable functional materials based on the secondary reactions of the hierarchical tannic acid (TA)-aminopropyltriethoxysilane (APTES) coating. *Chemical Engineering Journal* **2019**, *360*, 299-312.

(61) Yang, W.; Hu, W.; Zhang, J.; Wang, W.; Cai, R.; Pan, M.; Huang, C.; Chen, X.; Yan, B.; Zeng, H. Tannic acid/Fe3+ functionalized magnetic graphene oxide nanocomposite with high

loading of silver nanoparticles as ultra-efficient catalyst and disinfectant for wastewater treatment. *Chemical Engineering Journal* **2020**, 126629.

(62) Huang, X.; Lu, J.; Wang, W.; Wei, X.; Ding, J. Experimental and computational investigation of CO2 capture on amine grafted metal-organic framework NH2-MIL-101. *Applied Surface Science* **2016**, *371*, 307-313.

(63) Yang, W. J.; Cai, T.; Neoh, K.-G.; Kang, E.-T.; Teo, S. L.-M.; Rittschof, D. Barnacle cement as surface anchor for "clicking" of antifouling and antimicrobial polymer brushes on stainless steel. *Biomacromolecules* **2013**, *14* (6), 2041-2051.

(64) Qiao, C.; Wang, D.; Zhao, Z.; Yang, W.; Wu, F.; Chen, H.; Yin, T.; Zhang, L.; Liu, Q.; Yang, D. Bench-scale oil fouling/antifouling tests under high temperature and high pressure conditions and the underlying interfacial interaction mechanisms. *Fuel* **2022**, *314*, 122720.

(65) Zang, L.; Zheng, S.; Wang, L.; Ma, J.; Sun, L. Zwitterionic nanogels modified nanofibrous membrane for efficient oil/water separation. *Journal of Membrane Science* **2020**, *612*, 118379.

(66) Zhang, Y.; Ma, J.; Shao, L. Ultra-thin trinity coating enabled by competitive reactions for unparalleled molecular separation. *Journal of Materials Chemistry A* **2020**, *8* (10), 5078-5085.

(67) Shao, L.; Wang, Z. X.; Zhang, Y. L.; Jiang, Z. X.; Liu, Y. Y. A facile strategy to enhance PVDF ultrafiltration membrane performance via self-polymerized polydopamine followed by hydrolysis of ammonium fluotitanate. *Journal of Membrane Science* **2014**, *461*, 10-21.

(68) Wang, Z.; Ji, S.; He, F.; Cao, M.; Peng, S.; Li, Y. One-step transformation of highly hydrophobic membranes into superhydrophilic and underwater superoleophobic ones for high-efficiency separation of oil-in-water emulsions. *Journal of Materials Chemistry A* **2018**, *6* (8), 3391-3396.

(69) Xiong, Z.; Lin, H.; Zhong, Y.; Qin, Y.; Li, T.; Liu, F. Robust superhydrophilic polylactide (PLA) membranes with a TiO 2 nano-particle inlaid surface for oil/water separation. *Journal of Materials Chemistry A* **2017**, *5* (14), 6538-6545.

(70) Yang, H.-C.; Xie, Y.; Chan, H.; Narayanan, B.; Chen, L.; Waldman, R. Z.; Sankaranarayanan, S. K.; Elam, J. W.; Darling, S. B. Crude-oil-repellent membranes by atomic layer deposition: oxide interface engineering. *ACS nano* **2018**, *12* (8), 8678-8685.

(71) Shi, H.; He, Y.; Pan, Y.; Di, H.; Zeng, G.; Zhang, L.; Zhang, C. A modified mussel-inspired method to fabricate TiO2 decorated superhydrophilic PVDF membrane for oil/water separation. *Journal of membrane science* **2016**, *506*, 60-70.

(72) Yang, X.; Yan, L.; Ma, J.; Bai, Y.; Shao, L. Bioadhesion-inspired surface engineering constructing robust, hydrophilic membranes for highly-efficient wastewater remediation. *Journal of Membrane Science* **2019**, *591*, 117353.

Chapter 6. Conclusions and Future work

6.1 Original contributions and major Conclusions

The original contribution of this thesis can be summarized in the following two parts. In terms of fundamental knowledge, the molecular interaction mechanism in the mussel-inspired coating assembly process was investigated and the roles of different components in the mussel-inspired coating system were analyzed. This fundamental study will provide new insight into designing mussel-inspired coatings with desirable structure and functionality. In terms of practical application, three functional mussel-inspired coating materials were successfully designed to efficiently remove the organic pollutants and oily contaminants from water. For instance, the as-prepared nano catalyst showed a high catalytic rate towards organic dyes, which was about ten times faster than most reported catalysts. Moreover, the developed CNCs and PEGDE-coated membrane showed outstanding antifouling performances and enhanced water flux in the O/W emulsion separation process, demonstrating their great potential in oily wastewater purification.

The major conclusions are summarized below:

(1) A nano-catalyst with ultrahigh catalytic performance towards organic pollutants has been developed by anchoring abundant Ag NPs onto MGO substrate with the assistance of TA/Fe^{3+} coating by virtue of its strong metal coordination and reduction ability. The high load amount of Ag NPs and the synergetic dye adsorption effect of TA/Fe^{3+} coating contributes to the outstanding catalytic performance of Ag@MGO-TA/Fe^{3+} catalyst towards different kinds of organic dyes and nitrophenols. Moreover, the fabricated nanocomposite can be easily separated from the water phase and recycled due to its intrinsic magnetic property. The Ag NPs also endow the as-prepared nanocomposites with excellent antibacterial properties. Overall, this work provides useful

implications for the development of advanced multifunctional nanocomposites for various environmental applications.

(2) An antifouling CNCs coating has been developed by tightly anchoring CNCs onto the substrates with the assistance of TA/PEI/V intermediate adhesive layer, which provides abundant functional groups as the anchoring points to tightly link the CNCs onto substrates. The structure of CNCs coating can be well modulated by changing the V^{3+} ions concentration in the coating assembly process. The as-prepared CNCs coating shows excellent antifouling properties to prevent oil adhesion, protein adsorption, as well as cell attachment due to its super-hydrophilic nature. The developed CNCs coating can maintain its structural integrity after the cyclic friction test because of the rigid structure of CNC. Moreover, the CNCs-coated PVDF membrane shows outstanding separation performance and anti-oil fouling property in the O/W emulsion separation process. Thus, this work provides new insight into the precise designing of functional surface coating with tunable properties for a broad range of engineering and environmental applications.

(3) A durable antifouling coating has been developed by covalently anchoring the PEGDE polymer onto LP bio-glue layer via a ring-opening reaction. The as-prepared PEGDE/LP coating shows outstanding stability and can maintain its wettability after acid/alkaline/salt treatments. The super-hydrophilic nature of PEGDE polymer endows the as-prepared PEGDE/LP coating with excellent antifouling properties to effectively prevent the adhesion of various proteins onto its surface, which was mainly attributed to the strong surface hydration and steric repulsion of dense-packed PEGDE polymer on the substrate. Moreover, the fabricated PEGDE/LP-coated membrane can effectively separate O/W emulsion and prevent oil or protein adhesion on its surface in the O/W separation process. Overall, this developed PEGDE/LP coating strategy can be applied to

construct a durable antifouling coating onto various substrates applied in practical wastewater treatment processes.

6.2 Future work

(1) Although impressive progress has been achieved in the fabrication of NPs-based catalysts for organic pollutant removal, most NPs are still costly due to their complex synthesis process. The development of a new high-efficient and cost-effective nanocomposite catalyst can be explored with the assistance of a mussel-inspired coating strategy.

(2) For the CNCs antifouling coating, the durability of CNCs coating can be further improved by integrating self-healing properties into the fabricated coating. Such a self-healing property can be achieved by incorporating CNCs into a hydrogel network. The self-healing CNCs hydrogel coating can be fabricated onto the substrate with the assistance of an intermediate adhesive layer.

(3) The PEG coating holds great potential to be upgraded into a multifunctional coating for wastewater treatment. In future work, the PEG polymer will be further functionalized by incorporating functional monomers, such as amine-rich monomers, into the PEG polymer chain to endow the antibacterial property to the fabricated PEG coating.

Bibliography

(1) El Nemr, A.; Khaled, A.; Abdelwahab, O.; El-Sikaily, A. Treatment of wastewater containing toxic chromium using new activated carbon developed from date palm seed. *Journal of Hazardous Materials* **2008**, *152* (1), 263-275.

(2) Wacławek, S.; Lutze, H. V.; Grübel, K.; Padil, V. V.; Černík, M.; Dionysiou, D. D. Chemistry of persulfates in water and wastewater treatment: a review. *Chemical Engineering Journal* **2017**, *330*, 44-62.

(3) Biswas, A. K.; Tortajada, C. Water crisis and water wars: myths and realities. Taylor & Francis: **2019**; 35, 727-731.

(4) Simonovic, S. P. World water dynamics: global modeling of water resources. *Journal of Environmental Management* **2002**, *66* (3), 249-267.

(5) Santos, J. O.; Andrade, J. C. S.; Marinho, M. M. d. O.; Noyola, A.; Güereca, L. P. Greenhouse gas inventory of a state water and wastewater utility in Northeast Brazil. *Journal of Cleaner Production* **2015**, *104*, 168-176.

(6) Zhuang, S.; Qi, H.; Wang, X.; Li, X.; Liu, K.; Liu, J.; Zhang, H. Advances in Solar‐Driven Hygroscopic Water Harvesting. *Global Challenges* **2021**, *5* (1), 2000085.

(7) Song, Z.; Williams, C.; Edyvean, R. Sedimentation of tannery wastewater. *Water Research* **2000**, *34* (7), 2171-2176.

(8) Jury, W. A.; Vaux Jr, H. J. The emerging global water crisis: managing scarcity and conflict between water users. *Advances in agronomy* **2007**, *95*, 1-76.

(9) Qin, B.; Zhu, G.; Gao, G.; Zhang, Y.; Li, W.; Paerl, H. W.; Carmichael, W. W. A drinking water crisis in Lake Taihu, China: linkage to climatic variability and lake management. *Environmental management* **2010**, *45* (1), 105-112.

(10) Rashed, M. N. Adsorption technique for the removal of organic pollutants from water and wastewater. *Organic pollutants-monitoring, risk and treatment* **2013**, *7*, 167-194.

(11) Aleksić, M.; Kušić, H.; Koprivanac, N.; Leszczynska, D.; Božić, A. L. Heterogeneous Fenton type processes for the degradation of organic dye pollutant in water—The application of zeolite assisted AOPs. *Desalination* **2010**, *257* (1-3), 22-29.

(12) Mani, S.; Chowdhary, P.; Bharagava, R. N. Textile wastewater dyes: toxicity profile and treatment approaches. In *Emerging and eco-friendly approaches for waste management*, Springer, **2019**; pp 219-244.

(13) Saravanan, A.; Kumar, P. S.; Jeevanantham, S.; Karishma, S.; Tajsabreen, B.; Yaashikaa, P.; Reshma, B. Effective water/wastewater treatment methodologies for toxic pollutants removal: Processes and applications towards sustainable development. *Chemosphere* **2021**, *280*, 130595.

(14) Tkaczyk, A.; Mitrowska, K.; Posyniak, A. Synthetic organic dyes as contaminants of the aquatic environment and their implications for ecosystems: A review. *Science of the total environment* **2020**, *717*, 137222.

(15) Shafqat, M.; Khalid, A.; Mahmood, T.; Siddique, M. T.; Han, J. I.; Habteselassie, M. Y. Evaluation of bacteria isolated from textile wastewater and rhizosphere to simultaneously degrade azo dyes and promote plant growth. *Journal of Chemical Technology & Biotechnology* **2017**, *92* (10), 2760-2768.

(16) Islam, M. A.; Ali, I.; Karim, S. A.; Firoz, M. S. H.; Chowdhury, A.-N.; Morton, D. W.; Angove, M. J. Removal of dye from polluted water using novel nano manganese oxide-based materials. *Journal of Water Process Engineering* **2019**, *32*, 100911.

(17) Zhao, R.; Li, Y.; Sun, B.; Chao, S.; Li, X.; Wang, C.; Zhu, G. Highly flexible magnesium silicate nanofibrous membranes for effective removal of methylene blue from aqueous solution. *Chemical Engineering Journal* **2019**, *359*, 1603-1616.

(18) Dong, X.; Liu, H.; Chen, Z.; Wu, K.; Lu, N.; Zhang, Q. Enhanced oil recovery techniques for heavy oil and oilsands reservoirs after steam injection. *Applied energy* **2019**, *239*, 1190-1211.

(19) Wang, J.; He, J.; Ma, L.; Zhang, Y.; Zhao, Y.; Zhou, Y.; Li, K.; Qu, M. Buoyant and durable oil/water separation mesh for continuous and efficient collection of both oil slick and underwater oil leakage. *Separation and Purification Technology* **2019**, *229*, 115795.

(20) Chen, J.; Zhang, W.; Wan, Z.; Li, S.; Huang, T.; Fei, Y. Oil spills from global tankers: Status review and future governance. *Journal of cleaner production* **2019**, *227*, 20-32.

(21) Yong, J.; Huo, J.; Chen, F.; Yang, Q.; Hou, X. Oil/water separation based on natural materials with super-wettability: recent advances. *Physical Chemistry Chemical Physics* **2018**, *20* (39), 25140-25163.

(22) Liu, S.; Zhang, Q.; Fan, L.; Wang, R.; Yang, M.; Zhou, Y. 3D superhydrophobic sponge coated with magnesium hydroxide for effective oil/water mixture and emulsion separation. *Industrial & Engineering Chemistry Research* **2020**, *59* (25), 11713-11722.

(23) Wang, X.; Li, M.; Shen, Y.; Yang, Y.; Feng, H.; Li, J. Facile preparation of loess-coated membranes for multifunctional surfactant-stabilized oil-in-water emulsion separation. *Green Chemistry* **2019**, *21* (11), 3190-3199.

(24) Zhang, J.; Zeng, H. Intermolecular and Surface Interactions in Engineering Processes. *Engineering* **2021**, *7* (1), 63-83.

(25) Sutrisna, P. D.; Kurnia, K. A.; Siagian, U. W.; Ismadji, S.; Wenten, I. G. Membrane fouling and fouling mitigation in oil–water separation: A review. *Journal of Environmental Chemical Engineering* **2022**, 107532.

(26) Pang, Y. L.; Abdullah, A. Z. Current status of textile industry wastewater management and research progress in Malaysia: a review. *Clean–Soil, Air, Water* **2013**, *41* (8), 751-764.

(27) Dave, S. R.; Patel, T. L.; Tipre, D. R. Bacterial degradation of azo dye containing wastes. In *Microbial degradation of synthetic dyes in wastewaters*, Springer, **2015**; 57-83.

(28) Liu, Q. Pollution and Treatment of Dye Waste-Water. In *IOP Conference Series: Earth and Environmental Science*, **2020**; 514, 052001.

(29) Weldegebrieal, G. K. Synthesis method, antibacterial and photocatalytic activity of ZnO nanoparticles for azo dyes in wastewater treatment: A review. *Inorganic Chemistry Communications* **2020**, *120*, 108140.

(30) Khan, F. S. A.; Mubarak, N. M.; Tan, Y. H.; Khalid, M.; Karri, R. R.; Walvekar, R.; Abdullah, E. C.; Nizamuddin, S.; Mazari, S. A. A comprehensive review on magnetic carbon nanotubes and carbon nanotube-based buckypaper for removal of heavy metals and dyes. *Journal of Hazardous Materials* **2021**, *413*, 125375.

(31) Larous, S.; Meniai, A.-H. Elimination of organic pollutants from wastewater. Application to p-nitrophenol. *Desalination and Water Treatment* **2013**, *51* (25-27), 5014-5020.

(32) Deka, P.; Bhattacharjee, D.; Sarmah, P.; Deka, R. C.; Bharali, P. Catalytic reduction of water contaminant ‘4-nitrophenol’over manganese oxide supported Ni nanoparticles. *Trends in Asian water environmental science and technology* **2017**, 35-48.

(33) Bhatti, Z. I.; Toda, H.; Furukawa, K. p-Nitrophenol degradation by activated sludge attached on nonwovens. *Water Research* **2002**, *36* (5), 1135-1142.

(34) Katheresan, V.; Kansedo, J.; Lau, S. Y. Efficiency of various recent wastewater dye removal methods: A review. *Journal of environmental chemical engineering* **2018**, *6* (4), 4676-4697.

(35) Fan, J.; Shi, Z.; Lian, M.; Li, H.; Yin, J. Mechanically strong graphene oxide/sodium alginate/polyacrylamide nanocomposite hydrogel with improved dye adsorption capacity. *Journal of Materials Chemistry A* **2013**, *1* (25), 7433-7443.

(36) Liu, H.; Zhang, J.; Lu, M.; Liang, L.; Zhang, H.; Wei, J. Biosynthesis based membrane filtration coupled with iron nanoparticles reduction process in removal of dyes. *Chemical Engineering Journal* **2020**, *387*, 124202.

(37) Nataraj, S.; Hosamani, K.; Aminabhavi, T. Nanofiltration and reverse osmosis thin film composite membrane module for the removal of dye and salts from the simulated mixtures. *Desalination* **2009**, *249* (1), 12-17.

(38) Verma, A. K.; Dash, R. R.; Bhunia, P. A review on chemical coagulation/flocculation technologies for removal of colour from textile wastewaters. *Journal of environmental management* **2012**, *93* (1), 154-168.

(39) Guo, J.; Yang, Q.; Meng, Q.-W.; Lau, C. H.; Ge, Q. Membrane surface functionalization with imidazole derivatives to benefit dye removal and fouling resistance in forward osmosis. *ACS Applied Materials & Interfaces* **2021**, *13* (5), 6710-6719.

(40) Bhatia, D.; Sharma, N. R.; Singh, J.; Kanwar, R. S. Biological methods for textile dye removal from wastewater: A review. *Critical Reviews in Environmental Science and Technology* **2017**, *47* (19), 1836-1876.

(41) Jadhav, J.; Kalyani, D.; Telke, A.; Phugare, S.; Govindwar, S. Evaluation of the efficacy of a bacterial consortium for the removal of color, reduction of heavy metals, and toxicity from textile dye effluent. *Bioresource Technology* **2010**, *101* (1), 165-173.

(42) Couto, S. R. Dye removal by immobilised fungi. *Biotechnology advances* **2009**, *27* (3), 227-235.

(43) Kanagaraj, J.; Senthilvelan, T.; Panda, R. Degradation of azo dyes by laccase: biological method to reduce pollution load in dye wastewater. *Clean Technologies and Environmental Policy* **2015**, *17* (6), 1443-1456.

(44) Banerjee, P.; DasGupta, S.; De, S. Removal of dye from aqueous solution using a combination of advanced oxidation process and nanofiltration. *Journal of hazardous materials* **2007**, *140* (1-2), 95-103.

(45) Emami, Z.; Azizian, S. Preparation of activated carbon from date sphate using microwave irradiation and investigation of its capability for removal of dye pollutant from aqueous media. *Journal of Analytical and Applied Pyrolysis* **2014**, *108*, 176-184.

(46) García-Montaño, J.; Ruiz, N.; Munoz, I.; Domenech, X.; García-Hortal, J. A.; Torrades, F.; Peral, J. Environmental assessment of different photo-Fenton approaches for commercial reactive dye removal. *Journal of hazardous materials* **2006**, *138* (2), 218-225.

(47) Naseem, K.; Farooqi, Z. H.; Begum, R.; Irfan, A. Removal of Congo red dye from aqueous medium by its catalytic reduction using sodium borohydride in the presence of various inorganic nano-catalysts: a review. *Journal of cleaner production* **2018**, *187*, 296-307.

(48) Pinto, I. S.; Pacheco, P. H.; Coelho, J. V.; Lorençon, E.; Ardisson, J. D.; Fabris, J. D.; de Souza, P. P.; Krambrock, K. W.; Oliveira, L. C.; Pereira, M. C. Nanostructured δ-FeOOH: an efficient Fenton-like catalyst for the oxidation of organics in water. *Applied Catalysis B: Environmental* **2012**, *119*, 175-182.

(49) Zhang, C.; Yang, H.-C.; Wan, L.-S.; Liang, H.-Q.; Li, H.; Xu, Z.-K. Polydopamine-coated porous substrates as a platform for mineralized β-FeOOH nanorods with photocatalysis under sunlight. *ACS Applied Materials & Interfaces* **2015**, *7* (21), 11567-11574.

(50) Albukhari, S. M.; Ismail, M.; Akhtar, K.; Danish, E. Y. Catalytic reduction of nitrophenols and dyes using silver nanoparticles@ cellulose polymer paper for the resolution of waste water treatment challenges. *Colloids and Surfaces A: Physicochemical and Engineering Aspects* **2019**, *577*, 548-561.

(51) Azad, U. P.; Ganesan, V.; Pal, M. Catalytic reduction of organic dyes at gold nanoparticles impregnated silica materials: influence of functional groups and surfactants. *Journal of Nanoparticle Research* **2011**, *13* (9), 3951-3959.

(52) Dao, V.-D.; Tran, C. Q.; Ko, S.-H.; Choi, H.-S. Dry plasma reduction to synthesize supported platinum nanoparticles for flexible dye-sensitized solar cells. *Journal of Materials Chemistry A* **2013**, *1* (14), 4436-4443.

(53) Cui, K.; Yan, B.; Xie, Y.; Qian, H.; Wang, X.; Huang, Q.; He, Y.; Jin, S.; Zeng, H. Regenerable urchin-like Fe3O4@ PDA-Ag hollow microspheres as catalyst and adsorbent for enhanced removal of organic dyes. *Journal of hazardous materials* **2018**, *350*, 66-75.

(54) Xie, Y.; Yan, B.; Xu, H.; Chen, J.; Liu, Q.; Deng, Y.; Zeng, H. Highly regenerable mussel-inspired Fe3O4@ polydopamine-Ag core–shell microspheres as catalyst and adsorbent for methylene blue removal. *ACS applied materials & interfaces* **2014**, *6* (11), 8845-8852.

(55) Du, S.; Liao, Z.; Qin, Z.; Zuo, F.; Li, X. Polydopamine microparticles as redox mediators for catalytic reduction of methylene blue and rhodamine B. *Catalysis Communications* **2015**, *72*, 86-90.

(56) Ji, Z.; Shen, X.; Yue, X.; Zhou, H.; Yang, J.; Wang, Y.; Ma, L.; Chen, K. Facile synthesis of magnetically separable reduced graphene oxide/magnetite/silver nanocomposites with enhanced catalytic activity. *Journal of colloid and interface science* **2015**, *459*, 79-85.

(57) Mao, H.; Ji, C.; Liu, M.; Cao, Z.; Sun, D.; Xing, Z.; Chen, X.; Zhang, Y.; Song, X.-M. Enhanced catalytic activity of Ag nanoparticles supported on polyacrylamide/polypyrrole/graphene oxide nanosheets for the reduction of 4-nitrophenol. *Applied Surface Science* **2018**, *434*, 522-533.

(58) Yang, Y.; Ji, H.; Duan, H.; Fu, Y.; Xia, S.; Lü, C. Controllable synthesis of mussel-inspired catechol-formaldehyde resin microspheres and their silver-based nanohybrids for catalytic and antibacterial applications. *Polymer Chemistry* **2019**, *10* (33), 4537-4550.

(59) Islam, M. R.; Ferdous, M.; Sujan, M. I.; Mao, X.; Zeng, H.; Azam, M. S. Recyclable Ag-decorated highly carbonaceous magnetic nanocomposites for the removal of organic pollutants. *Journal of Colloid and Interface Science* **2020**, *562*, 52-62.

(60) Lu, J.; Fang, J.; Li, J.; Wang, C.; He, Z.; Zhu, L.-P.; Xu, Z.-K.; Zeng, H. Polydopamine Nanotubes Decorated with Ag Nanoparticles as Catalyst for the Reduction of Methylene Blue. *ACS Applied Nano Materials* **2019**.

(61) Lu, Q.; Danner, E.; Waite, J. H.; Israelachvili, J. N.; Zeng, H.; Hwang, D. S. Adhesion of mussel foot proteins to different substrate surfaces. *Journal of The Royal Society Interface* **2013**, *10* (79), 20120759.

(62) Zeng, H.; Hwang, D. S.; Israelachvili, J. N.; Waite, J. H. Strong reversible Fe3+-mediated bridging between dopa-containing protein films in water. *Proceedings of the National Academy of Sciences* **2010**, *107* (29), 12850-12853.

(63) Lee, H.; Dellatore, S. M.; Miller, W. M.; Messersmith, P. B. Mussel-inspired surface chemistry for multifunctional coatings. *science* **2007**, *318* (5849), 426-430.

(64) Wang, H.; Wang, Z.; Yue, R.; Gao, F.; Ren, R.; Wei, J.; Wang, X.; Kong, Z. Rapid preparation of adsorbent based on mussel inspired chemistry and simultaneous removal of heavy metal ions in water. *Chemical Engineering Journal* **2020**, *383*, 123107.

(65) Zhang, M.; Li, G.; Sun, X.; Jiang, Y.; Zhang, X. General promoting effect of polydopamine on supported noble metal catalysts. *Journal of Materials Chemistry A* **2017**, *5* (39), 20789-20796.

(66) Guo, L.; Liu, Q.; Li, G.; Shi, J.; Liu, J.; Wang, T.; Jiang, G. A mussel-inspired polydopamine coating as a versatile platform for the in situ synthesis of graphene-based nanocomposites. *Nanoscale* **2012**, *4* (19), 5864-5867.

(67) Zhang, C.; Ou, Y.; Lei, W. X.; Wan, L. S.; Ji, J.; Xu, Z. K. CuSO4/H2O2-induced rapid deposition of polydopamine coatings with high uniformity and enhanced stability. *Angewandte Chemie International Edition* **2016**, *55* (9), 3054-3057.

(68) Sileika, T. S.; Barrett, D. G.; Zhang, R.; Lau, K. H. A.; Messersmith, P. B. Colorless multifunctional coatings inspired by polyphenols found in tea, chocolate, and wine. *Angewandte Chemie* **2013**, *125* (41), 10966-10970.

(69) Rahim, M. A.; Björnmalm, M.; Suma, T.; Faria, M.; Ju, Y.; Kempe, K.; Müllner, M.; Ejima, H.; Stickland, A. D.; Caruso, F. Metal–phenolic supramolecular gelation. *Angewandte Chemie* **2016**, *128* (44), 14007-14011.

(70) Park, T.; Kim, W. I.; Kim, B. J.; Lee, H.; Choi, I. S.; Park, J. H.; Cho, W. K. Salt-induced, continuous deposition of supramolecular iron (III)–tannic acid complex. *Langmuir* **2018**, *34* (41), 12318-12323.

(71) Guo, Z.; Xie, W.; Lu, J.; Guo, X.; Xu, J.; Xu, W.; Chi, Y.; Takuya, N.; Wu, H.; Zhao, L. Tannic acid-based metal phenolic networks for bio-applications: a review. *Journal of Materials Chemistry B* **2021**, *9* (20), 4098-4110.

(72) Ejima, H.; Richardson, J. J.; Liang, K.; Best, J. P.; van Koeverden, M. P.; Such, G. K.; Cui, J.; Caruso, F. One-step assembly of coordination complexes for versatile film and particle engineering. *Science* **2013**, *341* (6142), 154-157.

(73) Li, D.; Xu, X.; Wang, X.; Li, R.; Cai, C.; Sun, T.; Zhao, Y.; Chen, L.; Xu, J.; Zhao, N. A General Surface Modification Method for Nanospheres via Tannic Acid-Fe Layer-by-Layer Deposition: Preparation of a Magnetic Nanocatalyst. *ACS Applied Nano Materials* **2019**.

(74) Zhang, J.; Liu, L.; Si, Y.; Yu, J.; Ding, B. Rational design of electrospun nanofibrous materials for oil/water emulsion separation. *Materials Chemistry Frontiers* **2021**, *5* (1), 97-128.

(75) Bozeman, B. The 2010 BP Gulf of Mexico oil spill: Implications for theory of organizational disaster. *Technology in Society* **2011**, *33* (3-4), 244-252.

(76) Kwon, G.; Post, E.; Tuteja, A. Membranes with selective wettability for the separation of oil–water mixtures. *MRS Communications* **2015**, *5* (3), 475-494.

(77) Lin, X.; Hong, J. Recent advances in robust superwettable membranes for oil–water separation. *Advanced Materials Interfaces* **2019**, *6* (12), 1900126.

(78) Yu, L.; Han, M.; He, F. A review of treating oily wastewater. *Arabian journal of chemistry* **2017**, *10*, S1913-S1922.

(79) Arumugham, T.; Kaleekkal, N. J.; Rana, D.; Doraiswamy, M. Separation of oil/water emulsions using nano MgO anchored hybrid ultrafiltration membranes for environmental abatement. *Journal of Applied Polymer Science* **2016**, *133* (1).

(80) Maggay, I. V.; Chang, Y.; Venault, A.; Dizon, G. V.; Wu, C.-J. Functionalized porous filtration media for gravity-driven filtration: Reviewing a new emerging approach for oil and water emulsions separation. *Separation and Purification Technology* **2021**, *259*, 117983.

(81) Pan, M.; Gong, L.; Xiang, L.; Yang, W.; Wang, W.; Zhang, L.; Hu, W.; Han, L.; Zeng, H. Modulating surface interactions for regenerable separation of oil-in-water emulsions. *Journal of Membrane Science* **2021**, 119140.

(82) Körbahti, B. K.; Artut, K. Electrochemical oil/water demulsification and purification of bilge water using Pt/Ir electrodes. *Desalination* **2010**, *258* (1-3), 219-228.

(83) Wang, R.; Feng, Y.; Xu, H.; Zou, Y.; Fan, L.; Zhang, R.; Zhou, Y. Effective demulsification for oil–water separation through metal–organic frameworks with an amphipathic micro-domain. *Materials Chemistry Frontiers* **2020**, *4* (10), 3086-3093.

(84) Liu, L.; Zhao, L.; Yang, X.; Wang, Y.; Xu, B.; Liang, B. Innovative design and study of an oil-water coupling separation magnetic hydrocyclone. *Separation and Purification Technology* **2019**, *213*, 389-400.

(85) Saththasivam, J.; Loganathan, K.; Sarp, S. An overview of oil–water separation using gas flotation systems. *Chemosphere* **2016**, *144*, 671-680.

(86) Jiang, J.; Zhang, Q.; Zhan, X.; Chen, F. A multifunctional gelatin-based aerogel with superior pollutants adsorption, oil/water separation and photocatalytic properties. *Chemical Engineering Journal* **2019**, *358*, 1539-1551.

(87) Chu, Z.; Feng, Y.; Seeger, S. Oil/water separation with selective superantiwetting/superwetting surface materials. *Angewandte Chemie International Edition* **2015**, *54* (8), 2328-2338.

(88) Al-Maas, M.; Hussain, A.; Matar, J. M.; Ponnamma, D.; Hassan, M. K.; Al-Maadeed, M. A. A.; Alamgir, K.; Adham, S. Validation and application of a membrane filtration evaluation protocol for oil-water separation. *Journal of Water Process Engineering* **2021**, *43*, 102185.

(89) Dmitrieva, E. S.; Anokhina, T. S.; Novitsky, E. G.; Volkov, V. V.; Borisov, I. L.; Volkov, A. V. Polymeric Membranes for Oil-Water Separation: A Review. *Polymers* **2022**, *14* (5), 980.

(90) Chen, W.; Su, Y.; Zheng, L.; Wang, L.; Jiang, Z. The improved oil/water separation performance of cellulose acetate-graft-polyacrylonitrile membranes. *Journal of Membrane Science* **2009**, *337* (1-2), 98-105.

(91) Qu, F.; Cao, A.; Yang, Y.; Mahmud, S.; Su, P.; Yang, J.; He, Z.; Lai, Q.; Zhu, L.; Tu, Z. Hierarchically superhydrophilic poly (vinylidene fluoride) membrane with self-cleaning fabricated by surface mineralization for stable separation of oily wastewater. *Journal of Membrane Science* **2021**, *640*, 119864.

(92) Zhu, X.; Tu, W.; Wee, K.-H.; Bai, R. Effective and low fouling oil/water separation by a novel hollow fiber membrane with both hydrophilic and oleophobic surface properties. *Journal of membrane science* **2014**, *466*, 36-44.

(93) Cai, Y.; Chen, D.; Li, N.; Xu, Q.; Li, H.; He, J.; Lu, J. A smart membrane with antifouling capability and switchable oil wettability for high-efficiency oil/water emulsions separation. *Journal of Membrane Science* **2018**, *555*, 69-77.

(94) Wang, Z.; Yang, J.; Song, S.; Guo, J.; Zheng, J.; Sherazi, T. A.; Li, S.; Zhang, S. Patterned, anti-fouling membrane with controllable wettability for ultrafast oil/water separation and liquid–liquid extraction. *Chemical Communications* **2020**, *56* (80), 12045-12048.

(95) Shen, X.; Xie, T.; Wang, J.; Liu, P.; Wang, F. An anti-fouling poly (vinylidene fluoride) hybrid membrane blended with functionalized ZrO 2 nanoparticles for efficient oil/water separation. *RSC advances* **2017**, *7* (9), 5262-5271.

(96) Zhao, Y.; Zhang, M.; Wang, Z. Underwater superoleophobic membrane with enhanced oil–water separation, antimicrobial, and antifouling activities. *Advanced Materials Interfaces* **2016**, *3* (13), 1500664.

(97) Zhu, Y.; Zhang, F.; Wang, D.; Pei, X. F.; Zhang, W.; Jin, J. A novel zwitterionic polyelectrolyte grafted PVDF membrane for thoroughly separating oil from water with ultrahigh efficiency. *Journal of Materials Chemistry A* **2013**, *1* (18), 5758-5765.

(98) Liu, Y.; Su, Y.; Cao, J.; Guan, J.; Zhang, R.; He, M.; Fan, L.; Zhang, Q.; Jiang, Z. Antifouling, high-flux oil/water separation carbon nanotube membranes by polymer-mediated surface charging and hydrophilization. *Journal of Membrane Science* **2017**, *542*, 254-263.

(99) Dong, D.; Zhu, Y.; Fang, W.; Ji, M.; Wang, A.; Gao, S.; Lin, H.; Huang, R.; Jin, J. Double-Defense Design of Super - Anti - Fouling Membranes for Oil/Water Emulsion Separation. *Advanced Functional Materials* **2022**, 2113247.

(100) Zhang, L.; Lin, Y.; Wu, H.; Cheng, L.; Sun, Y.; Yasui, T.; Yang, Z.; Wang, S.; Yoshioka, T.; Matsuyama, H. An ultrathin in situ silicification layer developed by an electrostatic attraction force strategy for ultrahigh-performance oil–water emulsion separation. *Journal of Materials Chemistry A* **2019**, *7* (42), 24569-24582.

(101) Yang, H.-C.; Pi, J.-K.; Liao, K.-J.; Huang, H.; Wu, Q.-Y.; Huang, X.-J.; Xu, Z.-K. Silica-decorated polypropylene microfiltration membranes with a mussel-inspired intermediate layer for oil-in-water emulsion separation. *ACS applied materials & interfaces* **2014**, *6* (15), 12566-12572.

(102) Zhang, C.; Xiang, L.; Zhang, J.; Gong, L.; Han, L.; Xu, Z.-K.; Zeng, H. Tough and alkaline-resistant mussel-inspired wet adhesion with surface salt displacement via polydopamine/amine synergy. *Langmuir* **2019**, *35* (15), 5257-5263.

(103) Xu, Z.; Li, L.; Liu, J.; Dai, C.; Sun, W.; Chen, J.; Zhu, Z.; Zhao, M.; Zeng, H. Mussel-inspired superhydrophilic membrane constructed on a hydrophilic polymer network for highly efficient oil/water separation. *Journal of Colloid and Interface Science* **2022**, *608*, 702-710.

(104) Qiu, W.-Z.; Wu, G.-P.; Xu, Z.-K. Robust coatings via catechol–amine codeposition: mechanism, kinetics, and application. *ACS applied materials & interfaces* **2018**, *10* (6), 5902-5908.

(105) Xiang, L.; Zhang, J.; Gong, L.; Han, L.; Zhang, C.; Yan, B.; Liu, J.; Zeng, H. Probing the interaction forces of phenol/amine deposition in wet adhesion: impact of phenol/amine mass ratio and surface properties. *Langmuir* **2019**, *35* (48), 15639-15650.

(106) Zhao, X.; Wang, R.; Lan, Y.; Wang, T.; Pan, J.; Liu, L. Engineering superwetting membranes through polyphenol-polycation-metal complexation for high-efficient oil/water separation: From polyphenol to tailored nanostructures. *Journal of Membrane Science* **2021**, *630*, 119310.

(107) Meng, L.; Lv, Y.; Deng, P.; Li, N.; Huang, M.; Mansouri, J.; Chen, V. Novel PVDF membrane with sandwich structure for enhanced membrane distillation. *Chemical Engineering Journal* **2021**, *415*, 128960.

(108) Zhang, Y.; Ma, J.; Shao, L. Ultra-thin trinity coating enabled by competitive reactions for unparalleled molecular separation. *Journal of Materials Chemistry A* **2020**, *8* (10), 5078-5085.

(109) Zeng, H. *Polymer adhesion, friction, and lubrication*; John Wiley & Sons, 2013.

(110) Magonov, S. N.; Reneker, D. H. Characterization of polymer surfaces with atomic force microscopy. *Annual Review of Materials Science* **1997**, *27* (1), 175-222.

(111) Eaton, P.; West, P. *Atomic force microscopy*; Oxford university press, 2010.

(112) Zhang, C.; Gong, L.; Xiang, L.; Du, Y.; Hu, W.; Zeng, H.; Xu, Z.-K. Deposition and adhesion of polydopamine on the surfaces of varying wettability. *ACS applied materials & interfaces* **2017**, *9* (36), 30943-30950.

(113) Xie, L.; Cui, X.; Liu, J.; Lu, Q.; Huang, J.; Mao, X.; Yang, D.; Tan, J.; Zhang, H.; Zeng, H. Nanomechanical insights into versatile polydopamine wet adhesive interacting with liquid-infused and solid slippery surfaces. *ACS Applied Materials & Interfaces* **2021**, *13* (5), 6941-6950.

(114) Gong, L.; Wang, J.; Xiang, L.; Huang, J.; Fattahpour, V.; Roostaei, M.; Mamoudi, M.; Fermaniuk, B.; Luo, J.-L.; Zeng, H. Characterizing foulants on slotted liner and probing the surface interaction mechanisms in organic media with implication for an antifouling strategy in oil production. *Fuel* **2021**, *290*, 120008.

(115) Tabor, D.; Winterton, R. H. S. The direct measurement of normal and retarded van der Waals forces. *Proceedings of the Royal Society of London. A. Mathematical and Physical Sciences* **1969**, *312* (1511), 435-450.

(116) Israelachvili, J. N.; Adams, G. Direct measurement of long range forces between two mica surfaces in aqueous KNO3 solutions. *Nature* **1976**, *262* (5571), 774-776.

(117) Israelachvili, J. N.; McGuiggan, P. M. Adhesion and short-range forces between surfaces. Part I: New apparatus for surface force measurements. *Journal of Materials Research* **1990**, *5* (10), 2223-2231.

(118) Israelachvili, J.; Min, Y.; Akbulut, M.; Alig, A.; Carver, G.; Greene, W.; Kristiansen, K.; Meyer, E.; Pesika, N.; Rosenberg, K. Recent advances in the surface forces apparatus (SFA) technique. *Reports on Progress in Physics* **2010**, *73* (3), 036601.

(119) Israelachvili, J. Thin film studies using multiple-beam interferometry. *Journal of Colloid and Interface Science* **1973**, *44* (2), 259-272.

(120) Israelachvili, J. N. *Intermolecular and surface forces*; Academic press, **2011.**

(121) Mohammed, A.; Abdullah, A. Scanning electron microscopy (SEM): A review. In *Proceedings of the 2018 International Conference on Hydraulics and Pneumatics—HERVEX, Băile Govora, Romania*, **2018**; 7-9.

(122) Zhou, W.; Apkarian, R.; Wang, Z. L.; Joy, D. Fundamentals of scanning electron microscopy (SEM). In *Scanning microscopy for nanotechnology*, Springer, **2006**; 1-40.

(123) Scimeca, M.; Bischetti, S.; Lamsira, H. K.; Bonfiglio, R.; Bonanno, E. Energy Dispersive X-ray (EDX) microanalysis: A powerful tool in biomedical research and diagnosis. *European journal of histochemistry: EJH* **2018**, *62* (1).

(124) Passos, M. L.; Saraiva, M. L. M. Detection in UV-visible spectrophotometry: Detectors, detection systems, and detection strategies. *Measurement* **2019**, *135*, 896-904.

(125) Guo, Y.; Liu, C.; Ye, R.; Duan, Q. Advances on water quality detection by UV-vis spectroscopy. *Applied Sciences* **2020**, *10* (19), 6874.

(126) He, K.; Chen, G.; Zeng, G.; Chen, A.; Huang, Z.; Shi, J.; Huang, T.; Peng, M.; Hu, L. Three-dimensional graphene supported catalysts for organic dyes degradation. *Applied Catalysis B: Environmental* **2018**, *228*, 19-28.

(127) Ali, I. New generation adsorbents for water treatment. *Chemical reviews* **2012**, *112* (10), 5073-5091.

(128) Atarod, M.; Nasrollahzadeh, M.; Sajadi, S. M. Green synthesis of Pd/RGO/Fe3O4 nanocomposite using Withania coagulans leaf extract and its application as magnetically separable

and reusable catalyst for the reduction of 4-nitrophenol. *Journal of colloid and interface science* **2016**, *465*, 249-258.

(129) Han, L.; Zhou, Y.; He, T.; Song, G.; Wu, F.; Jiang, F.; Hu, J. One-pot morphology-controlled synthesis of various shaped mesoporous silica nanoparticles. *Journal of materials science* **2013**, *48* (17), 5718-5726.

(130) Samadder, R.; Akter, N.; Roy, A. C.; Uddin, M. M.; Hossen, M. J.; Azam, M. S. Magnetic nanocomposite based on polyacrylic acid and carboxylated cellulose nanocrystal for the removal of cationic dye. *RSC Advances* **2020**, *10* (20), 11945-11956.

(131) Li, Y.; Du, Q.; Liu, T.; Peng, X.; Wang, J.; Sun, J.; Wang, Y.; Wu, S.; Wang, Z.; Xia, Y. Comparative study of methylene blue dye adsorption onto activated carbon, graphene oxide, and carbon nanotubes. *Chemical Engineering Research and Design* **2013**, *91* (2), 361-368.

(132) Zhang, P.; Gong, J.-L.; Zeng, G.-M.; Deng, C.-H.; Yang, H.-C.; Liu, H.-Y.; Huan, S.-Y. Cross-linking to prepare composite graphene oxide-framework membranes with high-flux for dyes and heavy metal ions removal. *Chemical Engineering Journal* **2017**, *322*, 657-666.

(133) Li, C.; Lou, Z.; Yang, Y.; Wang, Y.; Lu, Y.; Ye, Z.; Zhu, L. Hollowsphere nanoheterojunction of g-C3N4@ TiO2 with high visible light photocatalytic property. *Langmuir* **2019**, *35* (3), 779-786.

(134) Lei, J.; Liu, H.; Yin, D.; Zhou, L.; Liu, J. A.; Chen, Q.; Cui, X.; He, R.; Duan, T.; Zhu, W. Boosting the loading of metal single atoms via a bioconcentration strategy. *Small* **2020**, *16* (10), 1905920.

(135) Zhang, P.; Shao, C.; Zhang, Z.; Zhang, M.; Mu, J.; Guo, Z.; Liu, Y. In situ assembly of well-dispersed Ag nanoparticles (AgNPs) on electrospun carbon nanofibers (CNFs) for catalytic reduction of 4-nitrophenol. *Nanoscale* **2011**, *3* (8), 3357-3363.

(136) Xiao, W.; Zhang, Y.; Liu, B. Raspberrylike SiO2@ reduced graphene oxide@ AgNP composite microspheres with high aqueous dispersity and excellent catalytic activity. *ACS applied materials & interfaces* **2015**, *7* (11), 6041-6046.

(137) Wang, N.; Guan, B.; Zhao, Y.; Zou, Y.; Geng, G.; Chen, P.; Wang, F.; Liu, M. Sub‐10 nm Ag Nanoparticles/Graphene Oxide: Controllable Synthesis, Size‐Dependent and Extremely Ultrahigh Catalytic Activity. *Small* **2019**, *15* (23), 1901701.

(138) Jiao, T.; Zhao, H.; Zhou, J.; Zhang, Q.; Luo, X.; Hu, J.; Peng, Q.; Yan, X. Self-assembly reduced graphene oxide nanosheet hydrogel fabrication by anchorage of chitosan/silver and its potential efficient application toward dye degradation for wastewater treatments. *ACS Sustainable Chemistry & Engineering* **2015**, *3* (12), 3130-3139.

(139) Zhu, X.-Y.; Lv, Z.-S.; Feng, J.-J.; Yuan, P.-X.; Zhang, L.; Chen, J.-R.; Wang, A.-J. Controlled fabrication of well-dispersed AgPd nanoclusters supported on reduced graphene oxide with highly enhanced catalytic properties towards 4-nitrophenol reduction. *Journal of colloid and interface science* **2018**, *516*, 355-363.

(140) Huang, J.; Yan, Y.; Xie, L.; Liu, H.; Huang, C.; Lu, Q.; Qiu, X.; Zeng, H. Probing the Self-Assembly and Nonlinear Friction Behavior of Confined Gold Nano-Particles. *Langmuir* **2019**, *35* (48), 15701-15709.

(141) Jin, L.; Liu, B.; Louis, M. E.; Li, G.; He, J. Highly Crystalline Mesoporous Titania Loaded with Monodispersed Gold Nanoparticles: Controllable Metal–Support Interaction in Porous Materials. *ACS Applied Materials & Interfaces* **2020**, *12* (8), 9617-9627.

(142) Cao, H.-L.; Liu, C.; Cai, F.-Y.; Qiao, X.-X.; Dichiara, A.; Tian, C.; Lü, J. In situ immobilization of ultra-fine Ag NPs onto magnetic Ag@ RF@ Fe3O4 core-satellite nanocomposites for the rapid catalytic reduction of nitrophenols. *Water Research* **2020**, 115882.

(143) Ye, W.; Yu, J.; Zhou, Y.; Gao, D.; Wang, D.; Wang, C.; Xue, D. Green synthesis of Pt–Au dendrimer-like nanoparticles supported on polydopamine-functionalized graphene and their high performance toward 4-nitrophenol reduction. *Applied Catalysis B: Environmental* **2016**, *181*, 371-378.

(144) Zhou, J.; Duan, B.; Fang, Z.; Song, J.; Wang, C.; Messersmith, P. B.; Duan, H. Interfacial assembly of mussel-inspired Au@ Ag@ polydopamine core–shell nanoparticles for recyclable nanocatalysts. *Advanced Materials* **2014**, *26* (5), 701-705.

(145) Yihan, S.; Mingming, L.; Guo, Z. Ag nanoparticles loading of polypyrrole-coated superwetting mesh for on-demand separation of oil-water mixtures and catalytic reduction of aromatic dyes. *Journal of colloid and interface science* **2018**, *527*, 187-194.

(146) Liu, B.; Kuo, C. H.; Chen, J.; Luo, Z.; Thanneeru, S.; Li, W.; Song, W.; Biswas, S.; Suib, S. L.; He, J. Ligand-Assisted Co-Assembly Approach toward Mesoporous Hybrid Catalysts of Transition-Metal Oxides and Noble Metals: Photochemical Water Splitting. *Angewandte Chemie International Edition* **2015**, *54* (31), 9061-9065.

(147) Xu, D.; Lv, H.; Liu, B. Encapsulation of metal nanoparticle catalysts within mesoporous zeolites and their enhanced catalytic performances: a review. *Frontiers in chemistry* **2018**, *6*, 550.

(148) Liao, G.; Fang, J.; Li, Q.; Li, S.; Xu, Z.; Fang, B. Ag-Based nanocomposites: synthesis and applications in catalysis. *Nanoscale* **2019**, *11* (15), 7062-7096.

(149) Song, Y.; Jiang, H.; Wang, B.; Kong, Y.; Chen, J. Silver-incorporated mussel-inspired polydopamine coatings on mesoporous silica as an efficient nanocatalyst and antimicrobial agent. *ACS applied materials & interfaces* **2018**, *10* (2), 1792-1801.

(150) Huang, J.; Huang, G.; An, C.; Xin, X.; Chen, X.; Zhao, Y.; Feng, R.; Xiong, W. Exploring the use of ceramic disk filter coated with Ag/ZnO nanocomposites as an innovative approach for removing Escherichia coli from household drinking water. *Chemosphere* **2020**, *245*, 125545.

(151) Islam, M. S.; Akter, N.; Rahman, M. M.; Shi, C.; Islam, M. T.; Zeng, H.; Azam, M. S. Mussel-inspired immobilization of silver nanoparticles toward antimicrobial cellulose paper. *ACS Sustainable Chemistry & Engineering* **2018**, *6* (7), 9178-9188.

(152) Sharif, H. M. A.; Mahmood, A.; Cheng, H.-Y.; Djellabi, R.; Ali, J.; Jiang, W.-L.; Wang, S.-S.; Haider, M. R.; Mahmood, N.; Wang, A.-J. Fe3O4 Nanoparticles Coated with EDTA and Ag Nanoparticles for the Catalytic Reduction of Organic Dyes from Wastewater. *ACS Applied Nano Materials* **2019**, *2* (8), 5310-5319.

(153) Zhu, W.; Lei, J.; Li, Y.; Dai, L.; Chen, T.; Bai, X.; Wang, L.; Duan, T. Procedural growth of fungal hyphae/Fe3O4/graphene oxide as ordered-structure composites for water purification. *Chemical Engineering Journal* **2019**, *355*, 777-783.

(154) Tian, Q.; Yu, X.; Zhang, L.; Yu, D. Monodisperse raspberry-like multihollow polymer/Ag nanocomposite microspheres for rapid catalytic degradation of methylene blue. *Journal of colloid and interface science* **2017**, *491*, 294-304.

(155) Zhang, K.; Dwivedi, V.; Chi, C.; Wu, J. Graphene oxide/ferric hydroxide composites for efficient arsenate removal from drinking water. *Journal of hazardous materials* **2010**, *182* (1-3), 162-168.

(156) Li, B.; Cao, H.; Yin, G.; Lu, Y.; Yin, J. Cu 2 O@ reduced graphene oxide composite for removal of contaminants from water and supercapacitors. *Journal of Materials Chemistry* **2011**, *21* (29), 10645-10648.

(157) Bandara, N.; Esparza, Y.; Wu, J. Graphite oxide improves adhesion and water resistance of canola protein–graphite oxide hybrid adhesive. *Scientific reports* **2017**, *7* (1), 1-12.

(158) Cui, L.; Wang, Y.; Gao, L.; Hu, L.; Yan, L.; Wei, Q.; Du, B. EDTA functionalized magnetic graphene oxide for removal of Pb (II), Hg (II) and Cu (II) in water treatment: Adsorption mechanism and separation property. *Chemical engineering journal* **2015**, *281*, 1-10.

(159) Chi, Y.; Yuan, Q.; Li, Y.; Tu, J.; Zhao, L.; Li, N.; Li, X. Synthesis of Fe3O4@ SiO2–Ag magnetic nanocomposite based on small-sized and highly dispersed silver nanoparticles for catalytic reduction of 4-nitrophenol. *Journal of colloid and interface science* **2012**, *383* (1), 96-102.

(160) Das, R.; Sypu, V. S.; Paumo, H. K.; Bhaumik, M.; Maharaj, V.; Maity, A. Silver decorated magnetic nanocomposite (Fe3O4@ PPy-MAA/Ag) as highly active catalyst towards reduction of 4-nitrophenol and toxic organic dyes. *Applied Catalysis B: Environmental* **2019**, *244*, 546-558.

(161) Jeon, E. K.; Seo, E.; Lee, E.; Lee, W.; Um, M.-K.; Kim, B.-S. Mussel-inspired green synthesis of silver nanoparticles on graphene oxide nanosheets for enhanced catalytic applications. *Chemical Communications* **2013**, *49* (33), 3392-3394.

(162) Zhang, J.; Azam, M. S.; Shi, C.; Huang, J.; Yan, B.; Liu, Q.; Zeng, H. Poly (acrylic acid) functionalized magnetic graphene oxide nanocomposite for removal of methylene blue. *RSC Advances* **2015**, *5* (41), 32272-32282.

(163) Xu, Z.; Wang, X.; Liu, X.; Cui, Z.; Yang, X.; Yeung, K. W. K.; Chung, J. C.; Chu, P. K.; Wu, S. Tannic acid/Fe3+/Ag nanofilm exhibiting superior photodynamic and physical antibacterial activity. *ACS applied materials & interfaces* **2017**, *9* (45), 39657-39671.

(164) Chen, J.; Yao, B.; Li, C.; Shi, G. An improved Hummers method for eco-friendly synthesis of graphene oxide. *Carbon* **2013**, *64*, 225-229.

(165) Lei, J.; Guo, Q.; Yin, D.; Cui, X.; He, R.; Duan, T.; Zhu, W. Bioconcentration and bioassembly of N/S co-doped carbon with excellent stability for supercapacitors. *Applied Surface Science* **2019**, *488*, 316-325.

(166) Yu, K.; Shao, P.; Meng, P.; Chen, T.; Lei, J.; Yu, X.; He, R.; Yang, F.; Zhu, W.; Duan, T. Superhydrophilic and highly elastic monolithic sponge for efficient solar-driven radioactive wastewater treatment under one sun. *Journal of Hazardous Materials* **2020**, *392*, 122350.

(167) Peng, G.; Zhang, M.; Deng, S.; Shan, D.; He, Q.; Yu, G. Adsorption and catalytic oxidation of pharmaceuticals by nitrogen-doped reduced graphene oxide/Fe3O4 nanocomposite. *Chemical Engineering Journal* **2018**, *341*, 361-370.

(168) Shen, H.; Duan, C.; Guo, J.; Zhao, N.; Xu, J. Facile in situ synthesis of silver nanoparticles on boron nitride nanosheets with enhanced catalytic performance. *Journal of Materials Chemistry A* **2015**, *3* (32), 16663-16669.

(169) Mao, B.; An, Q.; Zhai, B.; Xiao, Z.; Zhai, S. Multifunctional hollow polydopamine-based composites (Fe 3 O 4/PDA@ Ag) for efficient degradation of organic dyes. *RSC Advances* **2016**, *6* (53), 47761-47770.

(170) Xiao, F.; Ren, H.; Zhou, H.; Wang, H.; Wang, N.; Pan, D. Porous Montmorillonite@ Graphene Oxide@ Au Nanoparticle Composite Microspheres for Organic Dye Degradation. *ACS Applied Nano Materials* **2019**, *2* (9), 5420-5429.

(171) Ma, A.; Xie, Y.; Xu, J.; Zeng, H.; Xu, H. The significant impact of polydopamine on the catalytic performance of the carried Au nanoparticles. *Chemical Communications* **2015**, *51* (8), 1469-1471.

(172) Luo, J.; Lai, J.; Zhang, N.; Liu, Y.; Liu, R.; Liu, X. Tannic acid induced self-assembly of three-dimensional graphene with good adsorption and antibacterial properties. *ACS Sustainable Chemistry & Engineering* **2016**, *4* (3), 1404-1413.

(173) Zhu, M.; Wang, C.; Meng, D.; Diao, G. In situ synthesis of silver nanostructures on magnetic Fe 3 O 4@ C core–shell nanocomposites and their application in catalytic reduction reactions. *Journal of Materials Chemistry A* **2013**, *1* (6), 2118-2125.

(174) Li, H.; Jiang, D.; Huang, Z.; He, K.; Zeng, G.; Chen, A.; Yuan, L.; Peng, M.; Huang, T.; Chen, G. Preparation of silver-nanoparticle-loaded magnetic biochar/poly (dopamine) composite as catalyst for reduction of organic dyes. *Journal of colloid and interface science* **2019**, *555*, 460-469.

(175) Schlesinger, H.; Brown, H. C.; Finholt, A.; Gilbreath, J. R.; Hoekstra, H. R.; Hyde, E. K. Sodium borohydride, its hydrolysis and its use as a reducing agent and in the generation of hydrogen1. *Journal of the American Chemical Society* **1953**, *75* (1), 215-219.

(176) Zhu, M.; Diao, G. Magnetically recyclable Pd nanoparticles immobilized on magnetic Fe3O4@ C nanocomposites: preparation, characterization, and their catalytic activity toward Suzuki and Heck coupling reactions. *The Journal of Physical Chemistry C* **2011**, *115* (50), 24743-24749.

(177) Deshmukh, S.; Dhokale, R.; Yadav, H.; Achary, S.; Delekar, S. Titania–supported silver nanoparticles: An efficient and reusable catalyst for reduction of 4-nitrophenol. *Applied surface science* **2013**, *273*, 676-683.

(178) Alshehri, S. M.; Almuqati, T.; Almuqati, N.; Al-Farraj, E.; Alhokbany, N.; Ahamad, T. Chitosan based polymer matrix with silver nanoparticles decorated multiwalled carbon nanotubes for catalytic reduction of 4-nitrophenol. *Carbohydrate polymers* **2016**, *151*, 135-143.

(179) Gao, S.; Zhu, Y.; Wang, J.; Zhang, F.; Li, J.; Jin, J. Layer-by-Layer Construction of Cu2+/Alginate Multilayer Modified Ultrafiltration Membrane with Bioinspired Superwetting Property for High-Efficient Crude-Oil-in-Water Emulsion Separation. *Advanced Functional Materials* **2018**, *28* (49), 1801944.

(180) Miao, D.; Huang, Z.; Wang, X.; Yu, J.; Ding, B. Continuous, spontaneous, and directional water transport in the trilayered fibrous membranes for functional moisture wicking textiles. *Small* **2018**, *14* (32), 1801527.

(181) Khatib, Z.; Faucher, M.; Sellman, E. Field Evaluation of Disc-Stack Centrifuges for Separating Oil/Water Emulsions on Offshore Platforms. In *SPE Annual Technical Conference and Exhibition*, **1995**; Society of Petroleum Engineers.

(182) Tanudjaja, H. J.; Hejase, C. A.; Tarabara, V. V.; Fane, A. G.; Chew, J. W. Membrane-based separation for oily wastewater: A practical perspective. *Water research* **2019**, *156*, 347-365.

(183) Chen, R.; Zhang, Y.; Xie, Q.; Chen, Z.; Ma, C.; Zhang, G. Transparent Polymer-Ceramic Hybrid Antifouling Coating with Superior Mechanical Properties. *Advanced Functional Materials* **2021**, *31* (19), 2011145.

(184) Fan, J. B.; Song, Y.; Wang, S.; Meng, J.; Yang, G.; Guo, X.; Feng, L.; Jiang, L. Directly coating hydrogel on filter paper for effective oil–water separation in highly acidic, alkaline, and salty environment. *Advanced Functional Materials* **2015**, *25* (33), 5368-5375.

(185) Chen, X.; Huang, G.; An, C.; Feng, R.; Wu, Y.; Huang, C. Plasma-induced PAA-ZnO coated PVDF membrane for oily wastewater treatment: Preparation, optimization, and characterization through Taguchi OA design and synchrotron-based X-ray analysis. *Journal of Membrane Science* **2019**, *582*, 70-82.

(186) Tummons, E.; Han, Q.; Tanudjaja, H. J.; Hejase, C. A.; Chew, J. W.; Tarabara, V. V. Membrane fouling by emulsified oil: A review. *Separation and Purification Technology* **2020**, *248*, 116919.

(187) Ge, J.; Zong, D.; Jin, Q.; Yu, J.; Ding, B. Biomimetic and superwettable nanofibrous skins for highly efficient separation of oil-in-water emulsions. *Advanced Functional Materials* **2018**, *28* (10), 1705051.

(188) Maan, A. M.; Hofman, A. H.; de Vos, W. M.; Kamperman, M. Recent developments and practical feasibility of polymer-based antifouling coatings. *Advanced functional materials* **2020**, *30* (32), 2000936.

(189) Wang, Z.; Yang, H.-C.; He, F.; Peng, S.; Li, Y.; Shao, L.; Darling, S. B. Mussel-inspired surface engineering for water-remediation materials. *Matter* **2019**, *1* (1), 115-155.

(190) Zhang, C.; Ma, M.-Q.; Chen, T.-T.; Zhang, H.; Hu, D.-F.; Wu, B.-H.; Ji, J.; Xu, Z.-K. Dopamine-triggered one-step polymerization and codeposition of acrylate monomers for functional coatings. *ACS applied materials & interfaces* **2017**, *9* (39), 34356-34366.

(191) Zhou, X.; Wang, L.; Wei, Z.; Weng, G.; He, J. An Adaptable Tough Elastomer with Moisture-Triggered Switchable Mechanical and Fluorescent Properties. *Advanced Functional Materials* **2019**, *29* (34), 1903543.

(192) Yu, Q.; You, X.; Wu, H.; Su, Y.; Zhang, R.; Liu, Y.; Yang, C.; Shen, J.; Yuan, J.; Jiang, Z. Ultrathin fluorinated self-cleaning membranes via coordination-driven metal-bridging assembly for water purification. *Journal of Materials Chemistry A* **2020**, *8* (8), 4505-4514.

(193) Wu, J.; Ding, Y.; Wang, J.; Li, T.; Lin, H.; Wang, J.; Liu, F. Facile fabrication of nanofiber- and micro/nanosphere-coordinated PVDF membrane with ultrahigh permeability of viscous water-in-oil emulsions. *Journal of Materials Chemistry A* **2018**, *6* (16), 7014-7020.

(194) Jin, L.; Su, X.; Shi, J.; Shih, K. C.; Cintron, D.; Cai, T.; Nieh, M. P.; Chen, O.; Suib, S. L.; Jain, M. Crystalline Mesoporous Complex Oxides: Porosity - Controlled Electromagnetic Response. *Advanced Functional Materials* **2020**, *30* (15), 1909491.

(195) Azam, M. S.; Cai, C.; Gibbs, J. M.; Tyrode, E.; Hore, D. K. Silica surface charge enhancement at elevated temperatures revealed by interfacial water signals. *Journal of the American Chemical Society* **2020**, *142* (2), 669-673.

(196) Zhu, Y.; Wang, J.; Zhang, F.; Gao, S.; Wang, A.; Fang, W.; Jin, J. Zwitterionic nanohydrogel grafted PVDF membranes with comprehensive antifouling property and superior cycle stability for oil-in-water emulsion separation. *Advanced Functional Materials* **2018**, *28* (40), 1804121.

(197) Yang, H.-C.; Xie, Y.; Chan, H.; Narayanan, B.; Chen, L.; Waldman, R. Z.; Sankaranarayanan, S. K.; Elam, J. W.; Darling, S. B. Crude-oil-repellent membranes by atomic layer deposition: oxide interface engineering. *ACS nano* **2018**, *12* (8), 8678-8685.

(198) Yang, X.; Sun, P.; Zhang, H.; Xia, Z.; Waldman, R. Z.; Mane, A. U.; Elam, J. W.; Shao, L.; Darling, S. B. Polyphenol - sensitized atomic layer deposition for membrane interface hydrophilization. *Advanced Functional Materials* **2020**, *30* (15), 1910062.

(199) Zhang, C.; Wu, B.-H.; Ma, M.-Q.; Wang, Z.; Xu, Z.-K. Ultrathin metal/covalent–organic framework membranes towards ultimate separation. *Chemical Society Reviews* **2019**, *48* (14), 3811-3841.

(200) Li, L.; Yan, B.; Yang, J.; Chen, L.; Zeng, H. Novel mussel-inspired injectable self-healing hydrogel with anti-biofouling property. *Advanced Materials* **2015**, *27* (7), 1294-1299.

(201) Kang, T.; Oh, D. X.; Heo, J.; Lee, H.-K.; Choy, S.; Hawker, C. J.; Hwang, D. S. Formation, removal, and reformation of surface coatings on various metal oxide surfaces inspired by mussel adhesives. *ACS Applied Materials & Interfaces* **2015**, *7* (44), 24656-24662.

(202) Zhang, F.; Ren, D.; Huang, L.; Zhang, Y.; Sun, Y.; Liu, D.; Zhang, Q.; Feng, W.; Zheng, Q. 3D Interconnected Conductive Graphite Nanoplatelet Welded Carbon Nanotube Networks for Stretchable Conductors. *Advanced Functional Materials* **2021**, 2107082.

(203) Qin, M.; Xu, Y.; Cao, R.; Feng, W.; Chen, L. Efficiently controlling the 3D thermal conductivity of a polymer nanocomposite via a hyperelastic double - continuous network of graphene and sponge. *Advanced Functional Materials* **2018**, *28* (45), 1805053.

(204) Yu, Y.; Yuk, H.; Parada, G. A.; Wu, Y.; Liu, X.; Nabzdyk, C. S.; Youcef - Toumi, K.; Zang, J.; Zhao, X. Multifunctional "hydrogel skins" on diverse polymers with arbitrary shapes. *Advanced Materials* **2019**, *31* (7), 1807101.

(205) Usov, I.; Nyström, G.; Adamcik, J.; Handschin, S.; Schütz, C.; Fall, A.; Bergström, L.; Mezzenga, R. Understanding nanocellulose chirality and structure–properties relationship at the single fibril level. *Nature communications* **2015**, *6* (1), 1-11.

(206) Li, F.; Biagioni, P.; Bollani, M.; Maccagnan, A.; Piergiovanni, L. Multi-functional coating of cellulose nanocrystals for flexible packaging applications. *Cellulose* **2013**, *20* (5), 2491-2504.

(207) Yao, K.; Meng, Q.; Bulone, V.; Zhou, Q. Flexible and responsive chiral nematic cellulose nanocrystal/poly (ethylene glycol) composite films with uniform and tunable structural color. *Advanced Materials* **2017**, *29* (28), 1701323.

(208) Bethke, K.; Palantöken, S.; Andrei, V.; Roß, M.; Raghuwanshi, V. S.; Kettemann, F.; Greis, K.; Ingber, T. T.; Stückrath, J. B.; Valiyaveettil, S. Functionalized cellulose for water purification, antimicrobial applications, and sensors. *Advanced Functional Materials* **2018**, *28* (23), 1800409.

(209) Thomas, B.; Raj, M. C.; Joy, J.; Moores, A.; Drisko, G. L.; Sanchez, C. m. Nanocellulose, a versatile green platform: from biosources to materials and their applications. *Chemical Reviews* **2018**, *118* (24), 11575-11625.

(210) Huang, S.; Wang, D. A Simple Nanocellulose Coating for Self‐Cleaning upon Water Action: Molecular Design of Stable Surface Hydrophilicity. *Angewandte Chemie* **2017**, *129* (31), 9181-9185.

(211) Wu, M.-B.; Zhang, C.; Pi, J.-K.; Liu, C.; Yang, J.; Xu, Z.-K. Cellulose nanocrystals as anti-oil nanomaterials for separating crude oil from aqueous emulsions and mixtures. *Journal of Materials Chemistry A* **2019**, *7* (12), 7033-7041.

(212) Park, C. H.; Jeon, S.; Park, S.-H.; Shin, M. G.; Park, M. S.; Lee, S.-Y.; Lee, J.-H. Cellulose nanocrystal-assembled reverse osmosis membranes with high rejection performance and excellent antifouling. *Journal of Materials Chemistry A* **2019**, *7* (8), 3992-4001.

(213) Hou, Y.; Guan, Q.-F.; Xia, J.; Ling, Z.-C.; He, Z.; Han, Z.-M.; Yang, H.-B.; Gu, P.; Zhu, Y.; Yu, S.-H. Strengthening and Toughening Hierarchical Nanocellulose via Humidity-Mediated Interface. *ACS nano* **2020,** *15*(1), 1310–1320.

(214) Li, L.; Yan, B.; Zhang, L.; Tian, Y.; Zeng, H. Mussel-inspired antifouling coatings bearing polymer loops. *Chemical Communications* **2015**, *51* (87), 15780-15783.

(215) Zeng, Y.; Du, X.; Hou, W.; Liu, X.; Zhu, C.; Gao, B.; Sun, L.; Li, Q.; Liao, J.; Levkin, P. A. UV‐Triggered Polydopamine Secondary Modification: Fast Deposition and Removal of Metal Nanoparticles. *Advanced Functional Materials* **2019**, *29* (34), 1901875.

(216) Xie, C.; Wang, X.; He, H.; Ding, Y.; Lu, X. Mussel‐inspired hydrogels for self‐adhesive bioelectronics. *Advanced Functional Materials* **2020**, *30* (25), 1909954.

(217) Xiang, L.; Lin, J.; Yang, Q.; Lin, S.; Chen, S.; Yan, B. Facile preparation of hierarchical porous polydopamine microspheres for rapid removal of chromate from the wastewater. *Journal of Leather Science and Engineering* **2020**, *2* (1), 1-10.

(218) Wang, G.; Xiang, J.; Lin, J.; Xiang, L.; Chen, S.; Yan, B.; Fan, H.; Zhang, S.; Shi, X. Sustainable Advanced Fenton-like Catalysts Based on Mussel-Inspired Magnetic Cellulose Nanocomposites to Effectively Remove Organic Dyes and Antibiotics. *ACS Applied Materials & Interfaces* **2020**, *12* (46), 51952-51959.

(219) Lee, B. P.; Messersmith, P. B.; Israelachvili, J. N.; Waite, J. H. Mussel-inspired adhesives and coatings. *Annual review of materials research* **2011**, *41*, 99-132.

(220) Lin, Q.; Gourdon, D.; Sun, C.; Holten-Andersen, N.; Anderson, T. H.; Waite, J. H.; Israelachvili, J. N. Adhesion mechanisms of the mussel foot proteins mfp-1 and mfp-3. *Proceedings of the National Academy of Sciences* **2007**, *104* (10), 3782-3786.

(221) Zhong, Q. Z.; Richardson, J. J.; He, A.; Zheng, T.; Lafleur, R. P.; Li, J.; Qiu, W. Z.; Furtado, D.; Pan, S.; Xu, Z. K. Engineered Coatings via the Assembly of Amino - Quinone Networks. *Angewandte Chemie International Edition* **2021**, *60* (5), 2346-2354.

(222) Lv, Y.; Yang, S.-J.; Du, Y.; Yang, H.-C.; Xu, Z.-K. Co-deposition kinetics of polydopamine/polyethyleneimine coatings: effects of solution composition and substrate surface. *Langmuir* **2018**, *34* (44), 13123-13131.

(223) Yang, S.-J.; Zou, L.-Y.; Liu, C.; Zhong, Q.; Ma, Z.-Y.; Yang, J.; Ji, J.; Müller-Buschbaum, P.; Xu, Z.-K. Codeposition of Levodopa and Polyethyleneimine: Reaction Mechanism and Coating Construction. *ACS Applied Materials & Interfaces* **2020**, *12* (48), 54094-54103.

(224) Podsiadlo, P.; Liu, Z.; Paterson, D.; Messersmith, P. B.; Kotov, N. A. Fusion of seashell nacre and marine bioadhesive analogs: high-strength nanocomposite by layer-by-layer assembly of clay and L-3, 4-dihydroxyphenylalanine polymer. *Advanced Materials* **2007**, *19* (7), 949-955.

(225) Holten-Andersen, N.; Jaishankar, A.; Harrington, M. J.; Fullenkamp, D. E.; DiMarco, G.; He, L.; McKinley, G. H.; Messersmith, P. B.; Lee, K. Y. C. Metal-coordination: using one of nature's tricks to control soft material mechanics. *Journal of Materials Chemistry B* **2014**, *2* (17), 2467-2472.

(226) Park, J. P.; Song, I. T.; Lee, J.; Ryu, J. H.; Lee, Y.; Lee, H. Vanadyl–catecholamine hydrogels inspired by ascidians and mussels. *Chemistry of Materials* **2015**, *27* (1), 105-111.

(227) Hutter, J. L.; Bechhoefer, J. Calibration of atomic-force microscope tips. *Review of Scientific Instruments* **1993**, *64* (7), 1868-1873.

(228) Butt, H.-J.; Cappella, B.; Kappl, M. Force measurements with the atomic force microscope: Technique, interpretation and applications. *Surface science reports* **2005**, *59* (1-6), 1-152.

(229) Han, L.; Xiang, L.; Zhang, J.; Chen, J.; Liu, J.; Yan, B.; Zeng, H. Biomimetic lubrication and surface interactions of dopamine-assisted zwitterionic polyelectrolyte coatings. *Langmuir* **2018**, *34* (38), 11593-11601.

(230) Yi, J.; Nguyen, K.-C. T.; Wang, W.; Yang, W.; Pan, M.; Lou, E.; Major, P. W.; Le, L. H.; Zeng, H. Polyacrylamide/Alginate double-network tough hydrogels for intraoral ultrasound imaging. *Journal of Colloid and Interface Science* **2020**.

(231) Wei, Q.; Liu, X.; Yue, Q.; Ma, S.; Zhou, F. Mussel-Inspired One-Step Fabrication of Ultralow-Friction Coatings on Diverse Biomaterial Surfaces. *Langmuir* **2019**, *35* (24), 8068-8075.

(232) Li, M.; Li, Y.; Xue, F.; Jing, X. A robust and versatile superhydrophobic coating: Wear-resistance study upon sandpaper abrasion. *Applied Surface Science* **2019**, *480*, 738-748.

(233) Wang, W.; Xiang, L.; Gong, L.; Hu, W.; Huang, W.; Chen, Y.; Asha, A. B.; Srinivas, S.; Chen, L.; Narain, R. Injectable, self-healing hydrogel with tunable optical, mechanical, and antimicrobial properties. *Chemistry of Materials* **2019**, *31* (7), 2366-2376.

(234) Prajatelistia, E.; Ju, S. W.; Sanandiya, N. D.; Jun, S. H.; Ahn, J. S.; Hwang, D. S. Tunicate-Inspired Gallic Acid/Metal Ion Complex for Instant and Efficient Treatment of Dentin Hypersensitivity. *Advanced healthcare materials* **2016**, *5* (8), 919-927.

(235) Yang, H.-C.; Liao, K.-J.; Huang, H.; Wu, Q.-Y.; Wan, L.-S.; Xu, Z.-K. Mussel-inspired modification of a polymer membrane for ultra-high water permeability and oil-in-water emulsion separation. *Journal of Materials Chemistry A* **2014**, *2* (26), 10225-10230.

(236) He, M.; Sun, H.; Sun, H.; Yang, X.; Li, P.; Niu, Q. J. Non-organic solvent prepared nanofiltration composite membrane from natural product tannic acid (TA) and cyclohexane-1, 4-diamine (CHD). *Separation and Purification Technology* **2019**, *223*, 250-259.

(237) Sever, M. J.; Wilker, J. J. Absorption spectroscopy and binding constants for first-row transition metal complexes of a DOPA-containing peptide. *Dalton Transactions* **2006**, (6), 813-822.

(238) Johnson, D. A.; Nelson, P. G. Factors determining the ligand field stabilization energies of the hexaaqua 2+ complexes of the first transition series and the Irving-Williams order. *Inorganic Chemistry* **1995**, *34* (22), 5666-5671.

(239) Guo, J.; Ping, Y.; Ejima, H.; Alt, K.; Meissner, M.; Richardson, J. J.; Yan, Y.; Peter, K.; Von Elverfeldt, D.; Hagemeyer, C. E. Engineering multifunctional capsules through the assembly of metal–phenolic networks. *Angewandte Chemie International Edition* **2014**, *53* (22), 5546-5551.

(240) Mesko, M.; Xiang, L.; Bohle, S.; Hwang, D. S.; Zeng, H.; Harrington, M. J. Catechol-Vanadium Binding Enhances Cross-Linking and Mechanics of a Mussel Byssus Coating Protein. *Chemistry of Materials* **2021**, *33*(16), 6530–6540.

(241) Wang, C.; Wang, T.; Hu, P.; Shen, T.; Xu, J.; Ding, C.; Fu, J. Dual-functional anti-biofouling coatings with intrinsic self-healing ability. *Chemical Engineering Journal* **2020**, *389*, 123469.

(242) Huang, J.; Qiu, X.; Xie, L.; Jay, G. D.; Schmidt, T. A.; Zeng, H. Probing the molecular interactions and lubrication mechanisms of purified full-length recombinant human proteoglycan 4 (rhPRG4) and hyaluronic acid (HA). *Biomacromolecules* **2019**, *20* (2), 1056-1067.

(243) Raviv, U.; Laurat, P.; Klein, J. Fluidity of water confined to subnanometre films. *Nature* **2001**, *413* (6851), 51-54.

(244) Chen, M.; Briscoe, W. H.; Armes, S. P.; Klein, J. Lubrication at physiological pressures by polyzwitterionic brushes. *science* **2009**, *323* (5922), 1698-1701.

(245) Jahn, S.; Klein, J. Hydration lubrication: the macromolecular domain. *Macromolecules* **2015**, *48* (15), 5059-5075.

(246) Yang, X.; Yan, L.; Ma, J.; Bai, Y.; Shao, L. Bioadhesion-inspired surface engineering constructing robust, hydrophilic membranes for highly-efficient wastewater remediation. *Journal of Membrane Science* **2019**, *591*, 117353.

(247) Cheng, X.; Sun, Z.; Yang, X.; Li, Z.; Zhang, Y.; Wang, P.; Liang, H.; Ma, J.; Shao, L. Construction of superhydrophilic hierarchical polyacrylonitrile nanofiber membranes by in situ asymmetry engineering for unprecedently ultrafast oil–water emulsion separation. *Journal of Materials Chemistry A* **2020**, *8* (33), 16933-16942.

(248) He, Z.; Miller, D. J.; Kasemset, S.; Wang, L.; Paul, D. R.; Freeman, B. D. Fouling propensity of a poly (vinylidene fluoride) microfiltration membrane to several model oil/water emulsions. *Journal of Membrane Science* **2016**, *514*, 659-670.

(249) Cheng, X.; Liang, H.; Ding, A.; Qu, F.; Shao, S.; Liu, B.; Wang, H.; Wu, D.; Li, G. Effects of pre-ozonation on the ultrafiltration of different natural organic matter (NOM) fractions: membrane fouling mitigation, prediction and mechanism. *Journal of membrane science* **2016**, *505*, 15-25.

(250) Zhang, J.; Zhang, L.; Cui, X.; Gong, L.; Xiang, L.; Shi, C.; Hu, W.; Zeng, H. Scalable polyzwitterion–polydopamine coating for regenerable oil/water separation and underwater self-cleaning of stubborn heavy oil fouling without pre-hydration. *Chemical Communications* **2018**, *54* (70), 9734-9737.

(251) Ren, J.; Han, P.; Wei, H.; Jia, L. Fouling-resistant behavior of silver nanoparticle-modified surfaces against the bioadhesion of microalgae. *ACS applied materials & interfaces* **2014**, *6* (6), 3829-3838.

(252) Guo, H.; Liu, X.; Zhao, W.; Xie, C.; Zhu, Y.; Wen, C.; Li, Q.; Sui, X.; Yang, J.; Zhang, L. A polyvinylpyrrolidone-based surface-active copolymer for an effective marine antifouling coating. *Progress in Organic Coatings* **2021**, *150*, 105975.

(253) Mandal, S.; Song, G.; Ackerman, M.; Paskaluk, S.; Gholamreza, F. Characterization of textile fabrics under various thermal exposures. *Textile research journal* **2013**, *83* (10), 1005-1019.

(254) Winkeljann, B.; Bauer, M. G.; Marczynski, M.; Rauh, T.; Sieber, S. A.; Lieleg, O. Covalent Mucin Coatings Form Stable Anti‐Biofouling Layers on a Broad Range of Medical Polymer Materials. *Advanced Materials Interfaces* **2020**, *7* (4), 1902069.

(255) Zander, Z. K.; Becker, M. L. Antimicrobial and antifouling strategies for polymeric medical devices. *ACS Macro Lett.* **2018**, *7*(1), 16–25.

(256) Liu, Q.; Singha, P.; Handa, H.; Locklin, J. Covalent grafting of antifouling phosphorylcholine-based copolymers with antimicrobial nitric oxide releasing polymers to enhance infection-resistant properties of medical device coatings. *Langmuir* **2017**, *33* (45), 13105-13113.

(257) Selim, M. S.; El-Safty, S. A.; Shenashen, M. A.; Higazy, S. A.; Elmarakbi, A. Progress in biomimetic leverages for marine antifouling using nanocomposite coatings. *Journal of Materials Chemistry B* **2020**, *8* (17), 3701-3732.

(258) Wang, F.; Zhang, H.; Yu, B.; Wang, S.; Shen, Y.; Cong, H. Review of the research on anti-protein fouling coatings materials. *Progress in Organic Coatings* **2020**, *147*, 105860.

(259) Rana, D.; Matsuura, T. Surface modifications for antifouling membranes. *Chemical reviews* **2010**, *110* (4), 2448-2471.

(260) Sun, X.; Zeng, H.; Tang, T. Effect of non-ionic surfactants on the adsorption of polycyclic aromatic compounds at water/oil interface: A molecular simulation study. *Journal of Colloid and Interface Science* **2021**, *586*, 766-777.

(261) Li, L.; Guo, Q.; Lv, B.; Zheng, M.; Zhan, W.; Liu, Y.; Xu, W.; Wang, R.; Zeng, H.; Mao, B. Surface modified silver/magnetite nanocomposite activating hydrogen peroxide for efficient degradation of chlorophenols. *Journal of Colloid and Interface Science* **2022**, *617*, 246-256.

(262) Hu, W.; Xie, L.; Zeng, H. Novel sodium alginate-assisted MXene nanosheets for ultrahigh rejection of multiple cations and dyes. *Journal of Colloid and Interface Science* **2020**, *568*, 36-45.

(263) Parashkooh, H. I.; Jian, C. Data Mining Guided Molecular Investigations on the Coalescence of Water-in-Oil Droplets. *Energy & Fuels* **2022**, *36* (4), 1811-1824.

(264) Zou, D.; Chen, X.; Drioli, E.; Ke, X.; Qiu, M.; Fan, Y. Facile co-sintering process to fabricate sustainable antifouling silver nanoparticles (AgNPs)-enhanced tight ceramic ultrafiltration membranes for protein separation. *Journal of Membrane Science* **2020**, *593*, 117402.

(265) Yang, X.; Sun, H.; Pal, A.; Bai, Y.; Shao, L. Biomimetic silicification on membrane surface for highly efficient treatments of both oil-in-water emulsion and protein wastewater. *ACS applied materials & interfaces* **2018**, *10* (35), 29982-29991.

(266) Zhao, X.; Zhang, R.; Liu, Y.; He, M.; Su, Y.; Gao, C.; Jiang, Z. Antifouling membrane surface construction: Chemistry plays a critical role. *Journal of Membrane Science* **2018**, *551*, 145-171.

(267) Mauter, M. S.; Wang, Y.; Okemgbo, K. C.; Osuji, C. O.; Giannelis, E. P.; Elimelech, M. Antifouling ultrafiltration membranes via post-fabrication grafting of biocidal nanomaterials. *ACS applied materials & interfaces* **2011**, *3* (8), 2861-2868.

(268) Jian, C.; Liu, Q.; Zeng, H.; Tang, T. A molecular dynamics study of the effect of asphaltenes on toluene/water interfacial tension: surfactant or solute? *Energy & fuels* **2018**, *32* (3), 3225-3231.

(269) Goetz, L. A.; Jalvo, B.; Rosal, R.; Mathew, A. P. Superhydrophilic anti-fouling electrospun cellulose acetate membranes coated with chitin nanocrystals for water filtration. *Journal of Membrane Science* **2016**, *510*, 238-248.

(270) Damodaran, V. B.; Murthy, N. S. Bio-inspired strategies for designing antifouling biomaterials. *Biomaterials research* **2016**, *20* (1), 1-11.

(271) Kim, S.; Gim, T.; Jeong, Y.; Ryu, J. H.; Kang, S. M. Facile construction of robust multilayered PEG films on polydopamine-coated solid substrates for marine antifouling applications. *ACS applied materials & interfaces* **2017**, *10* (9), 7626-7631.

(272) Xing, C.-M.; Meng, F.-N.; Quan, M.; Ding, K.; Dang, Y.; Gong, Y.-K. Quantitative fabrication, performance optimization and comparison of PEG and zwitterionic polymer antifouling coatings. *Acta biomaterialia* **2017**, *59*, 129-138.

(273) Zhao, M.; Yang, Y.; Yu, H.; Zhang, X.; Tian, X.; Fu, S.; Zhang, H. Improving the biofouling resistance of polyamide thin-film composite membrane via grafting polyacrylamide brush on the surface by in-situ atomic transfer radical polymerization. *Journal of Membrane Science* **2021**, *629*, 119283.

(274) Shin, E.; Lim, C.; Kang, U. J.; Kim, M.; Park, J.; Kim, D.; Choi, W.; Hong, J.; Baig, C.; Lee, D. W. Mussel-inspired copolyether loop with superior antifouling behavior. *Macromolecules* **2020**, *53* (9), 3551-3562.

(275) Zhai, Y.; Chen, X.; Yuan, Z.; Han, X.; Liu, H. A mussel-inspired catecholic ABA triblock copolymer exhibits better antifouling properties compared to a diblock copolymer. *Polymer Chemistry* **2020**, *11* (28), 4622-4629.

(276) Shui, T.; Pan, M.; Lu, Y.; Zhang, J.; Liu, Q.; Nikrityuk, P. A.; Tang, T.; Liu, Q.; Zeng, H. High-efficiency and durable removal of water-in-heavy oil emulsions enabled by delignified and carboxylated basswood with zwitterionic nanohydrogel coatings. *Journal of Colloid and Interface Science* **2022**, *612*, 445-458.

(277) Kang, T.; Banquy, X.; Heo, J.; Lim, C.; Lynd, N. A.; Lundberg, P.; Oh, D. X.; Lee, H.-K.; Hong, Y.-K.; Hwang, D. S. Mussel-inspired anchoring of polymer loops that provide superior surface lubrication and antifouling properties. *Acs Nano* **2016**, *10* (1), 930-937.

(278) Tian, S.; Jiang, D.; Pu, J.; Sun, X.; Li, Z.; Wu, B.; Zheng, W.; Liu, W.; Liu, Z. A new hybrid silicone-based antifouling coating with nanocomposite hydrogel for durable antifouling properties. *Chemical Engineering Journal* **2019**, *370*, 1-9.

(279) Zhang, X.; Chen, J.; He, J.; Bai, Y.; Zeng, H. Mussel-inspired adhesive and conductive hydrogel with tunable mechanical properties for wearable strain sensors. *Journal of Colloid and Interface Science* **2021**, *585*, 420-432.

(280) Yang, B.; Ayyadurai, N.; Yun, H.; Choi, Y. S.; Hwang, B. H.; Huang, J.; Lu, Q.; Zeng, H.; Cha, H. J. In vivo residue-specific dopa-incorporated engineered mussel bioglue with enhanced adhesion and water resistance. *Angewandte Chemie* **2014**, *126* (49), 13578-13582.

(281) Zhang, H.; Yu, L.; Ma, X.; Peng, Y.; Hu, J.; Ruan, S. Self-cleaning poly (L-dopa)-based coatings with exceptional underwater oil repellency for crude oil/water separation. *Applied Surface Science* **2020**, *510*, 145402.

(282) Huang, Q.; Liu, M.; Guo, R.; Mao, L.; Wan, Q.; Zeng, G.; Huang, H.; Deng, F.; Zhang, X.; Wei, Y. Facile synthesis and characterization of poly (levodopa)-modified silica nanocomposites via self-polymerization of levodopa and their adsorption behavior toward Cu 2+. *Journal of Materials Science* **2016**, *51* (21), 9625-9637.

(283) Wang, Z.; Han, M.; Zhang, J.; He, F.; Peng, S.; Li, Y. Investigating and significantly improving the stability of tannic acid (TA)-aminopropyltriethoxysilane (APTES) coating for enhanced oil-water separation. *Journal of Membrane Science* **2020**, *593*, 117383.

(284) Sun, Z. K.; Zhou, Y.; Jiao, Y.; Cheng, X. Q.; Zhang, Y.; Wang, P.; Liang, H.; Yang, X.; Drioli, E.; Figoli, A. Multi-hydrophilic functional network enables porous membranes excellent anti-fouling performance for highly efficient water remediation. *Journal of Membrane Science* **2020**, *608*, 118191.

(285) Tong, W.; Zhang, Y.; Zhang, Q.; Luan, X.; Duan, Y.; Pan, S.; Lv, F.; An, Q. Achieving significantly enhanced dielectric performance of reduced graphene oxide/polymer composite by covalent modification of graphene oxide surface. *Carbon* **2015**, *94*, 590-598.

(286) Liu, J.; Cui, X.; Huang, J.; Xie, L.; Tan, X.; Liu, Q.; Zeng, H. Understanding the stabilization mechanism of bitumen-coated fine solids in organic media from non-aqueous extraction of oil sands. *Fuel* **2019**, *242*, 255-264.

(287) Lim, C.; Huang, J.; Kim, S.; Lee, H.; Zeng, H.; Hwang, D. S. Nanomechanics of poly (catecholamine) coatings in aqueous solutions. *Angewandte Chemie International Edition* **2016**, *55* (10), 3342-3346.

(288) Tang, C.; Brodie, P.; Li, Y.; Grishkewich, N. J.; Brunsting, M.; Tam, K. C. Shape recoverable and mechanically robust cellulose aerogel beads for efficient removal of copper ions. *Chemical Engineering Journal* **2020**, *392*, 124821.

(289) Lau, S. K.; Yong, W. F. Recent Progress of Zwitterionic Materials as Antifouling Membranes for Ultrafiltration, Nanofiltration, and Reverse Osmosis. *ACS Applied Polymer Materials* **2021**, *3* (9), 4390-4412.

(290) Wang, Z.; Han, M.; Zhang, J.; He, F.; Xu, Z.; Ji, S.; Peng, S.; Li, Y. Designing preferable functional materials based on the secondary reactions of the hierarchical tannic acid (TA)-aminopropyltriethoxysilane (APTES) coating. *Chemical Engineering Journal* **2019**, *360*, 299-312.

(291) Yang, W.; Hu, W.; Zhang, J.; Wang, W.; Cai, R.; Pan, M.; Huang, C.; Chen, X.; Yan, B.; Zeng, H. Tannic acid/Fe3+ functionalized magnetic graphene oxide nanocomposite with high loading of silver nanoparticles as ultra-efficient catalyst and disinfectant for wastewater treatment. *Chemical Engineering Journal* **2020**, 126629.

(292) Huang, X.; Lu, J.; Wang, W.; Wei, X.; Ding, J. Experimental and computational investigation of CO2 capture on amine grafted metal-organic framework NH2-MIL-101. *Applied Surface Science* **2016**, *371*, 307-313.

(293) Yang, W. J.; Cai, T.; Neoh, K.-G.; Kang, E.-T.; Teo, S. L.-M.; Rittschof, D. Barnacle cement as surface anchor for "clicking" of antifouling and antimicrobial polymer brushes on stainless steel. *Biomacromolecules* **2013**, *14* (6), 2041-2051.

(294) Qiao, C.; Wang, D.; Zhao, Z.; Yang, W.; Wu, F.; Chen, H.; Yin, T.; Zhang, L.; Liu, Q.; Yang, D. Bench-scale oil fouling/antifouling tests under high temperature and high pressure conditions and the underlying interfacial interaction mechanisms. *Fuel* **2022**, *314*, 122720.

(295) Zang, L.; Zheng, S.; Wang, L.; Ma, J.; Sun, L. Zwitterionic nanogels modified nanofibrous membrane for efficient oil/water separation. *Journal of Membrane Science* **2020**, *612*, 118379.

(296) Shao, L.; Wang, Z. X.; Zhang, Y. L.; Jiang, Z. X.; Liu, Y. Y. A facile strategy to enhance PVDF ultrafiltration membrane performance via self-polymerized polydopamine followed by hydrolysis of ammonium fluotitanate. *Journal of Membrane Science* **2014**, *461*, 10-21.

(297) Wang, Z.; Ji, S.; He, F.; Cao, M.; Peng, S.; Li, Y. One-step transformation of highly hydrophobic membranes into superhydrophilic and underwater superoleophobic ones for high-efficiency separation of oil-in-water emulsions. *Journal of Materials Chemistry A* **2018**, *6* (8), 3391-3396.

(298) Xiong, Z.; Lin, H.; Zhong, Y.; Qin, Y.; Li, T.; Liu, F. Robust superhydrophilic polylactide (PLA) membranes with a TiO 2 nano-particle inlaid surface for oil/water separation. *Journal of Materials Chemistry A* **2017**, *5* (14), 6538-6545.

(299) Shi, H.; He, Y.; Pan, Y.; Di, H.; Zeng, G.; Zhang, L.; Zhang, C. A modified mussel-inspired method to fabricate TiO2 decorated superhydrophilic PVDF membrane for oil/water separation. *Journal of membrane science* **2016**, *506*, 60-70.